Approches problèmes inverses en microscopie holographique pour la reconstruction non-supervisée et quantitative d'échantillons microbiologiques

Dylan Brault

N°d'ordre NNT : 2022STET0062

THÈSE de DOCTORAT
DE L'UNIVERSITÉ JEAN MONNET SAINT-ÉTIENNE

Membre de la COMUE de LYON

École Doctorale 488
Science Ingénierie Santé

Spécialité / discipline de doctorat : Image

Soutenue publiquement le 19/12/2022, par :
Dylan Brault

Inverse problems approaches in digital holographic microscopy for unsupervised and quantitative multispectral reconstructions of microbiological samples

---

Devant le jury composé de :

Olivier Haeberlé	Professeur	Univ. de Haute Alsace	Président
François Goudail	Professeur	IOGS, Palaiseau	Rapporteur
Laurent Mugnier	Directeur de Recherche	ONERA	Rapporteur
Laure Blanc-Féraud	Directrice de Recherche	CNRS, I3S	Examinatrice
Emmanuel Soubies	Chargé de Recherche	CNRS, IRIT	Examinateur
Pauline Trouvé-Peloux	Ingénieure de Recherche	ONERA	Examinatrice
Ferréol Soulez	Astronome Adjoint	Univ. Claude Bernard Lyon 1	Encadrant
Corinne Fournier	Maître de conférences HDR	Univ. Jean Monnet	Directrice
Thomas Olivier	Maître de conférences	Univ. Jean Monnet	Invité
Fabien Momey	Maître de conférences	Univ. Jean Monnet	Invité
Nicolas Faure	Ingénieur de Recherche	bioMérieux	Invité

Remerciements

Tout d'abord j'aimerais adresser mes remerciements aux membres du jury pour leur analyse de ces travaux de thèse, leurs remarques ont permis de nombreuses discussions pour lesquelles je suis sincèrement reconnaissant. Je remercie Olivier Haeberlé d'avoir accepté la présidence de ce jury ainsi que pour les diverses discussions qui ont pu avoir lieu durant cette thèse me permettant notamment d'améliorer ma compréhension de l'imagerie de phase et en m'ouvrant à d'autres systèmes imageurs. Mes remerciements s'adressent ensuite à Laurent Mugnier et François Goudail pour leur lecture attentive de ce manuscrit. Leurs différentes suggestions et remarques ont permis d'améliorer certains points de ce document afin de le rendre plus pédagogique. Enfin je tiens à remercier Laure Blanc-Féraud, Pauline Trouvé-Peloux et Emmanuel Soubies d'avoir accepté d'examiner ces travaux. J'ai beaucoup apprécié la diversité des questions qui ont pu être posées notamment sur les limites de la méthodologie présentée dans ce manuscrit et sur ses applications potentielles.

Je tiens particulièrement à remercier Nicolas Faure, pour son analyse de ses travaux, ainsi que l'ensemble de l'équipe de BioAster, en particulier Sophie Dixneuf, pour leur aide précieuse quant à l'acquisition et l'annotation des données. L'application des développements de cette thèse à des données expérimentales m'a tenu énormément à cœur et leur implication dans ces travaux a été essentielle au bon déroulement de cette thèse. Les questionnements soulevés lors de nos discussions quant aux limites et aux applications ont toujours été très stimulants et motivants dans le développement de ces méthodologies.

Les remerciements suivants sont adressés aux personnes à qui je dois toute ma reconnaissance pour leur implication, leur soutien et leur enthousiasme à toute épreuve sans qui cette thèse n'aurait pu être possible.

Tout d'abord, je tiens à remercier vivement Corinne Fournier. Ton implication durant cette thèse a été plus qu'exceptionnelle et mon épanouissement alors que celle-ci touche à sa fin t'es en grande partie dû. Ton encadrement durant cette thèse, du traitement des images à l'analyse des résultats en passant par la rédaction m'a permis de ne pas m'éparpiller. Ton envie de transmettre aussi bien en recherche que dans l'enseignement force l'admiration et je te remercie sincèrement pour les différentes opportunités que tu as pu me proposer aussi bien dans l'encadrement de stagiaires que dans les travaux d'enseignements que nous avons pu effectuer ensemble. Parce qu'un travail de thèse im-

plique des moments de doutes, je tiens à souligner tes qualités humaines qui m'ont plus d'une fois permis de ne pas désespérer.
De la même manière j'aimerai remercier le deuxième pilier de cette thèse, Thomas Olivier, à qui je dois la plupart de ma compréhension des phénomènes de propagation. Si Corinne m'a appris à comprendre les problèmes inverses, tu m'as fait comprendre les modèles. Tes analyses complémentaires à celles de Corinne m'ont bien souvent permis de mieux visualiser les directions à prendre et à bien cerner les problématiques à résoudre. Nos discussions confrontant l'optique et le numérique pour mieux cerner les problématiques de l'un et de l'autre ont été des plus motivantes. Ton dynamisme dans l'exploration de nouveaux modèles et ton implication dans l'analyse des résultats, pour toujours mieux comprendre ce que nous observions ont toujours été stimulants pour moi. Enfin, merci pour ton soutien lorsque « tout était un peu trop corrélé » ou lorsque nous n'avions pas notre « effet wow » qui a souvent été source de remotivation.
Je tiens ensuite à remercier Ferréol Soulez, ton rôle a été plus qu'indispensable dans cette thèse. Bien qu'à distance, tes interventions ont toujours été très pertinentes. Je me rappelle d'une discussion en fin de deuxième année au sujet de l'histoire de cette thèse. Un petit moment de remise en question pour moi mais qui je crois a été bénéfique. J'ai fini par trouver l'histoire que je voulais raconter et je te remercie vraiment de m'avoir redirigé à ce moment-là.
Bien que ne faisant pas officiellement partie de la liste de mes encadrants, je tiens à remercier Loïc Denis pour les discussions que nous avons pu avoir. Loïc Denis est à l'origine de l'approche proposée dans le chapitre 3 et sa contribution dans cette thèse est loin d'être anodine. Je te remercie pour la disponibilité dont tu as fait preuve pour m'aider lorsque j'en avais besoin, pour répéter une présentation ou pour me donner ton avis sur telle ou telle méthode à employer.
Enfin je remercie Fabien Momey pour son encadrement durant cette thèse, tu m'as permis de m'ouvrir sur d'autres problématiques avec notamment les travaux de Laurence, et ton enthousiasme m'a souvent permis de relativiser sur certaines problématiques.

Quel privilège j'ai eu de pouvoir travailler avec vous !

Je remercie Christophe Ducottet, Olivier Alata, Hubert Konik et Mathieu Hebert pour leur confiance et leurs conseils lors de mes premiers pas dans l'enseignement. Je tiens à remercier Thierry Fournel, qui a toujours eu le bon mot pour me soutenir, Laurence Denneulin qui m'a initié au réglages automatique d'hyperparamètres et l'ensemble des collègues qui ont pu échanger avec moi dans le bureau E005 : Olivier Flasseur, Anthony Berdeux, Alexey Brodoline, Louis Thibon et Sachin Joshi. Enfin j'ai une pensée pour les étudiants que j'ai pu co-encadrer durant mon passage au laboratoire : Carlos Valadares, Alice Lesage, Sami Elouafkaoui, Thomas Brard, Dorian Pillard et Thomas Bultingaire. Un grand merci à vous tous pour les discussions toujours intéressantes que nous avons pu avoir !

Mes remerciements se dirigent ensuite vers mes amis avec qui j'ai pu déconnecter de cette thèse. Mes pensées se tournent vers une équipe de rôlistes qui se reconnaitra dans ces lignes et grâce à qui les moments de doutes se sont vites transformés en moments de rires ! Même Iris vous remercierait pour tout ce que vous avez fait pour moi !

Je tiens ensuite à remercier Orane, Greg, Flo, Raphaël, Louis et Alexis parce que leur présence à toute épreuve est une réelle source de joie. Parce qu'une thèse n'est pas qu'un travail scientifique, une partie de cette thèse leur est due.

Enfin mes remerciements se tournent vers mes piliers de vie. Bien plus que pour une thèse, leur implication est celle que j'admire le plus. Je remercie mes parents pour leur soutien sans faille. Cette thèse n'aurait pas pu avoir lieu si vous n'aviez pas été là. Vous êtes un exemple pour moi. Et je ne peux vous remercier assez pour ce que je vous dois. Je me tourne ensuite vers ma sœur... quelle chance j'ai de t'avoir à mes côtés ! Ne change pas d'un pouce ! Tu es essentielle à ma vie. Et je te remercie d'être toi-même. Je te remercie au passage, Kathleen, de mettre ce beau sourire sur le visage de ma sœur.

Et le dernier, mais pas des moindres, je te remercie Maxime pour tout ce que tu es. Notre histoire commence là où cette thèse s'achève... et je ne pourrai être plus heureux de cette conclusion.

Contents

Notations

Conventions of notation

$\boldsymbol{x}$	a vector/ a matrix
x	a scalar

Quantities specific to microscopy applications

$\boldsymbol{d}$	data
$\boldsymbol{h}_z$	propagator kernel
$\underline{\boldsymbol{h}}^{\mathrm{RS}}$	Rayleigh-Sommerfeld propagator kernel
$\underline{\boldsymbol{t}}$	transmittance plane
$\underline{\boldsymbol{a}}^{\mathrm{Mie}}$	complex Mie model
$\boldsymbol{m}$	model
$\cdot^{\mathrm{P}}$	parametric
$\cdot^{\mathrm{NP}}$	non-parametric
$\boldsymbol{\vartheta}$	parameters vector
$\boldsymbol{Z}$	Zernike Polynomials
$\boldsymbol{\alpha}$	Zernike coefficients
$\underline{\widetilde{p}}$	pupil function
$\boldsymbol{\Lambda}$	set of wavelengths

Other mathematical functions and notations

$*$	convolution operator
$\widetilde{\cdot}, \mathscr{F}$	Fourier transform
$\Re, \Im$	real/imaginary part

$\cdot^{\mathrm{T}}$ transpose operator

∇_i gradient with respect to i

$\mathrm{div}(\cdot)$ divergence

$\mathrm{tr}(\cdot)$ matrix trace

Statistics

$\hat{\cdot}$ estimator

$\mathbb{E}$ expectation

$\mathcal{N}(a, \boldsymbol{B})$ probability density function of a multivariate Gaussian of mean a and covariance matrix $\boldsymbol{B}$

$\mathcal{H}_0, \mathcal{H}_1$ binary hypothesis

LR Likelihood Ratio

$\mathscr{D}$ data-fidelity

$\mathscr{L}$ non-parametric cost function

$\mathscr{R}$ regularization

$\boldsymbol{\mu}$ regularization hyperparameters

Var variance

σ standard deviation

$< \cdot >$ average

$\boldsymbol{\Sigma}$ covariance matrix

Cor correlation matrix

$\mathscr{Q}$ quality of the reconstruction criterion

Scientific Context

Microscopy is routinely used in medical diagnosis, like infectious diseases detection and/or characterization, blood components morphological analysis and counting or cancerous tissue analysis. Most of these diagnoses are performed manually. Thus, the diagnosis is subjective, depending on the microbiologist, from the preparation of the sample to the analysis of the images. Automation of this process is then required to perform an objective diagnosis [Smith et al., 2018].

One of the main difficulty in this automation process is to obtain reproducible and quantitative data to analyze. Using simple microscopy setups is an easy way to increase this repeatability. Brightfield microscopy is thus one of the most popular microscopy technique to observe micrometers-sized objects like cells or bacteria. However this microscopy technique can only be used on absorbing objects. Thus to observe transparent objects, also called phase objects, the samples must be stained [Prescott et al., 2002], leading to an intrusive process, that may also introduce variability depending on the sample preparation.

Coherent imaging techniques, like digital in-line holographic microscopy, may provide a solution to this issue since they are not only sensitive to the sample absorption but also to the phase shift they introduce. This technique is based on the measurements of the diffraction patterns created by the objects. It is thus no more limited by the depth-of-field of the microscope and does not require an accurate and expensive translation stage. The autofocusing step is performed numerically making this technique valuable candidate for the automation procedure in bio-medical analysis.

This thesis has been prepared at the Hubert Curien Laboratory (LaHC), Saint-Etienne, France, and funded by the Auvergne-Rhônes-Alpes region under the DIAGHOLO (DIAGnostic microbiologique par microscopie HOLOgraphique) project. The LaHC is a joint research unit of the Jean Monnet University (UJM), the French National Centre for Scientific Research (CNRS), and the Institut d'Optique Graduate School (IOGS). In particular, the laboratory research covers two main subjects "Optics, Photonics and Microwave" and "Computer Science, Telecom and Image". I was involved in the Optical Design and Image Reconstruction team led by Loïc Denis, at the interface between optics and signal & image processing.

Holography microscopy, and more specifically in-line holographic reconstructions, is one of the team main research subject. In this field, many contributions have been applied to fluid mechanics starting with Corinne Fournier's thesis in 2003. Inverse problems approaches framework has been adopted to reconstruct hologram during Loïc Denis' (2006)

and Ferréol Soulez's (2008) thesis. Since then, Jerôme Gire's (2009) and Mozhdeh Seifi's (2013) thesis enforced the expertise of the team on inverse problems approaches by increasing the collaborations with the Centre d'Astrophysique de Lyon (CRAL) and the Laboratoire de Mécanique des Fluides et d'Acoustique (LMFA). Fréderic Jolivet's thesis (2018) pursued the work of Loïc Denis on non-parametric objects reconstructions [Denis et al., 2009] by applying them in fluid mechanics and microbiological samples providing to the team a first microscopic application for holography and a collaboration with bioMérieux [Jolivet et al., 2018]. Olivier Flasseur's thesis (2019) improved the reconstruction of parametric objects (like calibrations bead) by introducing robust processing in the inverse problem approaches [Flasseur et al., 2017a] and by reconstructing color (Red Green Blue) holograms with a self-calibrated microscope in the framework of parametric inverse problem approaches [Flasseur et al., 2017b].

This thesis extends the collaboration with bioMérieux to multispectral reconstructions of biological sample in the context of biomedical diagnosis automation using digital in-line holography. In this context, three main aspects of the reconstructions have been studied: their repeatability, their reproducibility and their quantitativity. These conditions are fundamental to perform an objective diagnosis whatever the sample and the setup.

The biological context of this thesis consists in reconstructing multispectral holograms in order to classify Gram stained bacteria. Thus two main axis have been studied during this thesis:

- **Axis 1: Automation of the numerical reconstruction**
  This axis rises the question of repeatable and reproducible unsupervised reconstructions in biological sample context, more specifically the reconstruction of bacteria surrounded by other biological objects introducing noise.

- **Axis 2: Bacteria discrimination using multispectral information**
  This axis rises the question of the quantitativity of the reconstructions and the use of spectral information to discriminate bacteria.

To improve the reconstructions, three main methodological solutions have been studied. These methodological solutions constitute the main parts of this manuscript:

- **Self-calibration of the image formation model**
  To perform repeatable and quantitative reconstructions, the image formation model (forward model) must be accurate, thus focusing distance and aberration depending of the setup must be calibrated using objective criteria.

- **Unsupervised tuning of the regularization hyperparameters**
  Since the reconstruction process require the use of prior, the weight of these priors must be objectively tuned to provide reproducible and quantitative reconstructions.

- **Exploiting phase diversity in multispectral reconstructions**
  To exploit the multispectral information contained in multispectral data stack, the registration of the data is crucial and can be compromised by chromatic aberrations. These aberrations must thus be taken into account in the reconstruction process.

In this thesis, we suggest to use objective criteria for automation of the reconstruction process that rely on calibration beads inserted in the sample. Thus, this thesis exploits

all the information provided by these calibration beads in order to automatize the reconstruction process.

During this thesis, all the algorithms were developped using the GlobalBioIm framework [Soubies et al., 2019]. This free Matlab library provides generic modules to facilitate the implementation of inverse problem approaches.

Part I

Introduction

CHAPTER 1

Image processing challenges for phase objects characterization in holographic microscopy

Abstract

Bloodstream infections are rapidly evolving infections for which each day of delay of the care causes high increasing of the mortality probability. Thus, fast identification of the pathogenic agent must be performed. Gram staining is a commonly used technique to classify bacteria and orient quickly the therapy by only using a brightfield microscope. However, Gram stain interpretation is a highly operator dependent process. Automatization of the Gram stain interpretation is thus required to perform faster and more objective diagnoses. Since in-line holographic microscopy is based on recording the diffraction patterns created by the sample, it is not limited by the depth-of-field. Thus, due to its simplicity and its adaptability to other setups, in-line holography is a method of choice to automatize the Gram stain interpretation process. Indeed, in addition to opacity information, in-line holography is sensitive to the phase information that can be a key to help imaging analysis and object classification.
In this chapter we present the biomedical context, digital holographic microscopy, numerical reconstruction of holograms and the thesis challenges.

Introduction: Biomedical context

Optical microscopy is a key tool in biomedical diagnosis [Forbes et al., 2007, Dey et al., 2015]. It consists in generating magnified images of small objects by using a light source and a system of lenses. Pathologists are able to investigate biological samples by interpreting the absorption, the color and the morphology of the sample.

In the context of analysis of infections in blood smear samples, as illustrated in this

manuscript, optical microscopy is used as a first step to orient the care. Indeed, for non-infected patient, blood is sterile, if not, identifying the bacteria responsible for the infection is a medical emergency [Barenfanger et al., 2008].

To perform the diagnosis on a blood smear sample, the first step consists in preincubating the patient blood in broth culture to detect the presence of bacteria. Few hours are needed to detect the bacteria. Once a sufficient number of bacteria have been developed, the blood culture is positive and can be analyzed using, for example Gram analysis.

The sample is spread out on a slide using either an inoculation loop or, as in our experiments, using the wedge technique. It is then fixed, *i.e.* dehydrated, by heating or using ethanol or methanol. However, if the sample is heated, red blood cells can be degraded. In our experiment, ethanol is used to fix the sample. Thus, the bacteria cell wall is degraded so that they become dehydrated.

Most cells and bacteria are thin and transparent thus not observable in bright field microscopy without staining the sample or without adding optics that allows the phase shift of light induced by the cells to be seen *e.g.* phase contrast microscopy [Zernike, 1942] or interferometric microscopy [Gabor, 1948, Wolf, 1969]. Figure 1.1 illustrates two samples containing the same biological objects with and without staining. As seen on this figure, bacteria are not visible when not stained.

After the fixation process, the sample can be stained so that bacteria can be discriminated. One of the most interesting staining is the Gram one, invented by Hans Christian Gram in 1884. Indeed, bacteria can be classified in two classes having different cell-walls. One is composed of a thick polypeptidic membrane (Gram+), while the other type (Gram-), has a thin polypeptidic and an external lipidic membranes. As most of the biocides are based on an interaction/degradation of the cell-wall, Gram staining is a first and fast method to orient the care.

Figure 1.2 illustrates the Gram staining procedure:

- Step 1: The sample is dyed with the violet dye so that all bacteria are stained.
- Step 2: The addition of iodine, which binds to crystal violet and traps the colorant in the bacteria.
- Step 3: The sample is then bleached using ethanol so that only gram positive bacteria are still stained.
- Step 4: Then a counterstaining is performed to stain Gram negative bacteria but with a pink or red dye

At this point, it should noticed that this whole sample preparation procedure is not standardized, thus variability depending on the biologist that prepares can be observed. Moreover, it should be noticed that at this point the dye concentration is high in the bacteria, thus their "natural" properties are modified.

If Gram staining provides a relevant information to discriminate the bacteria, their morphological properties can also be exploited. Thus, optical microscopy is commonly used to perform Gram analysis. In this manuscript we only focus on the automatization of the Gram analysis. Let us note that further non imaging studies of the sample are performed by biologists after this first step to identify accurately the bacteria in the sample. These studies require another bacteria culture and molecular analysis that are more complex and longer to perform.

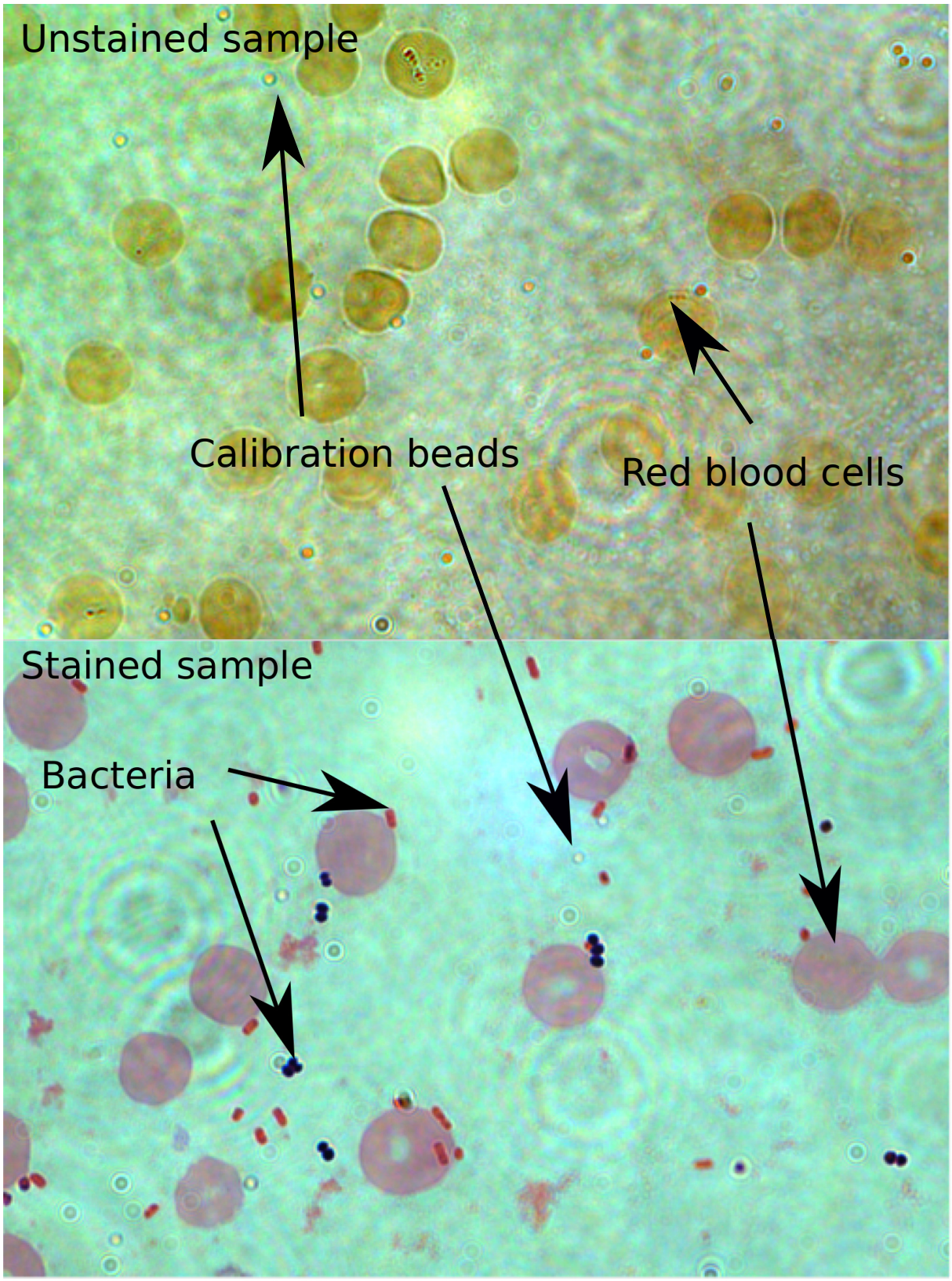

Figure 1.1: Unstained and stained blood smears observed using bright field microscopy

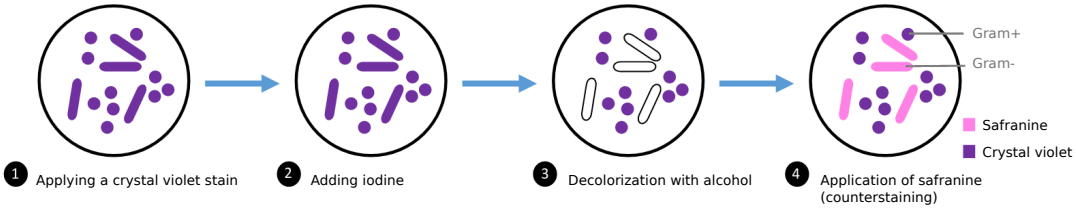

Figure 1.2: Illustration of the Gram staining procedure. Image adapted from [Jolivet, 2018].

Brightfield microscopy is the most common and simple microscopy technique to observe biological samples. The sample is illuminated so that the transmitted light is imaged on the sensor. The setup contains several adjustable optical elements to project a magnified in focus intensity image of the sample. The observed image includes dark shapes corresponding to the objects and a bright background corresponding to the light that has not been absorbed. Since the image is directly interpretable, this microscopy technique belongs to the class of conventional imaging. For example, to observe bacteria, a $\times 60$ - $\times 100$ objective are required, with a high numerical aperture ($NA \approx 1.4$) in an immersion oil medium ($n_0 \approx 1.519$). The resolution, as defined by Rayleigh's criterion ($R = 0.61\frac{\lambda}{NA} \approx 250nm$ in our case, $\lambda \approx 530nm$) is adapted to the observation of bacteria (that have a size of approximately 1-2 μm). This technique is commonly used for its simplicity. However, it is limited to the study of absorbing samples and by its small depth-of-field ($DOF = \frac{n\lambda}{NA^2} \approx 400nm$ in our case) and is highly dependent of the optical settings (illumination coherence, focus, aberrations, color of the source) as illustrated on Figure 1.3. In this Figure, the same types of bacteria are observed using different focusing distance and different spatial coherence of the illumination. These small changes in the optical system lead to high variations of the color of the observed sample. Figure 1.4 illustrates an even more difficult case to perform diagnosis as bacteria colors changes due to small defocus distances in the field-of-view. Due to the high variability of the observed images, standardization and automation of Gram analysis is needed to perform more objective diagnosis [Smith et al., 2018].

In this context, in-line holography provides a simple and low-cost alternative to observe transparent objects like cells or bacteria. Moreover, it is simply adaptable on existing systems. As this technique is based on the recording of the diffraction patterns induced by the biological objects, it is no more limited by the depth-of-field of the microscope. It is thus a valuable candidate for automation process and does not require an accurate and expensive translation stage.

Moreover, even with stained samples, holography provides an additional information, the phase shift introduced by the sample, that may lead to better fiability of the diagnosis.

However, the diffraction patterns are not directly interpretable, thus the holograms need post-processing algorithms, called *reconstruction* algorithms, to be interpreted. This microscopy technique belongs to the class of computational imaging.

At last, it should be mentioned that, due to the recording of the diffraction patterns of the objects, staining may even not be needed to observe the sample leading to *in vivo* applications. This subject is not covered in this manuscript.

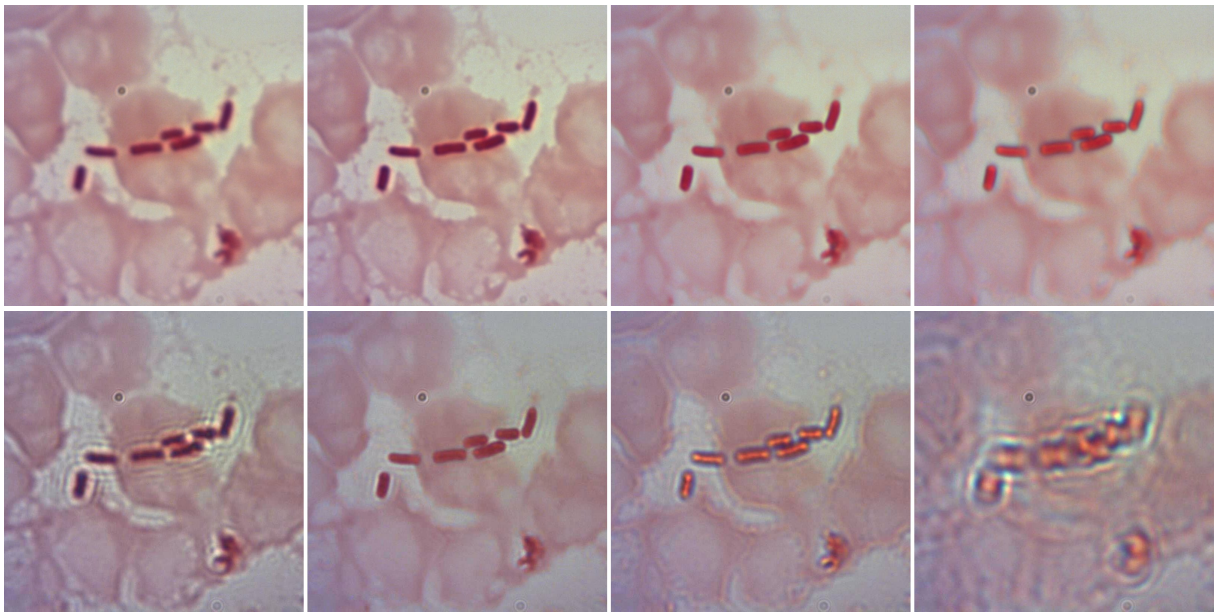

Figure 1.3: Brightfield acquisitions of the same sample under several optical settings: from left to right the focus varies, from top to bottom the spatial coherence of the light source varies (top: low coherence, bottom: high coherence) (©Thomas Olivier)

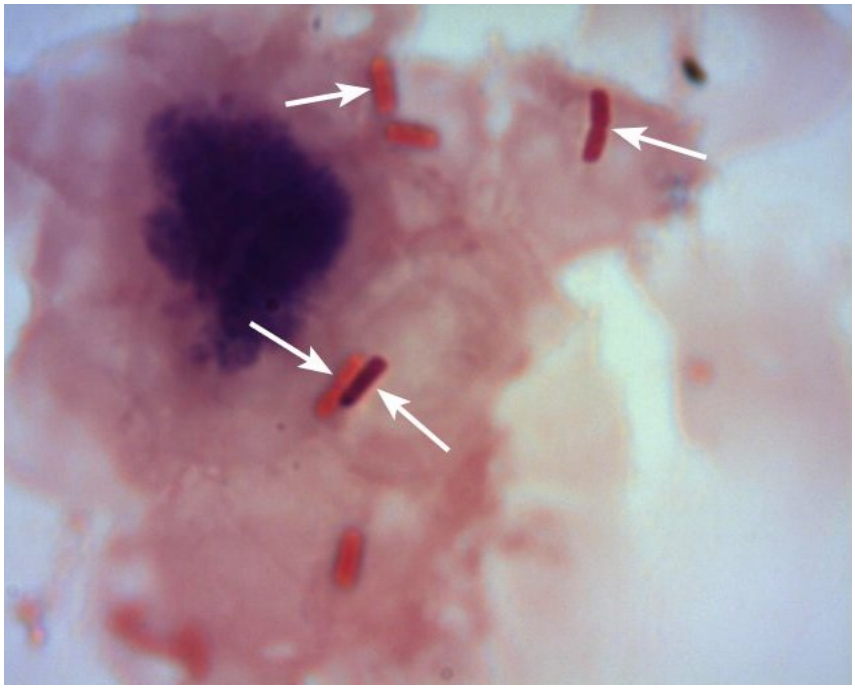

Figure 1.4: Brightfield acquisition of bacteria varying in color due to small focus differences (©Thomas Olivier)

A In-line holographic microscopy

Holographic microscopy is a widely known method to provide phase information (*i.e.* refractive properties) of weakly absorbing objects like cells or bacteria [Marquet et al.,

2005, Popescu, 2011]. This method was invented by D. Gabor in 1948 [Gabor, 1948] but remained a theoretical concept due to the low coherence of the light sources at the time. However with the development of laser sources, and by exploiting numerical reconstruction algorithms [Gerchberg, 1972, Fienup, 1982], holographic microscopy was able to develop and became a method of choice in the phase imaging domain.

Based on D. Gabor's setup, in-line holographic microscopy proposes to record the diffraction pattern (out of focus image) produced by the sample after propagation over the distance z when illuminated by a plane and coherent wave. The resulting image is the so-called *hologram*. Figure 1.5 illustrates the recording of a lensless in-line hologram.

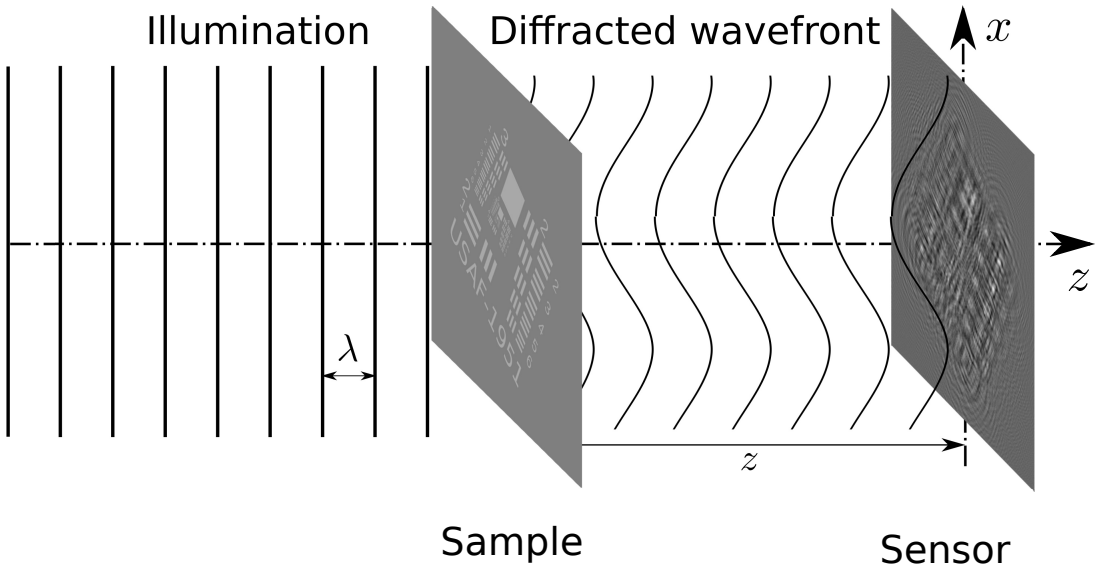

Figure 1.5: Illustration of the recording of a in-line hologram. Image from [Ferréol Soulez, TBP].

Digital holography is a two step process a illustrated on Figure 1.6: (a) the recording of the hologram, *i.e.* recording the intensity of the diffraction patterns of the sample on the sensor, (b) the reconstruction of the hologram, *i.e.* retrieving the complex amplitude of the wavefront (modulus and phase) that has been diffracted in the sample plane. This reconstruction step can be seen as a numerical focusing step.

A.1 Rayleigh-Sommerfeld diffraction model

First, let us interest in the *image formation model*. In this section the notations that will be used are reported on Figure 1.7.

In this model the sample is considered to be equivalent to a 2D transmittance plane $\underline{\boldsymbol{t}}$. After passing through the sample plane, the complex amplitude orthogonal to the optical axis $\underline{U}(x, y, 0^+)$ is expressed as:

$$\underline{U}(x, y, 0^+) = \underline{U}(\xi, \upsilon, 0^-) \cdot \underline{t}(\xi, \upsilon) \tag{1.1}$$

where $\underline{U}(\xi, \upsilon, 0^-)$ is the the complex amplitude of the incident wave on the sample plane.

The propagation can be modeled by the Rayleigh-Sommerfeld diffraction formula [Goodman, 2004]. For a monochromatic illumination wavefront with a wavelength λ,

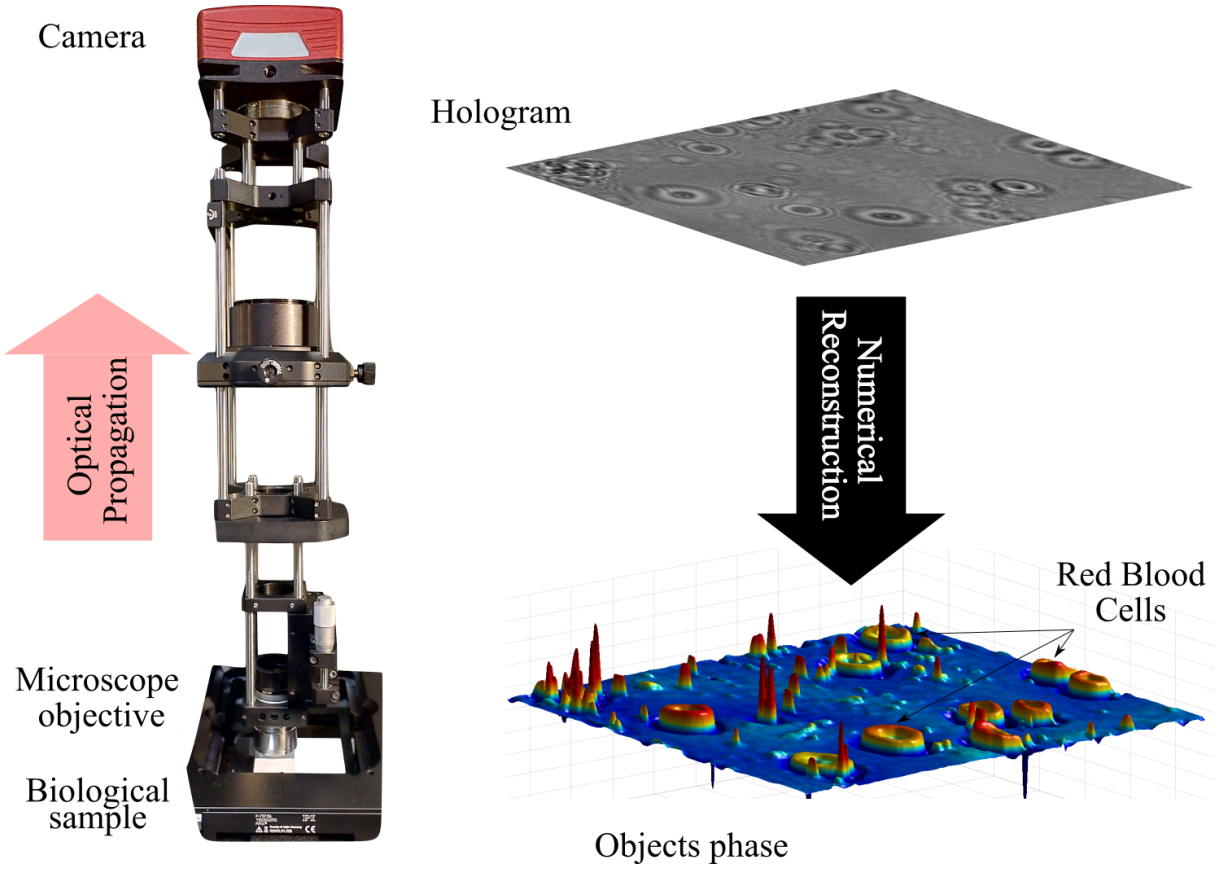

Figure 1.6: Principle of in-line holography

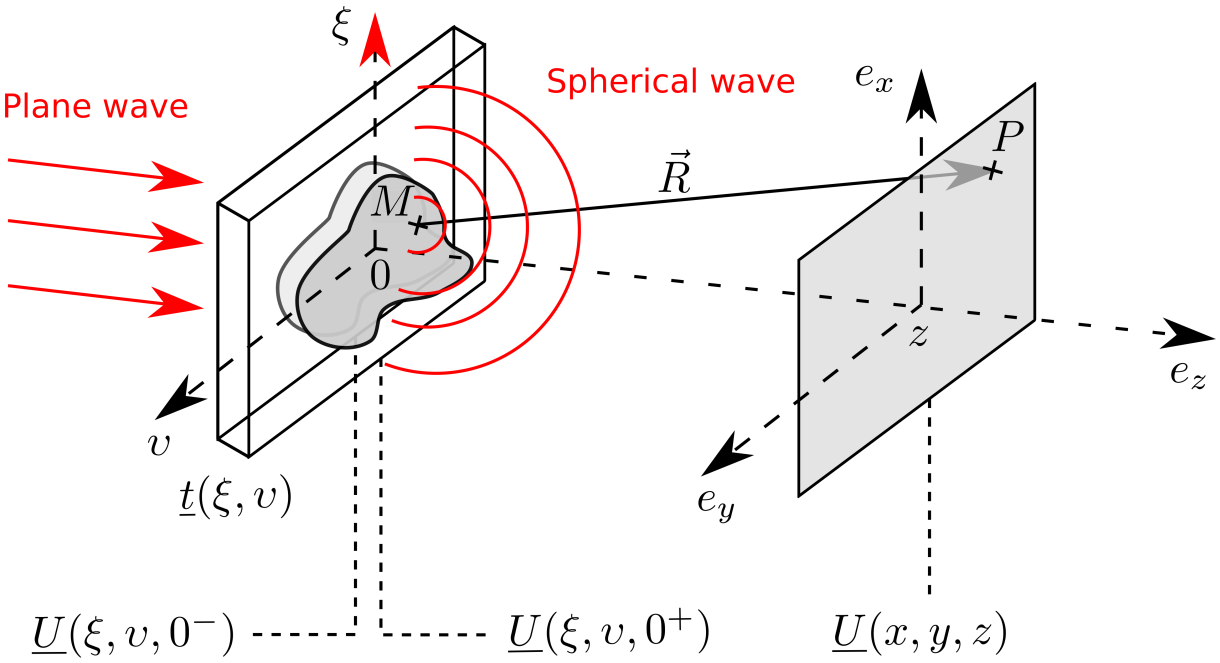

Figure 1.7: Illustration of the Rayleigh-Sommerfeld diffraction model

the amplitude of wavefront $\underline{U}(x,y,z)$ diffracted by a transmittance plane $\underline{\boldsymbol{t}}$ recorded on

the sensor at a given point $P(x, y, z)$ is modeled by:

$$\underline{U}(x, y, z) = \frac{1}{i\lambda} \iint_{-\infty}^{+\infty} \underline{U}(\xi, \upsilon, 0^+) \frac{e^{ikR}}{R} \cos(\theta) d\xi d\upsilon \tag{1.2}$$

where $R = \sqrt{(x-\xi)^2 + (y-\upsilon)^2 + z^2}$ is the distance between $M(\xi, \upsilon, 0)$, that can be considered as a secondary source (Huygens-Fresnel principle), and the observation point $P(x, y, z)$ and θ is the angle between the direction given by $\vec{e_z}$ and the direction given by $\vec{R} = \vec{MP}$. It should be noted that $\cos(\theta) = \frac{z}{R}$ is a factor corresponding to the inclination factor.

The term $\frac{e^{ikR}}{R}$ corresponds to the propagating spherical wave. Indeed, Equation 1.2 is the mathematical formulation of the Huygens-Fresnel principle [Goodman, 2004] (illustrated on Figure 1.8): the diffracted wavefront corresponds to the sum of all the spherical waves emitted by all the points of the sample. These complex amplitudes depend on the complex amplitude of the incident wave $\underline{U}(\xi, \upsilon, 0^-)$, the local transmittance $\underline{\boldsymbol{t}}$ of the sample and the propagation distance z. Using the convolution symbol $*$ Equation 1.2 can be rewritten:

$$\underline{\boldsymbol{U}} = \underline{\boldsymbol{h}}_z^{\mathrm{RS}} * \underline{\boldsymbol{U}}(\cdot, \cdot, 0^+) \tag{1.3}$$

were the Rayleigh-Sommerfeld kernel is defined by Equation A.1.

$$\underline{h}_z^{\mathrm{RS}}(x', y') = \frac{z}{i\lambda} \frac{\exp\left(i\frac{2\pi}{\lambda}\sqrt{x'^2 + y'^2 + z^2}\right)}{x'^2 + y'^2 + z^2} \tag{1.4}$$

To compute the propagation numerically, the discretization of the signal must be considered. Thus, in the following the model, the data and the convolution are discrete. Using the formulation given by equation 1.3 and the convolution theorem, the computation of the diffracted wavefront can be quickly performed in the Fourier domain. Moreover, the Fourier transform of the propagation kernel does not need to be computed as it can be done analytically (angular spectrum formula [Goodman, 2004]).

Some properties of the Rayleigh-Sommerfeld propagation [Goodman, 2004]

Rayleigh-Sommerfeld propagation has interesting properties :

- Back-propagating a complex amplitude from distance z is equivalent to conjugate the propagation kernel used for the propagation:

$$\underline{\boldsymbol{h}}_{-z}^{\mathrm{RS}} = \underline{\boldsymbol{h}}_z^{\mathrm{RS}*} \tag{1.5}$$

- Propagating and back-propagating a complex amplitude $\underline{\boldsymbol{U}}$ is equivalent to applying the identity operation on $\underline{\boldsymbol{U}}$:

$$\underline{\boldsymbol{h}}_{-z}^{\mathrm{RS}} * \left[\underline{\boldsymbol{h}}_z^{\mathrm{RS}} * \underline{\boldsymbol{U}}\right] = \underline{\boldsymbol{U}} \tag{1.6}$$

- Propagating a complex amplitude $\underline{\boldsymbol{U}}$ to distance z_1 and then propagating it to distance z_2 is equivalent to propagating $\underline{\boldsymbol{U}}$ to distance $z_1 + z_2$:

$$\underline{\boldsymbol{h}}_{z_2}^{\mathrm{RS}} * \left[\underline{\boldsymbol{h}}_{z_1}^{\mathrm{RS}} * \underline{\boldsymbol{U}}\right] = \underline{\boldsymbol{h}}_{z_1+z_2}^{\mathrm{RS}} * \underline{\boldsymbol{U}} \tag{1.7}$$

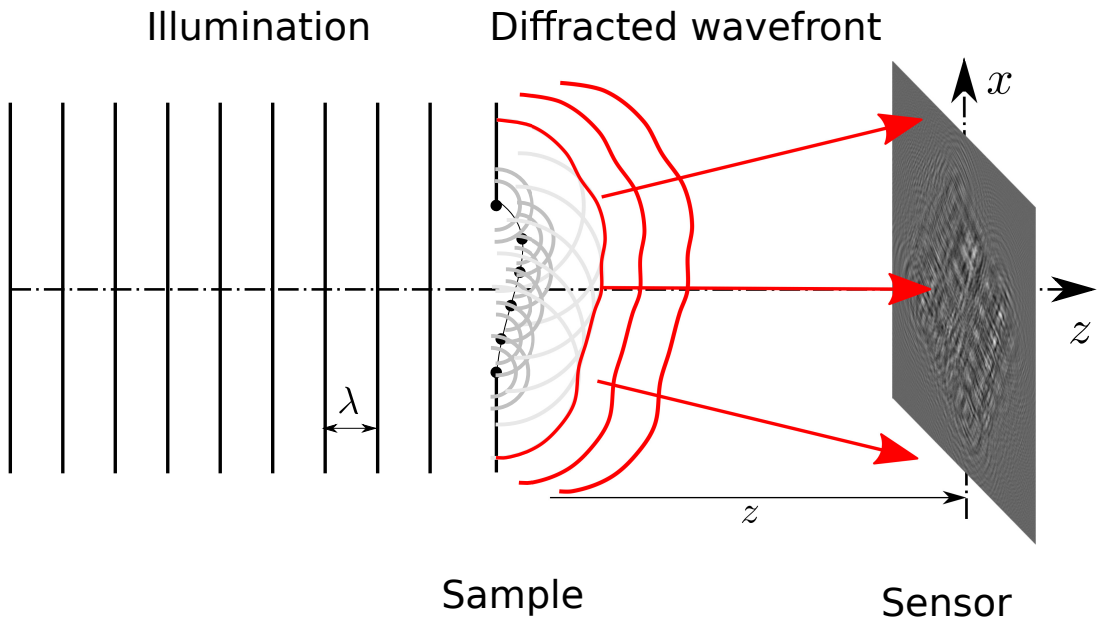

Figure 1.8: Illustration of the Huygens-Fresnel principle

In this manuscript, it is assumed that $\underline{\boldsymbol{U}}(\cdot,\cdot,0^-) = 1$ so that the phase origin is located on the object plane, thus the Rayleigh-Sommerfeld propagation formula is:

$$\underline{\boldsymbol{U}} = \underline{\boldsymbol{h}}_z^{\mathrm{RS}} * \underline{\boldsymbol{t}} \tag{1.8}$$

These equations provide a simple propagation model to compute the complex amplitude diffracted by a sample. As mentioned earlier, the computation of this model can be performed using Fast Fourier Transform (FFT) to reduce the computational time. However the field of view must be extended to avoid border effects of the convolution. If this propagation method is really efficient for propagating complex field of view, it should not be used to back-propagate a hologram to its focus plane. Indeed, the sensor is only sensitive to intensity thus the recorded hologram $\boldsymbol{d}$ can be expressed as follows:

$$\boldsymbol{d} = |\underline{\boldsymbol{U}}|^2 + \eta = \left|\underline{\boldsymbol{h}}_{\boldsymbol{z}}^{\mathrm{RS}} * \underline{\boldsymbol{t}}\right|^{\boldsymbol{2}} + \eta \tag{1.9}$$

where η is assumed to be an additive Gaussian noise (more details on the noise in the image are provided in Section A.2). Due to the loss of the phase information, back-propagating the hologram to a distance $-z$ leads to the so-called twin-image problem.

A.2 Noise in the data

As this thesis focuses on numerical processing of images, assumptions on the noise should be considered. As mentioned in the previous Section, in the rest of the manuscript the noise in the image will be considered to be white and Gaussian. A few explanation on the origin of this assumption is provided in this section. In the following, some of the most common noises are reminded :

Shot noise (also called Photon noise) occurs in the acquisitions since the camera detects a discrete number of photons. It can be modeled using a Poisson statistic. Thus, the variance of the measured signal depends on its energy. In in-line holography, the energy

of the flux on the sensor is high and the variations of the intensity of the signal due to the diffraction patterns of the objects are low. Thus, the variance of the signal is assumed to be uniform in our images. When the Poisson law parameter $\lambda > 100$, as it occurs in our case, the Gaussian approximation is a very good approximation of the Poisson law.

Thermal noise depends on the temperature of the sensor. It corresponds to the measured signal when the sensor is not illuminated. Its statistics can be modeled by a Poisson law. Its parameter λ depends on the temperature and not on the intensity of the diffraction patterns.

Dust diffraction patterns are due to the coherence of the light source. Indeed, since holography is a coherent imaging method, the diffraction patterns of out-of-focus objects like dust particles can interfere with the signal. This noise is correlated and thus can not be considered as white. However, as these objects are still, most of the dust particles diffraction patterns in the optical system can be removed from the hologram by dividing it with a background obtained without any sample.

Speckle noise is a correlated noise that can be observed when using a coherent light source. However, in this manuscript, most the images where acquired with LED which have a limited partial coherence. Thus, effects of speckle noise can be neglected.

Salt and peppers noise occurs with dead pixels or when data are badly transmitted. This noise can easily be taken into account in the reconstructions by using the inverse of the co-variance matrix $\boldsymbol{W}$ as mentioned in Section B.2.2.1.

A.3 Twin-image problem

In our model, the transmittance plane $\underline{\boldsymbol{t}}$ corresponds to the interference between the objects and the background, thus $\underline{\boldsymbol{t}} = 1 + o$. A hologram can be seen as the interference beetween an unscattered field $\underline{\boldsymbol{U}}_0 = \underline{\boldsymbol{h}}_z^{\mathrm{RS}} * 1$ and a scatterred field $\underline{\boldsymbol{U}}_1 = \underline{\boldsymbol{h}}_z^{\mathrm{RS}} * \underline{\boldsymbol{o}}$ since $\underline{\boldsymbol{h}}_z^{\mathrm{RS}} * \underline{\boldsymbol{t}} = \underline{\boldsymbol{h}}_z^{\mathrm{RS}} * [1 + \underline{\boldsymbol{o}}] = \underline{\boldsymbol{U}}_0 + \underline{\boldsymbol{U}}_1$ with $\underline{\boldsymbol{t}} = 1 + \underline{\boldsymbol{o}}$. If $\underline{\boldsymbol{U}} = \underline{\boldsymbol{U}}_0 + \underline{\boldsymbol{U}}_1$ is known, inverting the model is performed by back-propagating $\underline{\boldsymbol{U}}$. However in-digital holography only the intensity of $\underline{\boldsymbol{U}}$, $\boldsymbol{d}$, is known. Let us consider the back-propagation of equation 1.9 over a distance $-z$ [Goodman, 2004]:

$$
\begin{aligned}
\underline{\boldsymbol{h}}_{-z}^{\mathrm{RS}} * \boldsymbol{d} &= \underline{\boldsymbol{h}}_z^{\mathrm{RS}^*} * \left|\underline{\boldsymbol{h}}_z^{\mathrm{RS}} * \underline{\boldsymbol{t}}\right|^2 + \underline{\boldsymbol{h}}_z^{\mathrm{RS}^*} * \eta \\
&= \underline{\boldsymbol{h}}_z^{\mathrm{RS}^*} * \left[\underline{\boldsymbol{h}}_z^{\mathrm{RS}} * [1 + \underline{\boldsymbol{o}}]\right] \left[\underline{\boldsymbol{h}}_z^{\mathrm{RS}} * [1 + \underline{\boldsymbol{o}}]\right]^* + \underline{\boldsymbol{h}}_z^{\mathrm{RS}^*} * \eta \\
&= \underline{\boldsymbol{h}}_z^{\mathrm{RS}^*} * \left[\left|\underline{\boldsymbol{h}}_z^{\mathrm{RS}} * 1\right|^2 + \left|\underline{\boldsymbol{h}}_z^{\mathrm{RS}} * \underline{\boldsymbol{o}}\right|^2 + \underline{\boldsymbol{U}}_0 \cdot \underline{\boldsymbol{h}}_z^{\mathrm{RS}^*} * \underline{\boldsymbol{o}}^* + (\underline{\boldsymbol{h}}_z^{\mathrm{RS}} * \underline{\boldsymbol{o}}) \cdot \underline{\boldsymbol{U}}_0^*\right] + \underline{\boldsymbol{h}}_z^{\mathrm{RS}^*} * \eta \\
&= \underline{\boldsymbol{h}}_z^{\mathrm{RS}^*} * \left[|\underline{\boldsymbol{U}}_0|^2 + |\underline{\boldsymbol{U}}_1|^2 + \underline{\boldsymbol{U}}_0 \cdot \underline{\boldsymbol{h}}_z^{\mathrm{RS}^*} * \underline{\boldsymbol{o}}^* + \underline{\boldsymbol{U}}_0^* \cdot \underline{\boldsymbol{h}}_z^{\mathrm{RS}} * \underline{\boldsymbol{o}}\right] + \underline{\boldsymbol{h}}_z^{\mathrm{RS}^*} * \eta \\
&= \underline{\boldsymbol{h}}_z^{\mathrm{RS}^*} * |\underline{\boldsymbol{U}}_0|^2 + \underline{\boldsymbol{h}}_z^{\mathrm{RS}^*} * |\underline{\boldsymbol{U}}_1|^2 + \underline{\boldsymbol{U}}_0 \cdot \underline{\boldsymbol{h}}_{-2z}^{\mathrm{RS}} * \underline{\boldsymbol{o}} + \underline{\boldsymbol{U}}_0^* \cdot \underline{\boldsymbol{o}} + \underline{\boldsymbol{h}}_z^{\mathrm{RS}^*} * \eta
\end{aligned}
$$

The first term is spatially constant and, for small and/or slightly dephasing objects, the second one is negligible. Thus, only the last three terms are relevant:

$$
\underline{\boldsymbol{h}}_{-z}^{\mathrm{RS}} * \boldsymbol{d} \approx \underbrace{\underline{\boldsymbol{U}}_0 \cdot \underline{\boldsymbol{h}}_{-2z}^{\mathrm{RS}} * \underline{\boldsymbol{o}}}_{\text{Virtual image}} + \underbrace{\underline{\boldsymbol{U}}_0^* \cdot \underline{\boldsymbol{o}}}_{\text{Real image}} + \underline{\boldsymbol{h}}_z^{\mathrm{RS}^*} * \eta + \underline{\boldsymbol{C}} \tag{1.10}
$$

where $\underline{\boldsymbol{C}} = \underline{\boldsymbol{h}}_z^{\mathrm{RS}^*} * |\underline{\boldsymbol{U}}_0|^2$. Thus by back-propagating the hologram instead of the complex amplitude, *i.e.* if we focus numerically on the plane of the sample, we would see an

overlap of the focused image (real) and an out of focus ("twin") image corresponding to the back-propagation of the virtual image over a distance $2z$ as illustrated on Figure 1.9. Indeed, due to the intensity recording, the back-propagation is no more the inverse of the model. This problem can be seen as if two unknowns (the modulus and the phase) were to be retrieved from only one measurement. Phase diversity consists in improving the reconstructions by adding several measurements [Greenbaum and Ozcan, 2012, Luo et al., 2015]

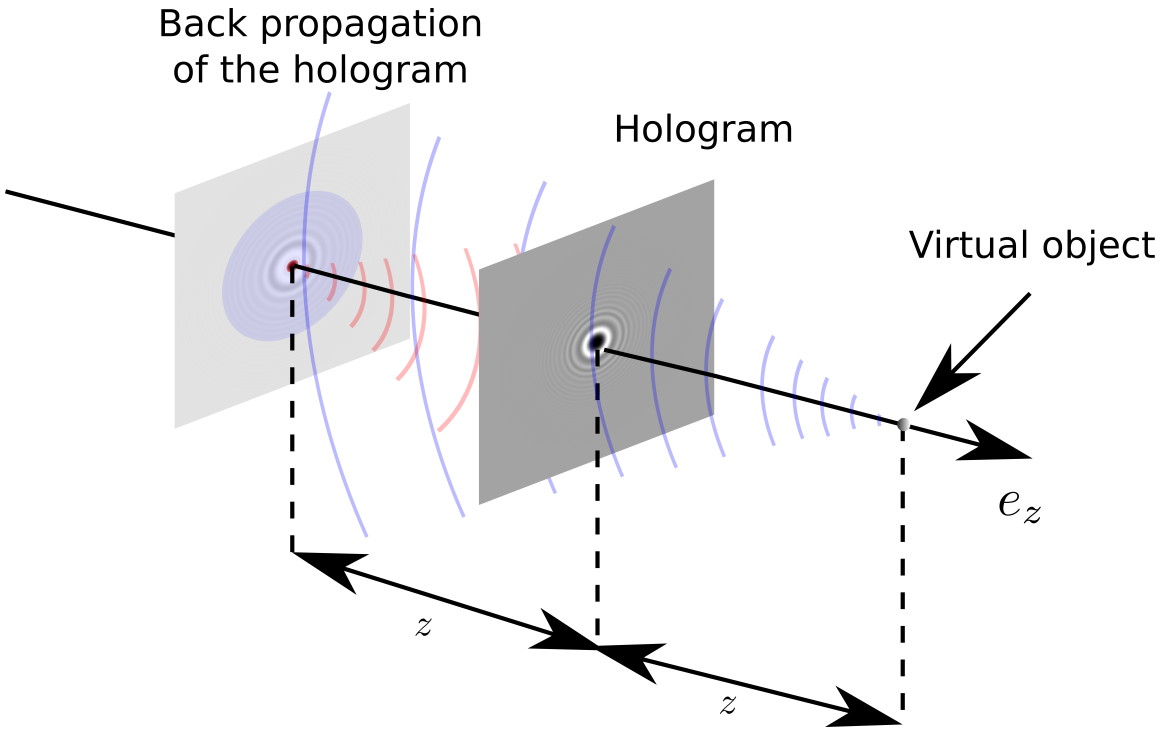

Figure 1.9: Illustration of the twin-image artifacts

To overcome the so-called *twin-image* problem, several methods have been developed. The first ones are based on improvement of the experimental setup, like off-axis holography, that allows to separate the real image of the virtual image [Leith and Upatnieks, 1962]. This method uses a carrier wave to modulate the object wave. The complex amplitude (modulus and phase) of the object wave on the sensor can be computed by demodulating the hologram. However, it requires a more complex setup that leads to less reproducibility. To overcome this issue common-path configurations have been developed [Singh et al., 2012]. Other methods based on improving the reconstruction algorithm have emerged. Due to the loss of the phase information on the sensor more specific reconstruction algorithms have to be used. Some of the most common algorithms are presented in Section B.

B Numerical reconstructions of in-line holograms

B.1 Fienup algorithm

One of the most popular reconstruction algorithm for phase retrieval is the Gerchberg-Saxton algorithm [Gerchberg, 1972]. Most reconstructions are based on this scheme. It exploit phase diversity based on the acquisition of two holograms at different defocus distances to reconstruct the transmittance plane of the sample. Fienup proposed a slightly different algorithm replacing the need of two acquisition by inserting priors in the reconstruction [Fienup, 1980]. The Fienup error reduction algorithm is described in Algorithm 1. This class of algorithm is still widely used today [Rodriguez et al., 2013, Rivenson et al., 2016, Latychevskaia and Fink, 2015] Since the intensity of the diffracted wavefront is recorded on the sensor, the phase is lost but the modulus of the propagated wavefront is well known. It corresponds to the square root of the data.

The Fienup error reduction algorithm is based on iterative back and forward-propagation of the data in between the sensor plane and the reconstruction plane while ensuring that the modulus of the reconstructed wavefront is the square root of the data (see Figure 1.10).

Thus, the initial step consists in considering the modulus of the amplitude $\underline{\boldsymbol{a}}$ in the sensor plane to be the square root of the data and its phase to be null.

Then a back-propagation of $\underline{\boldsymbol{a}}$ to the object plane is performed in Step 1.

In step 2 constraints are applied in the object plane *e.g.* a non emissive objects prior can be considered by applying a positivity constraint.

Then a forward-propagation is performed in Step 3 to apply constraints in the hologram plane *e.g.* imposing the amplitude of the model to be the square root of the data (Step 4).

Figure 1.10 illustrates the principle of this algorithm.

Several iterations of this algorithm lead to suppression of the twin-image artifacts, as well as an estimation of the phase shift induced by the sample.

These methods are often use to reconstruct the phase of $\underline{\boldsymbol{t}}$ in digital in-line holography due to their simplicity and computational complexity. Since they are mostly based on propagations that can be computed using convolution, their computational time is low.

Good results can be obtained using these methods. However their formulation do not allow to take into account more complex image formation model or priors.

It has been demonstrated that Fienup algorithm is equivalent to an inverse problem algorithm [Momey et al., 2019]. However a more general inverse problem formulation, as described in the next section, can provide a more flexible framework to reconstruct in-line holograms.

B.2 Inverse problem approaches

As stated by J.B. Keller [Keller, 1976], *"We call two problems inverses of one another if the formulation of each involves all or part of the solution of the other. Often for historical reasons, one of the two problems has been studied extensively for some time, while the other has never been studied and is not so well understood. In such cases, the former in called the direct problem, while the latter is the inverse problem".* In physics, the direct problem is described as a cause-consequence sequence [Turchin et al., 1971]. For example, in in-line

Algorithm 1: Fienup algorithm for the reconstruction of $\underline{\boldsymbol{t}}$

input : Data $\boldsymbol{d}$ ($L \times C$ image)
input : Propagation kernel $\underline{\boldsymbol{h}}_z$ ($L \times C$ image)
input : Number of iterations N (N integer)
output: Reconstructed transmittance plane $\underline{\boldsymbol{t}}$ ($H \times W$ complex image)

Step 0: Initialization:
$\underline{\boldsymbol{a}} \leftarrow \sqrt{\boldsymbol{d}}$

for $n = 1$ **to** N **do**
  Step 1: Back propagation to the reconstruction plane:
  $\underline{\boldsymbol{t}} \leftarrow \underline{\boldsymbol{h}}_z^* * \underline{\boldsymbol{a}}$

  Step 2: Application of priors in the reconstruction plane:
  for $i = 1$ **to** H **do**
    for $j = 1$ **to** W **do**
      if $|\underline{t}(i,j)| \geq 1$ **then**
        $\underline{t}(i,j) \leftarrow 1 \times \exp\left(i \times \texttt{GetPhase}(\underline{\texttt{t}}\texttt{(i,j)})\right)$
      end
    end
  end

  Step 3: Propagation of the reconstructed transmittance plane:
  $\boldsymbol{m} \leftarrow \underline{\boldsymbol{h}}_z * \underline{\boldsymbol{t}}$

  Step 4: Replacing the modulus of $\boldsymbol{a}$ by the square root of $\boldsymbol{d}$:
  for $i = 1$ **to** H **do**
    for $j = 1$ **to** W **do**
      $\underline{a}(i,j) \leftarrow \sqrt{d(i,j)} \times \exp\left(i \times \texttt{GetPhase}(m(i,j))\right)$
    end
  end
end

where `GetPhase` is a function extracting for complex $z = x + iy$ the phase of z, $\texttt{GetPhase}(z) = \arctan(y/x)$.

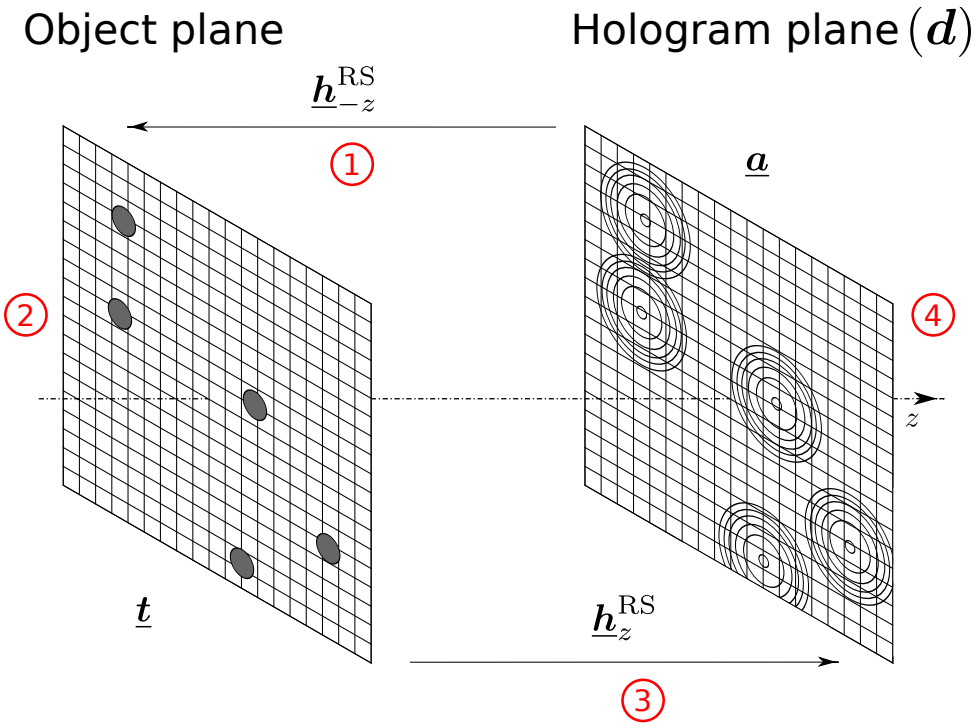

Figure 1.10: Fienup error reduction algorithm principle.

holography, the direct problem, also known as forward problem describe the propagation of the light from the object plane to the sensor from the knowledge of the source and the obstacles it encounters. The direct problem is also a problem that involves a loss of information. For example, the measurement of the intensity of the diffracted wavefront leads to a loss of the phase information on the sensor. This property is common to most inverse problems and introduces in in-line holography an "ill-posedness" of the problem.

B.2.1 Ill-posedness of an inverse problems approaches

In 1902, Jaques Hadamard proposed a first definition of "well-posedness" [Hadamard, 1902]. A problem is well-posed when:

- a solution exists for arbitrary data,
- its solution is unique,
- the solution should not be very sensitive to small perturbation of the data, i.e. there should be a continuous dependence between the solutions and the data.

A problem that is not *well-posed* is referred as *ill-posed*.
In-line holography would be a well-conditioned problem if the complex amplitude of the diffraction patter was recorded since the modulus of the Fourier transform of the Rayleigh Sommerfeld propagator is equal to 1.
However the intensity is recorded and the phase information on the sensor is lost. Thus, the uniqueness (as seen with the twin image) and the well-conditioned properties of the solution are compromised. Thus, in-line holography reconstruction is an ill-posed problem. Numerical inversion of the data, may then lead to physically unrealistic solutions. Thus

to solve the ill-posedness of the problem, constraints have to be added in the inversion process. These constraints can be added by using diversity in the acquisitions of one sample (*e.g.* phase diversity) or by using regularization. In Part III of this manuscript, we will mainly focus on the use of regularizations. Part IV will provide an example of phase diversity used to achieve more quantitative reconstructions in in-line holography.

B.2.2 Regularized inverse problems approaches

In conclusion inverse problems approaches tend to inverse a non-invertible model by using an accurate and complete forward model $\boldsymbol{m}$ and minimizing its discrepancy with the data $\boldsymbol{d}$. The solution of the problem is obtained by minimizing a loss function $\mathscr{L}$ that contains a data fidelity term $\mathscr{D}$, and, since the problem is ill-posed, regularization terms $\mathscr{R}_i$:

$$\mathscr{L}(\underline{\boldsymbol{t}}) = \mathscr{D}(\underline{\boldsymbol{t}}) + \sum_i \mu_i \mathscr{R}_i(\underline{\boldsymbol{t}}) \tag{1.11}$$

where $\boldsymbol{\mu}$ represents a vector of regularization hyperparameters. Indeed to transform the ill-posedness of the problem into a well-posedness, priors are added by the use of regularization. However, regularization hyperparameters correspond to the balance between having a full confidence in the data and a full confidence in the priors. Thus, they must be tuned carefully.

B.2.2.1 Data fidelity term

The data fidelity term $\mathscr{D}$ evaluates the error between the data $\boldsymbol{d}$ and the model $\boldsymbol{m}(\boldsymbol{\vartheta})$. In phase-retrieval reconstruction $\vartheta = \underline{\boldsymbol{t}}$ and the model is defined as $\boldsymbol{m}(\underline{\boldsymbol{t}}) = \left|\underline{\boldsymbol{h}}_z^{\mathrm{RS}} * \underline{\boldsymbol{t}}\right|^2$.

One of the most popular data-fidelity term is the weighted least squares criterion that derives from Gaussian errors assumption. This criterion is expressed as follows:

$$\begin{aligned}
\mathscr{D}(\underline{\boldsymbol{t}}) &= \|\boldsymbol{d} - \boldsymbol{m}(\underline{\boldsymbol{t}})\|_{\boldsymbol{W}}^2 \\
&= (\boldsymbol{d} - \boldsymbol{m}(\underline{\boldsymbol{t}}))^{\mathrm{T}} \boldsymbol{W} (\boldsymbol{d} - \boldsymbol{m}(\underline{\boldsymbol{t}})) \\
&\quad \text{if errors are not correlated, } \boldsymbol{W} \text{ is diagonal, } \boldsymbol{W} = \mathrm{diag}(\boldsymbol{w}), \\
\mathscr{D}(\underline{\boldsymbol{t}}) &= \sum_k w_k (d_k - m_k(\underline{\boldsymbol{t}}))^2
\end{aligned} \tag{1.12}$$

where d_k is the k-th pixel of the data, $m_k(\underline{\boldsymbol{t}})$ is k-th pixel of the model and w_k is the weight associated to pixel k. For example, dead pixels can be taken into account by setting w_k to 0 on these pixels and 1 everywhere else. The matrix $\boldsymbol{W}$ is the inverse of the covariance matrix and thus allows to take into account the statistics of the noise. In the case of stationary white Gaussian noise, $\boldsymbol{W}$ is the inverse of the noise variance σ_ϵ^2 an $\|\boldsymbol{u}\|_{2,\mathbf{W}}^2 = (1/\sigma_\epsilon^2) \sum_{k,l} u_{k,l}^2$.

The data fidelity term evaluates how much the solution fits the data. However, the minimization of this criterion depends on the accurate knowledge of the image formation model. Thus, establishing an accurate image formation model, is a crucial step in the use of inverse problem approaches. Here, the Rayleigh-Sommerfeld diffraction model is limited by the knowlegde of the propagation distance z. Thus, the quantitativity of the transmittance reconstruction depends on the accuracy of the estimation of z.

B.2.2.2 Regularization

As previously mentioned, the problem is ill-posed, thus priors must be added to the reconstruction algorithms. These priors promote the convergence to physically realistic solutions. To add priors in the reconstruction, three options are possible:

- to add priors in the model: for example, if the sample only contains spherical objects, the Rayleigh-Sommerfeld model should be replaced by a Mie model that characterizes accurately the diffraction by a sphere (solution of the Maxwell equations) [Slimani et al., 1984],
- to add strict constraints: for example, reconstructing only non emissive objects corresponds to the constraint $\forall i, j, |\underline{\boldsymbol{t}}(i,j)| \leq 1$,
- to add regularization terms: for example, in holography, the sample is supposed to be sparse, L_1-norm regularization promotes this physical prior.

In the following section, some of the most popular regularization terms are presented.

Tikhonov's regularization

Introduced by Andreï Tikhonov, the Tikhonov's regularization term $\mathscr{R}^{\text{Tikhonov}}$ [Tikhonov, 1963] is expressed as :

$$\mathscr{R}^{\text{Tikhonov}}(\boldsymbol{\vartheta}) = \|\boldsymbol{\Gamma}\boldsymbol{\vartheta}\|_2^2 \tag{1.13}$$

where $\boldsymbol{\Gamma}$ is the Tikhonov matrix. $\boldsymbol{\Gamma}^T\boldsymbol{\Gamma}$ is the inverse of the covariance matrix of the objects to reconstruct. Depending on the values of $\boldsymbol{\Gamma}$, the effects of Tikhonov regularization may vary. Indeed, if $\boldsymbol{\Gamma} = \boldsymbol{I}$, the Tikhonov regularization is equivalent to L_2-regularization leading to smaller norm of the reconstructions. If $\boldsymbol{\Gamma}$ is a high pass filter, the Tikhonov regularization will enforce smooth reconstructions since the prior corresponds to a decreasing power density spectrum.

L_1 regularization

The L_1 regularization term $\mathscr{R}^{\text{L1}}$ is expressed as:

$$\mathscr{R}^{\text{L1}}(\boldsymbol{\vartheta}) = |\boldsymbol{\vartheta}| \tag{1.14}$$

This type of regularization tends to promote sparse solutions [Denis et al., 2009]. This regularization lead to a solution that fits the data with the lowest number of pixels.

Edge preserving regularization

The Total Variation (TV) regularization term $\mathscr{R}^{\text{TV}}$ [Rudin et al., 1992] is expressed as:

$$\mathscr{R}^{\text{TV}}(\boldsymbol{\vartheta}) = \sum_{i,j} \|(\nabla\boldsymbol{\vartheta})_{i,j}\|_2 \tag{1.15}$$

with

$$(\nabla\boldsymbol{\vartheta})_{i,j} = \begin{pmatrix} \nabla_i\boldsymbol{\vartheta} \\ \nabla_j\boldsymbol{\vartheta} \end{pmatrix} = \begin{pmatrix} \boldsymbol{\vartheta}_{i+1,j} - \boldsymbol{\vartheta}_{i,j} \\ \boldsymbol{\vartheta}_{i,j+1} - \boldsymbol{\vartheta}_{i,j} \end{pmatrix} \tag{1.16}$$

This regularization enforce sparsity of the gradients of the reconstruction and is thus a common regularization for reconstructing piecewise-flat objects. As illustrated by Figure 1.11 on a denoising task, and as previously mentioned, the total variation regularization reduces the modulus of the gradient of the image and thus promotes flat objects reconstructions. However it can be seen that a correct regularization for a certain size of object (Zoom 1) is not valid for another one (Zoom 2). The tuning of the regularization hyperparameters will thus correspond to tuning the scale of the structure to reconstruct.

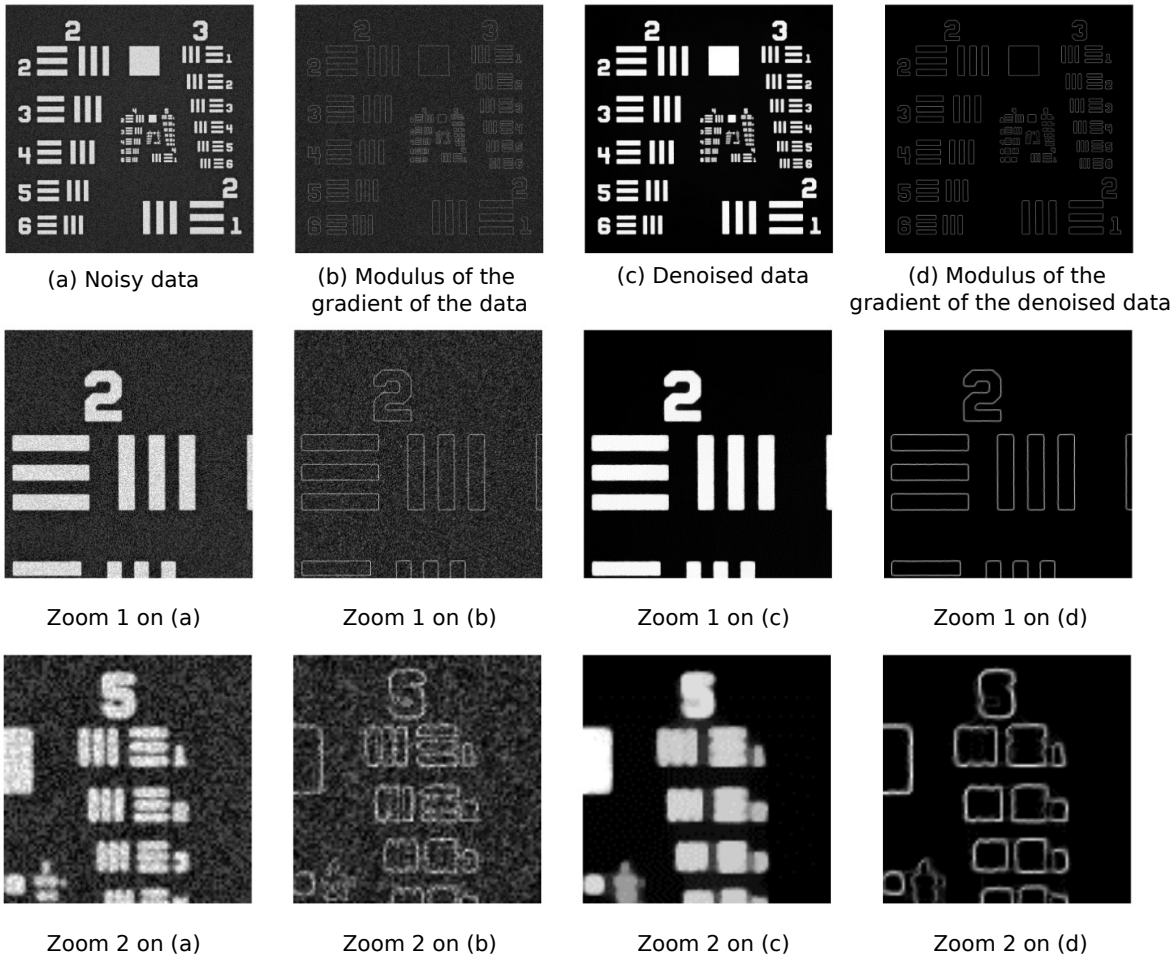

Figure 1.11: Effects of the total variation regularization term. Image from [Jolivet, 2018]

One of the main drawback of using the total variation regularization is that it is not differentiable. Thus, proximal algorithms can be used to avoid the optimization issues due to this non differentiability. Another method to avoid this issue the differentiable approximation of the total variation [Charbonnier et al., 1997]:

$$\mathscr{R}_{\epsilon}^{\mathrm{TV}_{\epsilon}}(\boldsymbol{\vartheta}) = \sum_{i,j} \sqrt{(\nabla_i \boldsymbol{\vartheta})^2 + (\nabla_j \boldsymbol{\vartheta})^2 + \epsilon^2} - \epsilon \tag{1.17}$$

where $\epsilon > 0$ is small-valued.

Note that the parameter ϵ should also be chosen carefully since it may change the dynamic of the reconstruction and the staircase effect due to total variation regularization.

In the reconstruction presented in this manuscript, the complex approximation of the total variation will be used:

$$\mathscr{R}_{\epsilon}^{\mathrm{EP}_{\epsilon}}(\boldsymbol{\vartheta}) = \sum_{i,j} \sqrt{(\nabla_i \Re(\boldsymbol{\vartheta}))^2 + (\nabla_j \Re(\boldsymbol{\vartheta}))^2 + (\nabla_i \Im(\boldsymbol{\vartheta}))^2 + (\nabla_j \Im(\boldsymbol{\vartheta}))^2 + \epsilon^2} - \epsilon \quad (1.18)$$

where $\epsilon > 0$ is small-valued.

This term promotes the same properties as the total variation but also promote a co-localization of the gradient of the modulus and phase of the reconstructed object.

In conclusion, the presented regularizations provides tools to correct the ill-posedness of the inverse problem. However the balance between these regularization terms and the data fidelity, *i.e.* the regularizations hyperparameters, must be carefully chosen.

C Thesis challenges

Brightfield microscopy is an imaging system commonly used by biologists. It can be used to detect, classify or characterize objects in the sample. However, brightfield microscopy provides a low contrast for translucent objects due to their low absorption. Thus, these objects must be stained to be observed. For example Gram staining allows to differentiate bacteria according to their coloration (see Figure 1.1). In this context, this thesis, try to answer the question: is it possible to automatize the Gram analysis using digital holography? To answer this question several issues must be solved:

- Repeatability: Is the reconstructed phase/transmission similar for the same type of bacteria?
- Reproducibility: Is the reconstructed phase/transmission similar when changing the setup?
- Quantitativity: Are the phase/transmission reconstructions representative of the real phase shift introducted by the objects of interest?

This thesis aims at improving the reconstructions to solve these issues. To assess the performance of the method, biological data were acquired by BIOASTER and are presented in this manuscript. Even though these data are stained (to be able to identify the bacteria), their modulus and phase are reconstructed.

To improve the quantitativity of the reconstruction and thus the final diagnoses, several methodological solutions have been studied:

- **Self-calibration of the image formation model:**
  Rayleigh-Sommerfeld diffraction is an accurate model of the propagation of the light, however the propagation distance z should be accurately estimated. Moreover, this diffraction formula considers a perfect imaging system, free of aberrations or misalignment of the optics in the setup. These issues may compromise the quantitativity of the reconstructions. An accurate calibration of the whole setup must be performed.

- **Unsupervised tuning of the regularization hyperparameters:**
  The tuning of the regularization hyperparameters is a crucial part. Indeed under-regularization and over-regularization may lead to physically unrealistic reconstructions. For reproducibility reasons, hand-tuning of the regularization hyperparameters should be avoided. Several unsupervised methods to tune the regularization hyperparameters have been proposed, however most of them are based on a criterion that depends on the data. Thus, the reproducibility of these methods is not guaranteed.

- **Exploiting phase diversity in multispectral reconstructions:**
  Regularization is an efficient way to clean the twin-image of a hologram. However, it may introduce biases in the reconstructions. By using the redundancy in multispectral stacks, less biased, i.e. more quantitative, reconstructions become possible.

After this first introduction part, this thesis manuscript is composed of three parts and eight chapters that are summarized in the following:
Part II: This second part describes a complete methodology to improve the forward model used in inverse problems approaches. It is based on calibration of the model thanks to spherical objects.
Chapter 2: This chapter proposes a parametric inverse problems approach in order to estimate the propagation distance between the sample and the sensor. The methodology is based on the positioning of the slide plane instead of a plane estimated with image-based criteria.
Chapter 3: This chapter details a fast robust detection methodology that is applied on the calibration beads. The proposed method improve significantly the number of detected beads.
Chapter 4: This chapter extends the approach proposed in Chapter 3 to aberration estimation. We propose to estimate and take into account spatially varying point spread function (PSF) in the regularized reconstructions.
Part III: This third part addresses the issue of regularization hyperparameter tuning by proposing an unsupervised method to achieve quantitative reconstructions.
Chapter 5: We propose a comparison between several state-of-the-art automatic hyperparameter tuning. This chapter is a first work on the use of Stein's Unbiaised Risk Estimator in in-line holography.
Chapter 6: We propose a quantitative criterion based on the reconstruction of calibration beads in order to improve the quantitativity of the reconstructed biological sample. This chapter is a pre-feasibility study on the use of this criterion.
Part IV: This fourth part uses the whole potential of the previously mentionned methodologies on multispectral acquisitions in order to improve the repeatability, the reproducibility and the quantitativity of the reconstructions.
Chapter 7: This chapter present an inverse problems approach using multispectral regularization to reconstruct multispectral data.
Chapter 8: This chapter uses the methodologies previously presented in this manuscript to reconstruct multispectral data and highlight the benefits of adding calibration beads in the sample.

Each chapters begins with an introduction detailing the issues tackled in the chapter. It is then followed by a preliminary section that reminds basics tools and state-of-the-art methods. At last, the contributions of this thesis are then presented.

Part II

Calibration of the image formation model

CHAPTER 2

Automatic numerical focusing

Abstract

If in-line holograms can be recorded at any defocus distance, their reconstructions require the accurate knowledge of this distance. This distance is usually estimated on contrast "image-based" criteria. In this chapter, we present a new method to achieve autofocus in digital holographic microscopy. It is based on inserting calibrated objects into a sample placed on a slide. Parametric Inverse Problems Approaches make it possible to precisely locate and characterize the inserted objects and thereby derive the slide plane location. Numerical focusing using regularized reconstructions can then be performed in a plane at any chosen distance from the slide plane of the sample in a reproducible manner and independently of the diversity of the objects in the sample. In this chapter, after a preliminary section, we detail the proposed methodology to accurately estimate the defocus distance z. Then we validate it on simulated and real holograms. Finally this distance is used in regularized reconstructions to perform autofocus. This chapter is adapted from the paper [Brault et al., 2022b] .

Introduction

Autofocusing is one of the first requirements for automation of the process in most microscopy techniques. Efficient autofocusing methods may be required, in particular for long-time acquisitions [Bon et al., 2015], exhaustive imaging of samples [Bian et al., 2020], or simply for the automation of microscopy systems for high throughput inspection of slides. Another reason for precise focusing in the context of automation is simply the need for the repeatability and standardization of the imaging conditions, which is crucial for automated image processing, analysis and classification.

However, with incoherent imaging methods, autofocusing can be tricky for several reasons. When high-magnification and high-numerical aperture objectives are used (which

is the case when examining blood samples, for example), the depth of field of the microscope may be less than 1 μm. In the case of brightfield microscopy of stained samples, the density, opacity, size, axial locations of the various objects present inside the sample may not be the same, with variations in size or in axial locations that may be greater than the depth of field. In these conditions, even the definition of the best focus becomes problematic. In most cases, it may be better to measure the position of the slide surface as a reference plane to be tracked. This can be done by including additional optical elements solely dedicated to the autofocusing problem (triangulation with oblique illumination, confocal pinhole detection, dual-LED illumination, tilted sensor, etc.) [Bian et al., 2020]. These technical solutions are beyond the scope of this work. Here, we focus on techniques that require no dedicated optical elements other than the imaging system itself.

With coherent imaging methods, like digital holography, it is possible to measure or estimate the complex amplitude of the wave diffracted by a given sample. Thus, the limitations due to the depth of field is no more an issue in the recording step. The in-line (or Gabor) configuration [Gabor, 1948] is the simplest to set up as, unlike the off-axis configuration, it does not require a reference beam, and can be used without any objective (lensless microscopy). It can also be adapted for use on a traditional microscope. The only requirements are a temporally and spatially coherent (or partially coherent) source and to record an out-of-focus image of the object on the sensor. Physical focusing on the sample is then no longer required, making it possible to design imaging systems without the need for an expensive automated axial positioning system with sub-micrometer resolution. However, as the hologram is the intensity image of the wave diffracted by the sample, the phase of the wave is not directly accessible and in-line digital holography requires numerical reconstructions that consist in a phase retrieval problem. This problem can be numerically solved by using alternating projection strategies or Inverse Problem Approaches (IPA) [Fienup, 1982, Latychevskaia and Fink, 2007, Momey et al., 2019]. One of the main drawbacks of these phase retrieval algorithms is that they require the knowledge of the propagation distance z between the sample and the sensor (see Chapter 1). The conventional way to perform numerical autofocusing reproduces the numerical autofocusing in brightfield microscopy by analyzing a stack of reconstructed images at various distance z (see Figure 2.2). It is however important to find a criterion that can estimate the z distance in a reproducible and physical meaningful way. With traditional focusing criteria [Gillespie and King, 1989, Dubois et al., 2006, Langehanenberg et al., 2011, Lamadie et al., 2012, Memmolo et al., 2014, Zhang et al., 2017, Malik et al., 2020], this location is likely to vary depending on the density, spatial distribution, size, and transmission of the objects.

In this chapter, we present a new approach to estimate with sub-micrometer accuracy the axial distance between the focal plane of the optical system and a physical reference plane corresponding to the top of the slide (or the coverslip, depending on the microscope configuration).

This approach is based on the insertion of stable calibrated objects (non-porous spherical beads) in the sample (see Figure 2.3 and Appendix A). These beads can be reconstructed by standard object positioning algorithms that use focusing criteria [Langehanenberg et al., 2011, Zhang et al., 2017, Lamadie et al., 2012] or parametric IPA which have already proven their ability to detect simple shaped objects and to accurately estimate their position and size [Lee et al., 2007, Soulez et al., 2007a, Cheong et al., 2010]. The slide surface can be thus reconstructed accurately from the estimation of the position and

the size of the beads. Then, the focusing reconstruction planes can be chosen relatively to this reference plane. The main advantage of this method is that it requires only one recorded hologram and provides objective information on the location of the reference plane. Unlike image-based criteria, it does not suffer from the influence of the type or diversity of the sample. Moreover, the positioning and sizing of several beads in the same field of view enables estimation of potential tilting of the slide surface, as well as a more precise axial location.

In the following section, we will first detail several classical autofocusing methods used in holography. Secondly, we will describe the principle of parametric inverse problem approaches applied on in-line holographic microscopy, finally we will discuss on their accuracy. Then, we will detail a methodology based on parametric inverse problem approach and apply it to simulated and experimental holograms. At last, we will present an example of regularized reconstruction using the estimated propagation distance.

A Preliminaries

A.1 Classical autofocusing methods in in-line holography

In image-based autofocusing, the best focus is typically defined by choosing a global or local criterion (combining image properties) to be maximized or minimized [Bian et al., 2020] in a reconstructed z-stack. The efficiency of different criteria vary depending on, among others, whether the objects of interest are opaque or transparent, isolated, or embedded in a dense medium. The following section presents two state of the art image-based method to perform autofocusing in digital in-line holography. They are based on an analysis of a back-propagated z-stack.

A.1.1 GRA criterion

GRA [Langehanenberg et al., 2011] is a classical criterion for autofocusing. It is based on the search for an extremum along z direction in the integral over the image of the magnitude of the gradient of the back-propagated stack. The modulus of the gradient of the back-propagated fields is computed. The criteria corresponds to sum these values for all pixels. Algorithm 2 details how to perform autofocusing using this method :

A.1.2 ToG Criterion

ToG [Zhang et al., 2017] is a sparsity criterion applied to the magnitude of the gradient of the complex back-propagated field by searching for a maximum value in the Tamura of the gradient. The Tamura of an image $\boldsymbol{I}$ is expressed as:

$$TC(\boldsymbol{I}) = \sqrt{\frac{\sigma_{\boldsymbol{I}}}{<\boldsymbol{I}>}} \tag{2.1}$$

where σ_I is the standard deviation of the image and $<\boldsymbol{I}>$ its average. To perform this criteria, back-propagations of the data are performed for several z propagation distances as previously done for GRA criterion. The Tamura of the gradient of these back-propagated fields are then computed. Algorithm 3 details how to perform autofocusing using this method :

Algorithm 2: Image-based autofocusing by computation of GRA criterion

input : Data $\boldsymbol{d}$ ($L \times C$ image)
input : Search domain sampling $\boldsymbol{z} = \{z_i\}_{1,\dots,K}$ ($1 \times K$ vector)
output: Autofocusing distance $z^\dagger$

for $i = 1$ **to** K **do**
  Compute $\underline{\boldsymbol{h}}^{\mathrm{RS}}_{z_i}$.
  $\mathbf{BP} \leftarrow \underline{\boldsymbol{h}}^{\mathrm{RS}}_{-z_i} * \boldsymbol{d}$
  $\mathbf{G} \leftarrow \nabla_{i,j}\mathbf{BP}$
  $\mathbf{M} \leftarrow \mathrm{Modulus}(\mathbf{G})$
  $\mathrm{GRA}_i \leftarrow \sum_{i,j} \mathbf{M}$
end
$z^\dagger = \arg\min \mathrm{GRA}$ for phase objects, $\arg\max \mathrm{GRA}$ for absorption objects

Algorithm 3: Image-based autofocusing by computation of ToG criterion

input : Data $\boldsymbol{d}$ ($L \times C$ image)
input : Search domain sampling $\boldsymbol{z}$ ($1 \times K$ vector)
output: Autofocusing distance $z^\dagger$

for $i = 1$ **to** K **do**
  Compute $\underline{\boldsymbol{h}}^{\mathrm{RS}}_{z_i}$.
  $\mathbf{BP} \leftarrow \underline{\boldsymbol{h}}^{\mathrm{RS}}_{z_i} * \boldsymbol{d}$
  $\mathbf{G} \leftarrow \nabla_{i,j}\mathbf{BP}$
  $\mathbf{T} \leftarrow TC(\mathbf{G})$
  $\mathrm{ToG}_i \leftarrow \sum_{i,j} \mathbf{T}$
end
$z^\dagger = \mathrm{argmin}\, \mathbf{ToG}$

A.2 Mie Model

The solutions of Maxwell's equations for a spherical particle were provided by Mie in 1908 [Slimani et al., 1984]. Since the objects only depends on few parameters, *i.e.* their radius r and their complex refractive index n, the holograms of spherical objects only depends on few parameters: the 3D position of the bead (x, y, z), r and n as illustrated on Figure 2.1. The Mie model is expressed in terms of an infinite series and it can only be approximated numerically. The reconstruction of these objects can be performed easily with parametric inverse problems approaches as presented in Section A.3. It should be noted that when beads are transparent, the refractive index is real.

A.3 Parametric Inverse Problems Approach to accurately locate the calibration objects

Inverse problems are a general class of problems where unknowns are linked to measurements through a known image formation model (see Chapter 1). The main idea relies on minimizing the discrepancy between the measured data and a model. If the model

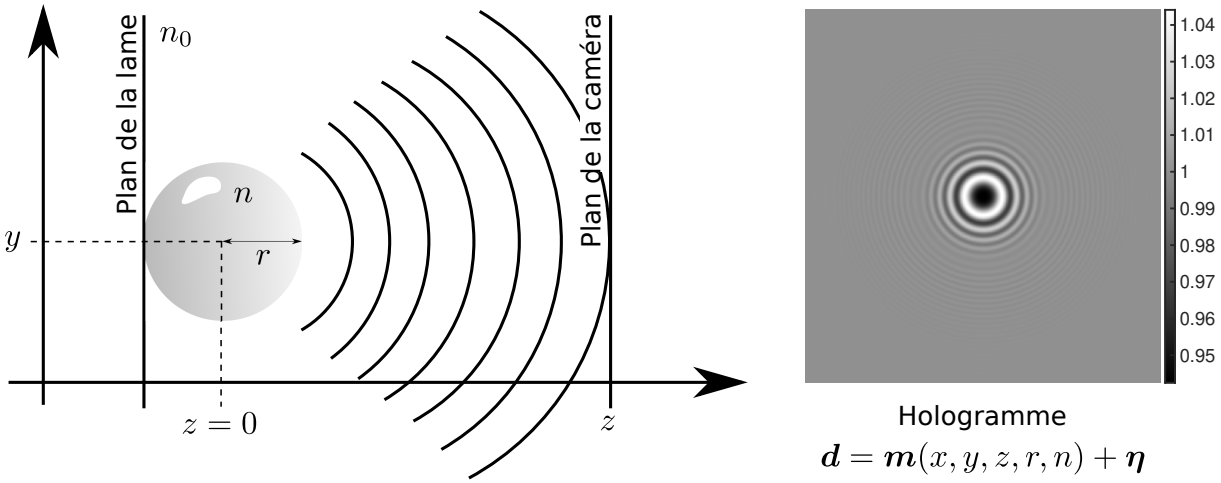

Figure 2.1: Illustration of the parameters of the Mie model

depends on only a few parameters and has an analytical form, the parameter can be reconstructed using parametric IPA methods [Tarantola, 2005]. When the image formation model is accurately known and sufficiently constrained, full-confidence to the data is given. In this case, priors are only added in the image formation model. The parametric IPA can be seen as a fitting problem.

The reconstruction of beads from an in-line hologram is equivalent to estimating their spatial position (x, y, z), shape (radius r) and optical parameters (refractive index n). The diffracted wavefront of a single spherical bead is accurately modeled by the Lorenz-Mie model [Slimani et al., 1984] which depends on the set of bead parameters $\boldsymbol{\vartheta} = \{x, y, z, r, n\}$. In our model, $\underline{\boldsymbol{a}}^{\mathrm{Mie}}(\boldsymbol{\vartheta}^{(i)})$ represents the interference on the sensor plane between the diffraction patterns of the i-th bead and the incident beam $\underline{\boldsymbol{U}}_0 = \underline{\boldsymbol{h}}^{\mathrm{RS}} * 1$. This is a non-linear parametric model. It has been successfully used to reconstruct spherical object from holograms by least square fitting methods [Lee et al., 2007, Cheong et al., 2010] or, in a more general framework, by parametric IPA [Soulez et al., 2007a, Soulez et al., 2007b, Méès et al., 2013]. A brief summary of the approach is given below.

A hologram $\boldsymbol{d}$ is modeled by the interference between the diffraction patterns of the objects and the incident beam:

$$\boldsymbol{d} = \left| \underline{\boldsymbol{U}}_0 + \sum_{\mathrm{i}=1}^{N_{\mathrm{beads}}} (\underline{\boldsymbol{a}}^{\mathrm{Mie}}(\boldsymbol{\vartheta}^{(i)}) - \underline{\boldsymbol{U}}_0) \right|^2 + \eta \tag{2.2}$$

where, after a proper hologram normalization step, the reference beam is assumed to be of unit magnitude, η is a noise term and N_{beads} represents the number of objects in the hologram. For the rest of this chapter, we define $\boldsymbol{m}^{\mathrm{P}}(\boldsymbol{\vartheta}^{(i)})$ the image formation model of the i-th bead as:

$$\boldsymbol{m}^{\mathrm{P}}(\boldsymbol{\vartheta}^{(i)}) = \left| \underline{\boldsymbol{a}}^{\mathrm{Mie}}(\boldsymbol{\vartheta}^{(i)}) + \underline{\boldsymbol{A}}_i \right|^2 \tag{2.3}$$

where $\underline{\boldsymbol{A}}_i = \sum_{\mathrm{j} \neq i} (\underline{\boldsymbol{a}}^{\mathrm{Mie}}(\boldsymbol{\vartheta}^{(j)}) - \underline{\boldsymbol{U}}_0)$. Note that if the hologram contains only one bead:

$$\boldsymbol{m}^{\mathrm{P}}(\boldsymbol{\vartheta}) = \left| \underline{\boldsymbol{a}}^{\mathrm{Mie}}(\boldsymbol{\vartheta}) \right|^2 \tag{2.4}$$

Accurate estimates of $\boldsymbol{\vartheta}^{(i)}$) can be obtained by maximizing a likelihood function. Assuming the noise is Gaussian, the maximum likelihood estimation of model parameters $\boldsymbol{\vartheta}^{(i)}$

of the i^{th} bead corresponds to weighted least squares fitting [Soulez et al., 2007b, Lee et al., 2007], *i.e.* to find the parameters of a single diffraction pattern model $\boldsymbol{m}^{\mathrm{P}}(\boldsymbol{\vartheta}^{(i)})$ that minimize the weighted square distance to the residuals:

$$\mathscr{D}^{\mathrm{P}}(\boldsymbol{\vartheta}^{(i)}) = \left\| \boldsymbol{d} - \boldsymbol{m}^{\mathrm{P}}(\boldsymbol{\vartheta}^{(i)}) \right\|_{\boldsymbol{W}}^{2} \tag{2.5}$$

where $\boldsymbol{W}$, the inverse of the covariance matrix of noise. To guarantee the rapid and accurate reconstruction of a set of objects, an iterative detection/localization scheme, based on the matching pursuit algorithm, was proposed in [Soulez et al., 2007a]. A slightly modified version is given below. It consists of two steps: a detection step and an estimation step.

The first step consists in detecting the calibration beads inside the sample. This provides a rough estimate of all beads parameters that are then used in the estimation step as initialization points for minimization of the cost function (2.5) in a discrete parameters space. Since the beads are calibrated, a narrow parameter research domain $\mathbb{C}$ can be chosen depending on the size and refractive index of the calibrated beads used experimentally. This guarantees the selection of the calibration beads among the other objects. To prevent excessive computation time due to the dimension of the parameter space, $\mathbb{C}$ must be carefully sampled. Cramér-Rao Lower Bounds (see Section A.4.2) make it possible to find the correct sampling step [Fournier et al., 2010]. Estimating the cost function value for every subset (x, y, z, r, n) of $\mathbb{C}$ is time consuming. As the model is shift-invariant in the x and y directions, minimizing $\mathscr{D}^{\mathrm{P}}$ on a (x, y) pixel grid is equivalent to maximizing the discrete cross-correlation between the data and the image formation model. In order to reduce computational complexity, the cross-correlations are computed using Fast Fourier Transforms (FFT). Cross-correlation maps are computed for each subset (z, r, n) of $\mathbb{C}$, resulting in 5D correlation maps. All the cross-correlations are saved as a z-buffer to only keep the maximum of the correlation maps on $\mathbb{C}$ in the memory. A threshold based on a percentage of the maximum value of this z-buffer is applied to limit detection to the best correlation between models and data. Robust detection is possible and presented in Chapter 3.

After this first detection step, all the parameters are roughly estimated: (x, y) with accuracy corresponding to the pixel size, and the other parameters (z, r, n) with accuracy that depends on the sampling steps of $\mathbb{C}$.

The second step, the estimation step, aims at refining these parameters using an optimization algorithm. The minimization of the cost function $\mathscr{D}^{\mathrm{P}}$ is then performed in a continuous parameter domain $\mathbb{C}$. It is performed sequentially for all the beads. At each iteration of this refinement step, the i-th bead parameters are estimated. During this step, the parameters of the beads already processed $j < i$ are set to their estimated values and the parameters of the beads that remain to be processed $j > i$ are set to the rough values obtained for them in the detection step. Consequently, the interferences between the diffraction patterns of all the beads are all accounted for in the optimization problem contrary to the algorithms of previous publications.

A.4 Estimation accuracy

In this section, we detail statistical tools of estimation [Kay, 1993]. They provide an insight into accuracy and correlations between the estimated parameters.

A.4.1 Covariance and correlation matrices

Variance/Covariance matrix définition

The covariance matrix $\boldsymbol{\Sigma}$ of a vector $\boldsymbol{\vartheta}$ is defined by :

$$\Sigma_{i,j}\left(\boldsymbol{\vartheta}\right) = \mathrm{Cov}(\vartheta_i, \vartheta_j) \tag{2.6}$$

where

$$\mathrm{Cov}(\vartheta_i, \vartheta_j) = \mathbb{E}(\vartheta_i \vartheta_j) - \mathbb{E}(\vartheta_i)\mathbb{E}(\vartheta_j) \tag{2.7}$$

This matrix generalizes the notion of variance to multiple dimensions. It is a useful statistical description of the estimated parameter since the diagonal coefficients correspond to the variance of the estimation of each parameter. It is strongly linked with the correlation matrix:

Correlation matrix définition

$$\mathrm{Cor}_{i,j}\left(\boldsymbol{\vartheta}\right) = \frac{\left[\boldsymbol{\Sigma}(\boldsymbol{\vartheta})\right]_{i,j}}{\sigma_{\vartheta_i}\sigma_{\vartheta_j}} \tag{2.8}$$

where σ_{ϑ_i} is the standard deviation of the estimation of parameter ϑ_i. It corresponds to the square root of i-th diagonal coefficient of $\boldsymbol{\Sigma}$. This matrix describes how linear is the relation between two variables. If $|\mathrm{Cor}_{i,j}| = 1$, ϑ_i and ϑ_j are linearly related.

A.4.2 Cramér-Rao Lower Bounds

In this section, we aim at estimating the achievable accuracy on each estimated parameter and study the correlation between these parameters. Cramér-Rao Lower Bounds (CRLB) is a statistical tool to compute a lower bound of this accuracy.

Cramér-Rao inequality

According to Cramér-Rao inequality, the variance of any unbiased estimator $\hat{\vartheta}_i$ of the unknown vector parameter ϑ_i is bounded from below by the i-th diagonal coefficient of the inverse of the Fisher information matrix:

$$\mathrm{Var}\left(\hat{\vartheta}_i\right) \geq \left[\boldsymbol{I}^{-1}(\boldsymbol{\vartheta})\right]_{i,i} = {\sigma_{\vartheta_i}^{\mathrm{CRLB}}}^2 \tag{2.9}$$

where $\boldsymbol{I}(\boldsymbol{\vartheta})$ is the Fisher information matrix. It is linked to the curvature of the cost function in the parameter space:

$$\left[\boldsymbol{I}(\boldsymbol{\vartheta})\right]_{i,j} = \mathbb{E}\left[\left|\frac{\partial^2 \mathscr{D}^{\mathrm{P}}(\cdot)}{\partial\vartheta_i \partial\vartheta_j}\right|_{\boldsymbol{\vartheta}}\right] \tag{2.10}$$

In the case of white Gaussian noise of standard deviation σ_η, neglecting quantization effect and considering a centered model [Fournier et al., 2010] :

$$\left[\boldsymbol{I}(\boldsymbol{\vartheta})\right]_{i,j} = \frac{1}{\sigma_\epsilon^2}\sum_k \left(\frac{\partial \boldsymbol{m}^{\mathrm{P}}(x_k, y_k, \boldsymbol{\vartheta})}{\partial\vartheta_i}\frac{\partial \boldsymbol{m}^{\mathrm{P}}(x_k, y_k, \boldsymbol{\vartheta})}{\partial\vartheta_j}\right) \tag{2.11}$$

Note that to obtain the best achievable precision, the CRLB should be computed at the point that minimizes $\mathscr{D}^{\mathrm{P}}$. In our case, we compute them at a coarse estimation of this point.

B Automatic numerical focus plane estimation using calibration beads

In this section we propose a robust and repeatable autofocusing method based on the insertion of calibration beads in the sample. It is applied on simulated and experimental holograms.

B.1 Proposed methodology for reproducible axial localization of samples

In the next section, we illustrate, using simulations, the need for a spatially well-defined reference plane.

B.1.1 Interest of a reference plane localization

In order to emphasize the need for a reference plane, 5 simulations of spherical objects holograms were computed (see Fig.2.2.a) using Mie model [Slimani et al., 1984] using similar setup parameters as the Setup-BIOASTER ones (see Appendix A Section B). The illumination is a monochromatic plane wave of wavelength $\lambda = 532nm$. The 5 beads are considered in contact with the microscope slide located at $12\mu m$ from the conjugate of the camera plane (see Fig.2.3). The 5 beads differ in radius, refractive index, and transmittance in order to mimic the diversity of biological objects in a stained sample (see Appendix A Section C). These parameters are given in Table 2.1. Figures 2.2.b display the modulus of the back propagated wave (using angular spectrum propagation [Goodman, 2005]) in the beads cross section XZ of the z-stack. The slide plane is displayed by a green line which is the same for all simulations. The beads edges are represented by black dotted circles and the planes that goes through the beads center by black dotted lines. The orange and blue dashed lines represent respectively the focusing position obtained using two image-based methods GRA and ToG detailed in Section A.1.1 and Section A.1.2. Figures 2.2.c show the GRA (orange dashed curves) and ToG (blue dashed curves)

	(1)	(2)	(3)	(4)	(5)
radius r (μm)	1	0.4	0.5	0.5	0.5
z (μm)	11	11.6	11.5	11.5	11.5
refractive index n	1.4	1.35	1.44	1.44	1.35
transmittance	1	0.5	1	0.01	1

Table 2.1: Simulations parameters for the 5 holograms of Figure 2.2. The transmittance parameter is defined as $t = e^{-2\pi n_i \frac{2r}{\lambda}}$ where n_i is the extinction coefficient.

focusing criteria for the five holograms. As in Figures 2.2.b, the slide plane position (green line), the bead center plane (dotted black line) and GRA/ToG focusing positions (orange

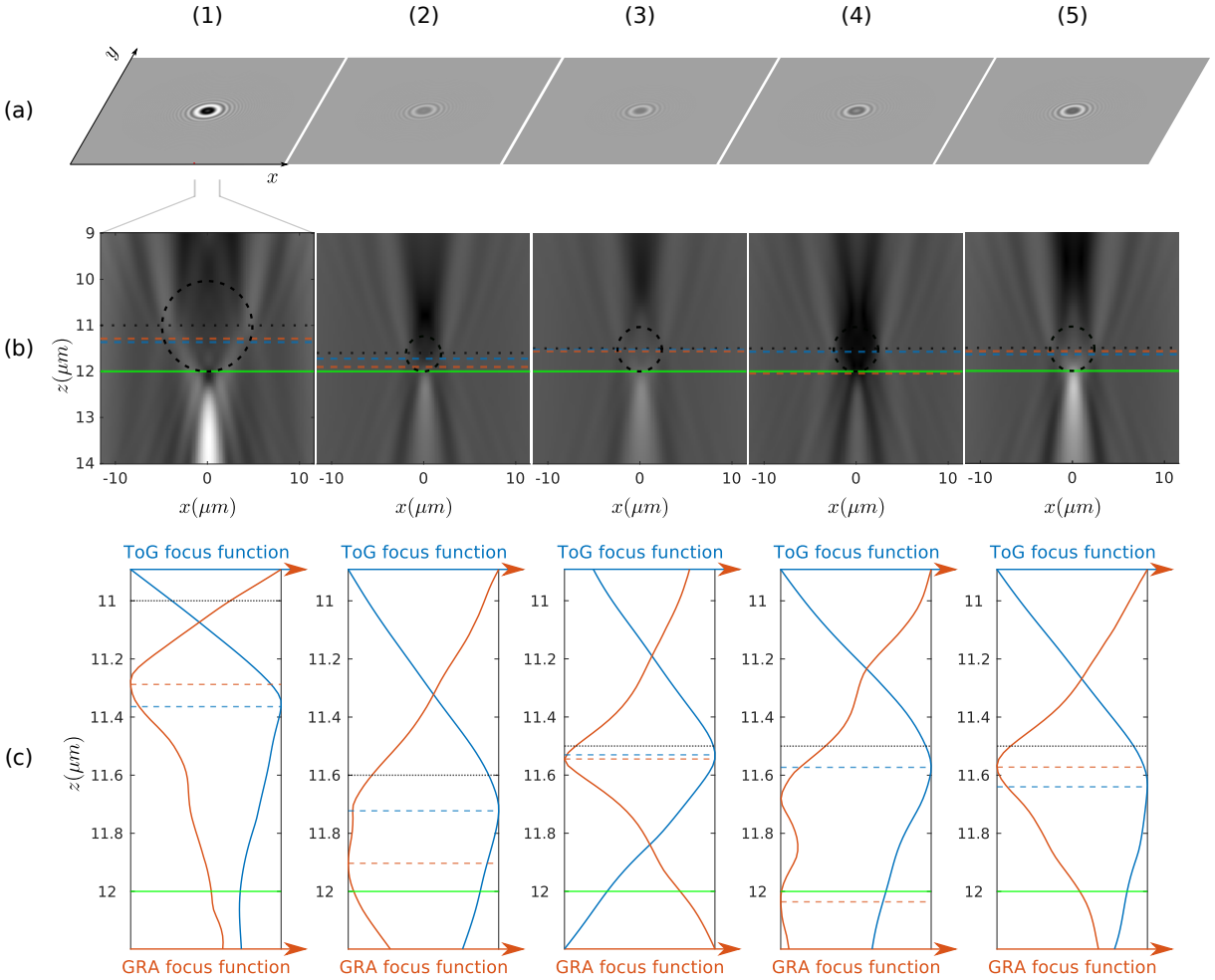

Figure 2.2: Illustration of the need for an object independent reference plane : (a) in-line holograms simulated with experimental parameters given in Table 2.1, (b) amplitude of the back propagation of the holograms, the green line represents the slide plane, the black line and the black circles represent the beads center planes and the beads edges, the orange and blue lines represent the focus plane estimated using GRA and ToG focusing criteria, (c) evolution of the focusing function GRA (orange color) and ToG (blue color) along the direction z, the slide plane (green color) and the beads center planes (black color) are also displayed as in (b)

and blue dashed lines) are also displayed. These simulations show that the focusing planes positions, estimated from image-based criteria, vary according to the criterion used (GRA or ToG), according to the optical characteristics of the objects imaged (transmittance, refractive index) and according to their sizes. Even if the ToG criterion gives positions close to the center of the objects, it deviates from them differently depending on the type and size of the objects imaged. For example, the deviation between focusing and bead center position are not negligible : up to $0.4\mu m$ for ToG and $0.5\mu m$ for GRA. In addition, the focusing functions can have several close extrema (for example, bead 2 and 4) which can lead to bias and instability in the measurement.

To detect and classify objects on a large number of various samples, it is important to

have a numerical reconstruction in a plane positioned relatively to a physical plane, for example the slide surface. This will make the technique reproducible (the same object will always give the same pattern in the reconstructed plane) and simplify the subsequent classification task. The approach we propose makes it possible to precisely estimate the upper plane of the microscope slide (or coverslip) called hereafter *the reference plane*.

B.1.2 Principle of the proposed method

As previously mentioned, the need for an accurate, reproducible, and objective focusing criteria is still crucial, even more so in the context of automation or quantitative microscopy of highly dispersed samples.

Our approach consists in inserting well-chosen calibrated objects (calibrated spherical objects) inside the sample in order to estimate their individual locations from a single hologram using a precise parametric IPA as described in Section A.3. Assuming that the beads are in contact with the slide, the 3D coordinates of the bead-slide contact point can be deduced from the size and 3D location of the beads. A slide plane can then be adjusted on the set of the 3D point cloud. This reference plane is an objective, physical position, independent of specific maximum focusing criteria. Any focusing distance can be then defined relatively to this reference plane. For example since bacteria are supposed to be around 1 μm diameter sized, the focus will be performed at 0.5 μm from the slide. More details on the choice of the calibration beads are provided in Appendix A Section C.

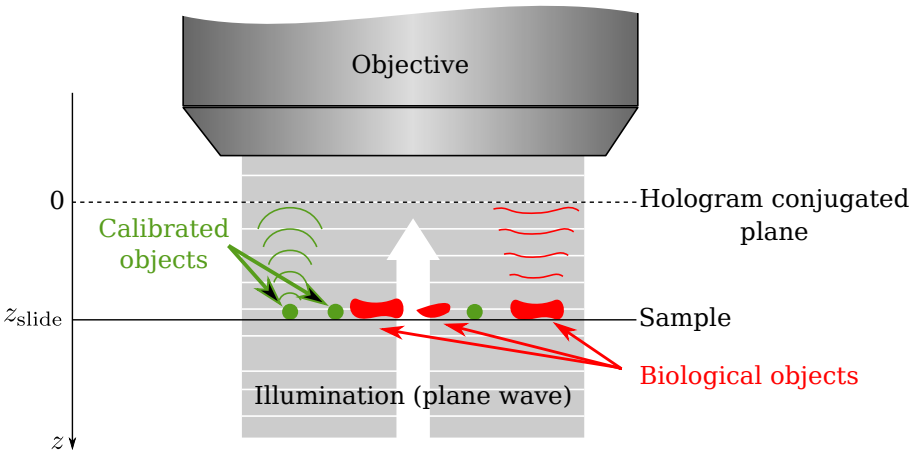

Figure 2.3: Example of an in-line digital holographic upright microscope with calibrated objects inserted in the biological sample.

Fig. 2.3 shows the proposed setup: an in-line digital holographic microscopy setup, *i.e.* a traditional microscopy setup with coherent illumination and a slight defocus.

B.2 Application of axial localization of the sample and discussion

In this section, we first apply the proposed method to simulated holograms to demonstrate the robustness of our approach to samples made of objects that vary in size, transmittance

and refractive index. We then apply it to experimental holograms of beads inserted in a sample of red blood cells. We compare results with state-of-the-art numerical autofocus algorithms in both simulated and experimental cases.

B.2.1 Validation on simulated holograms

B.2.1.1 Simulated holograms

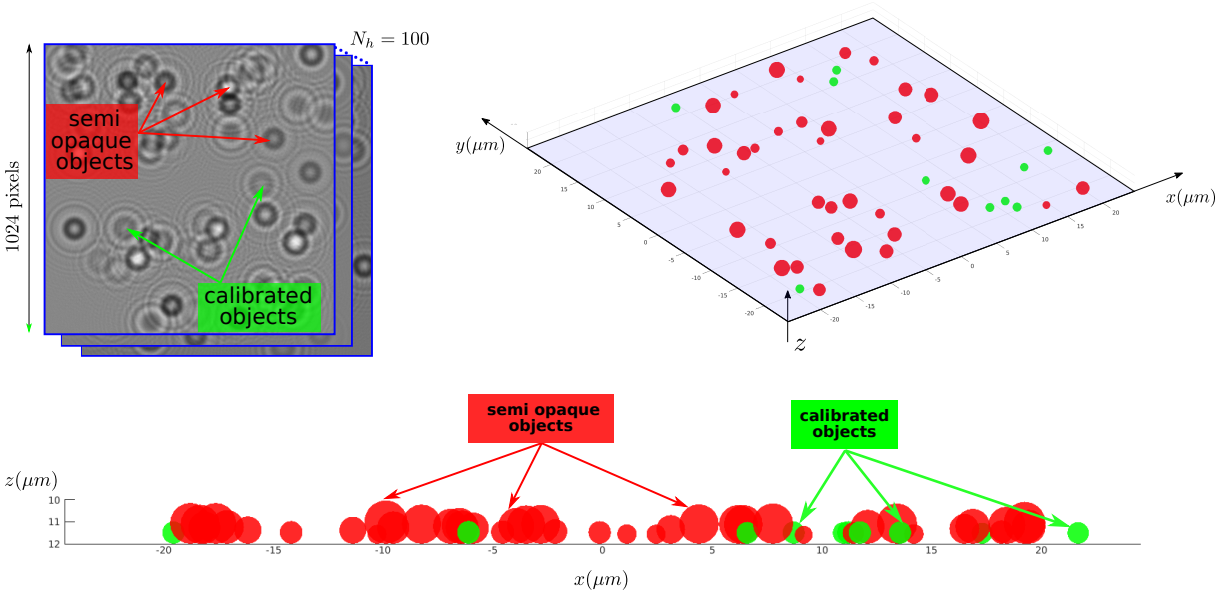

Figure 2.4: Illustration of the simulation of holograms stack.

A stack of one hundred in-line holograms based on stained sample experimental conditions is simulated (see Appendix A Section C). For each hologram, 10 silica beads and 50 spherical objects that stand for the biological material, are simulated on a plane surface corresponding to a virtual slide perpendicular to the optical axis (see Fig 2.4). Lorenz–Mie models are used to generate the interferences between the incident wavefront and the complex amplitude of the diffracted waves on the sensor $\{\underline{\boldsymbol{a}}^{\text{Mie}}(\vartheta^{(i)}\}_{i=1..N_{\text{beads}}}$ (cf. Equation 2.2).

In this simulation, the sensor plane is composed of 1024×1024 pixels with experimental parameter similar to the ones of Setup-BIOASTER (see Appendix A Section B). It is located at $z_s = 12\mu m$ from the slide plane. Finally, a white Gaussian noise η is added, leading to holograms with a signal-to-noise ratio (SNR) of 10 (where the SNR is defined a the ratio between the semi-amplitude of the signal and the standard deviation). All the object transversal coordinates $\{x^{(i)}, y^{(i)}\}_{i=1..N_{\text{beads}}}$ are randomly distributed on the sensor support. Objects overlap is avoided.

The objects are considered to be immersed in oil with a refractive index of 1.519. The beads parameters are those of standard silica calibration beads used for microscopy. Their mean radius is $r_b = 500nm$ and their mean refractive index is $n_b = 1.44$. To test our approach in a polydispersed case, the bead radii and refractive indices are drawn from a uniform law with a width equal to $\Delta r_b = 50nm$ for the radius and $\Delta n_b = 0.02$ for the refractive index. Their transmittance is assumed to be equal to 1 (pure phase object). The other spheres, standing for the biological sample, have more dispersed parameters

	silica beads (10)	other objects (50)
radius mean (nm)	500	700
range of the radii (nm)	$[475, 525]$	$[400, 1000]$
refractive index mean	1.44	1.5545
range of the refractive indices	$[1.43, 1.45]$	$[1.519, 1.590]$
transmittance mean	1	0.5
range of the transmittance	-	$[0, 1]$

Table 2.2: Simulation parameters for the stack of 100 holograms (illustrated in Figure 2.4). The bead radii and refractive indices are drawn from uniform laws. The transmittance is equal to 1 for the beads and is drawn from a uniform law for the other objects. The mean values and the ranges of the uniform laws are given in the table.

also drawn from uniform distributions. The central value of the radius distribution is $r_s = 700nm$ and its width is $\Delta r_s = 600nm$. The central value of the dispersion of the refractive indices is $n_s = 1.5545$ and its width is $\Delta n_s = 0.0710$. This leads to radii in the range $[400, 1000]$ nm and refractive indices in the range $[1.519, 1.590]$. The transmittance of the spheres also varies from 0 (opaque objects) to 1 (phase object) with a uniform distribution. To better underline the diversity of the simulated samples, a summary of the parameters of these objects is given in the Table2.2. It should be noted that, for these simulations, the setup parameters (wavelength, pixel size, z_s) were chosen in accordance with the experimental parameters in the following section.

B.2.1.2 z estimate of the reference plane

The beads are detected and their parameters estimated for each hologram using the parametric IPA described in Section A.3. The optimization algorithm we used to minimize (2.5) in the estimation step is the SQP algorithm [Nocedal and Wright, 2006]. Note that the other spheres representing the biological sample are not reconstructed here: in this calibration step where the focus distance is estimated, their diffraction patterns are only considered as a source of disturbance for the reconstruction of the beads. From the estimation of the couple $(z^{(i)}, r^{(i)})$ of the i^{th} bead, the z coordinate of the contact point $P^{(i)}$ of the bead-slide can be easily derived:

$$z_P^{(i)} = z^{(i)} + r^{(i)} \tag{2.12}$$

To be less sensitive to possible outliers in the estimations of z contact-points, the q^{th} slide z-position is estimated from the median z values:

$$z_{\text{slide}}^{(q)} = \text{median}\left(\{z_P^{(i)}\}_{i \in \text{detected beads}}\right) \tag{2.13}$$

B.2.1.3 Statistical results

Considering 100 holograms and 10 beads per hologram, 1000 beads can be detected among 5000 objects.

The detection step uses a search parameter space $\mathbb{C}$ that is centered on the average values of the ground truth parameters but that is three times bigger than the width of its

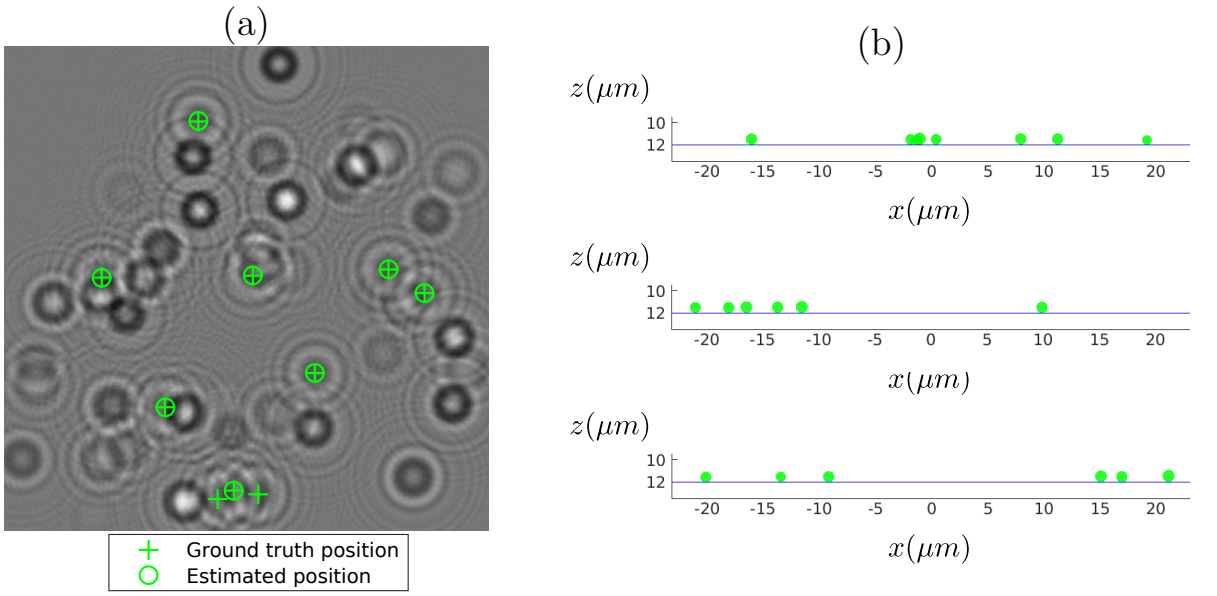

Figure 2.5: (a) Example of a simulated hologram with green circles on estimated positions and crosses on ground truth positions, (b) Examples of XZ-views of the reconstructed beads

distribution. This step detects the objects corresponding to the beads using a restrictive threshold coefficient on the correlation map equal to 75% of the maximum of the map, chosen in order to limit false detections. The estimation step uses much larger ranges (10 times the range of parameter distributions) so as to be less constrained.

Out of the total set of beads, 72.1 % were detected (on average 7.2 per hologram). Only 3 false detections were observed (objects that were not beads but were detected as beads) corresponding to 99.6% of true positive detections. The z contact point coordinate is computed for all the detected beads. For each hologram, the axial location of the reference plane, z_{slide}, is calculated using equation (2.13). An illustration is given on Figure 2.5.

The number of true detections could be improved by using robust detection and estimation techniques [Fitch et al., 2005].

The z_{slide} is computed for each hologram and compared to the focusing distance z_{focus} estimated by two state-of-the-art algorithms, GRA and ToG, currently used in the literature (see Section A.1.1 and A.1.2):

For both methods, back-propagated fields are computed using angular spectrum propagation [Goodman, 2005]. Whatever the criterion, GRA or ToG, it is based on the search for an extremum of a focus function in the stack of back propagated field maps. 50 maps were computed in the z range $[9.5, 13.5]\mu m$. A parabolic interpolation is performed on the focus function to precisely locate the extremum.

The image-based methods estimate a focus distance z_{focus} using the whole field of view, thus considering all the objects (with their diversity). Results obtained with IPA, GRA and ToG methods are displayed on the box-and-whisker plot in Figure 2.6. As expected, the median values of z_{slide} and z_{focus} (red line on the box and whisker) differ from one method to another : $12.00\mu m$ for IPA, $11.56\mu m$ for GRA and $11.30\mu m$ for ToG . Actually, only the IPA method produces an estimate of z_{slide}. z_{slide} is estimated with a very small

bias of $2nm$, which can be considered as non-significant given the standard error. Image-based methods estimate a focus distance z_{focus} located within the objects and thus smaller than z_{slide}. The interquartile ranges (distance between the upper and lower quartiles) are respectively $13nm$, $149nm$ and $79nm$ for IPA, GRA and ToG methods. It shows that the IPA is more accurate than image-based approaches, which makes sense because of the diversity of the simulated objects in the field of view and the global estimation of the image-based methods.

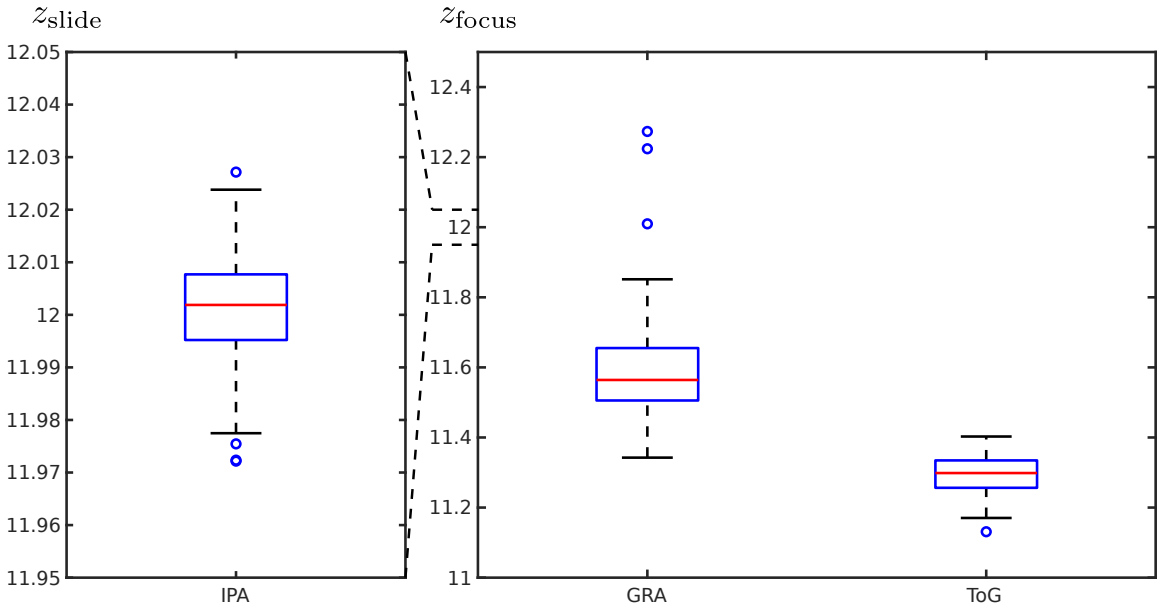

Figure 2.6: Box and whiskers plot of the axial locations (in μm) of z_{slide} for IPA and of z_{focus} for GRA and ToG criteria. The red lines represent the median values, the boxes extends from the 25th to the 75th percentile, the black lines represent the non-outlier minimum and the non-outlier maximum and the circles represent the outliers. Four outliers obtained with GRA method are not represented for visualization sake.

B.2.2 Application to experimental holograms

In this section, we apply our approach to blood smear samples. For this experiment we use holograms from Setup-BIOASTER with stained sample as described in Appendix A Section C.

B.2.2.1 Experiment

A set of 40 distinct fields of view has been recorded on a sensor of 3208×2200 pixels. Each field correspond to a $144\mu m \times 99\mu m$ view of the sample. Because of the mechanical stability and backlash effects of the automated XYZ-stage, it was not possible to have an axial positioning repeatability better than $\pm 1\mu m$ (typically) during the lateral translations of the sample on the whole explored area. A physical autofocus step was then performed on each field, using a high-precision piezoelectric objective scanner (PIFOC, PI) with a bidirectional repeatability of $\pm$5nm and a classical focusing criteria adapted for brightfield

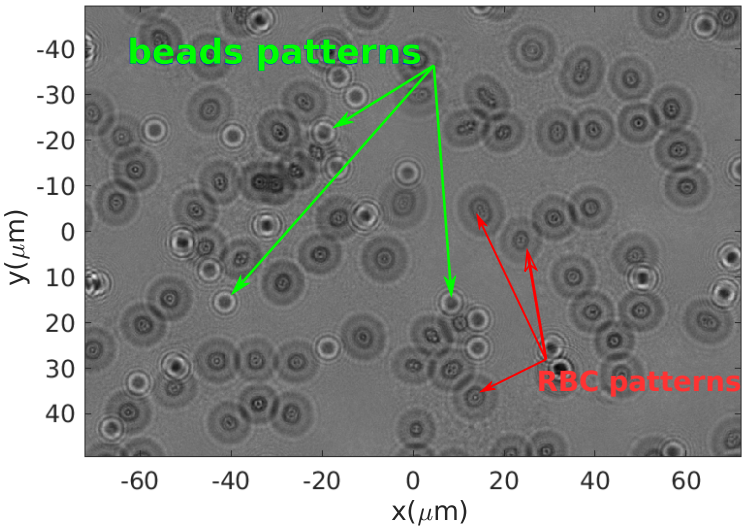

Figure 2.7: Example of an experimental hologram

images. This autofocusing step will not be described in detail here. However, this implies that the precision of the physical position of the slide is limited by the autofocusing accuracy. We should emphasize that this autofocus step was only necessary here to evaluate the feasibility of our approach, and is no longer necessary now that the method is validated : the autofosing can be performed numerically.

In order to compare our Inverse Problem Approach (IPA) to other autofocusing algorithms (GRA and ToG, previously described in section B.2.1), we have extracted 3 sets of positioning data from each hologram, with three different approaches :

- The first set is the (x, y, z) contact point cloud corresponding to the contact point $(z_P = z + r)$ estimated by parametric inverse problem approach described in Section A.3. An example of such a reconstruction is displayed on Figure.2.8.

- The second set is also a (x, y, z) point cloud corresponding to the focus estimation with the GRA criterion performed on patches extracted from each hologram (each hologram was divided into 25 non-overlapping sub-images (5×5). The patches size is 640×440 pixels.

- The third set is exactly the same as the second, but with the ToG algorithm instead of the GRA criterion.

In these conditions, we generated 40 point clouds (x, y, z) with 3 different methods that will be referred as IPA, GRA and ToG in the following. With the IPA method, we reconstructed 1129 contact point locations, randomly distributed from one field to the other. The median value is 29 contact points per field (with a minimum of 18 and a maximum of 37). The computation time of the proposed reconstruction method depends on the number of beads to reconstruct. For these experiments, with an Intel Xeon CPU 2.20GHz with 65GBytes of RAM the IPA algorithm take 7 seconds per bead (for both the detection and the estimation).

For GRA and ToG sets, it must be noticed that the reconstructed axial position are the best numerical focus obtained on the patches. In these patches, most of the pixels are occupied by red blood cells. Moreover, contrary to the IPA reconstruction of the beads, the 25 patches are equally distributed over the field. The goal here was to generate comparable sets of data for the local IPA approach and the global image-based methods (GRA and ToG). With the patch approach, the image-based algorithms are able to evaluate the focus at a more local scale. The number of locations on a field are also similar: 29 for IPA, 25 for patches approaches.

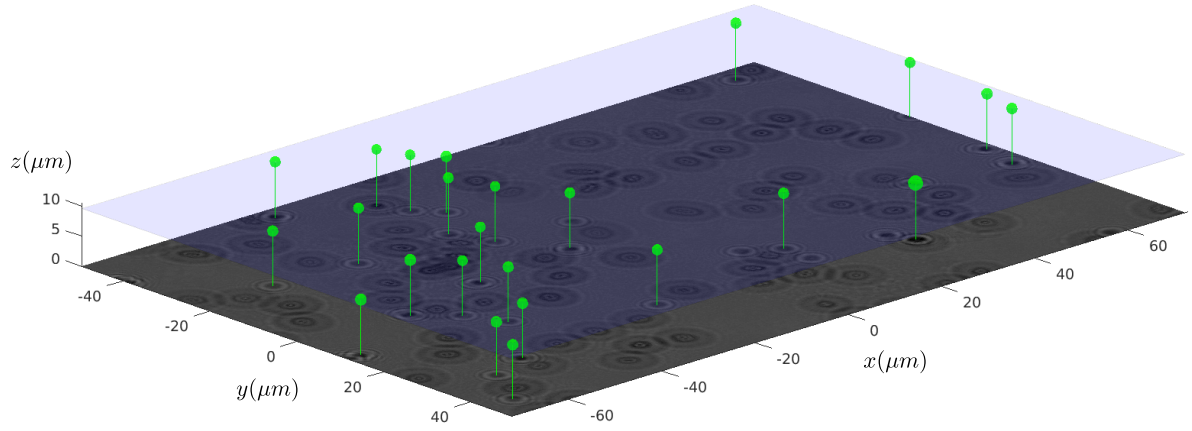

Figure 2.8: Illustration of the beads reconstruction from one hologram. For visualisation purposes, the size of the beads is doubled.

B.2.2.2 3D positionning of the reference plane

For each hologram and each method (IPA, GRA, ToG), a robust plane fit was performed on the point cloud (x, y, z), using iterative re-weighted least squares with a Cauchy robust function. The plane is defined by the parametric equation $z = \hat{a}.x + \hat{b}.y + \hat{c}$, where $(\hat{a}, \hat{b}, \hat{c})$ are the estimated parameters. Parameter $\hat{c}$ is then the estimated axial position in the center of the field, which represents the contact point for the IPA, and the best focus in the center patch for GRA and ToG.

For our approach (IPA), the dispersion of the estimated contact point axial locations from the fitted plane is presented in the form of a box and whiskers plot of the residuals on Fig. 2.9(A). As can be seen, the point axial positions are close to the fitted plane but with some outliers. The plot has been cropped to exclude a few outliers with an error larger than $\pm 0.5 \mu m$ (16 outliers over 1129 beads). This behavior can be due to false detections, or faulty estimations of altered or agglomerated beads. The use of robust plane fitting is then justified, as it gives less weight to outliers. This presence of outliers can be also seen with the patch approaches (GRA, ToG), but to a lesser extent. In this case, the variability of the blood cells distribution among the patches is to be blamed, even if this distribution is quite dense and uniform. Incidentally, in the rest of our analyses, it has been chosen to use median values, rather than averages and a robust estimation of the dispersion using the median absolute deviation (MAD) of the data: $\sigma_{\text{MAD}} = 1.4826 \times \text{MAD}$.

From the IPA reconstructions, the estimated parameters of the 40 planes are presented on Fig. 2.9(B-D). The estimated parameters are the axial position in the center of the

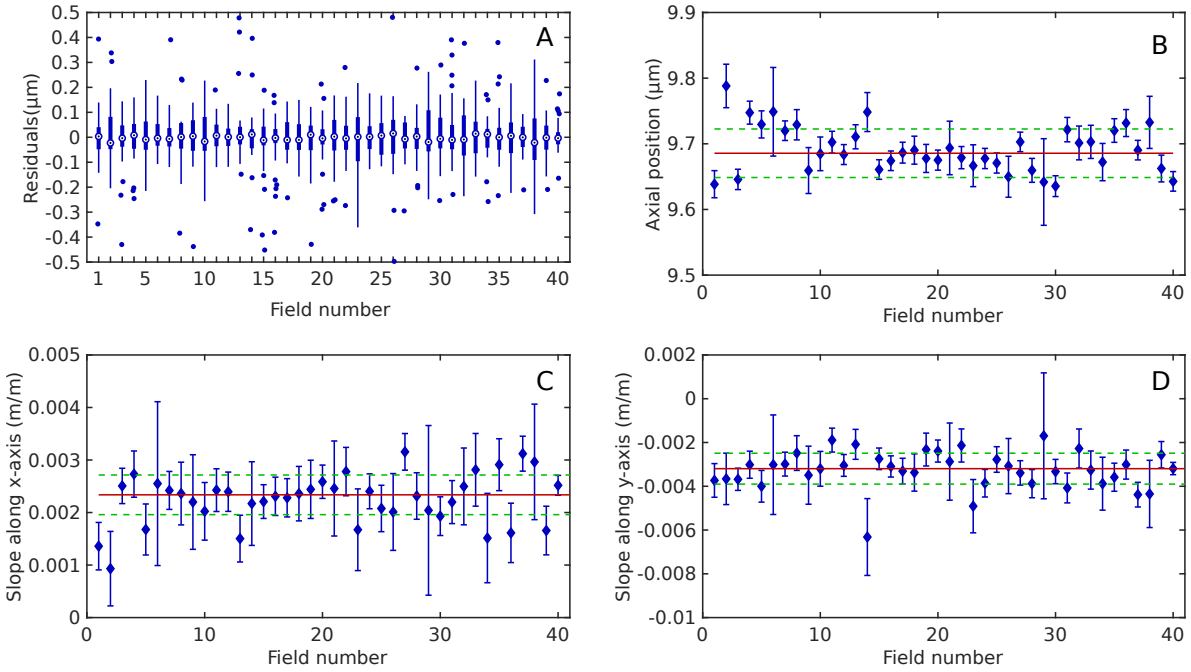

Figure 2.9: Robust plane fitting results for IPA. **A:** Box and whiskers plot of the residuals of the axial locations of the reconstructed beads contact points (using eq.2.12) from the fitted plane as a function of the field number. The dotted circles represent the median values, the thick line extends from the 25th to the 75th percentile, the thin line extends from the non-outlier minimum to the non-outlier maximum and the circles represent the outliers. **B,C,D:** Estimated parameters on the 40 fields and the standard errors (from the robust fit). B: axial position in the middle of the field $\hat{c}$, C: slope along x direction $\hat{a}$, D: slope along y direction $\hat{b}$). The red line represents the median value over the fields, the green dashed line represents the dispersion from the median value $\pm\sigma_{\text{MAD}}$.

field ($\hat{c}$), the slope along x ($\hat{a}$) and the slope along y ($\hat{b}$). The error bars represent the estimated standard errors on these parameters, evaluated in the robust plane fitting step. Thus, these errors only depend on the accuracy of the fit, which may be related to the accuracy of the IPA reconstruction, the number of beads and their distribution within each field and the presence and number of outliers. This error must not be confused with the dispersion of the parameters measured from one field to the other (presented later).

Table 2.3 presents the fitted parameters evaluated on the 3 sets of data (IPA, GRA, ToG). The value and dispersion given in this table are, respectively, the median value of the parameters $(\hat{a}, \hat{b}, \hat{c})$ on the 40 holograms and the median value of the standard error on parameters found for the 40 holograms. As expected, there is a difference in the median value of the axial position between the IPA set ($9.686\mu m$) and the GRA and ToG sets (respectively $8.973\mu m$ and $8.635\mu m$). Indeed, it is reasonable to find such a difference (around $1\mu m$) as the IPA method is expected to locate the slide surface while the other methods can only locate the best focus on red blood cells whose thickness is around $2\mu m$. What is most striking is the fact that the two image-based methods (GRA, ToG) give axial locations almost $0.34\mu m$ apart, which is not negligible, compared with the associated errors. This means that the best-focus axial position is sensitive to the chosen image-based criterion, which is one of the problem that our autofocusing approach

propose to prevent, or at least reduce. Concerning the fitting errors, it is quite low for IPA (±19nm). This tends to demonstrate that the plane fitting is quite precise, which indirectly validate our approximation about the fact that the beads are close to the slide. The higher median errors for image-based approaches (±51nm for GRA and ±123nm for ToG) indicate that a precise location using an image-based criterion on more dispersed objects (red blood cells) is a little more difficult, as the cells are thicker than the beads, more dispersed in sizes and shapes and their distribution may vary from one patch to another. Concerning the slopes of the fitted planes, the results are quite similar for the 3 sets of data. It is interesting to see that the IPA method, as well as the patches approaches with standard algorithms (GRA and ToG) are able to estimate a slope typically less than 2.5×10^{-3} (along the X-axis), which corresponds to an axial shift of only 360nm on the total width of a field ($144\mu m$).

Parameters	IPA	GRA	ToG
Axial position ($\hat{c}$) (μm)	9.686 ± 0.019	8.973 ± 0.051	8.635 ± 0.123
Slope along x ($\hat{a}$) $\times 10^{-3}$	2.337 ± 0.462	2.438 ± 0.461	2.459 ± 1.130
Slope along y ($\hat{b}$) $\times 10^{-3}$	-3.196 ± 0.683	-3.094 ± 0.671	-3.061 ± 1.641

Table 2.3: Fit parameters estimated from the robust plane fitting on 40 holograms with our Inverse Problem Approach (IPA) and the two state of the art algorithms (GRA, ToG) performed on 25 patches of each hologram. The estimated value are median values on the 40 holograms and the dispersion is evaluated with the median value of the standard error estimated during the robust fitting of the plane.

Finally, Table 2.4 presents the median value and the dispersion of the fitted parameters evaluated with the 40 holograms. For a better illustration of the estimated tilt of the slide, the slopes have been converted into angles: θ_z being the angle between the normal of the estimated plane and the Z-axis and θ_x being the angle between the projection of this normal on the XY-plane and the X-axis. These angles can be seen as an equivalent of an azimuth (θ_x) and an elevation angle (θ_z). The median value of the axial position is the same as in table 2.3, but the dispersion values are obtained by calculating the σ_{MAD} of the 40 estimated parameters. These dispersion values include now the variability of the axial position of the slide and possibly of the tilt angle from one field to another. The variability of the slide position include the effect of the physical refocusing for each field. The dispersion of the axial position is still very good for IPA, with only ±37nm, which is slightly more than the ±19nm median of the standard errors previously reported on our numerical simulations, as could be expected. However, as this value includes the physical refocusing step for each field, this result indicates that the physical autofocusing step was very stable on the 40 fields under concern. For the GRA and ToG data sets, the σ_{MAD} dispersion values of the axial position over the 40 fields (±63nm for GRA, ±109nm for ToG) are similar to the median of the fitting standard errors of Table 2.3. Once again, ToG seems to be a little less precise in estimating the axial position. For the tilt angle θ_z, the results are very similar with a value of 0.22-0.23 degrees with the 3 methods. For the angle θ_x, the dispersion is greater, which is understandable as the projection of the normal of the plane on the XY-plane is very small and very sensitive to any error on the plane reconstruction. In particular, it must be noted that ToG is less effective in the present experimental conditions than IPA and GRA, particularly for the θ_x estimation.

As a conclusion, by comparing our local IPA approach with the state-of-the-art algorithms GRA and ToG performed on image patches, it comes out that it is possible, with all 3 methods, to use a robust fit of a plane to evaluate both an axial position, as well as a very small tilt of the slide, with a pretty good repeatability on 40 non-overlapping fields-of-view of the same slide. As expected, there is a difference in the axial locations with IPA and standard approaches. Indeed, the IPA aims at locating the slide surface while the standard approaches aims at locating the best focus on dispersed objects (blood cells). While the tilt angle of the slide is quite precisely evaluated (except for ToG, which is less precise here), the error on the estimated parameters of the fit indicate that the axial position of the slide is more precisely evaluated with our approach. This last point indicates also that a major hypothesis of our approach seems to be validated: except for some rare outliers that could be detected and filtered, the axial positions of the beads are close to a single plane with a good stability over the 40 analysed fields. Finally, the IPA dispersion is not very far and quite comparable to the GRA algorithm, but it must be mentioned that the experiment was performed with a sample (blood smear) in which the most represented objects (red blood cells) were eventually very similar and quite uniformly distributed. As demonstrated on the simulations of section B.2.1, the efficiency of GRA and ToG algorithms can really degrade with more dispersed biological objects.

Parameters	IPA	GRA	ToG
Axial position ($\hat{c}$) (μm)	9.686 ± 0.037	8.973 ± 0.063	8.635 ± 0.109
θ_z (degrees)	0.224 ± 0.035	0.227 ± 0.018	0.221 ± 0.072
θ_x (degrees)	125.6 ± 7.2	129.8 ± 10.6	130.5 ± 23.0

Table 2.4: Median value and dispersion on various parameters amongst the 40 fields tested. The dispersion is still evaluated with σ_{MAD}. θ_z is the angle between the Z-axis (optical axis) and the normal to the plane surface. θ_x is the angle between the X-axis direction and the projection of the normal on the horizontal plane (XY-plane).

B.3 Regularized reconstruction of a hologram

Once the propagation distance z has been calibrated using a parametric inverse problem approach, it is possible to use a regularized inverse problem approach to reconstruct the holograms. Algorithm 4 summarize the whole methodology to reconstruct a hologram at any chosen distance Δz of the slide plane using the proposed autofocusing methodology.

Algorithm 4: Reconstruction of a sample plane based on inverse problem approaches using auto-calibration of the propagation distance z

Input : Data $\boldsymbol{d}$
Input : Distance between the slide and the reconstruction plane Δz
Output : Parameters of the beads
$\boldsymbol{\Theta} = \{\boldsymbol{\vartheta}^{(i)}\}_{i\in[1,N_{\text{beads}}]}, \boldsymbol{\vartheta}^{(i)} = \{x^{(i)}, y^{(i)}, z^{(i)}, r^{(i)}, n^{(i)}\}$
Output : Object complex transmittance in focus plane $\underline{\boldsymbol{a}}_0$

1. Parametric estimation:
(Minimization of the parametric data fidelity $\mathscr{D}(\cdot, \boldsymbol{d})$)
$\boldsymbol{\Theta} \leftarrow$ First estimation of the parameters of the beads (Coarse estimation)
for *k=1 à N* **do**
  $\boldsymbol{\vartheta}^{(k)} \leftarrow$ Local minimization of $\mathscr{D}$ using an optimization algorithm
end
$z_{\text{slide}} \leftarrow$ Median of the estimated $\{z_P^{(i)}\} = z^{(i)} + r^{(i)}$.

2. Non parametric reconstruction:
(Minimization of the non parametric loss function $\mathscr{L}$)
$\underline{\boldsymbol{t}} \leftarrow \boldsymbol{d} * \underline{\boldsymbol{h}}^*_{z_{\text{slide}}-\Delta z}$
$\underline{\boldsymbol{t}} \leftarrow$ Minimization of $\mathscr{L}$ using an optimization algorithm

Figure 2.10, illustrates first reconstruction results on experimental data performed using the methodology described in this chapter. Five beads have been reconstructed using parametric IPA. The distance between the slide and the sensor is then estimated from the parameters of the beads. It is then possible to reconstruct the hologram at distance $\Delta z = 0.5\mu m$ of the slide. In this example, a complex total variation regularization (see Chapter 1) has been used and the regularization hyperparameters have been tuned manually. Figure show first modules and phase reconstruction of a hologram. The residuals illustration correspond to the difference between the data and the image formation model. As seen on these images, most of the signal has been reconstructed, however strong reconstruction artefacts are still visible. This can be explained by bad regularization hyperparameter tuning or errors in the image formation model. These issues will be assessed in the following chapters of this manuscript.

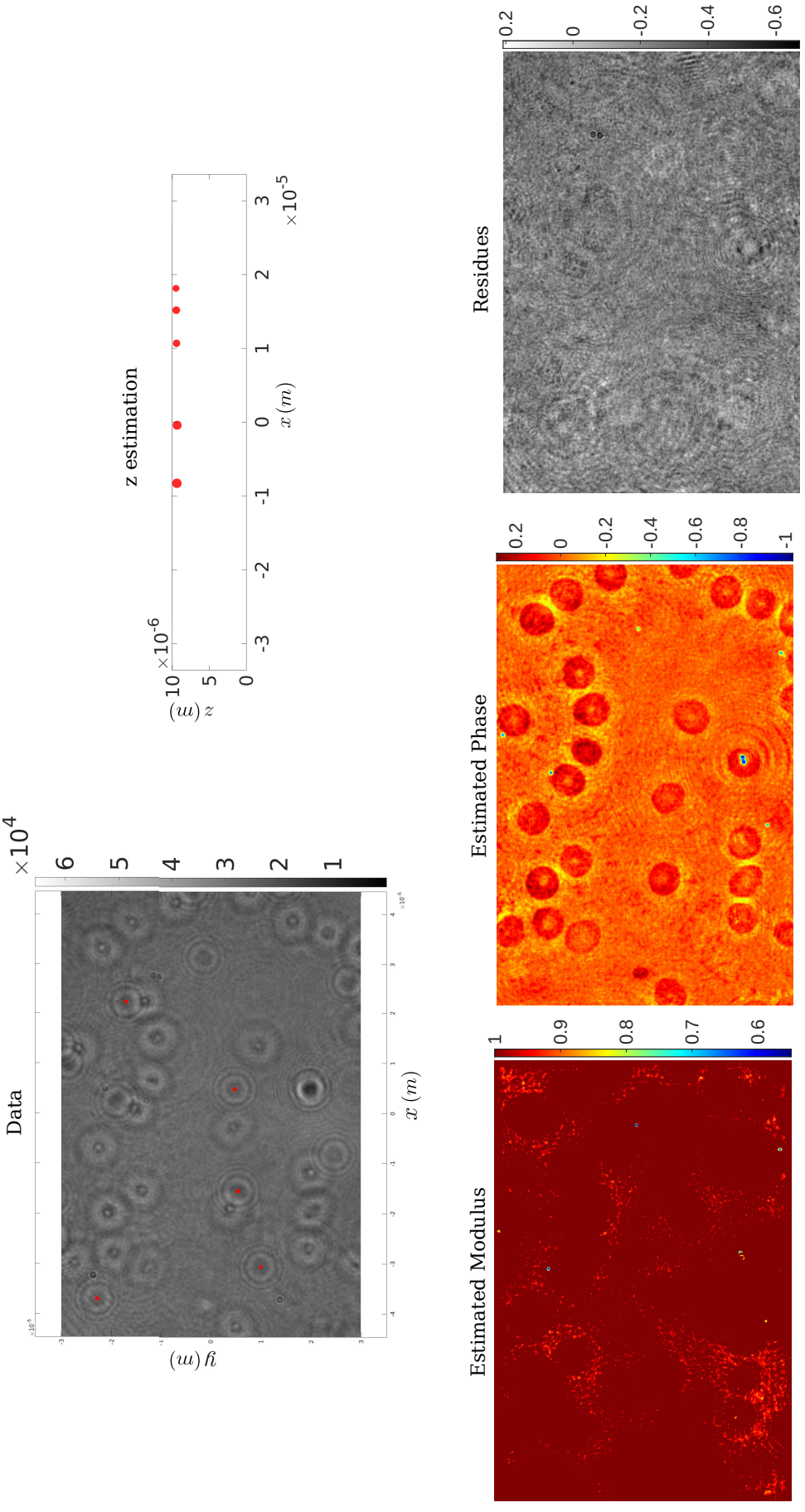

Figure 2.10: Illustration of a regularized reconstruction of a blood smear sample using a autofocusing technique based on parametric inverse problem approach reconstructions of calibration beads

C Conclusion

This chapter presents a method for estimating the position of the plane on which the sample is placed. It is based on the insertion and detection of calibration beads inserted in the biological sample. Estimating the location and size of the beads using a parametric IPA makes it possible to accurately reconstruct the surface of the slide on which the beads and the biological sample are placed. Knowledge of the location of this reference plane allows the user to objectively choose the position of the reconstruction plane.

Unlike other approaches, the reference plane is independent of the type of objects present in the biological sample and therefore enables reproducible focusing on an objective physical surface, which could be useful for whole slide imaging, drift compensation or automated high-throughput sample classification. Moreover, it also makes it possible to estimate a tilt of the slide, which could allows tilt corrections.

The study provides proof of the feasibility of the method. Its limits in terms of robustness to high density and variety of objects in the field still need to be studied. The proposed methodology was applied to an in-line holographic configuration, but it is also applicable to off-axis holography when the samples are composed of objects of different shapes and different optical characteristics.

The need for inserting calibrated objects inside a sample (or using known patterns engraved on the slides) adds additional experimental complexity or cost to the sample preparation step. However, the method proposed here offers interesting perspectives for reconstructing a slide surface that is not flat or taking into account aberrations as described in Chapter 4. Other calibration objects can be considered. Further studies on the choice of the calibration objects can be performed to improve the estimation accuracy. However, in this thesis, proof of feasibility have been performed on calibration beads as described in Appendix C.

It must be noted that this approach does not particularly requires mono-dispersed calibration beads because the size of the beads are evaluated and taken into account in the reconstruction of the slide plane. Moreover, depending on the application, the use of purely absorbing objects of micrometer or even sub-micrometer sizes is also possible.

It is important to notice that this methodology is not adapted nor required for any microscopy situations. For dense samples (*e.g.* biological tissues), whole slide imaging, or especially with low magnification objective, the requirements for sub-micrometric focusing is not an issue, as the depth of field is more important, as well as the thickness of the sample. The main requirement would be then to find a way to keep a stable focus throughout the slide. For this, many methods mentioned previously would do the job. Moreover, in some samples, it can be difficult or undesirable to insert objects, because of the sample nature or to avoid contamination. However, our methodology is adapted to the context of automated microscopy analyses of liquid samples (*e.g.*, blood, urine, cerebrospinal fluid). As they represent an important part of the medical microscopy analyses, their automation is of major importance. In this context, our methodology, in its principle, aims at being repeatable and robust to a large diversity of size and absorption of the objects present in the sample, contrary to image-based methods. In the context of automation, it aims at locating, for each slide/field of view, a spatial reference position with a sub-micrometric resolution.

CHAPTER 3

Fast and robust pattern detection in in-line holographic microscopy

Abstract

The detection of calibration beads is an essential step in the autofocusing method proposed in Chapter 2. Yet, the detection of diffraction patterns can be difficult due to interferences between the holograms. In this case, detecting the pattern of interest requires robust detection techniques. A major drawback of robust pattern matching is the high computational complexity when fast Fourier-based correlations are replaced by systematic evaluations of a non-quadratic loss function. In the case of spatially extended patterns, like digital holography, the complexity becomes prohibitive. In this chapter, we propose a fast detection algorithm that still relies on fast correlations to approximate various robust loss functions. In this chapter, after a preliminary section, we present the proposed detection scheme and validate it on simulated and experimental data. This chapter is adapted from the paper [Brault et al., 2022a]. A video submitted for the IEEE European Signal Processing Conference (EUSIPCO) 09/2022 is available at the following link: Video Chapter 2

Introduction

Direct object detection by matching a diffraction pattern model to the hologram fringes is useful in many applications, from holographic microscope calibration to 3D particle location and tracking. To perform the numerical refocusing proposed in Chapter 2, Section B.1.2, spherical calibration beads can be used to accurately locate the sample plane. The 3D localization of spherical objects can be estimated from a digital hologram by a greedy algorithm similar to continuous matching pursuit [Mallat and Zhang, 1993, Soulez et al., 2007a, Brault et al., 2022b]. The diffraction pattern produced by a homogeneous

spherical bead is well modelled by Mie theory [Slimani et al., 1984] and depends only on a few parameters: the 3D location of the bead (x, y, z), the radius r of the bead and its refractive index n.

Matching pursuit algorithms identify the location of objects one at a time, based on a maximum correlation criterion corresponding to the minimization of a least-square criterion. When spherical beads are added on a slide that contains biological samples, the detection and localization of the beads becomes much more difficult, especially when the diffraction patterns of the beads are less contrasted than the other diffraction patterns: the cross-correlation between the model and the data displays maxima at locations corresponding to well-contrasted biological structures. Robust detection strategies, more tolerant to marked deviations in the measurements, are then necessary for the detection [Rousseeuw and Hubert, 2011, Denis et al., 2016, Flasseur et al., 2019] and accurate localization [Flasseur et al., 2017a] of the beads.

An important practical advantage of maximum correlation approaches is the possibility to quickly compute detection maps using fast Fourier transforms to identify the (x, y) location for a hypothesized set of parameters $\boldsymbol{\varpi} = (z, r, n)$ (that can be optimized).

While it is relatively straightforward to adapt a local optimization method to account for a non-quadratic loss function (e.g. Iterative Reweighted Least Squares (IRLS) [Holland and Welsch, 1977, Flasseur et al., 2017a]), it is much more challenging to detect a large pattern robustly in 2D due to the enormous increase in computational complexity caused by dropping the fast correlations.

Some approaches taken from robust signal processing [Rousseeuw and Hubert, 2011] have been used for pattern location, e.g., in the case of weak signals buried in a zero-mean non-Gaussian noise [Denis et al., 2016], when collections of background images can be used to capture the spatial correlations of the disturbance terms [Flasseur et al., 2019]. Deep learning methods have also been used for particle localization but may suffer generalization issues and need a training dataset [Altman and Grier, 2020].

Several methods have been proposed to speed up the process of robust template matching e.g., computation based on multi-resolution computation of the robust cost function [Chen et al., 2003] or a template matching strategy based on the Inverted Location Index for non-decreasing bounded robust functions [Sibiryakov, 2011].

In this chapter, we extend the fast robust correlation approach proposed by Fitch *et al.* [Fitch et al., 2005] to approximate detection maps for arbitrary robust functions as a sum of correlations. It is applicable to pattern detection problems in different fields.

In the Preliminaries section we detail classical correlation-based detection techniques. Then, we introduce some of the most popular robust penalizations. At last the robust detection method proposed by Fitch *et al.* is reminded. The proposed extension of this methodology is described in Section B.1. The proposed method is then illustrated in Section B.2 on a challenging bead location problem in holographic microscopy, using both simulated and experimental images.

A Preliminaries

A.1 Correlation-based pattern detection

A.1.1 Detection by correlation

In the presence of observed data $\boldsymbol{d} \in \mathbb{R}^{H \cdot W}$ (an $L \cdot C$ pixels image), finding the (x, y) location of an object modelled by $\boldsymbol{m}(x, y) \in \mathbb{R}^{L \cdot C}$ amounts to identifying parameters (x, y) that minimize the discrepancy between $\boldsymbol{d}$ and $\boldsymbol{m}$ In the presence of white Gaussian noise, this discrepancy is measured using a L_2 norm. The minimization problem is equivalent to a least squares fitting:

$$\begin{aligned}\{x^\dagger, y^\dagger\} &= \arg\min_{\{x,y\}} \|\boldsymbol{d} - \boldsymbol{m}\|_2^2 \\ &= \arg\min_{\{x,y\}} \sum_{i,j} (d_{i,j} - m_{i,j}(x, y))^2 \\ &= \arg\min_{\{x,y\}} \sum_{i,j} d_{i,j}^2 + \sum_{i,j} m_{i,j}(x, y)^2 - 2 \sum_{i,j} d_{i,j} m_{i,j}(x, y)\end{aligned}$$

$\sum_{i,j} d_{i,j}^2$ is constant and since the model is shift invariant $\sum_{i,j} m_{i,j}(x, y)^2$is constant too (whitout taking into account the truncation of the field of view, thus,

$$\{x^\dagger, y^\dagger\} = \arg\max_{\{x,y\}} \sum_{i,j} d_{i,j} m_{i,j}(x, y) \tag{3.1}$$

Since the model is shift-invariant a coarse estimation of the (x, y) location of the object on a pixel grid noted (x, y) can be obtained by maximizing a simple correlation between the data and a model centred in the field of view:

$$\{\mathrm{x}^\dagger, \mathrm{y}^\dagger\} = \arg\max_{\{x(i),y(j)\}} \sum_{l=-L/2}^{L/2} \sum_{c=-C/2}^{C/2} d_{l,c} m^*_{l-j,c-i}(0, 0) \tag{3.2}$$

To detect an object pattern in the data under white Gaussian noise assumptions, this detection can be performed using Fast Fourier Transforms (FFT) to reduce the computational time.

A.1.2 Normalized correlation

To avoid sensitivity to a scale factor and offset changes between the data and the model, a normalized correlation can be used, in this case:

$$\{\mathrm{x}^\dagger, \mathrm{y}^\dagger\} = \arg\max_{\{x(i),y(j)\}} \sum_{l=-L/2}^{L/2} \sum_{c=-C/2}^{C/2} \frac{(d_{l,c} - <\boldsymbol{d}>)(m^*_{l-j,c-i}(0, 0) - <\boldsymbol{m}>)}{\sqrt{\sum_{i,j} [d_{l,c} - <\boldsymbol{d}>]^2 + \sum_{i,j} [m_{l,c} - <\boldsymbol{m}>]^2}} \tag{3.3}$$

A.2 Robust detection

A.2.1 Robust loss functions

In the presence of noise plus disturbances caused by the presence of other objects the residuals $\boldsymbol{d} - \boldsymbol{m}$ are no longer Gaussian and the discrepancy has to be evaluated using a robust loss function.

In robust statistics, Huber [Huber, 2011] introduced M-estimators that replace the square function by another objective function ρ, which reduces sensitivity to outliers by penalizing less the largest deviations (Fig. 3.1). Below, we give the expressions of 3 robust loss functions ρ that we will compare in our experiments:

- Cauchy loss function :

$$\rho(u) = \frac{1}{2}\log(1+u^2) \tag{3.4}$$

- Huber loss function (δ is a positive parameter):

$$\rho_\delta(u) = \begin{cases} \frac{1}{2}u^2 \text{ for } |u| \leq \delta \\ \delta \cdot (|u| - \frac{1}{2}\delta) \text{ otherwise.} \end{cases} \tag{3.5}$$

- Tuckey loss function (t is a positive parameter):

$$\rho_t(u) = \begin{cases} \frac{t^2}{6}\left\{1 - \left[1 - \left(\frac{u}{t}\right)^2\right]^3\right\} \text{ for } |u| \leq t \\ \frac{t^2}{6} \text{ otherwise.} \end{cases} \tag{3.6}$$

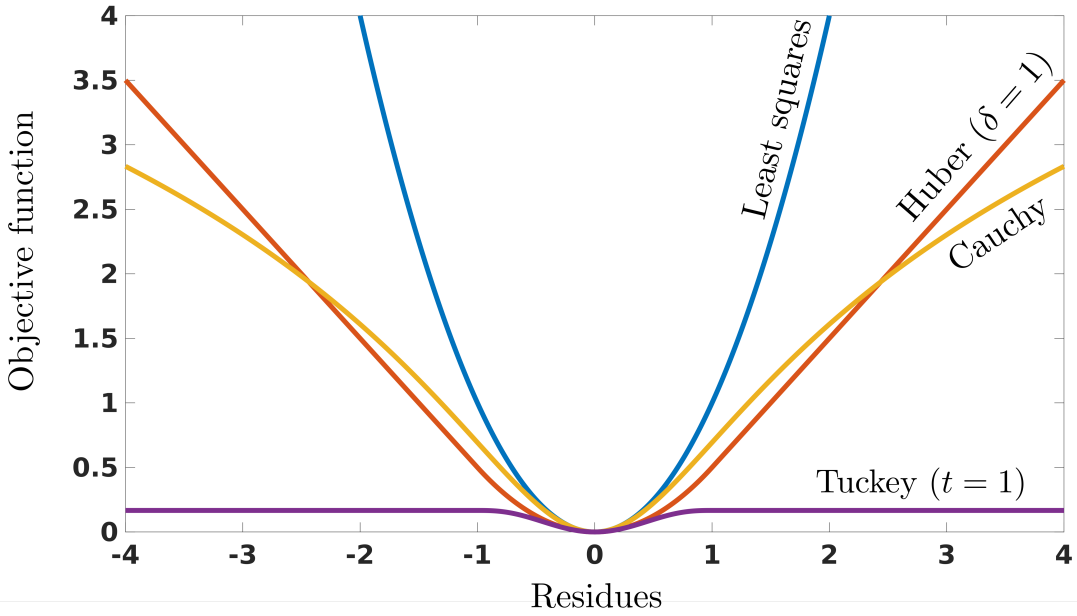

Figure 3.1: The least squares and 3 robust loss functions.

The robust loss function ρ either corresponds to the neg-log-likelihood of a heavy-tailed distribution or is selected for its mathematical properties (in particular, asymptotic behaviors).

A.2.2 Likelihood Ratio Test

The differences between the model and the data are generally not independent from one pixel to another due to the spatially extended patterns of the other objects. However,

when considering a robust loss function (as presented in Section A.2.1), these spatial dependencies are less of an issue and in the following, we make the simplifying assumption that those differences are independent. The interpretation as a neg-log-likelihood then motivates the location problem to be formulated as a hypothesis test that leads to the Likelihood Ratio Test (LRT):

$$\begin{cases} \mathcal{H}_0 : \\ \text{(no object)} \end{cases} \quad -\log \mathrm{p}(\boldsymbol{d}|\mathcal{H}_0) = \sum_{i,j} \rho\left[\frac{d_{i,j}}{s}\right] + c$$
$$\begin{cases} \mathcal{H}_1 : \\ \text{(object at } (x,y)) \end{cases} -\log \mathrm{p}(\boldsymbol{d}|\mathcal{H}_1, x, y) = \sum_{i,j} \rho\left[\frac{d_{i,j} - m_{i,j}(x,y)}{s}\right] + c\,, \tag{3.7}$$

where s is a scaling factor that sets the boundary between inliers and outliers, and c is a constant to ensure that the probability density functions sum to one. This parameter is commonly chosen based on a robust estimate of the standard deviation of the data under $\mathcal{H}_0$ using the Median Absolute Deviation (MAD) of the data [Huber, 2011]:

$$s^{MAD} = 1.48 \cdot \mathrm{median}(|\boldsymbol{d} - \mathrm{median}(\boldsymbol{d})|)\,. \tag{3.8}$$

The LR is computed by forming the ratio between the likelihoods of $\mathcal{H}_1$ and $\mathcal{H}_0$:

$$\begin{aligned} \mathrm{LR}(x,y) &= \log \frac{\mathrm{p}\big(\boldsymbol{d} \,\big|\, \mathcal{H}_1, x, y\big)}{\mathrm{p}(\boldsymbol{d}|\mathcal{H}_0)} \\ &= \sum_{i,j} \rho\left[\frac{d_{i,j}}{s}\right] - \rho\left[\frac{d_{i,j} - m_{i,j}(x,y)}{s}\right] \qquad (3.9) \\ &= \sum_{i,j} f_s(d_{i,j}, m_{i,j}(\mathrm{x},\mathrm{y}))\,, \qquad (3.10) \end{aligned}$$

were $f_s(a,b) = \rho[a/s] - \rho[(a-b)/s]$.

The strategy used to locate objects modeled by $\boldsymbol{m}$ typically consists in (i) detecting an object if there is a location (x,y) such that $\mathrm{LR}(x,y)$ is above a given detection threshold (chosen according to a false alarm rate), (ii) refining the location (x,y). Generally, for computational efficiency reasons, only (x,y) locations (x,y) centered on the pixel grid are considered during step (i). If several locations (x,y) are above the detection threshold, only the location leading to the largest LR value is usually kept. Step (ii) then refines the (x,y) location by maximizing LR. The contribution of the detected object can then be subtracted from the data and the detection procedure repeated on the residuals, like in the standard matching pursuit procedure.

A.2.3 Fitch's robust detection

In [Fitch et al., 2005], Fitch *et al.* proposed to decompose the robust penalization function ρ on a limited number n_{max} of trigonometric functions, so that:

$$\rho(u) \approx \sum_{n=1}^{n_{max}} c_n(1 - \cos(l_n \pi u))\,. \tag{3.11}$$

Note that when $l_n = n$, (3.11) is a Fourier cosine series. With this expansion, f_s can be written as :

$$f_s(a,b) \approx \gamma(a) + \sum_{n=1}^{n_{max}} c_n \cos(n\pi(a-b)) \,, \tag{3.12}$$

where $\gamma(a) = -\sum_{n=1}^{n_{max}} c_n \cos(n\pi a)$. Using the properties of trigonometric functions, f_s can be expanded as follows:

$$f_s(a,b) = \gamma(a) + \sum_{n=1}^{n_{max}} c_n \big[\cos(n\pi a)\cdot\cos(n\pi b) + \sin(n\pi a)\cdot\sin(n\pi b)\big] \,. \tag{3.13}$$

This leads to the following efficient detection criterion, based on discrete correlations computed with FFTs:

$$\begin{aligned} \mathrm{LR}_{\mathrm{Fitch}}(\mathrm{x},\mathrm{y}) = &\sum_{n=1}^{n_{max}} c_n \left[\cos(n\pi \boldsymbol{d}) \otimes \cos(n\pi \boldsymbol{m}(0,0))\right]_{\mathrm{x,y}} \\ &+ \sum_{n=1}^{n_{max}} c_n \left[\sin(n\pi \boldsymbol{d}) \otimes \sin(n\pi \boldsymbol{m}(0,0))\right]_{\mathrm{x,y}} \\ &+ \sum_{i,j} \gamma(d_{i,j}) \,. \end{aligned} \tag{3.14}$$

Note that if the Fourier Cosine Series (FCS) approximation is limited to n_{max} terms, the evaluation of $\mathrm{LR}_{\mathrm{Fitch}}$ requires $2n_{max}$ correlations.

B Proposed robust detection method

B.1 Proposed robust detection scheme

In the first step of the object detection procedure described in Section A.2.2 a map of the following form has to be computed:

$$\mathrm{LR}(\mathrm{x},\mathrm{y}) = \sum_{i,j} f_s(d_{i,j}, m_{i,j}(\mathrm{x},\mathrm{y})) \,, \tag{3.15}$$

were $f_s(a,b) = \rho[a/s] - \rho[(a-b)/s]$. Direct computation of these terms requires $\mathcal{O}(LC)$ operations for each pixel of the map. Evaluating LR on the whole pixel grids requires then $\mathcal{O}(L^2C^2)$ operations, which is prohibitive in most applications. If function f_s can be expanded into a sum of a few separable terms:

$$f_s(a,b) = \sum_{k}^{k_{\max}} g_k(a)\cdot h_k(b) \,, \tag{3.16}$$

then a fast evaluation is possible using FFT-based correlations:

$$\mathrm{LR}(\mathrm{x},\mathrm{y}) = \sum_{k}^{k_{\max}} \left[g_k(\boldsymbol{d}) \otimes h_k(\boldsymbol{m}(0,0))\right]_{\mathrm{x,y}} \,, \tag{3.17}$$

where $\otimes$ represents the bidimensional correlation operator, functions g_k and h_k are applied pixelwise, and the possible locations (x, y) are restricted to the pixel grid. With FFTs, the computation of LR on the whole pixel grid only requires $\mathcal{O}(LC \log(LC))$ operations.

When $\rho(u) = u^2$, the expansion $f_s(a, b) = a^2/s^2 - (a - b)^2/s^2 = 2ab/s^2 - b^2/s^2$ shows that LR(x, y) can be computed using a FFT-based correlation. For more general loss functions ρ, a closed-form separable expansion is not usually available. To circumvent this problem, we quantize values a and b and define matrix $\boldsymbol{F}$ such that $F_{p,q} = f_s(a_p, b_q)$, where values $(a_p)_{p=1..P}$ and $(b_q)_{q=1..Q}$ uniformly span the range $[\min(\boldsymbol{d}), \max(\boldsymbol{d})]$ and $[\min(\boldsymbol{m}(0,0)), \max(\boldsymbol{m}(0,0))]$, respectively.

A singular value decomposition (SVD) of $\boldsymbol{F}$ is then performed so that $\boldsymbol{F} = \sum_{k=1}^{\min(P,Q)} \boldsymbol{u}_k \sigma_k \boldsymbol{v}_k^t$. By truncating and interpolating this expansion, we obtain the approximation:

$$f_s(a, b) \approx \sum_{k=1}^{k_{\max}} \varphi(\sqrt{\sigma_k}\boldsymbol{u}_k, a) \cdot \psi(\sqrt{\sigma_k}\boldsymbol{v}_k, b)\,, \tag{3.18}$$

where k_{max} is the rank of the approximation, $\varphi(\sqrt{\sigma_k}\boldsymbol{u}_k, a)$ is the value interpolated at location a based on the points $(\sqrt{\sigma_k}[\boldsymbol{u}_k]_p, a_p)_{p=1..P}$, and $\psi(\sqrt{\sigma_k}\boldsymbol{v}_k, b)$ is the value interpolated at location b based on the points $(\sqrt{\sigma_k}[\boldsymbol{v}_k]_q, b_q)_{q=1..Q}$. This leads to the Algorithm 5.

Algorithm 5: Fast computation of the detection map LR

input : Data $\boldsymbol{d}$ ($L \times C$ image)
input : Model $\boldsymbol{m}$ ($L \times C$ image: $\boldsymbol{m}(0, 0, \boldsymbol{\varpi})$)
`Accuracy parameters:` P, Q, $k_{\max}$
output: Detection map LR ($L \times C$ image)

(Build matrix $\boldsymbol{F}$ and compute its SVD decomposition)
for $p = 1$ **to** P **do**
  for $q = 1$ **to** Q **do**
    $a_p \leftarrow \min(\boldsymbol{d}) + \frac{p-1}{P-1}(\max(\boldsymbol{d}) - \min(\boldsymbol{d}))$
    $b_q \leftarrow \min(\boldsymbol{m}) + \frac{q-1}{Q-1}(\max(\boldsymbol{m}) - \min(\boldsymbol{m}))$
    $F_{p,q} \leftarrow f_s(a_p, b_q)$
  end
end
$[\boldsymbol{U}, \boldsymbol{S}, \boldsymbol{V}] \leftarrow$`SVD`$(\boldsymbol{F})$
(Compute detection map using FFT-based correlations)
$\mathscr{L} \leftarrow \boldsymbol{0}$
for $k = 1$ **to** $k_{\max}$ **do**
  $\boldsymbol{g} \leftarrow \varphi(S_{k,k}\boldsymbol{u}_k, \boldsymbol{d})$ (1D interpolation for all $\boldsymbol{d}$)
  $\boldsymbol{h} \leftarrow \psi(S_{k,k}\boldsymbol{v}_k, \boldsymbol{m})$ (1D interpolation for all $\boldsymbol{m}$)
  LR $\leftarrow$ LR $+ \boldsymbol{g} \otimes \boldsymbol{h}$ (2D correlation by FFT)
end

Our robust detection criterion LR generalizes the formulation $\mathrm{LR}_{\mathrm{Fitch}}$ of Fitch *et al.* (described in Section A.2.3) by replacing trigonometric functions by modes computed by SVD on $\boldsymbol{F}$. Comparison between the FCS approximation and the low rank approximation

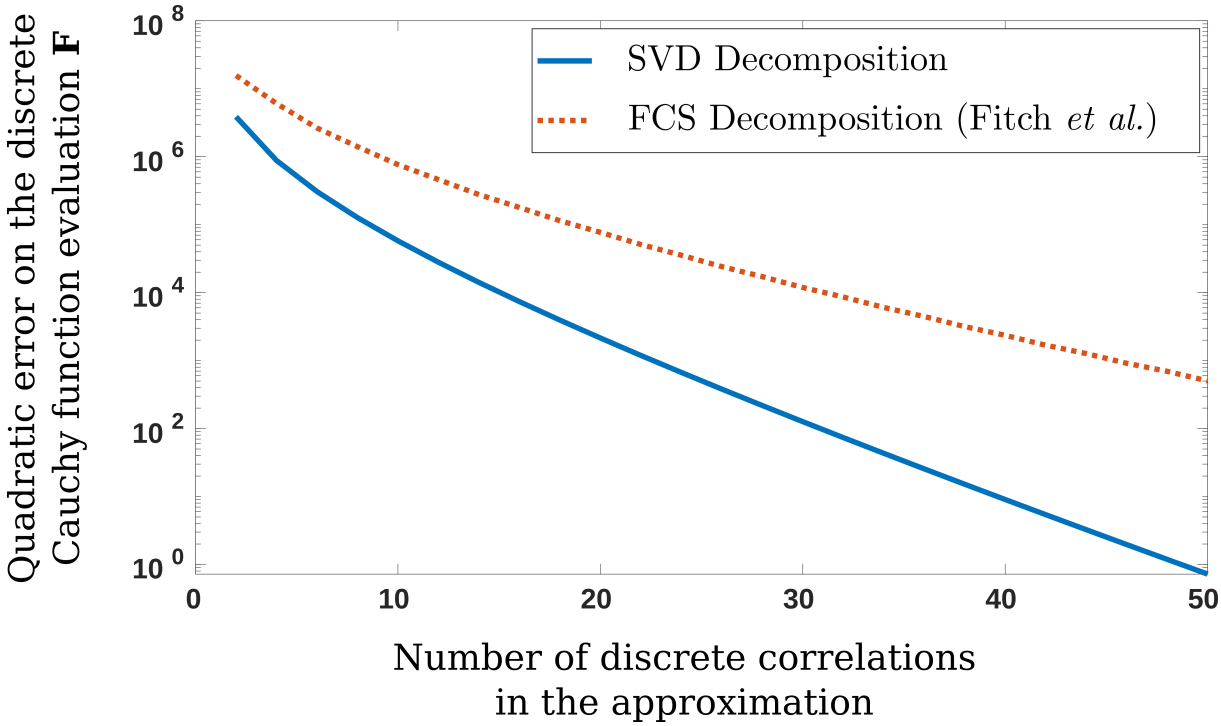

Figure 3.2: Reduction of the approximation error on $\boldsymbol{F}$ with the number of correlations under Fourier series approximation (Fitch & al.) vs low rank approximation (this paper)

(SVD) on $\boldsymbol{F}$ are presented in Fig. 3.2 for the Cauchy robust penalization function. While both approaches reduce the quadratic error when more terms are included in the expansion, this reduction is much faster with the low-rank approximation. To reach a given approximation error, our expansion $\mathscr{L}$ requires much fewer terms, leading to a reduced computation time.

B.2 Application to spherical bead detection in holographic microscopy

B.2.1 Robustness evaluation on simulations

In this paragraph, we assess the performance of the proposed method. For this purpose, non-absorbing silica beads of radius $r = 0.5\,\mu\text{m}$, refractive index $n = 1.45$ are simulated at a propagation distance $z = 10\,\mu\text{m}$ (Config-STAINED see Appendix A Section C). A small dispersion of the parameters is generated to match the variability of commercial calibration silica beads. The beads are mixed with other spherical absorbing objects with parameters ($z = 10\,\mu\text{m}$, $r = 0.5\,\mu\text{m}$, $n = 1.45$ and transmittance 0.005) chosen to simulate the biological objects. Their patterns are also 2.5 time more contrasted than the calibration beads. They can be considered as a nuisance term in the task of locating the calibration beads (see Fig. 3.3). The data are simulated on a $5 \times 7.4\,\text{mm}^2$ sensor. The microscope objective considered is a $85\times$ oil immersion objective, giving a field of view of $60.8 \times 90.4\,\mu\text{m}^2$ area. The illumination source is a coherent red-light at 622 nm (Setup-BIOASTER see Appendix A Section B). The simulated holograms contain the diffraction patterns of 20 spherical objects in each set (calibration beads and biological objects) and

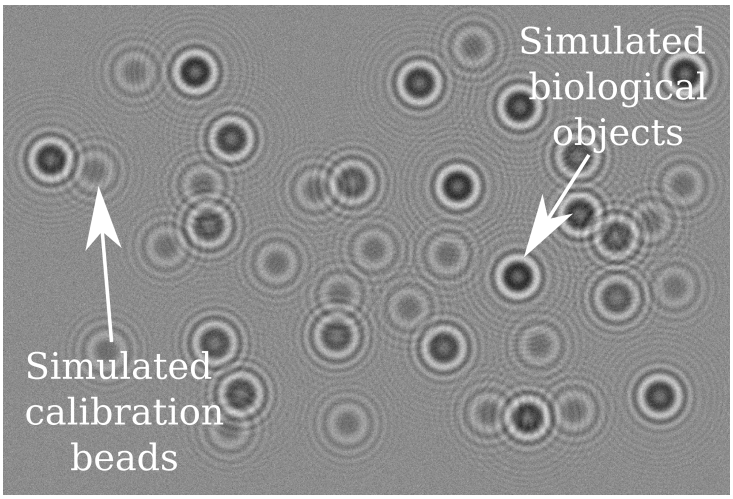

Figure 3.3: A simulated hologram with two populations of spherical objects, one representing calibration beads and the other biological objects.

are corrupted by an additive Gaussian noise leading to a signal-to-noise ratio of 1.5. To quantify the performance of the robust approach, we consider the detection and location of the calibration beads. Each object detected with an error less than 2 pixels is counted as a correct detection. The robustness of the method is assessed through ROC curves that show the number of true detections as a function of the number of false detections. These curves are plotted by increasing the detection threshold. The evolution of these curves according to the scaling factor s is shown in Fig. 3.4a. When s is large ($s = 15 \times \mathrm{MAD}$)), the robust penalization curve approaches the least-squares minimization curve which is characterized by numerous false detections. If a calibration process is performed on the detected beads, it is important to limit the number of false detections, even if this implies missing some true detections.

When s is close to the value of the MAD ($s = 1.48 \times \mathrm{MAD}$) [Huber, 2011], all the calibration beads in this experiment are correctly detected before the first false detection occurs.

Fig. 3.4b compares the performance of several robust penalization functions using the fast computation algorithm. As can be seen in Fig.3.4a with the Cauchy function, when the robustness parameter s is overestimated the Huber and Tuckey loss functions are more sensitive to outliers.

The number of operations involved in the FFT-based computation of $\mathrm{LR}(x, y)$ is proportional to the number of terms $k_{\max}$ in the separable expansion. To limit the computational cost, $k_{\max}$ should be kept low. Fig. 3.5 shows the logarithm of the mean relative error between an estimation of the robust function using an expansion of 100 terms and a smaller number of terms $k_{\max}$.

The approximation error decreases quickly when only a few terms are considered. In our case, $k_{\max} = 5$ is sufficient for robust detection. This is the value we use in the following paragraph. Note that, depending on the robust loss function, the number of terms required to reach a given approximation error will vary.

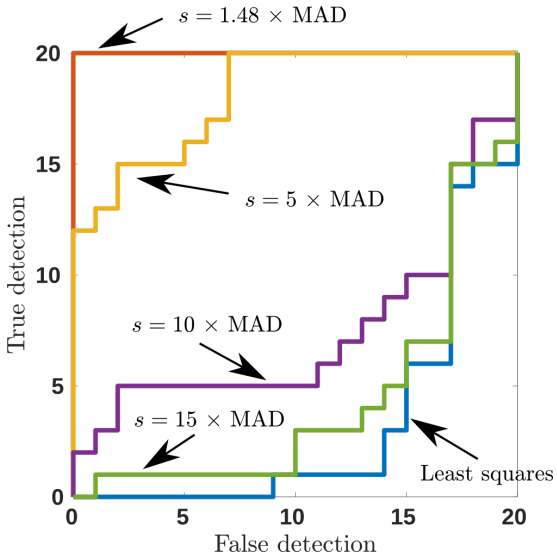

(a) Influence of the scaling parameter s when using the Cauchy loss function.

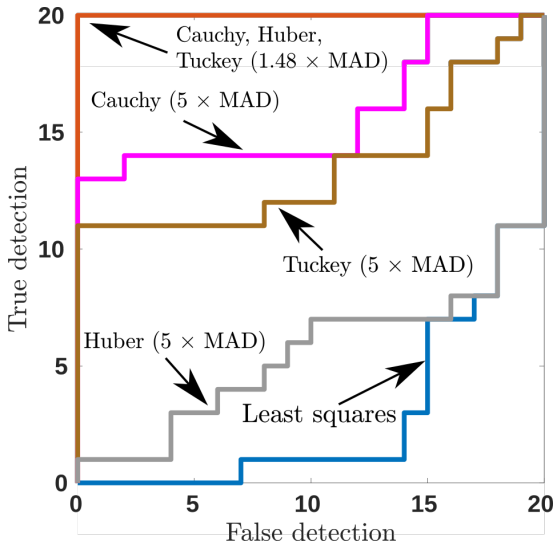

(b) Impact of the loss function on the detection performance.

Figure 3.4: Influence of the scaling parameter and of the loss function on the detections

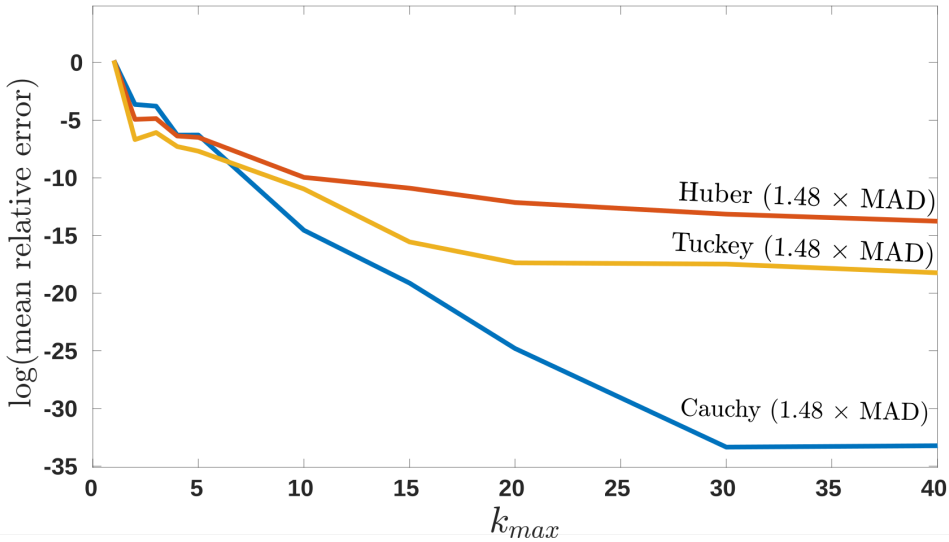

Figure 3.5: Reduction of the approximation error with the number of terms $k_{\max}$.

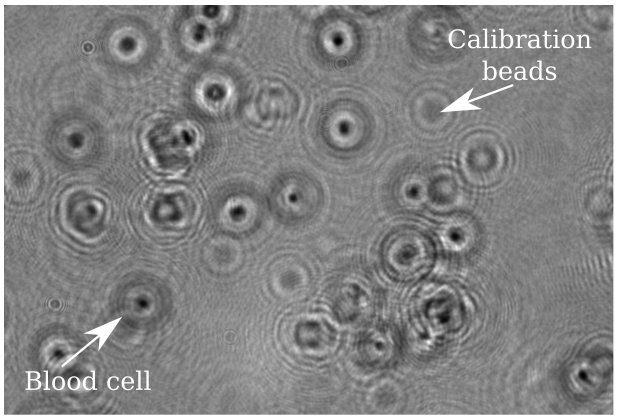

(a) Experimental hologram of a mixture of blood, bacteria and calibration beads.

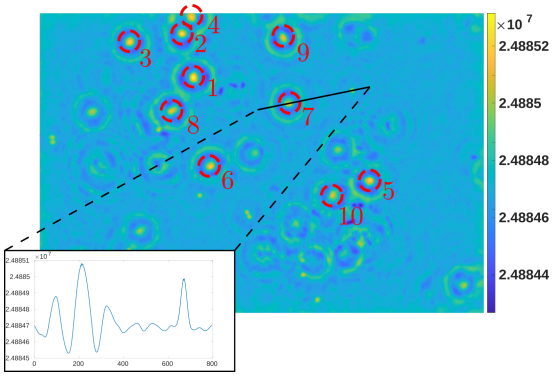

(b) Detection map computed with a quadratic loss function on the hologram of calibration beads.

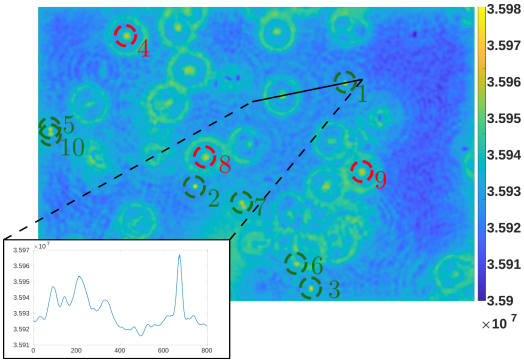

(c) Detection map computed with the Cauchy loss function on the hologram of calibration beads ($k_{max} = 5$).

Figure 3.6: Detection of calibration beads in a hologram of a blood smear: (a) experimental data; (b) detection map and the first 10 detections with a non-robust criterion; (c) detection map with a robust Cauchy criterion ($s = 1.48 \times$ MAD). False detections and true detections are circled respectively in red and green.

B.2.2 Experimental case

The proposed robust detection scheme was applied to experimental in-line holograms. The sample used was a Gram stained smear of a positive blood culture; the latter was spiked with a bacillus and coccus bacteria strain. Calibration objects (spherical silica beads) were added to the sample placed on a microscope slide. The experimental parameters are the same as the simulated ones (Setup-BIOASTER/Config-STAINED see Appendix A Section C.

The red blood cells in the sample produce more contrasted diffraction patterns than the beads (see Fig.3.6(a)) that are strongly correlated with the bead model. The use of a conventional quadratic loss function leads to a detection map where the first 10 detections are wrong detections corresponding to blood cells (see Fig. 3.6(b)). Since the autofocus [Brault et al., 2022b] is performed using the median of the z parameters of the detected beads, these detections would lead to strong errors. With a robust loss function such as Cauchy, 7 of the first 10 detections were meaningful (6 out of the first 7). Some red blood cell diffraction patterns are highly correlated with the patterns of the beads, leading to large values even with the robust detection criterion.
This detection map was obtained using an expansion of 5 terms ($k_{\max} = 5$) representing a computational cost 2.5 times larger than in the case of the non-robust quadratic loss, which is a moderate increase given the improvement in the detection.

C Conclusion

We proposed a method to reduce the computational cost when computing detection maps with a robust penalization function. This method approximates the GLR based on a separable expansion that is suitable for FFT-based implementation. We show that the use of a robust loss function increases the number of correct detections of calibration objects in in-line holographic microscopy. To accurately estimate the parameters of the calibration objects, this robust detection step can be followed by a local refinement using the same robust cost function [Holland and Welsch, 1977, Flasseur et al., 2017a]. Let us note that this robust detection is not always necessary (depending and the sample) and was not required for the following chapters. However this method has been tested on 20 simulated images and hundreds of experimental images.
A supplementary example and the source code are available at `https://github.com/braultd/FastRobustPatternDetection` .

CHAPTER 4

Accurate unsupervised estimation of aberrations for improved quantitative reconstruction

Abstract

In order to tackle the problem of reproducibility and quatitativity in digital holographic microscopy, we need to calibrate accurately the aberrations of the setup. Similarly to Chapter 2, the proposed method is based on the estimation of the aberration parameter using parametric inverse problems approach on beads diffraction patterns. The forward model is based on a Lorenz-Mie model distorted by optical aberrations described by Zernike polynomials. This methodology is thus able to characterize varying aberrations in the field of view in order to take them into account to improve the reconstruction of any sample. We show that this approach increases the repeatability and quantitativity of the reconstructions in both simulations and experimental data. We use the Cramér-Rao lower bounds to study the accuracy of the estimation of the aberration parameters. Finally, we demonstrate the efficiency of this aberration calibration by using them in image reconstructions using a commonly used phase retrieval algorithm as well as a regularized inverse problems algorithm. In this chapter, after a preliminary section, we present the proposed methodology to calibrate the aberrations and validate it on simulated and experimental data. Finally we use the aberration model to reconstruct experimental data. This chapter is based on the published article [Brault et al., 2022c].

Introduction

Optical microscopy can be used to extract several characteristics from a biological sample, such as morphological parameters, birefringence or a phase shifts introduced by an unstained sample. For quantitative measurement of these properties, an accurate optical model is required [Alexander et al., 2020]. Accounting for the characteristics of the optical system is an essential component of reconstruction algorithms. For example, in fluorescence microscopy, accurate modeling of the Point Spread Function (PSF) is a way to improve the deconvolution step [McNally et al., 1999, Sarder and Nehorai, 2006, Soulez et al., 2012, Li et al., 2017]. It can be performed using either a dedicated calibration step (by directly measuring the PSF on "point-like" objects [McNally et al., 1999]) or by estimating the PSF directly on an image that presents aberrations [Soulez et al., 2012, Aristov et al., 2018, Li et al., 2018]). In the literature, estimating aberrations or PSF have been widely addressed using various microscopy methods (fluorescence, single-molecule localization, wide-field microscopy, holography, etc.), with different measurement or reconstruction approaches and models of the PSF. These models can be very simple (*e.g.* Gaussian model), more realistic, like the Gibson-Lanni model [Gibson and Lanni, 1991, Li et al., 2017, Li et al., 2018], or more versatile and general, like the Zernike polynomials of the pupil function [Lakshminarayanan and Fleck, 2011, Zheng et al., 2013, Aristov et al., 2018]. In the two latter cases, the coherent PSF is modeled as a phase error function in the exit pupil plane of the objective.

In the particular case of digital holographic microscopy, the issues of aberrations estimation and correction have been widely studied for off-axis configuration (e.g. [Ferraro et al., 2003, Colomb et al., 2006, Min et al., 2017, Xu et al., 2001]). However, it concerns essentially the wavefront mismatch between the object and the reference beams, which creates distortions of the interference fringes, thus inducing errors in the reconstruction.

In-line digital holographic microscopy requires a simpler setup involving a single beam. It is less bulky and less sensitive to vibrations than off-axis holographic setups [Garcia-Sucerquia et al., 2006, Kreis, 2006]. Image processing makes it possible to reconstruct the optical properties of the sample including its absorption and its phase shift. The aberrations of an in-line holographic optical system can have different causes, such as non standard uses of the objective, tilts or collimation errors in the illumination. These aberrations are dependent on the setup, its alignment and vary in the field of view. They lead to reconstruction errors, not only in the quantitative estimation of the modulus and the phase but also in the geometrical properties of the reconstructed objects. Thus, the repeatability as well as the reproductibility of the reconstructions is affected. However, the aberrations of the optical system are usually not considered in the reconstruction step. Accounting for the aberrations in the image formation model makes it possible to reduce the bias introduced in the reconstructions. These aberrations are an important issue to overcome in applications such as medical diagnoses that require reconstructions to be as accurate as possible to make the decision as robust as possible. To our knowledge, it is only recently that the influence of optical aberrations has been studied in the context of in-line digital holographic microscopy [Alexander et al., 2020, Martin et al., 2021, Olivier et al., 2022]. These studies underlined the need for a fine estimation of aberrations in order to improve the quantitativity and the repeatability of the phase reconstructions as well as the axial positioning, by reducing the aberration-driven biases.

In the present chapter, we first address the problem of estimating aberrations in the

context of in-line digital holographic microscopy. To that end, we use as in Chapter 2 calibration beads to estimate an aberrated forward model. Using a parametric Inverse Problems Approach (IPA), we simultaneously fit Zernike coefficients and calibration beads parameters, which are parameters of the forward model, on data. Unlike many PSF estimation studies, our approach does not require axial stacks of images *i.e.* only one hologram is needed. Moreover, we made no assumption of an aberration-free PSF in the center of the field, like in Zheng's *et al.* study [Zheng et al., 2013]. Finally, this model of aberration is more general than the Gibson-Lanni model [Martin et al., 2021, Li et al., 2017, Li et al., 2018]. As a forward model, we use a Lorenz-Mie model of the calibration beads that has been extended to account for the aberrations of the optical system using Zernike polynomials [Lakshminarayanan and Fleck, 2011]. To jointly estimate the calibration beads and aberration parameters, we choose a parametric IPA as it is known to be accurate in estimating the parameters of simple shape objects [Lee et al., 2007, Soulez et al., 2007a, Cheong et al., 2010] and of the experimental parameters required for calibration. It has already been successfully applied in the context of autofocusing [Brault et al., 2022b], for the estimation of the spectral crosstalk on a Bayer sensor [Flasseur et al., 2017b] and to estimate the parameters of an astigmatic reference wave [Verrier et al., 2014].

Once Zernike coefficients are estimated locally for each bead, they can be used to perform aberration free reconstruction of the sample. These reconstructions can be performed using regularized IPA algorithm [Denis et al., 2009, Jolivet et al., 2018] or Fienup algorithm [Fienup, 1982, Latychevskaia and Fink, 2007]. To test the proposed methodology, we use the experimental procedure of Martin *et al.* in [Martin et al., 2021], *i.e.* the use of a water immersion microscope objective with a correction collar that causes aberrations when not set correctly. In the following section, we describe the Zernike polynomials basis. Then we describe the method to estimate aberration parameters (Zernike coefficients) and use them to refine the PSF model of our holographic setup in order to reconstruct aberration-free images. We then demonstrate the robustness of the approach to reconstruct various kinds of aberrations, we first present the estimation of both aberrations and beads parameters on simulated holograms and on experimental holograms. Finally, to illustrate the relevance of our approach on experimental data. These experimental data are reconstructed with phase retrieval algorithms (Fienup and regularized IPA algorithms) that take into account the estimated aberrations.

A Preliminaries: Zernike Polynomials

As mentioned earlier, due to imperfections in the optical system geometric, aberration can occur and have a significant impact on the image formation model. Since inverse problem approach are very sensitive to model errors, the effect of these aberration must be taken into account. To consider the geometric aberration in the image formation model, Zernike polynomials are a commonly used mathematical description of the aberrated wavefront in the pupil plane (Fourier plane). The Zernike polynomials are orthogonal and continuous over a unit disk. However, it should be noticed that Zernike polynomials will no longer be orthogonal in a discrete space [Goodwin and Wyant, 2006, Lakshminarayanan and Fleck, 2011].

Definition of the Zernike polynomials

Zernike polynomials depend on two parameters: the azimuthal angle $\phi = \arctan(\frac{\kappa_y}{\kappa_x})$ and the radial distance $\rho = \frac{\lambda}{\mathrm{NA}}\sqrt{\kappa_x^2 + \kappa_y^2}$. The Zernike polynomials are defined as follows :

$$Z_n^m(\rho, \phi) = \begin{cases} R_n^{|m|}(\rho)\sin(m\phi) \text{ if } m > 0 \\ R_n^{|m|}(\rho)\cos(m\phi) \text{ otherwise,} \end{cases} \tag{4.1}$$

where $n \in \mathbb{N}$, $m \in \mathbb{Z}$ and $R_n^m(\rho)$ is defined as :

$$R_n^m(\rho) = \sum_{k=0}^{\frac{n-m}{2}} \frac{(-1)^k (n-k)!}{k!\left[\frac{n+m}{2} - k\right]!\left[\frac{n-m}{2} - k\right]!} \rho^{n-2k}, \tag{4.2}$$

with $n \geq |m|$ and $n - |m|$ even.

The independance of Zernike polynomials on the unit disk means that every aberrated wavefront is described by a unique linear combination of Zernike polynomials called the Zernike coefficients $\boldsymbol{\alpha} = \{\alpha_n^m\}_{n\in\mathbb{N},m\in\mathbb{Z}}$. The total Aberration Correction $\boldsymbol{AC}$ is thus expressed $\boldsymbol{AC} = \sum_{n,m} \alpha_n^m \boldsymbol{Z}_n^m$

Some properties of the Zernike polynomials

Zernike polynomials have interesting properties :

- A common metric to measure the flatness of the wavefront correction is the wavefront correction variance. It can be computed directly from the Zernike coefficient:

$$\sigma_{\boldsymbol{AC}} = \sum_{\substack{n\in\mathbb{N}^*, m\in\mathbb{Z} \\ n\geq|m| \\ n-|m| \text{ even}}} (\alpha_n^m)^2$$

- When $m = 0$, Zernike polynomials are radially symmetric.

An illustration of the polynomials is given on Fig. 4.1 [Hsieh et al., 2020].

Considering the Zernike coefficient to be of the depth, Figure 4.2 illustrates the effects of spherical aberration, vertical astigmatism and vertical coma on the PSF and in the hologram plane. Spherical aberrations maintains the radial symmetry of the propagation kernel due to the radial symmetry of Z_4^0. For vertical astigmatism and coma the phase of the MTF has a non radial profile. The symmetry is then lost in the hologram plane. Note that these effects almost invisible for high z distance. Therefore it is necessary to look at the focus plane to see them.

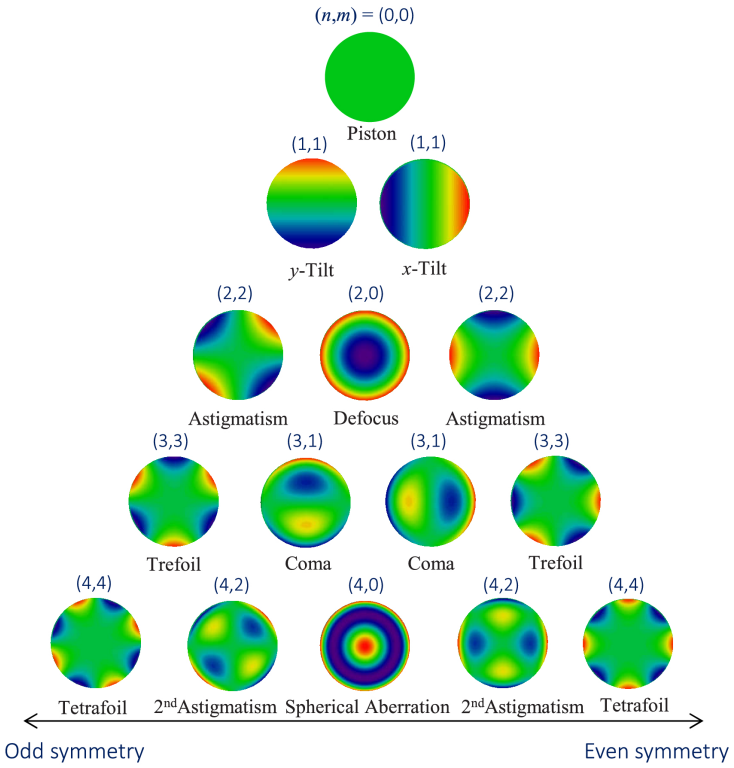

Figure 4.1: Illustration of the 15 first Zernike polynomials (adapted from [Hsieh et al., 2020]). Visualization of the pupil plane changes in function of (n, m) couples.

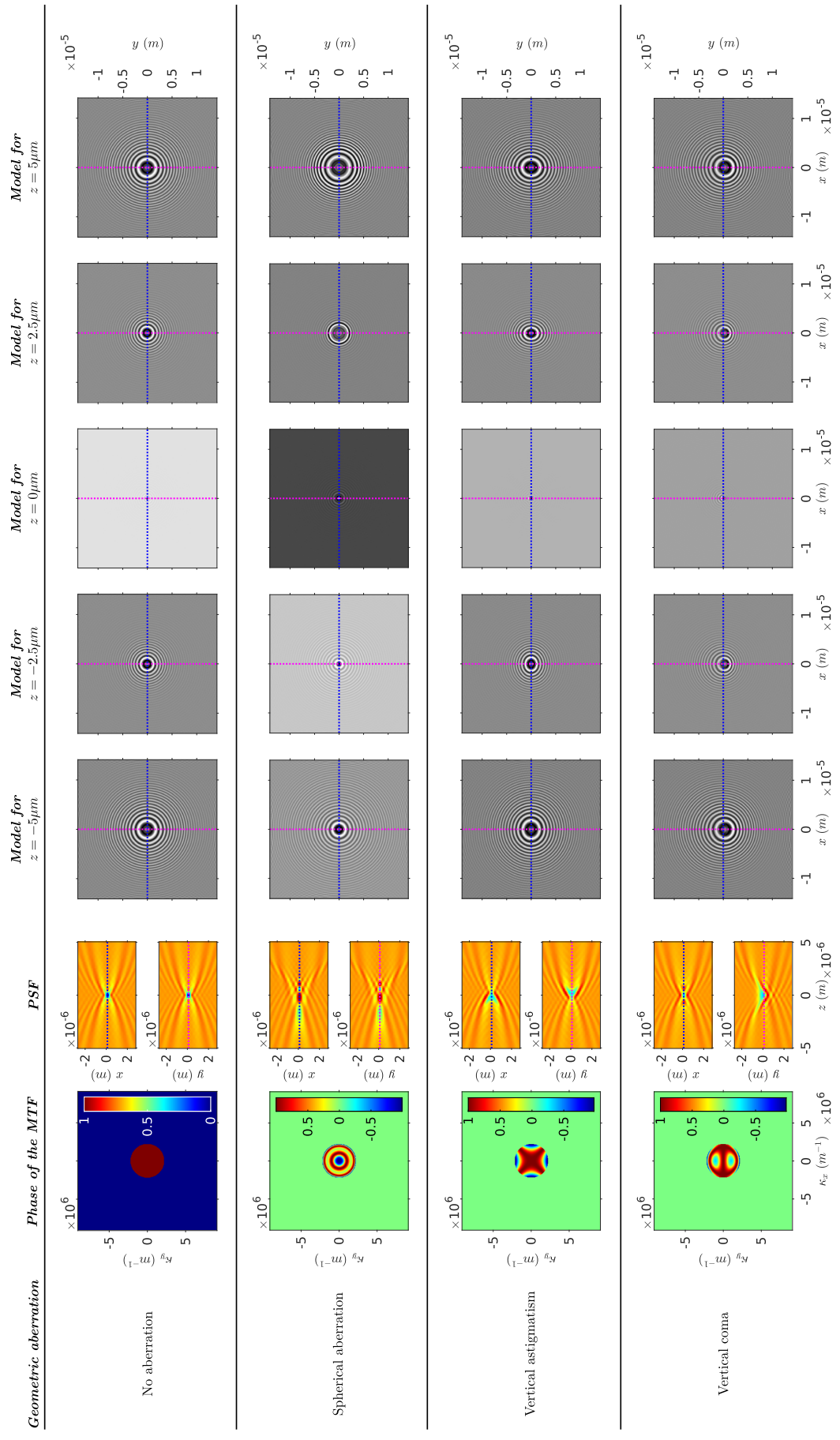

Figure 4.2: Illustration of spherical aberration, vertical astigmatism and vertical coma effects on the PSF and in the hologram plane

B Aberration estimation

B.1 Estimation of the aberration parameters and reconstruction

In the framework of inverse problem approaches, reconstructions are based on minimizing the discrepancy between the hologram (the data) $\boldsymbol{d}$ and an image formation model (forward model) $\boldsymbol{m}$. This framework is well suited to calibrate the aberrations using holograms of spherical objects as the image formation model depends only on the parameters of the objects (position, diameter and refractive index) and on the aberrations that can be modelled with a complex pupil function described by few parameters. Once these aberrations are estimated, they can be used in a regularized reconstruction method to reconstruct any sample without any aberration artefacts. Figure 4.3 shows a flowchart representing the two main steps, the calibration and the reconstruction, that are detailed here after.

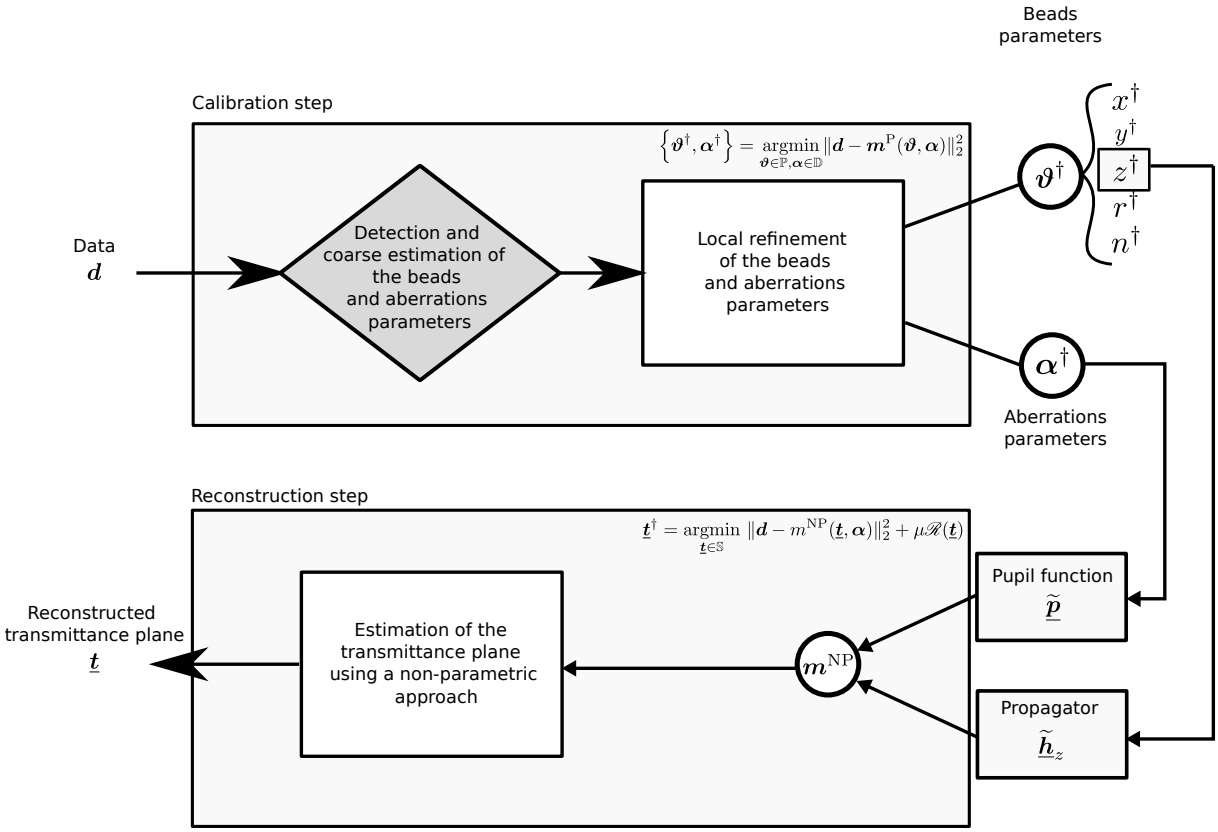

Figure 4.3: Flowchart representing the two main steps of the proposed method: calibration and reconstruction.

B.1.1 Calibration : aberration parameters estimation

As described in Chapter 2, the diffraction pattern $\underline{\boldsymbol{a}}^{\mathrm{Mie}}$ of a spherical bead is accurately modeled by the Lorenz-Mie model [Slimani et al., 1984] which depends on the set of bead parameters $\boldsymbol{\vartheta} = \{x, y, z, r, n\}$, where x, y, z corresponds to the 3D position, r is the

radius and n is the refractive index. The Lorenz-Mie model has been successfully used to reconstruct spherical objects from holograms by fitting methods (see Chapter 2). In the presence of aberrations, the new image formation model of the beads $\boldsymbol{m}^{\mathrm{P}}$ also depends on the aberration parameters $\boldsymbol{\alpha}$ of the optical system that can be included in the model by mean of a complex pupil plane as follows:

$$\boldsymbol{m}^{\mathrm{P}}(\boldsymbol{\vartheta}, \boldsymbol{\alpha}) = \left| \mathscr{F}^{-1} \left[\widetilde{\underline{p}}(\boldsymbol{\alpha}) \odot \widetilde{\underline{\boldsymbol{a}}}^{\mathrm{Mie}}(\boldsymbol{\vartheta}) \right] \right|^2 \tag{4.3}$$

where $\mathscr{F}^{-1}$ is the inverse Fourier Transform, $\widetilde{\underline{p}}(\boldsymbol{\alpha})$ is the pupil function in Fourier domain that depends on (κ_x, κ_y), the spatial frequency coordinates. For the sake of compactness, Fourier space coordinates and spatial coordinates are omitted in the equations when they are not required. $\boldsymbol{\alpha} = \{\alpha_n^m\}_{(m,n)\in\mathbb{Z}^2}$ is a vector of aberration parameters, that will be referred as Zernike coefficients in this work. $\widetilde{\underline{\boldsymbol{a}}}^{\mathrm{Mie}}$ is the Fourier Transform of $\underline{\boldsymbol{a}}^{\mathrm{Mie}}$, and $\odot$ is the Hadamard product.

As described in [Lakshminarayanan and Fleck, 2011, Noll, 1976], Zernike polynomials $\{\boldsymbol{Z}_n^m\}_{m,n}$ provide a suitable basis to describe the pupil function $\widetilde{\underline{p}}$ (see Section A for details):

$$\widetilde{\underline{p}}(\kappa_x, \kappa_y, \boldsymbol{\alpha}) = e^{i\left[\sum\limits_{n,m} \alpha_n^m \boldsymbol{Z}_n^m(\kappa_x, \kappa_y)\right]} \tag{4.4}$$

To characterize the aberration effects of the optical system, the Zernike coefficients $\boldsymbol{\alpha} = \{\alpha_n^m\}_{m,n}$ have to be estimated. Assuming a white and Gaussian noise, the maximum likelihood estimation of model parameters $\{\boldsymbol{\vartheta}, \boldsymbol{\alpha}\}$ of the bead and the aberrations corresponds to a least squares fitting problem:

$$\left\{\boldsymbol{\vartheta}^{\dagger}, \boldsymbol{\alpha}^{\dagger}\right\} = \underset{\boldsymbol{\vartheta}\in\mathbb{C}, \boldsymbol{\alpha}\in\mathbb{D}}{\operatorname{argmin}} \|\boldsymbol{d} - \boldsymbol{m}(\boldsymbol{\vartheta}, \boldsymbol{\alpha})\|_{\boldsymbol{W}}^2 \tag{4.5}$$

where $\{\mathbb{C}, \mathbb{D}\}$ are optimization constraints and $\|\cdot\|_2$ is the L_2-norm. To numerically solve this optimization problem (equation 4.5), only the first 15 Zernike coefficients are estimated in the following. As a phase piston has no effect on the image formation model (intensity image formation model), α_0^0 is set to 0. As a lateral shift of the beads (change of (x,y)) have the same effects than the Zernike coefficients α_1^{-1} and α_1^1, these Zernike coefficients are also set to 0. The coefficient α_2^0 corresponds to the Fresnel defocus that is also estimated using the z parameter (more precisely, z corresponds to the Rayleigh-Sommerfeld defocus). Thus, it is set to 0. In these conditions, sixteen parameters are studied:

$$x, y, z, r, n, \alpha_2^{-2}, \alpha_2^2, \alpha_3^{-3}, \alpha_3^{-1}, \alpha_3^1, \alpha_3^3, \alpha_4^{-4}, \alpha_4^{-2}, \alpha_4^0, \alpha_4^2, \alpha_4^4.$$

A study of the correlations between the estimated parameters is presented in Section B.1.2. It shows some high correlations in the correlation matrix. All the parameters $\{\boldsymbol{\vartheta}, \boldsymbol{\alpha}\}$ should therefore be estimated simultaneously. An iterative global/local optimization scheme [Soulez et al., 2007a] is used to guarantee the rapid and accurate reconstruction of a set of objects. Since the beads are monodispersed, a narrow parameter research domain $\mathbb{C}$ can be chosen depending on the size and refractive index of the beads used experimentally.

Since the aberration can differ depending on the location of the beads in the field of view, the aberration parameters have to be estimated for several different bead locations.

B.1.2 Theoretical study of the aberrations parameters accuracy

In this section, we aim at estimating the achievable precision on each estimated parameter and to study the correlation between these parameters. For these purposes, Cramér-Rao Lower Bounds (see Chapter 2 Section A.4.2) and the correlation matrix are computed [Kay, 1993] using our aberrated model $\boldsymbol{m}^{\mathrm{P}}$ presented in section B.1.1 eq. (4.3). These bounds are computed for a bead at the center of the field of view and for several defocus distances with parameters of Setup-LaHC for unstained samples (see Appendix A Section A, $\boldsymbol{\vartheta}\,(x = 0\ \mu m, y = 0\ \mu m, z, r = 0.5\ \mu m, n = 1.58)$).

As the aberrations happen to be quite low in our case, the accuracy study has been performed with Zernike coefficient set to zero. Thus, the accuracy on the Zernike coefficents has been studied around a zero value.

Figure 4.4 illustrates the evolution of the CRLB with the propagation distance z (*i.e.* the lower bound variance of each parameter versus z value).

These CRLB have been computed considering σ_ϵ constant and using numerical derivatives. For most parameters the best accuracy is obtained for defocus distances between 12 and 17 μm. In this study, the defocus distance $z = 12\mu m$ was considered.
The presence of an optimum for the z parameter can be explained. Indeed, when z decreases, the number of pixels on which the diffraction pattern of a bead is recorded also decreases. Thus the estimation is less robust and accurate. On the contrary if z increases, the number of pixels on which the diffraction pattern is recorded also increases leading to smaller CRLB. At one point the hologram is also truncated. Thus, the accuracy of the estimation is altered.

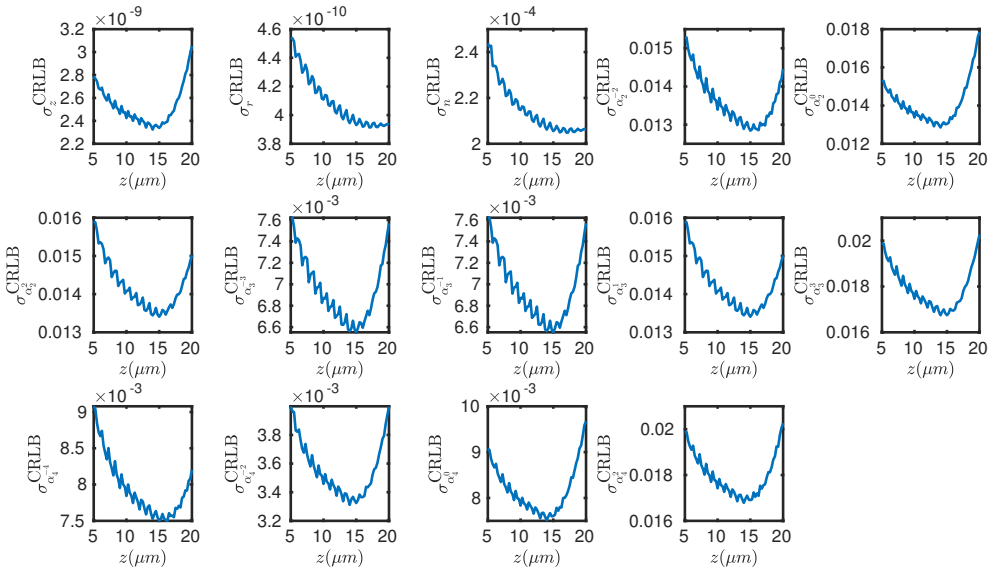

Figure 4.4: Evolution of Cramér-Rao Lower Bounds on each parameter as a function of z. The experimental parameters of the model are given in Appendix A. These CRLB have been computed for a hologram without aberrations.

Table 4.1 shows the correlation matrix for the selected seventeen parameters. Coefficients below 0.05 are set to zero for a better visualization.

	x	y	z	r	n	α_2^{-2}	α_2^2	α_3^{-3}	α_3^{-1}	α_3^1	α_3^3	α_4^{-4}	α_4^{-2}	α_4^0	α_4^2	α_4^4
x	1	0	0	0	0	0	0	0	-0.89	0	0	0	0	0	0	0
y	0	1	0	0	0	0	0	0	0	-0.89	0	0	0	0	0	0
z	0	0	1	0.34	0.31	0	0	0	0	0	0	0	0	-0.85	0	0
r	0	0	0.24	1	-0.85	0	0	0	0	0	0	0	0	0.33	0	0
n	0	0	-0.13	-0.85	1	0	0	0	0	0	0	0	0	0.39	0	0
α_2^{-2}	0	0	0	0	0	1	0	0	0	0	0	0	0.72	0	0	0
α_2^2	0	0	0	0	0	0	1	0	0	0	0	0	0	0	0.72	0
α_3^{-3}	0	0	0	0	0	0	0	1	0	0	0	0	0	0	0	0
α_3^{-1}	-0.89	0	0	0	0	0	0	0	1	0	0	0	0	0	0	0
α_3^1	0	-0.89	0	0	0	0	0	0	0	1	0	0	0	0	0	0
α_3^3	0	0	0	0	0	0	0	0	0	0	1	0	0	0	0	0
α_4^{-4}	0	0	0	0	0	0	0	0	0	0	0	1	0	0	0	0
α_4^{-2}	0	0	0	0	0	0.72	0	0	0	0	0	0	1	0	0	0
α_4^0	0	0	-0.85	0.33	0.39	0	0	0	0	0	0	0	0	1	0	0
α_4^2	0	0	0	0	0	0	0.72	0	0	0	0	0	0	0	1	0
α_4^4	0	0	0	0	0	0	0	0	0	0	0	0	0	0	0	1

Table 4.1: Correlation matrix of the 5 beads parameters and 11 Zernike coefficients. High correlation or anti-correlations are represented in red, moderate correlation or anti-correlations in yellow, low correlations or anti-correlations in green.

The correlation matrix indicates strong correlations between several parameters. Unsurprisingly, r and n are highly correlated as the phase shift induced by a an object depends on the product of these two parameters and the phase shift has a strong effect on the propagation. It is interesting to notice that coma coefficients represented by α_3^{-1} and α_3^1 are highly correlated with x and y. Therefore, ignoring the coma aberration could lead to lateral shifts in the reconstructions. Correlations between α_2^{-4} and α_2^{-2}, α_4^0 and z or α_4^2 and α_2^2, may lead to misestimations of these coefficients. This is studied in section B.3.2 on simulation experiments. However, it would be probably worse not to take them into account because that would systematically introduce errors in the model. Most of the other coefficients of the correlation matrix are low or null and the corresponding parameters can then be considered as decorrelated. Because of the high correlation values in the correlation matrix, all parameters must be estimated at the same time to prevent estimation errors.

B.1.3 Reconstruction: including aberration model

Once the aberrations are modeled, they are taken into account to better reconstruct the modulus and the phase of the objects of interest. Let us consider a sample modeled by a 2D transmittance plane $\underline{t}(x, y)$. For an infinite aperture and aberration free imaging system, the non parametric model is the squared modulus of the convolution between the Rayleigh-Sommerfeld propagation kernel $\underline{\boldsymbol{h}}_z^{\mathrm{RS}}$ and the transmittance plane $\underline{\boldsymbol{t}}$ [Goodman, 2004] (see Chapter 1).

In order to account for aberrations in the image formation model, an aberrated PSF model should be used. Assuming a shift invariance of the pupil function with z, the Optical Transfer Function (OTF), which is equal to the Fourier Transform of the complex-valued PSF $\underline{\boldsymbol{h}}_z$, can be expressed as follows:

$$\widetilde{\underline{\boldsymbol{h}}_z}(\boldsymbol{\alpha}) = \widetilde{\underline{p}}(\boldsymbol{\alpha}) \odot \widetilde{\underline{\boldsymbol{h}}_z}^{\mathrm{RS}} \tag{4.6}$$

where $\widetilde{\underline{\boldsymbol{h}}}_z^{\mathrm{RS}}$ is also called the angular spectrum and is the Fourier transform of the Rayleigh-Sommerfeld kernel $\underline{h}_z^{\mathrm{RS}}$ [Goodman, 2004] (see Chapter 1).

Thus, the aberration corrected non-parametric model $\boldsymbol{m}^{\mathrm{NP}}$ can be expressed as:

$$\boldsymbol{m}^{\mathrm{NP}}(\underline{\boldsymbol{t}}, \boldsymbol{\alpha}) = |\underline{\boldsymbol{h}}_z(\boldsymbol{\alpha}) * \underline{\boldsymbol{t}}|^2 \tag{4.7}$$

Unlike the parametric case (section B.1.1), minimizing the discrepancy between data and model is not sufficient to solve this ill-posed problem. *A priori* information about the sample must be added in the form of constraints on the optimization space $\mathbb{T}$ and in the form of a regularization term $\mathscr{R}$ [Sotthivirat and Fessler, 2004, Jolivet et al., 2018, Soulez et al., 2022]:

$$\underline{\boldsymbol{t}}^{\dagger} = \underset{\underline{\boldsymbol{t}} \in \mathbb{T}}{\operatorname{argmin}} \ \|\boldsymbol{d} - \boldsymbol{m}^{\mathrm{NP}}(\underline{\boldsymbol{t}}, \boldsymbol{\alpha})\|_2^2 + \mu \mathscr{R}(\underline{\boldsymbol{t}}) \tag{4.8}$$

where μ is a regularization hyperparameter.

In the following, the regularization term is a hyperbolic total variation term [Charbonnier et al., 1997]. The hyperparameter is chosen empirically. The optimization domain is restricted to the unitary disk corresponding to a non-emissive object hypothesis. A FISTA algorithm is used to perform this minimization [Beck and Teboulle, 2009].

B.2 Experimental study

B.2.1 Principle

High quality microscope objectives are supposed to be diffraction limited as long as they are used in the standard conditions for which they have been optimized (coverslip thickness, refractive indices of the immersion medium, the sample medium and the coverslip and position of the sample relative to the coverslip) [Gibson and Lanni, 1991, Haeberlé, 2004]. Yet, in some applications, these golden rules may be broken (wrong coverslip thickness, for instance). In inset A of Fig. A.1, the refraction of the beam in the coverslip is shown before entering the objective. This illustrates the origin of the possible wavefront errors that may occur between the paraxial rays and the high angle rays when the standard conditions of use are not met. This wavefront error has been described by several authors [Gibson and Lanni, 1991, Haeberlé, 2004] in on-axis situations, but it may vary with the position in the field of view. Finally, even when the rules are strictly applied, residual aberrations may still exist, especially out of the optical axis, and may differ from one objective to another. To experimentally study the influence of such aberrations, we used a water immersion objective with a coverslip correction collar. Thus, for a given coverslip thickness, a wrong correction collar setting will give rise to aberrations. This idea was recently used by Martin *et al.* in 2021 [Martin et al., 2021].

B.2.2 Experimental protocol

In this chapter, the holograms were acquired using the LaHC-Setup with label-free sample as presented in Appendix A. The sample was composed of $1\mu m$-diameter polystyrene beads diluted in glycerol. The diameter of the beads is chosen to be similar to biological objects such as bacteria. Usually, sub-resolution objects are used for PSF calibrations. However, in our context, with sub-resolution beads embedded in the biological sample, the contrast of holograms would be too low.

As polystyrene beads float in glycerol and thanks to its high viscosity, the beads were located just below the coverslip and did not move during the exposure of one hologram (typically, few milliseconds). According to the Gibson-Lanni model of the aberrations [Gibson and Lanni, 1991] induced by wrong coverslip thicknesses and/or refractive indices, the fact that the sample medium was glycerol instead of water should not induce additional aberrations as the beads were just below the coverslip.

Five cases of aberration were tested in this experiment with the correction collar at different settings (0.13, 0.15, 0.17, 0.19 and 0.21mm). The coverslip thickness was measured to be 0.170mm with a digital indicator (with a resolution of $\pm 1\mu m$). Thus, the 0.17mm setting of the correction collar is assumed to be the aberration free situation. A single bead was tracked through the whole field of view in regular steps in the X and Y directions. A total of 35 images (7×5) were acquired in order to regularly cover the whole field of view ($273 \times 204\mu m$). For each XY-position in the field, an axial stack was recorded with defocus positions ranging from $-10\mu m$ to $+20\mu m$ from the focus position with a step size of $0.5\mu m$. This stack is used for the illustration of Fig. 4.5, but only one axial position will be reconstructed in the next section. It should be noted that the sample is the only moving part, which is important for recording a background image by calculating the median value of the 35 XY-shifted images recorded at focus.

A view of a typical hologram is shown in the top part of Fig. 4.5. XZ-views of the stack along the vertical axis of the bead are represented at the bottom of Fig. 4.5. As shown in the figure, a change in the focus position is observed as a function of the setting of the correction collar, as well as modifications in the XY-profiles. The radial symmetry of the PSF is not always valid, as can be seen, for example, for the 0.13mm setting of the correction collar (green). This asymmetry is due to aberration effects that may break the radial symmetry of the holograms (*e.g.* coma, astigmatism, etc.). All aberrations may originate from the objective, but also from the tube lens or from misalignment of the illumination or the imaging parts. Moreover, aberrations can also originate from inhomogeneities of the slide and the coverslip.

B.3 Aberrations estimations implementation

In this section, we first apply the proposed method to simulated holograms to demonstrate the robustness of our approach for several kind of aberrations, especially in cases of difficult optimizations, *i.e* with highly correlated Zernike coefficients. We then apply it to experimental holograms of beads. We compare our results with state-of-the-art parametric reconstruction algorithms in both simulated and experimental cases and finally evaluate and discuss the effects of aberration on regularized reconstructions.

B.3.1 Aberrations parameters estimations on simulated data

A mosaic of 7×5 in-line holograms was simulated with aberrations varying in the field of view (see Fig. 4.6). Each hologram is a 512×512 pixels sub-image simulated with the experimental parameters described in Appendix A (Setup LaHC, Config-LABELFREE) and with the aberrated Lorenz-Mie model (see equation 4.3). The defocus is set to 12μm. This distance was chosen to improve the accuracy of the estimation of the Zernike coefficients, as indicated by CRLB analysis of this parameter (see Section B.1.2 Fig. 4.4).

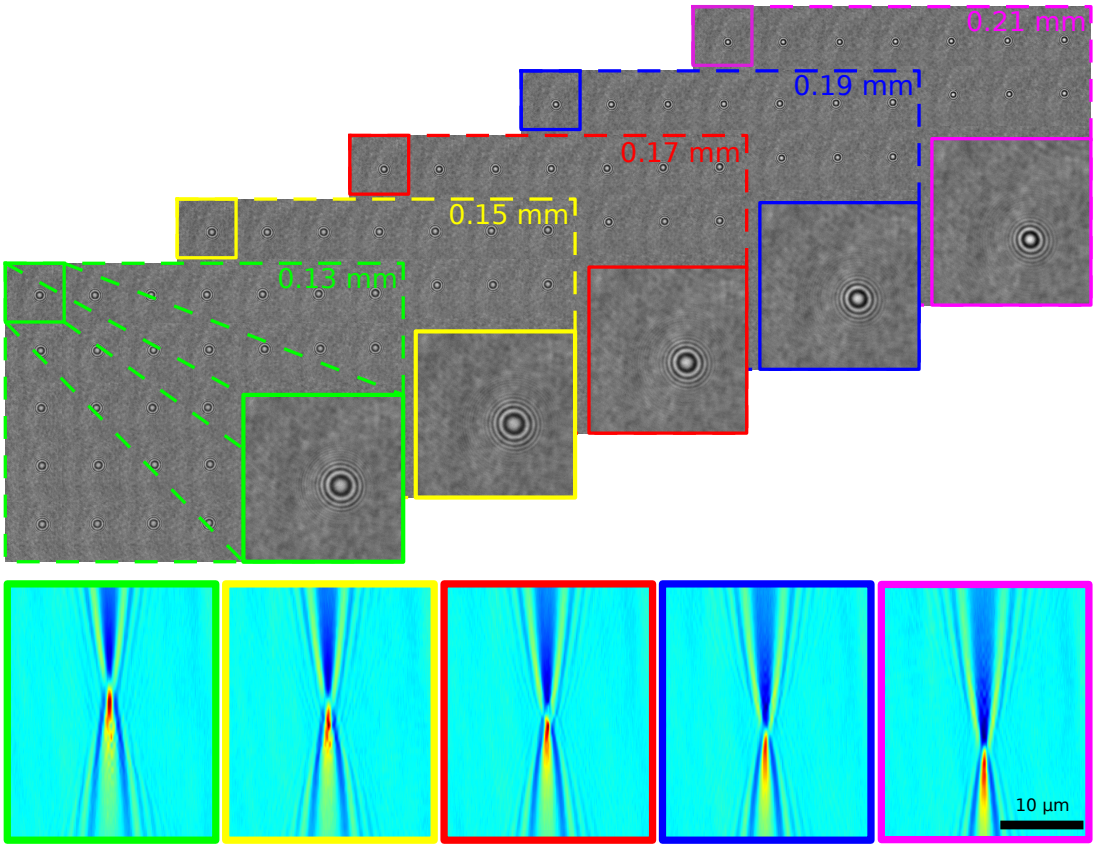

Figure 4.5: Example of a mosaic of holograms (top) of 1μm-diameter polystyrene beads in glycerol for an approximate defocus of 12μm under 5 different settings of the correction collar (from left to right: 0.13 (green), 0.15 (yellow), 0.17 (red), 0.19 (blue) and 0.21mm (magenta). XZ-views of the hologram stacks for the different correction collar settings (bottom).

To simulate a varying PSF in the field of view, the aberrated pupil function was considered to depend on the position of the bead in the field of view. This pupil function corresponds to a linear combination of oblique astigmatism ($\boldsymbol{Z}_2^{-2}$), vertical coma ($\boldsymbol{Z}_3^{-1}$), horizontal coma ($\boldsymbol{Z}_3^{1}$), spherical aberration ($\boldsymbol{Z}_4^{0}$) and oblique secondary astigmatism ($\boldsymbol{Z}_4^{-2}$) (see Section A). This linear combination is weighted by the corresponding Zernike coefficients $\boldsymbol{\alpha}$ (see Section B.1.1). We arbitrarily chose to set a linear behavior along y for α_2^{-2} and α_3^{1}, a linear behavior along x for α_3^{-1} and α_4^{-2}, and we set α_4^{0} constant in the field of view. This set of coefficients was chosen to demonstrate the performance of the proposed method in difficult cases, *i.e.* we chose Zernike coefficients that were highly correlated in the corrected model (see Section B.1.2).

Finally, a white Gaussian noise η was added to the simulated holograms, which led to a Signal-to-Noise Ratio (SNR) of 4 in the holograms (SNR $= \frac{\Delta \boldsymbol{m}}{2\sigma_\eta}$, where $\Delta \boldsymbol{m}$ is the peak-to-peak amplitude of the model).

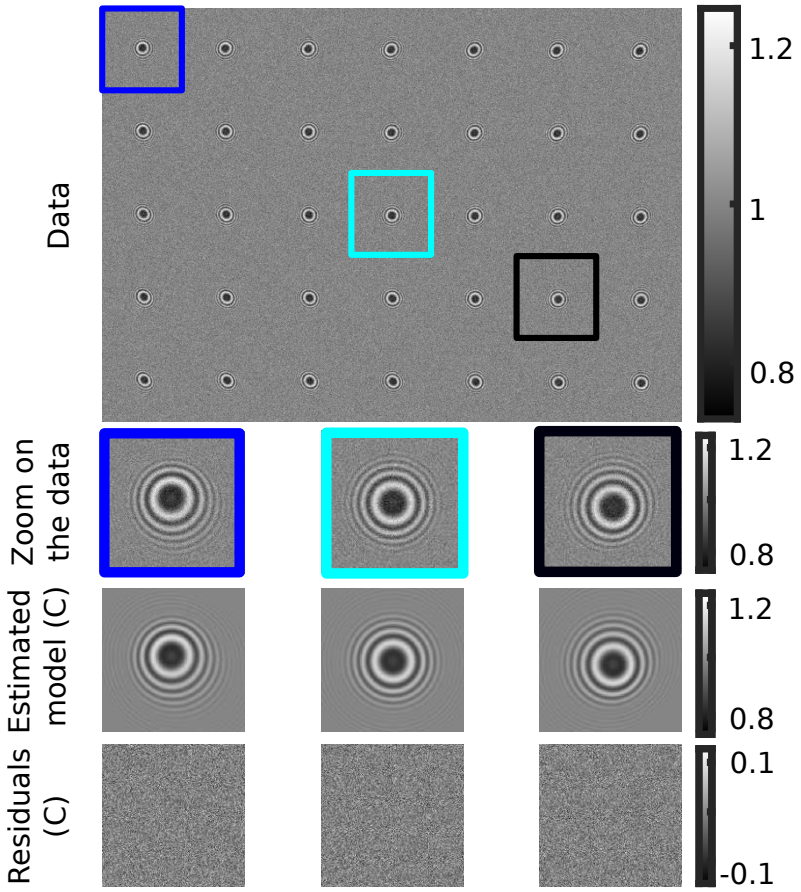

Figure 4.6: **Top:** 35 holograms simulated with variable Zernike coefficients depending on the position in the field of view. **Bottom:** magnifications of 3 holograms from different areas (first line), estimated model accounting for aberrations (C) (second line), residuals i.e. difference between the first line and the second one (third line).

For each simulated hologram, the estimations were performed using parametric IPA with or without aberration corrections in the model. The abbreviations C (standing for Corrected), and UC (standing for UnCorrected) will be used in the following. The

optimization algorithm we used was the LINCOA algorithm [Powell, 2015]. To perform the reconstructions with the corrected model (C), the first step implies an exhaustive search in a 17 parameters space, which can be really demanding in terms of computational time. To reduce this exhaustive search, it can be fairly convenient to have at least a coarse knowledge of the Zernike coefficients. As our aberrations were quite low, we performed this step by considering no aberration, *i.e.* all Zernike coefficients were set to zero.

Then, the optimization step was performed with the fully corrected model (eq.4.5), with the constraints on parameters described in Table 4.2. The optimization domains $\{\mathbb{C}, \mathbb{D}\}$ were chosen quite large in order to check the robustness of the proposed method.

	z	r	n	α_2^{-2}	α_2^2	α_3^{-3}	α_3^{-1}
Lower bound	10	0.2	1.52	-10	-10	-10	-10
Upper bound	14	0.7	1.63	10	10	10	10
	α_3^1	α_3^3	α_4^{-4}	α_4^{-2}	α_4^0	α_4^2	α_4^4
Lower bound	-10	-10	-10	-10	-10	-10	-10
Upper bound	10	10	10	10	10	10	10

Table 4.2: Optimization constraints for each estimated parameters (z and r are in micrometers)

Table 4.3 shows the bead parameters reconstructed without (UC) or with (C) taking the aberration into account in the model. It shows the biases introduced by geometrical aberrations. When using an unaberrated model (UC), the reconstructions converge either on a local optimization minimum or to the constraint domain bounds. Conversely, when using an aberrated model, the reconstructions always converge to the global minimum with low bias and a standard deviation close to the theoretical lower bound given by Cramér-Rao analysis.

ϑ_i	ϑ_i^{GT}	$< \hat{\vartheta}_i >^{UC}$	$< \hat{\vartheta}_i >^{C}$	$\sigma_{\vartheta_i}^{\text{CRLB}}$	$\sigma_{\hat{\vartheta}_i}^{UC}$	$\sigma_{\hat{\vartheta}_i}^{C}$
$z(\mu m)$	12	11.048	12.001	0.002	0.579	0.004
$r(\mu m)$	0.5	0.267	0.500	0.001	0.030	0.001
n	1.58	1.619	1.5798	0.0006	0.0311	0.0007

Table 4.3: Statistical results on the estimated bead parameters with aberration corrected (C) and uncorrected (UC) models: Ground Truth (GT) parameters ϑ_i^{GT}, means of the estimated parameters $< \hat{\vartheta}_i >$, lower bounds of their theoretical standard deviations $\sigma_{\vartheta_i}^{\text{CRLB}}$ and standard deviations of their estimates $\sigma_{\hat{\vartheta}_i}$

Residuals between the data and the model are very low, indicating that the model fits the data accurately (see the bottom line in Figure 4.6). On the upper part of Fig. 4.7 are presented the phase of the pupil functions that were simulated in each part of the field of view. This gives another view, in Fourier space, of the type of phase errors that aberrations may imply. On the lower part of Fig. 4.7 are presented the residuals of the estimated pupil functions (from the simulated ground truth). From these residuals, we see that our estimations of the Zernike coefficients are accurately describing the phase function introduced by aberrations in Fourier space.

In the most difficult cases (upper part and lower part of the field on Fig. 4.7), the residuals are not negligible for the highest spatial frequencies, close to the cutoff frequency imposed by the numerical aperture of the objective (represented by a black dashed circle). Indeed, as we did not use a sub-resolution object, the power spectrum of the object is not filling the entire pupil. In the inset of Fig. 4.7, the typical power spectrum of the object is presented and a white dashed circle show the part of the spectrum including 95% of its energy. In this white dashed circle, the residuals remain low. Actually, this is an unsurprising limitation of this approach: as the object spectrum does not cover the whole aperture of the objective, the pupil phase function can not be estimated precisely for the highest frequencies. However, the pupil function is correctly estimated for the spatial frequencies corresponding to the spectrum of the object, which ensures that a similar object will be correctly reconstructed. If the aberrations are important, this effect must be considered for the choice of the calibration objects: the size of the beads chosen for aberration estimation must be at least equal or smaller than the objects of interest.

B.3.2 Aberrations parameters estimations on experimental data

The experimental parameters were the same as those used in the simulations. Once again, since the accuracy of the estimated parameters is better in a specific range of defocus z (see SectionB.1.2), the holograms to be reconstructed were located approximately 12μm from the focus position, as in the simulations. They were reconstructed using parametric IPA, with the same workflow that was described in the reconstructions of the previous subsection. Again, to compare the effect of aberrations on the estimation of the beads parameters, both corrected (C) and uncorrected (UC) models are used for the reconstructions. As illustrated in Section B.2, the position of the focus varied with the setting of the correction collar. Parametric IPA provides an estimation of the defocus distance z between the sample and the focal plane of the objective.

Table 4.4 presents a list of the mean values and the standard deviations of all 35 positions in the field for parameters z, r and n and for both (UC) and (C) reconstructions. According to the comparison of standard deviations for each collar setting, the dispersion over the field was only moderately modified by the model (UC) or (C). However, the mean values changed, especially that of the estimated defocus $\hat{z}$. A maximum difference of 1.68μm in the estimated defocus was found between the two models (UC) and (C).

Moreover, the estimated defocus highly depends on the correction collar setting, which varied from 8.8 to 13.9μm (UC) and from 10.5 to 12.5μm (C). Thus, this dispersion was reduced by taking the aberrations into account, indicating a correction of the bias in the evaluation of the defocus. Since regularized reconstruction algorithms rely on a precise knowledge of the image formation model (including the defocus distance), any misestimation of the axial position of the sample would bias the reconstructions. Finally, it must be noted that the remaining dependence of the estimated defocus with the correction collar setting may have a physical origin. Indeed, wrong settings of the correction collar may really change the focus position as it changes the properties of the objective.

For the estimated radii $\hat{r}$ and refractive indices $\hat{n}$, the dispersion over the field was reduced when the aberrations were taken into account. The averages were also less dispersed, but to a lesser extent. Indeed, some biases that depend on the correction collar setting appeared to remain.

Fig. 4.8 presents the estimated bead parameters as scatter plots. This makes it possible

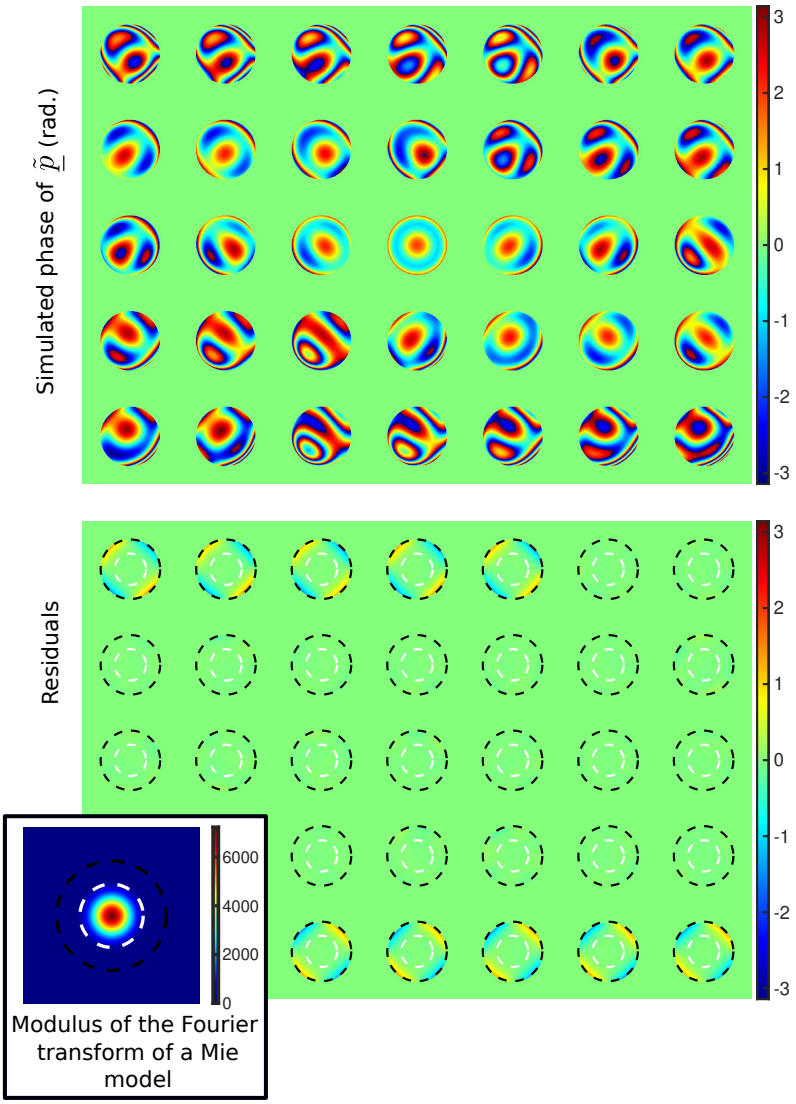

Figure 4.7: Simulated phase correction in the pupil (top) and residuals of the estimated pupil functions from the ground truth (bottom). The white dashed circles correspond to the disk in which 95% of the energy of the power spectrum of the object (inset) is contained. The black dashed circles correspond to the aperture (calculated from the numerical aperture of the objective).

	UC	C	UC	C
Collar	$<\hat{z}>$	$<\hat{z}>$	σ_z	σ_z
0.13	13.913	11.769	0.802	0.864
0.15	13.049	12.239	0.483	0.482
0.17	11.706	12.221	0.548	0.527
0.19	10.496	12.112	0.510	0.595
0.21	8.838	11.436	0.442	0.769
Collar	$<\hat{r}>$	$<\hat{r}>$	σ_r	σ_r
0.13	0.526	0.494	0.008	0.008
0.15	0.519	0.504	0.006	0.008
0.17	0.502	0.512	0.007	0.005
0.19	0.495	0.518	0.007	0.010
0.21	0.497	0.522	0.007	0.010
Collar	$<\hat{n}>$	$<\hat{n}>$	σ_n	σ_n
0.13	1.5733	1.5945	0.0041	0.0034
0.15	1.5773	1.5890	0.0027	0.0062
0.17	1.5856	1.5847	0.0044	0.0031
0.19	1.5902	1.5819	0.0036	0.0040
0.21	1.5878	1.5806	0.0032	0.0053

Table 4.4: For the 5 correction collar settings, averages $<\hat{\vartheta}_i>$ and standard deviations $\sigma_{\hat{\vartheta}_i}$ of the estimated parameter $\hat{z}$, $\hat{r}$ and $\hat{n}$. All lengths are in micrometers.

to visualize the correlations between the estimated parameters z, r and n.

Moreover, for each collar setting (one color for one collar setting), taking the aberrations into account improved the repeatability of the parameter estimation independently of the introduced aberrations. Indeed, the aberration corrections not only reduce the biases between the different collar settings (differences from one color point cloud to another) but also reduce correlations coefficients between parameter estimations (correlations within one color point cloud). This is presented quantitatively on Table 4.5, for both models (C) and (UC) and for the less aberrated case (0.17mm). According to Table 4.5, the decorrelation is particularly important between r and n.

Uncorrected (UC)

ϑ_i	z	r	n
z	1	0.02	0.51
r	0.02	1	-0.56
n	0.51	-0.56	1

Corrected (C)

ϑ_i	z	r	n
z	1	0.28	-0.55
r	0.28	1	0.13
n	-0.55	0.13	1

Table 4.5: Correlation coefficients between the estimated parameters without aberration correction (left) and with aberration correction (right) for a correction collar setting of 0.17mm (less aberrated case)

According to the manufacturer's specifications, the radius should be (0.5±0.03)μm and the refractive index should be around 1.587. The estimated parameters obtained with or without an aberration model were within the manufacturer's confidence interval (0.47-0.53μm). It is important to note that the fit with the Mie model is constrained by

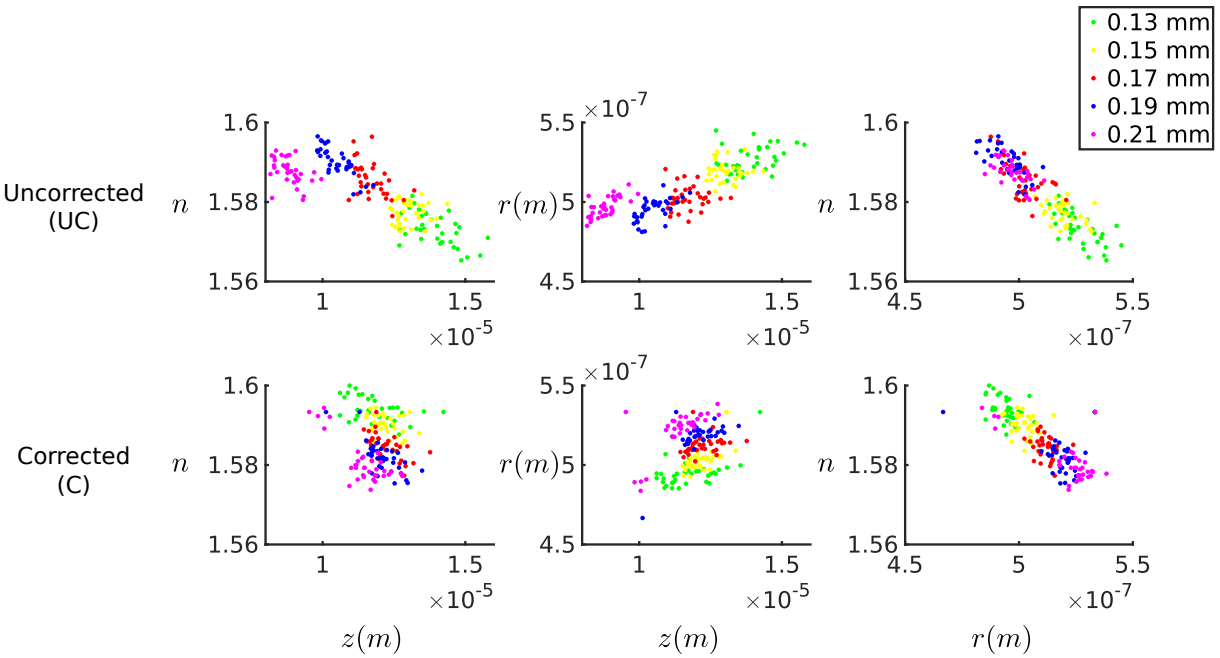

Figure 4.8: Scatter plots showing the biases and correlations between the estimated defocus $\hat{z}$, radius $\hat{r}$ and refractive index $\hat{n}$ for a single bead, for the 35 positions in the field, for the 5 settings of the coverslip correction collar and with corrected models (C) and uncorrected models (UC). With correction of the aberrations, the bias and the dispersion of the estimations due to aberrations are reduced.

the spherical hypothesis and thus may be quite robust to errors in the model, contrary to the case of regularized reconstruction that have more degrees of freedom, and will be more sensitive to aberrations, especially to non-radially symmetric ones, as it will be seen later on regularized reconstructions.

With the 35 recorded holograms corresponding to 35 bead positions in the field of view, we were able to check that the Zernike coefficients vary in the field of view, following continuous evolutions similar to those described in another work [Zheng et al., 2013]. The Figure 4.9, illustrates the evolution of the Zernike coefficients associated with oblique astigmatism, vertical coma, horizontal coma and spherical aberrations. These appeared to be the main components of the aberrated pupil function $\widetilde{p}$. The evolution of these coefficients is continuous and, not surprisingly, increases with increasing errors in the correction collar setting. Spherical aberration does not depend on the location in the field of view but change with the correction collar setting, with almost no spherical aberration for the less aberrated case (0.17mm). This is quite logical as a coverslip thickness error is known to induce spherical aberrations [Martin et al., 2021]. On the contrary, oblique astigmatism varies in the field of view without depending too much on the correction collar setting.

Figure 4.10 illustrates the evolution of the phase correction for the 35 positions in the field of view and for a correction collar of 0.17mm. For this supposedly aberration-free case, the setup still suffer from aberrations that change in the field of view. These phase functions show significant aberration effects but, as expected, lower than for the other correction collar settings (not represented). This indicates the necessity of taking aberrations into account for hologram reconstruction even when the optical system is supposed

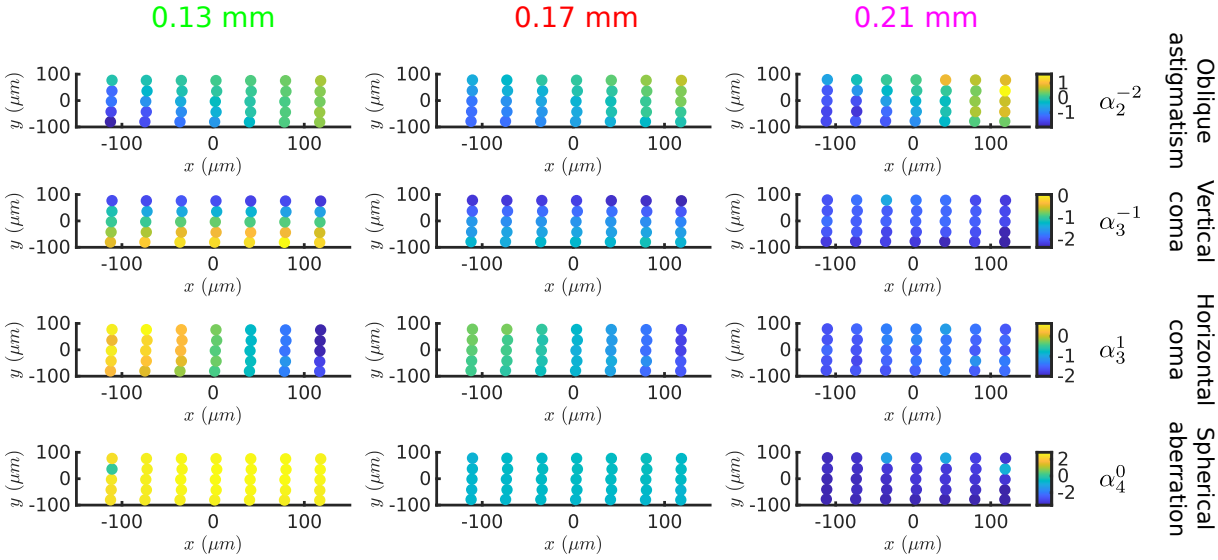

Figure 4.9: Estimated Zernike coefficients α_n^m as a function of the position in the field of view and for 3 settings of the coverslip correction collar (0.13 mm, 0.17 mm, 0.21 mm). The evolution of the Zernike coefficients is continuous in the field of view. The coma and astigmatism coefficients depend on the position in the field of view and on the correction collar setting whereas defocus and spherical aberration only depend on the correction collar setting.

to be compensated for aberrations. Indeed, these aberrations may come from residual aberrations of the objective, but also from other sources, like thickness inhomogeneities of the slide and the coverslip, as well as alignment issues.

From the numerical point of view, the detection of all 35 beads in the mosaic takes around 30 seconds on a 3296×2472 pixels image. The local optimization step for each bead takes around 10 seconds when not considering aberrations while it takes 45 seconds when considering them. These estimations have been realized using an Intel Core i9-11950H CPU 2.60GHz with 16GBytes of RAM.

B.4 Reconstructions on experimental data

To evaluate the improvement of the reconstructions due to the refinement of the direct model (by accounting for aberrations), beads holograms are used. This allows us to compare quantitatively the reconstructed transmittance with a ground truth (assumed to be the transmittance of the bead whose parameters are estimated by parametric IPA). However, since the non-parametric model is very general (not limited to spherical objects), similar results will be obtained with an aspherical sample. The reconstruction is performed with (C) and without (UC) the previously estimated aberration pupil function $\underline{\widetilde{p}}$ and the $\hat{z}$ parameters.

A Fienup phase retrieval algorithm [Fienup, 1982, Latychevskaia and Fink, 2007],, as well as a regularized IPA (as presented in B.1.3) are used to reconstruct the data. These reconstructions are performed using the uncorrected propagator $\underline{\boldsymbol{h}}_z^{\mathrm{RS}}$ (UC) or the corrected propagator $\underline{\boldsymbol{h}}_z$ (C) in the model (eq.4.7). Fig. 4.11 illustrates the reconstructions

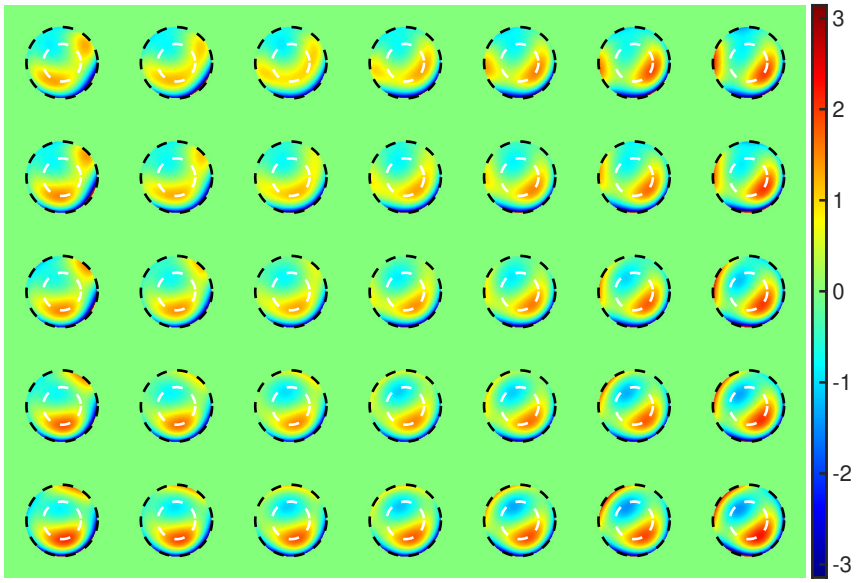

Figure 4.10: Evolution of the phase (in radians) of the pupil function correction in the field of view for a setting of the coverslip correction collar of 0.17mm and for the 7×5 positions in the field where the aberrations were estimated. The black and white dashed circles are defined on Fig.4.7

results for both algorithms. The estimated aberrated Mie model that fits the data has been back propagated at the center plane of the bead (BPMie-C) and is considered as the ground truth here because it is the most accurate model. Similarly, a back propagation of the Mie model estimated without aberration has also been computed (BPMie-UC). Because of the coma aberrations, the bead position (x, y) is not the same for (BPMie-C) and (BPMie-UC) parametric inversions, as mentioned in Section B.1.2. For comparison purpose the beads have then been centered in Fig. 4.11.

When aberrations are not considered in the reconstruction model, the morphological properties and quantitativity of the reconstructions are compromised. Indeed, either with Fienup or regularized IPA, the bead does not show a circular shape. As the aberrations vary in the field of view, the same bead does not have the same shape for each lateral position. The back-propagation of the Mie model without aberration illustrates the model error when the aberrations are not considered, but the radial symmetry is maintained as the Mie model is based on a spherical model. The regularized reconstructions without aberrations do not match with this model indicating bias in the estimation of the bead parameters. However, with aberrations correction the reconstructions fit the corresponding back-propagated Mie model and have the expected geometrical and quantitative properties. It demonstrates that whatever the reconstruction algorithm, aberrations should be taken into account to restore accurately the morphological and quantitative properties of the sample.

Taking into account the aberrations in regularized reconstructions has no effect on the computational time as the aberrated forward model has the same complexity as angular spectrum propagation. In the example of Figure 4.11, reconstructing a whole field of view (2472×3296) and considering the spatial evolution of the PSF takes less 10 minutes. These estimations have been realized using an Intel Core i9-11950H CPU 2.60GHz with

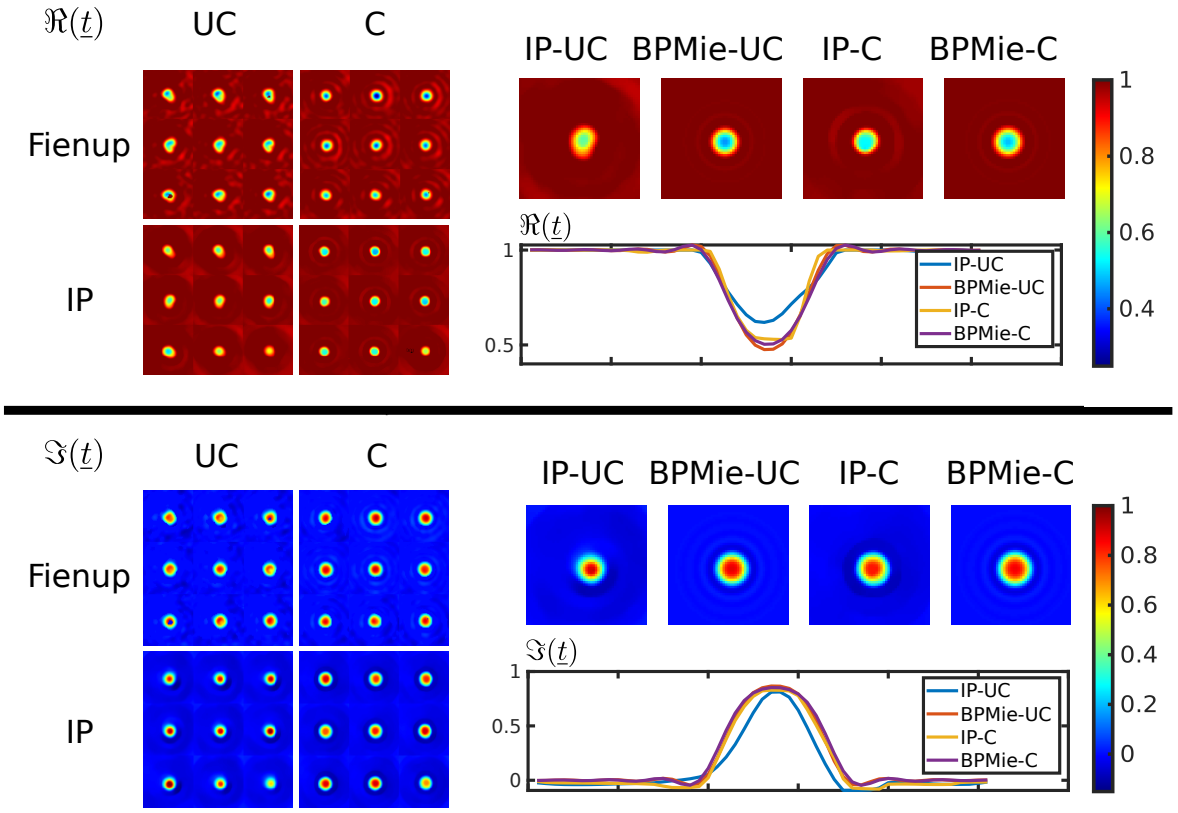

Figure 4.11: Non-parametric reconstructions using regularized IPA and Fienup algorithm with (C) or without (UC) aberrations correction. The reconstructions are presented in real part an imaginary part. A reconstruction is compared with the back-propagation of the estimated Mie model without aberration estimation (BPMie-UC) and the back-propagation of the Mie model with aberration estimation (BPMie-C). Profiles of the real part and imaginary part at the center of the bead are also presented.

16GBytes of RAM. This computational time can be reduced using GPU.

C Conclusion

In this chapter, we present a method to estimate the aberrations and thus reduce reconstruction errors, by using a more accurate image formation model, in in-line holographic microscopy. This method is based on the use and detection of calibration beads. We show that an aberrated Mie model can be used to estimate bead parameters and Zernike coefficients at the same time with a good precision and repeatability. Moreover, this approach requires only one hologram and does not require any assumption on the PSF evolution in the field of view. This calibration step could be done sequentially, like standard calibrations or *in-situ* by inserting calibrated beads in the biological sample itself. However, this may depend on the application or on the main origin of the aberrations (from the optical setup or from the sample itself). Actually, adding calibration beads in the sample has already proven to be useful for autofocusing (see Chapter 2). In this context, with the present method of correction of aberrations, this autofocusing would be even more accurate.

Once the Zernike coefficients have been estimated, it is then possible to use them in a non-parametric approach framework to reconstruct any biological objects (spherical or not). This methodology of aberration estimation was applied for the improvement of non-parametric reconstruction of holograms with the in-line holographic microscopy configuration. However, it is also applicable to off-axis holography or other coherent imaging techniques or simply used as a calibration method for microscopy systems.

The method proposed here offers interesting perspectives for reconstructing more accurately and with more quantitativity the absorption and the phase of the objects of interest, even with poorly corrected or misaligned optical systems, non-standard optical configurations (various sample media, variable axial position of the objects below the coverslip) and more generally, for any non-standard microscopy configurations that may introduce aberrations.

It should be noted that other effects like integration on the pixel or partial spatial coherence [Olivier et al., 2022] could also be considered using the same approach. These effects will be neglected for the rest of the manuscript. However they could be considered when these effects are not negligible (for example for objects smaller than the pixel pitch, pixel integration is not negligible) to improve the quantitativity and reproductibility of the reconstructions.

In this study, we estimated aberrations parameters on a discrete grid. The next step could be to interpolate the spatially varying PSF. This PSF can then be used in the image reconstruction step, but with a high computational cost. Nevertheless, fast algorithms can be used [Denis et al., 2011, Denis et al., 2015].

Part III

Unsupervised regularization hyperparameters tuning

CHAPTER 5

Unsupervised hyperparameters tuning based on the minimization of SURE in digital in-line holography

Abstract

Inverse problem approaches are mostly based on the minimization of a criterion constructed as a combination of two components: a data-fidelity term that measures the discrepancy between the data and the image formation model and a prior information enforcement taking the form of regularization terms or bound constraints. To compensate for the lack of phase information, a trade-off between the data-fidelity and prior is tuned by weighting the regularizers thanks to scalar parameters named regularization hyperparameters. Finding the optimal value for these lasts is an issue. Since hand tuning of the regularization hyperparameter is fastidious and that a badly chosen hyperparameter may bias the reconstructions, unsupervised tuning of the regularization hyperparameters have to be found. In this work, we discuss a method for unsupervised tuning of the regularization parameter using the Stein Unbiased Risk Estimator (SURE) criterion in the context of digital holography. In this chapter, after a preliminary section, we present how to tune the regularization hyperparameters with SURE in digital holography and an implementation of this state-of-the-art method on simulated holograms. This chapter ends with a discussion that introduces Chapter 6.

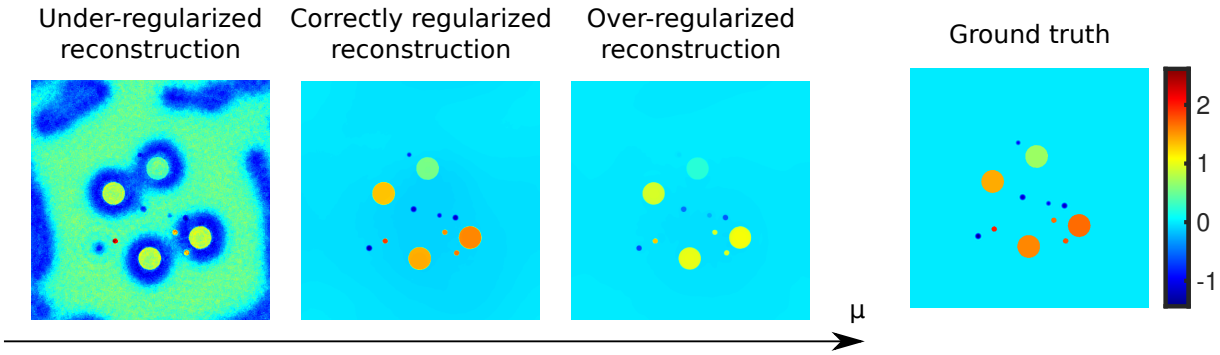

Figure 5.1: Exemple of reconstruction under several hyperparameter values. Here μ represents a weighting parameter of the complex total variation prior.

Introduction

Digital in-line holography consists in recording the intensity of the diffraction pattern from a defocused sample. Due to the loss of phase information, the reconstruction technique consisting in back propagating the hologram does not allow to retrieve a physically feasible 2D transmittance plane reflecting a realistic transmittance of the objects. The obtained transmittance plane suffers from twin-image artefacts (see Chapter 1). Inverse problem approaches propose to clean the twin-image artefacts by minimizing a cost function constructed with a data-fidelity term and a regularization term enforcing a priori information on the reconstruction plane. The most popular priors are based on the sparsity of the sample [Denis et al., 2009, Candes et al., 2013, Shechtman et al., 2014, Fogel et al., 2016, Rivenson et al., 2016, Cai et al., 2016], on the sparsity of the gradient of the image (Total Variation) prior [Chang et al., 2016, Fournier et al., 2017, Momey et al., 2019] or learned regularizations [Tillmann et al., 2016, Chang et al., 2021]. The data-fidelity term minimization depends mostly on the quality of the image formation model. Since the problem is ill-posed, the regularization term is added to lead to a physically feasible solution. Each regularization term added into the cost function is weighted by a hyperparameter (see Chapter 1). The quality of the reconstruction depends on the tuning of the hyperparameter which is critical to ensure the consistency of the inverse problem and its solution. Indeed, a bad tuning of the regularization hyperparameters may lead to biases in the reconstructions as seen on Figure 5.1 with the hyperbolic total variation regularization.

Hand tuning of hyperparameters is time consuming and may lead to wrong solutions depending on the subjective criterion chosen to qualify what a good reconstruction is. A good looking reconstruction is not necessarily a quantitative reconstruction. If the ground truth is known, the optimal hyperparameter choice would be the one that minimizes the error between the reconstruction and the ground truth (for example the Mean Square Error). In practice, this ground truth is not known and this criterion cannot be computed. In this context, several methods can be used to proceed to a blind tuning of the regularization hyperparameters, like Morozov's discrepancy principle [Karl, 2005], L-curve [Hansen, 1992, Hansen and O'Leary, 1993, Karl, 2005, Oraintara et al., 2000] generalized cross validation (GCV) [Golub et al., 1979, Wahba, 1990, Karl, 2005], Stein's Unbiased Risk Estimator (SURE) [Stein, 1981, Ramani et al., 2008, Deledalle et al., 2014] or its generalization exponential families by Eldar [Eldar, 2008]. In this chapter, we discuss

the performance of SURE unsupervised tuning of regularization hyperparameters in the context of in-line holography. We focus here on the complex edge-preserving smoothing regularization. This chapter is structured as follows: first, we will present several criteria to measure the reconstruction quality. In a second part, two state-of-the-art methods will be highlighted to compare their results with the methodology we propose. The third part will focus on bi-level approaches framework that will be used in the both following chapters. After these preliminaries, we will discuss in this chapter about the performance of SURE for the tuning of regularization hyperparameters in the context of in-line holographic microscopy.

A Preliminaries

A.1 Reconstruction quality criteria

The automatic tuning of the regularization hyperparameters $\boldsymbol{\mu}$ is based on the minimization of a reconstruction quality criterion. In this section, three of the classical reconstruction quality criteria are presented.

A.1.1 Mean square error

The mean square error measures the accuracy of the estimation of a parameter ϑ when the true value of this parameter ϑ^{GT} is known.

Mean square error definition

The mean square error of an estimation is defined by:

$$\mathrm{MSE}(\hat{\vartheta}) = \mathbb{E}\left[(\hat{\vartheta} - \vartheta^{\mathrm{GT}})^2\right] \tag{5.1}$$

The mean square error can be expressed as a function of the bias and of the variance of the estimator:

$$\begin{aligned}
\mathrm{MSE}(\hat{\vartheta}) &= \mathbb{E}\left[(\hat{\vartheta} - \vartheta^{\mathrm{GT}})^2\right] \\
&= \mathbb{E}\left[\left(\hat{\vartheta} - \mathbb{E}\left[\hat{\vartheta}\right] + \mathrm{Bias}\left(\hat{\vartheta}\right)\right)^2\right] \\
&= \mathbb{E}\left[\left(\hat{\vartheta} - \mathbb{E}\left[\hat{\vartheta}\right]\right)^2 + 2\left(\hat{\vartheta} - \mathbb{E}\left[\hat{\vartheta}\right]\right)\mathrm{Bias}\left(\hat{\vartheta}\right) + \mathrm{Bias}\left(\hat{\vartheta}\right)^2\right] \\
&= \mathbb{E}\left[\left(\hat{\vartheta} - \mathbb{E}\left[\hat{\vartheta}\right]\right)^2\right] + 2\mathbb{E}\left[\left(\hat{\vartheta} - \mathbb{E}\left[\hat{\vartheta}\right]\right)\right]\mathrm{Bias}\left(\hat{\vartheta}\right) + \mathrm{Bias}\left(\hat{\vartheta}\right)^2 \\
&= \mathrm{Var}\left(\hat{\vartheta}\right) + 2\left(\mathbb{E}\left[\hat{\vartheta}\right] - \mathbb{E}\left[\hat{\vartheta}\right]\right)\mathrm{Bias}\left(\hat{\vartheta}\right) + \mathrm{Bias}\left(\hat{\vartheta}\right)^2 \\
&= \mathrm{Var}\left(\hat{\vartheta}\right) + \mathrm{Bias}\left(\hat{\vartheta}\right)^2
\end{aligned} \tag{5.2}$$

In an ideal world, the transmittance plane, that represents the absorption and refractive properties of the objects, is known. The mean square error is then a metric that can

be used to quantify the quality of the reconstruction. Note that our main objective is to reduce the biais in the reconstructions. However, the MSE can be expressed as a function of the variance and the bias. Thus, minimizing the MSE do not guarantee to minimize the bias. Yet, it is a popular criterion to characterize the quality of the reconstructed image. Moreover the main issue with this metric is that a ground truth has to be known. Thus the mean square error can only be used in simulation studies.

A.1.2 Prediction mean square error pMSE

To evaluate the quality of the reconstruction, it is also possible to measure an error in the model domain. The prediction mean square error is the mean square error between the estimated model $\boldsymbol{m}\left(\hat{\vartheta}\right)$ and the true model $\boldsymbol{m}\left(\vartheta^{\mathrm{GT}}\right)$.

Prediction mean square error definition

The prediction mean square error of an estimation is defined by :

$$\mathrm{pMSE}(\hat{\vartheta}) = \mathbb{E}\left[\|\boldsymbol{m}\left(\hat{\vartheta}\right) - \boldsymbol{m}\left(\vartheta^{\mathrm{GT}}\right)\|_{\boldsymbol{W}}^2\right] \tag{5.3}$$

With an invertible model the minimum of the MSE would be obtained for the same parameter than the one that minimize the pMSE. In our case, the ground truth model is unknown since we only have access to the data $\boldsymbol{d} = \boldsymbol{m}\left(\vartheta^{\mathrm{GT}}\right) + \eta$. Since the model is not easily invertible, regularization term are added in the reconstruction process introducing small bias to avoid overfitting of the noise. Thus the pMSE and the MSE do not share the same minimum. Moreover, it should be noted that in this case we suppose to have a perfect model and additive Gaussian noise. Both assumptions are not exactly true leading to small biases in the reconstructions.

In the end these quality criteria still needs the true model which is unknown and is then only computable for simulation reconstructions. However it is possible to estimate this criteria using the Stein Unbiased Risk Estimator.

A.2 Automatic tuning of the hyperparameters

The reconstruction algorithm can be thought of as an operator (which depends on regularization hyperparameters) that maps the hologram onto the estimation of the reconstructed autofocused plane. Note that in this Chapter z is supposed to be known. Adjusting the regularization hyperparameters to obtain the best performances may be a difficult task.

A.2.1 Morozov's discrepency principle

Morozov's discrepancy principle tends to chose the regularization hyperparameter by matching the norm of the residuals to an upper bound [Karl, 2005]. Thus a good regularized reconstruction will be obtained when the estimated model follows Equation 5.4:

$$\boxed{\|\boldsymbol{d} - \boldsymbol{m}(\underline{\boldsymbol{t}}(\boldsymbol{\mu}))\|^2 \leq c^2} \tag{5.4}$$

where c is a constant that can be chosen depending on the noise level. A common choice of c is $c^2 = LC\sigma^2$. Let us note that to use this value of c, the variance of the noise σ^2

must be known. Using this choice of c means that the discrepancy between the data and the model is inferior to the noise level.

A.2.2 L-Curve

Introduced by Lawson and Hanson [Lawson and Hanson, 1995], the L-curve method is another method to tune the regularization hyperparameter. This method is based on "balancing" the effects of the data fidelity term and regularization terms. It consists in plotting $(\log(\mathscr{R}(\underline{\boldsymbol{t}}(\boldsymbol{\mu}))), \log(\|\boldsymbol{d} - \boldsymbol{m}(\underline{\boldsymbol{t}}(\boldsymbol{\mu}))\|^2_{\boldsymbol{W}})$ for various values of $\boldsymbol{\mu}$ [Hansen, 1992]. Hopefully the L-curve has a "L-shape" and the chosen regularization hyperparameter is the corner point of the L-curve. This point corresponds to the point of maximum curvature of the L-curve [Hansen and O'Leary, 1993]. Figure 5.2 illustrates how to tune the hyperparameter using the L-curve method. Note that when the variance of the noise increases, the value of the hyperparameter to tune increases. However one of the main drawback of this method is due to the fact that with multiple sized objects several corner are observable.

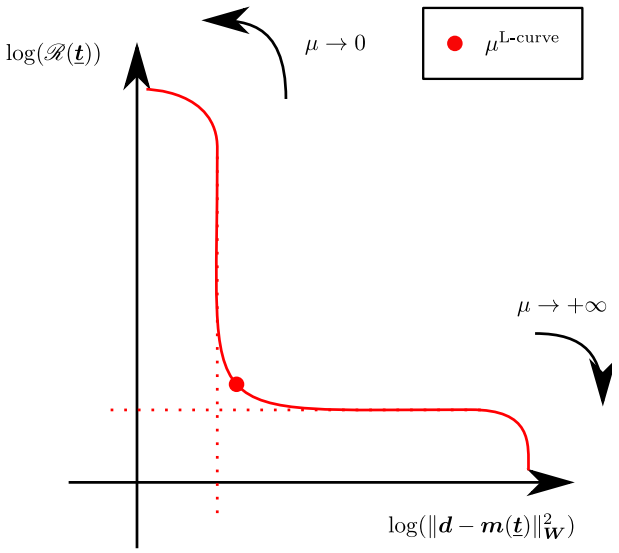

Figure 5.2: Principle of hyperparameter tuning with the L-curve method

A.2.3 Stein Unbiased Risk Estimator

Stein Unbiaised Risk Estimator (SURE) in an unbiased estimator of the prediction mean square error. This estimator gives an estimate of the accuracy of the estimator without any knowledge of the true model.

Prediction mean square error definition

Stein Unbiased Risk Estimator is defined by :

$$\text{SURE}(\hat{\vartheta}) = \|\boldsymbol{d} - \boldsymbol{m}(\hat{\vartheta})\|^2_{\boldsymbol{W}} + 2 \ \text{tr}\left(\frac{\partial \boldsymbol{m}(\hat{\vartheta})}{\partial \boldsymbol{d}}\right)\Bigg|_{\mathcal{K}} - \text{Card}(\mathcal{K}) \tag{5.5}$$

where $\mathcal{K} = \{k \in [1, ..., K] \text{ so that } \boldsymbol{W}_k \neq 0\}$

It is interesting to note that the computation of SURE criterion does not depend on a ground truth neither on an object plane ground truth like for the MSE nor a model ground truth like for the pMSE. Moreover it is possible to show that [Stein, 1981, Denneulin, 2020]:

$$\boxed{\mathbb{E}\left[\text{SURE}(\hat{\vartheta})\right] = \text{pMSE}(\hat{\vartheta})} \tag{5.6}$$

In 2008, Ramani [Ramani et al., 2008] proposed to compute the SURE criterion using on Monte Carlo method based on the approximation :

$$\text{tr}\left(\frac{\partial \boldsymbol{m}(\hat{\vartheta})}{\partial \boldsymbol{d}}\right) \approx \text{div}\left(\boldsymbol{m}(\hat{\vartheta})\right)$$

where div represents the divergence of the model relative to the data.
Let $\boldsymbol{n} \sim \mathcal{N}(0_{\mathbb{R}^K}, \mathbf{Id}_{\mathbb{R}^K \times \mathbb{R}^K})$ be a perturbation, $\tau > 0$ a small value, $\delta\boldsymbol{d} = \boldsymbol{d} + \tau\boldsymbol{n}$ data that have been perturbed by an additive centered Gaussian noise of variance τ^2, $\delta\hat{\boldsymbol{\vartheta}}$ is the reconstruction of the perturbed data $\delta\boldsymbol{d}$ using the model $\boldsymbol{m}$. Ramani showed that:

$$\boxed{\text{div}\left(\boldsymbol{m}(\hat{\vartheta})\right) \approx \left.\frac{\langle \boldsymbol{n}, \boldsymbol{m}\left(\delta\hat{\boldsymbol{\vartheta}}\right) - \boldsymbol{m}\left(\hat{\boldsymbol{\vartheta}}\right)\rangle}{\tau}\right|_{\mathcal{K}} = \text{Card}(\mathcal{K}) \left.\frac{\langle \delta\boldsymbol{d} - \boldsymbol{d}, \boldsymbol{m}\left(\delta\hat{\boldsymbol{\vartheta}}\right) - \boldsymbol{m}\left(\hat{\boldsymbol{\vartheta}}\right)\rangle}{\langle \delta\boldsymbol{d} - \boldsymbol{d}, \delta\boldsymbol{d} - \boldsymbol{d}\rangle}\right|_{\mathcal{K}},} \tag{5.7}$$

leading to the Monte-Carlo based Algorithm 6. Let us notice that in our case $\vartheta = \underline{\boldsymbol{t}}(\boldsymbol{\mu})$,

Algorithm 6: SURE criterion computation based on [Ramani et al., 2008]

input : Data $\boldsymbol{d}$
input : Perturbated data $\delta\boldsymbol{d}$
input : Model
input : μ
output: SURE$(\hat{\vartheta})$

Step 1: $\hat{\boldsymbol{\vartheta}} \leftarrow$ Reconstruction of the data $\boldsymbol{d}$ using hyperparameter μ.
Step 2: $\delta\hat{\boldsymbol{\vartheta}} \leftarrow$ Reconstruction of the perturbated data $\delta\boldsymbol{d}$ using hyperparameter μ.
Step 3: Compute the divergence term using 5.7 and SURE$(\hat{\vartheta})$ using 5.5.

thus, the finding the optimal hyperparameter by minimizing requires the computation of SURE for multiple values of $\boldsymbol{\mu}$. The computation of the SURE criterion for a given hyperparameter is performed using two reconstructions. It should be noted that the computation of the pMSE and of the SURE criteria depend both on the model. Thus, error in the image formation model may lead to bad estimation of the optimal hyperparameter and compensation of the model errors into the regularization term.

A.3 Bi-level approaches

Bi-level approaches [Colson et al., 2007, Sinha et al., 2017] allow to solve an optimization problem for which the objective function depends on the optimization of another

optimization problem. For example, in our case the optimization of a regularization hyperparameter on a criterion that depends on the reconstruction algorithm. The inner optimization task is called the lower-level optimization task. It corresponds to the reconstruction task in our case. The outer optimization task is called the upper-level optimization task and corresponds in our case to the optimization of the regularization hyperparameter. In this context the upper-level, the leader, take a decision by minimizing its objective function (the quality criterion) that depends on the results of the lower-level, the follower. The lower-level, minimizes its own objective function (the reconstruction algorithm) assuming the decision of the leader (the hyperparameter) has been taken.

Mathematical formulation of bi-level optimization problem

For an upper-level objective function $\mathscr{U}$ that depends on parameter $\boldsymbol{x}_u \in \mathbb{U}$ and a lower-level objective function $\mathscr{L}$ that depends on $\boldsymbol{x}_l \in \mathbb{L}$, the bi-level problem is given by :

$$\begin{aligned} &\boldsymbol{x}_u^\dagger = \underset{\boldsymbol{x}_u \in \mathbb{U}}{\operatorname{argmin}} \, \mathscr{U}(\boldsymbol{x}_l^\dagger(\boldsymbol{x}_u), \boldsymbol{x}_u) \text{ (Upper-level)} \\ &\text{subject to} \\ &\boldsymbol{x}_l^\dagger = \underset{\boldsymbol{x}_l \in \mathbb{L}}{\operatorname{argmin}} \, \mathscr{L}_{\boldsymbol{x}_u}(\boldsymbol{x}_l) \text{ (Lower-level)} \end{aligned} \tag{5.8}$$

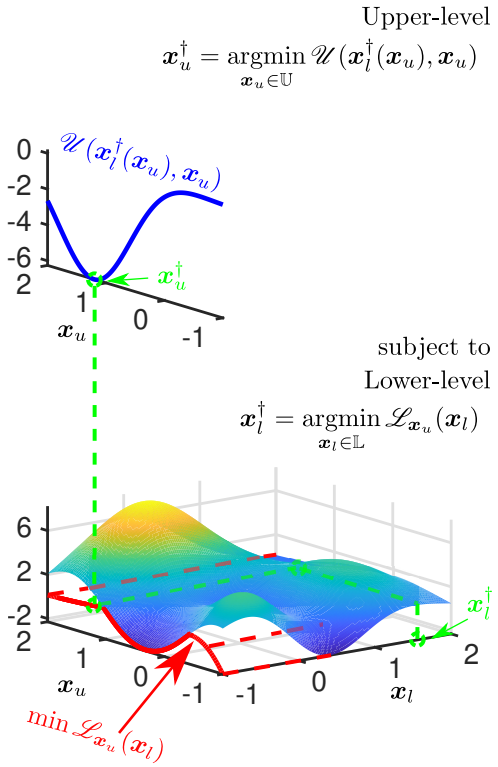

Figure 5.3: General sketch of a bi-level problem with a 1D upper-level and a 1D lower level

Figure 5.3 illustrates the principle of bi-level problem approaches. In a context of choosing a regularization hyperparameter $\mathscr{X}_u$ the upper-level objective function can be

seen as a quality criterion that depends on the reconstruction outcome $\mathscr{X}_l$. This reconstruction has been realized using the regularization hyperparameter $\mathscr{X}_u$ and thus depends on it.

B Regularization hyperparameter tuning using SURE

B.1 Stein's Unbiased Risk Estimator in in-line holography

Regularization in digital in-line holography reconstruction is crucial since the data-fidelity minimization problem that consists in minimizing the discrepancy between the data and the model is ill-posed. Indeed, due to the loss of the phase information, priors on the objects have to be added into the reconstruction process to ensure convergence to a physical solution. However, if they are crucial, the tuning of the regularization hyperparameters is a fastidious task since choosing the wrong hyperparameter may lead to bad bias-variance trade-off. This problem can be addressed using unsupervised methods. The next section focuses on the use of SURE criterion for tuning the hyperparameters in digital in-line holography.

In this chapter, we compare the automatic tuning of the regularization hyperparameters $\boldsymbol{\mu} = \{\mu_{\text{EP}}, \epsilon_{\text{EP}}\}$ for the complex edge preserving (EP) smoothing prior $\mathscr{R}^{\text{EP}}$ given by

$$\mathscr{R}^{\text{EP}}_{\epsilon_{\text{EP}}}(\underline{\boldsymbol{t}}) = \sum_{i,j} \sqrt{\nabla_{i,j}\Re(\underline{\boldsymbol{t}})^2 + \nabla_{i,j}\Im(\underline{\boldsymbol{t}})^2 + \epsilon^2_{\text{EP}}} - \epsilon_{\text{EP}} \tag{5.9}$$

However since only data disturbed by an additive noise are known, the ground truth model $\boldsymbol{m}(\boldsymbol{\vartheta}^{\text{GT}})$ is not known. Thus the pMSE can not be directly computed. However the SURE criterion is an non-biased estimator of the pMSE. For the computation of the SURE criterion, the ground truth model knowledge is not needed. The bi-level problem associated to the unsupervised tuning of the regularization hyperparameter and thus the optimal reconstruction problem for the SURE criterion can be expressed as follows:

$$\begin{aligned}
&\mu^{\dagger} = \underset{\boldsymbol{\mu}\in\mathbb{M}}{\operatorname{argmin}}\, \text{SURE}(\underline{\boldsymbol{t}}^{\dagger}(\boldsymbol{\mu}), \boldsymbol{\mu}) \text{ (Upper-level)} \\
&\text{subject to} \\
&\underline{\boldsymbol{t}}^{\dagger}(\boldsymbol{\mu}) = \underset{\underline{\boldsymbol{t}}\in\mathbb{T}}{\operatorname{argmin}} \|\boldsymbol{d} - \boldsymbol{m}(\underline{\boldsymbol{t}})\|^2 + \mu_{\text{EP}}\mathscr{R}^{\text{EP}}_{\epsilon_{\text{EP}}}(\underline{\boldsymbol{t}}) \text{ (Lower-level)}
\end{aligned} \tag{5.10}$$

where $\mathbb{M}$ and $\mathbb{T}$ define bound constraints for the upper and lower-levels of the bi-level problem. In the following reconstructions $\mathbb{T}$ corresponds to the unitary complex disk. In practice the SURE criterion is computed using Ramani Monte Carlo algorithm (Algorithm 6)as presented in Section A.2.3. The SURE criterion can then be computed for one point using two reconstructions.

B.2 Results

To assess the performance of the hyperparameters tuning based on the minimization of SURE criterion in in-line holographic reconstructions, the bi-level approach presented in Section A.3 was solved on 4 simulated holograms. Each hologram contains simulated

biological sample of different sizes and calibration beasd of 0.5 μm radius and of refractive index of 1.58 in glycerol of refractive index 1.47. These holograms are represented on Figure 5.4.

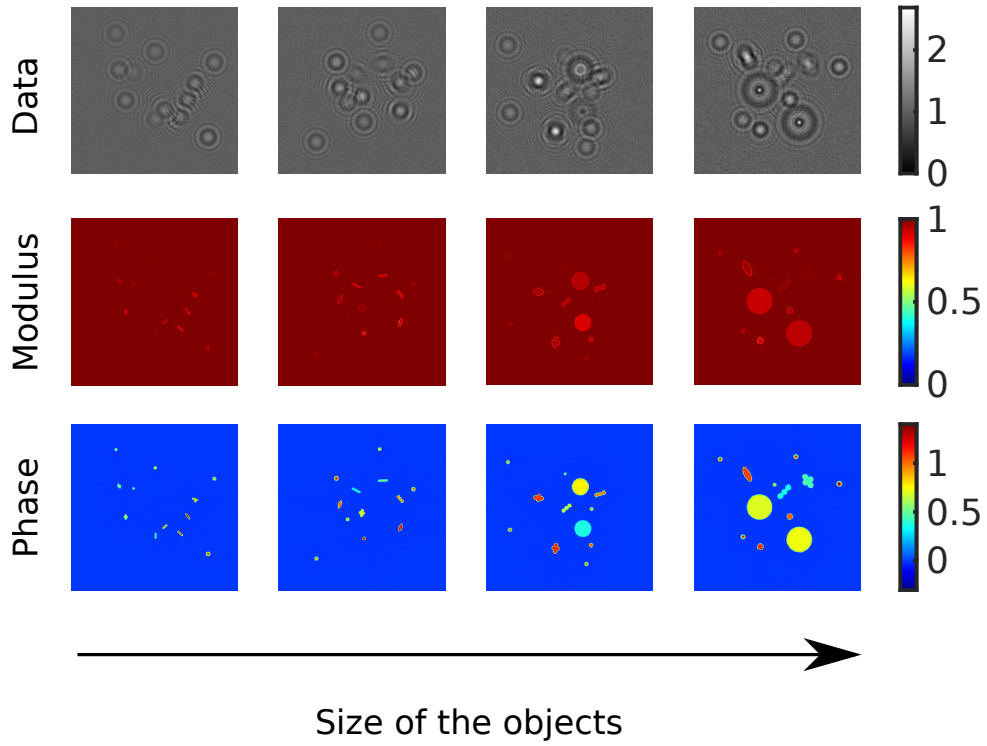

Figure 5.4: Simulated holograms, modulus and phase ground truth for simulation (Data)

In the next section we will focus on the reconstruction of one hologram (third from left) using an automatic tuning of the regularization hyperparameter using minimization of SURE criterion. Then we will highlight the main drawbacks of this unsupervised hyperparameter tuning method.

B.2.1 Tuning of the regularization hyperparameters on simulated data

To tune automatically the regularization hyperparameter, the use of SURE criterion gives an estimation of the pMSE that should be minimized. Figure 5.5 provides a map of the pMSE and of SURE criterion as a function of μ_{EP} and ϵ_{EP}. As seen on this figure, both criterion have the same shape and share the same minimum value. Thus, minimizing the SURE criterion, corresponds to minimizing the pMSE which represents the discrepancy between the estimated model and the true model. Note that in experimental cases the true model is unknown.The pMSE can not be minimized and SURE criterion has to be used as in Equation 5.10. Figure 5.5 also illustrates that the SURE/pMSE critera are not really sensitive to small changes of the regularization hyperparameters. However the minimum of pMSE/SURE criterion is obtained for $\epsilon_{\text{EP}} = 10^{1.5}$ and $\mu_{\text{EP}} = 10^{-2.75}$. Note that in this chapter the minimization is obtained by using minimum of discrete map of hyperparameters. However, the automatic tuning of the hyperparameters could be obtained much more quickly by minimizing the upper-level with an optimization algorithm like a Powell method [Powell, 2015].

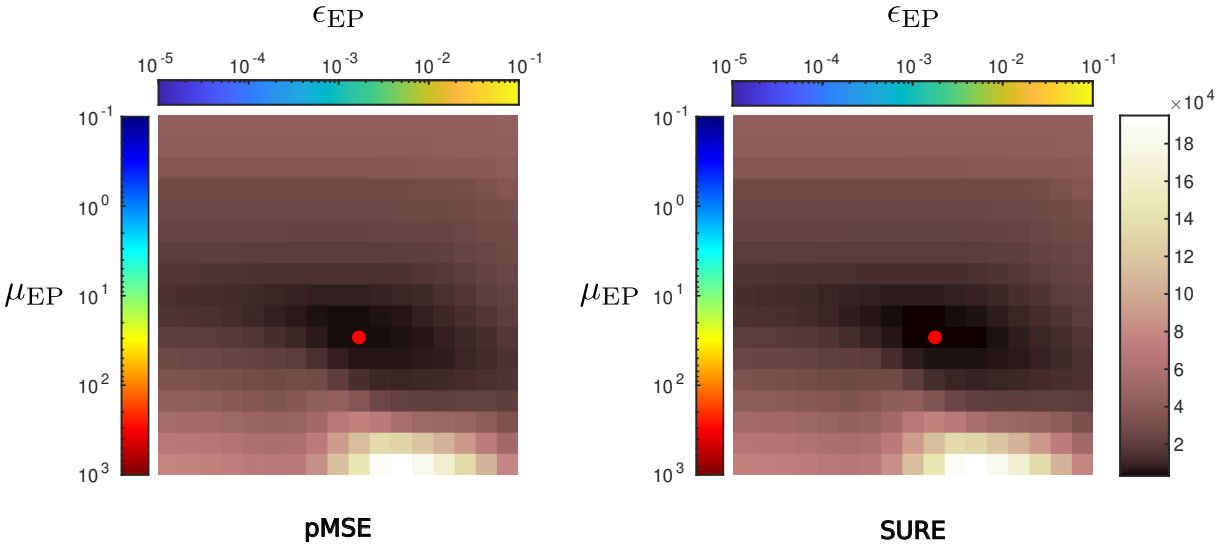

Figure 5.5: pMSE and SURE criterion depending on the regularization hyperparameters μ_{EP} and ϵ_{EP}

For comparison purposes the automatic tuning of hyperparameters ϵ_{EP} and μ_{EP} have been performed using the L-Curve method and Morozov's discrepancy principle as seen on Figure 5.6. These curves have been computed using several values of $\{\mu_{EP}, \epsilon_{EP}\}$ couples. For each couple a reconstruction has been performed leading to a point of the L-Curve. Thus both curves are the same and only the color changes and codes the parameters values. It should be noticed that the L-Curve method is adapted to tune correctly μ_{EP}, however it does not provide good results on the tuning of ϵ_{EP} since this method is adapted for only one hyperparameter tuning. The L-Curve method provides on this hologram the most quantitative result either in terms of modulus or phase on the whole image. However since the computation of this curve is time consuming (one reconstruction for each point), this method should be avoided. The Morozov's discrepancy leads to a more regularized reconstruction than the two others. Figure 5.7 shows the modulus and phase reconstructions obtained using the several unsupervised methods.

B.2.2 Drawbacks of the proposed method

Since all of the method presented earlier are based on the minimization of a criteria defined in the model space, the optimum obtained for each method depends on the quality of the image formation model. For the SURE/pMSE criterion, the quality is measured by the mean square error between the estimated model and the ground truth. For the L-Curve and for the Morozov's discrepancy principle the optimum depends on the mean square error between the model and the data. Thus, error in the image formation model may lead to bad estimation of the hyperparameters. Moreover there is no guarantee that minimizing the quality criterion in the model space is equivalent to minimizing a quality criterion in the object domain. Figure 5.8 represents the MSE criterion, that can be measured in the case of simulated data. The pMSE and the MSE do not have the same evolution and do not share the same minimum. Thus one of the main drawbacks of all the presented method is the lack of guarantee of quantitativity in the reconstructions which may be critical in bio-medical applications.

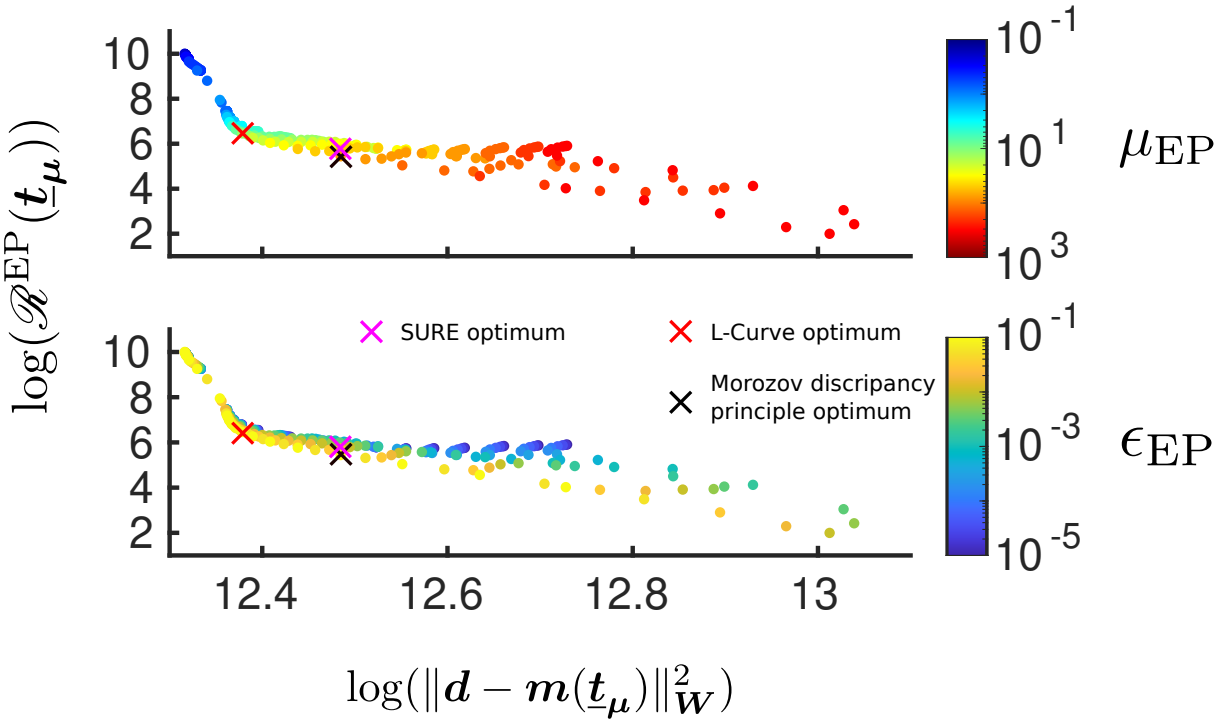

Figure 5.6: L-Curve, Morozov's discrepancy principle and SURE unsupervised tuning of hyperparameter

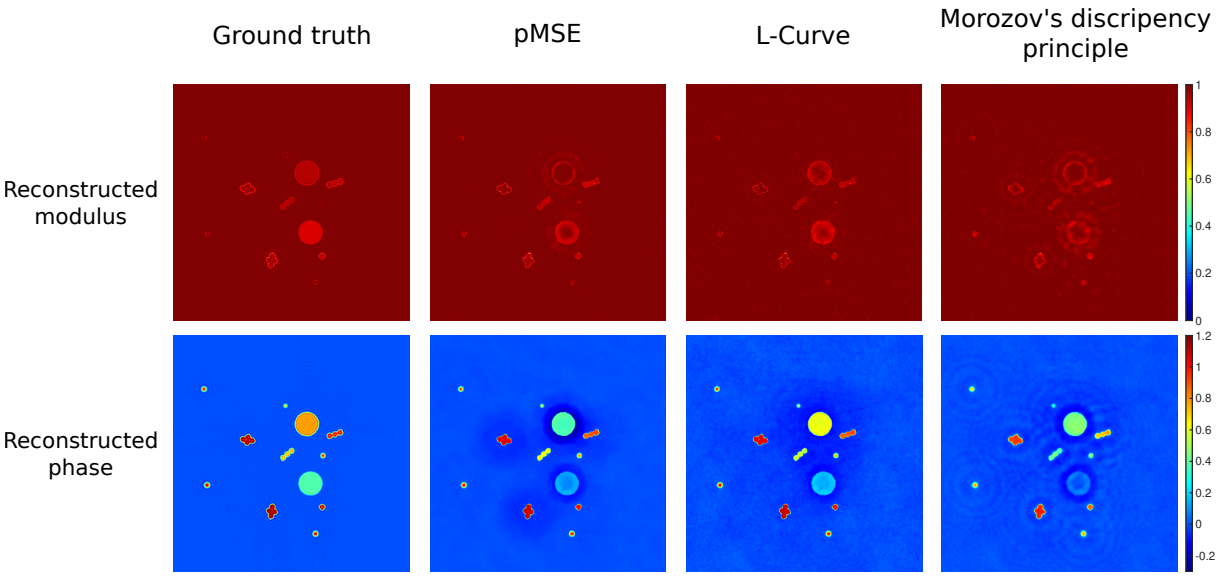

Figure 5.7: Hologram reconstruction using several unsupervised hyperparameters tuning method

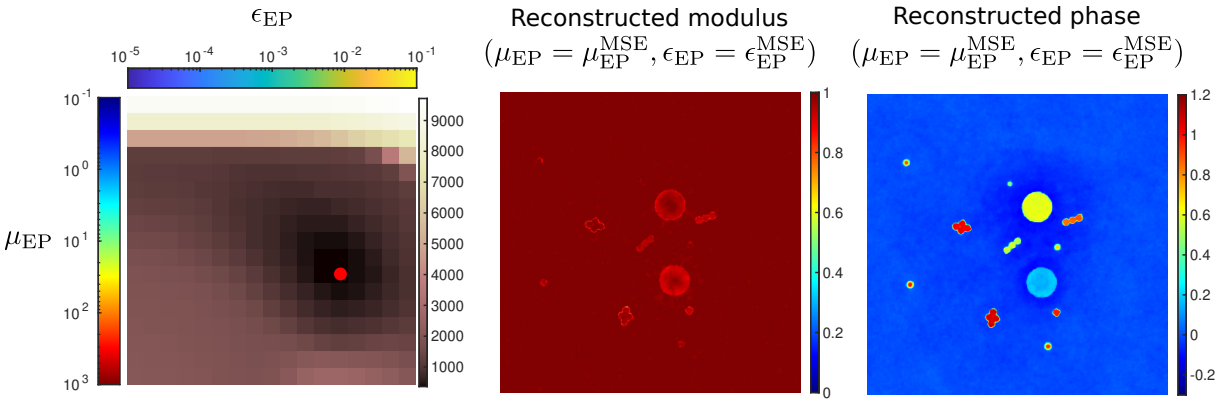

Figure 5.8: MSE criterion depending on the regularization hyperparameters and the reconstructions for the minimum of the MSE criterion

All the presented criteria are "image-based" criteria. Thus, these criteria tend to reconstruct at best the whole image leading to compromises on the quantitativity of the modulus and the phase of the reconstructed objects. This may be an issue in diagnostic applications since most of the time, the quantitativity is needed on specific objects. For example in Gram+/Gram- classification problems, the quantitativity is needed on the bacteria but can be biased with "image-based" criterion due to the high number of red blood cells in the sample which are not objects of interest and thus for which the quantitativity of the reconstructions is not needed. Figure 5.9 shows SURE-based regularized reconstructions of a mosaic of 4 holograms with different objects sizes using only one set of regularization hyperparameters. This figure illustrates that the quantitativity of the obtained reconstructions is a compromise to reconstruct at best all the objects. This leads to quantitatively correct reconstructions for specific object size (green reconstructions), over-regularized reconstructions for smaller objects (red reconstructions) and under-regularization with twin image artifacts for bigger objects. Thus the proposed methods are qualitatively effective to reconstruct the holograms but it is harder to evaluate their quantitativity on specific objects of interest.

C Conclusion

In this chapter, we studied several unsupervised tuning of hyperparameters and applied the SURE criterion method to in-line holography reconstruction. If the several proposed methods provide good qualitative results, *i.e.* "good looking" results, the quantitavity that we want to achieve in this manuscript is not guaranteed due to the "image-based" nature of the reconstructions. To offers better quantitativity to the reconstructions of the objects of interest, the tuning of hyperparameters must use an "object-based" approach. Moreover "model-based" hyperparameter tuning may not ensure to find the best solution in the object plane since "model-based" approaches minimum may differ from "object-plane-based" criterion minimum like the MSE. This difference may from the non-invertibility of the model or from image formation model errors. Due to the diversity of objects in a biological sample, the automatic tuning of regularization hyperparameters must be performed using more specific approaches that tends to reconstruct quantitatively a transmittance plane equivalent to the objects of interest.

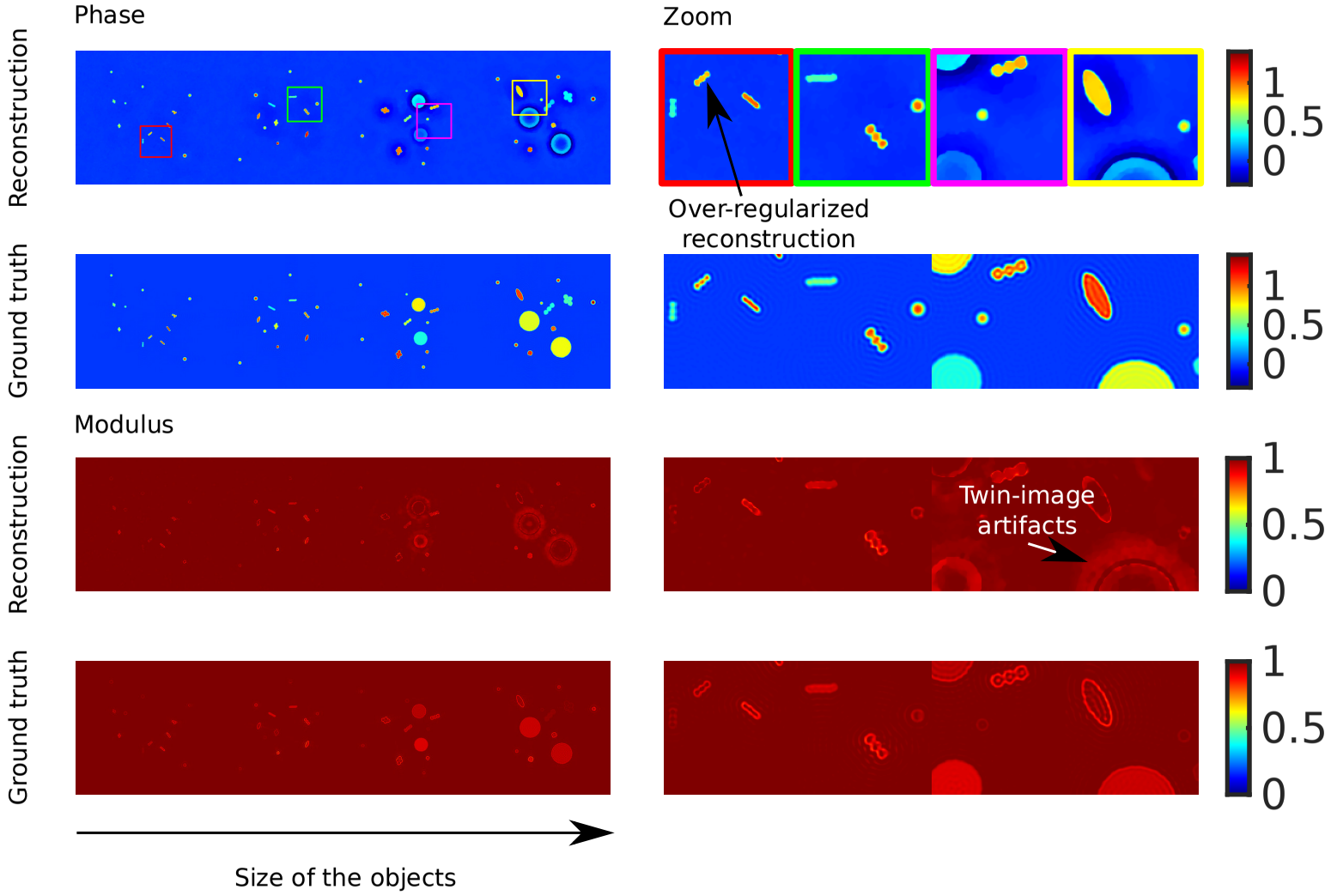

Figure 5.9: Unsupervised reconstruction of the transmittance plane of a multi-sized objects sample using SURE criterion minimization.

CHAPTER 6

Unsupervised hyperparameters tuning based on calibration beads reconstructions in digital in-line holography

Abstract

Unsupervised hyperparameter tuning is one of the most challenging task to perform quantitative reconstructions using inverse problem approaches in digital in-line holography. Most of the state-of-the art methods tend to find the best hyperparameter to reconstruct the whole image. However biological diagnosis is mostly based on the detection/characterization of one specific type of object surrounded by multiple other outliers. The reconstruction quantitativity is then compromised due to the surrounding environment of the objects of interest. Thus, more specific methods must be exploited to ensure the reproducibility and the quantitativity of the reconstructions. We propose, here, an automatic tuning of the regularization hyperparameters based on the quantitativity of calibration beads reconstructions. In this chapter, we present a new optimization criterion to tune hyperparamers and apply it to reconstruct simulated and experimental holograms.

Introduction

As detailed in Chapter 5, unsupervised method for hyperparameter tuning are mostly based on a criterion involving features of the whole image like the variance of the residuals for Morozov's discrepancy principle, the balance between the data fidelity term and the regularization term for L-Curve methods or the computation of an estimation of the pMSE for the SURE minimization. If those methods provide "good-looking" reconstructions, there is no guarantee on their quantitativity since bad tuning of the hyperparameters may lead to biased reconstructions. Indeed, one of the main drawbacks of the regular-

ization priors added into the reconstruction algorithms is their objects size and contrast dependency. To reconstruct a whole sample quantitatively, the regularization hyperparameters have to change depending on the object to reconstruct. Indeed, the twin-image artifacts (see Chapter 1) depend on the object size and the refractive index of the objects to reconstruct. Figure 6.1 illustrates the evolution of the twin-image on calibration beads of various radius r and refractive index n in an immersion oil of refractive index $n_0 = 1.518$ at $\lambda = 666nm$. As seen on Figure 6.1, the level of the noise due to the twin-image artifacts depends on the scale and refractive index of the objects and thus the amount of prior to use, *i.e.* the regularization hyperparameters, changes with the objects to reconstruct.

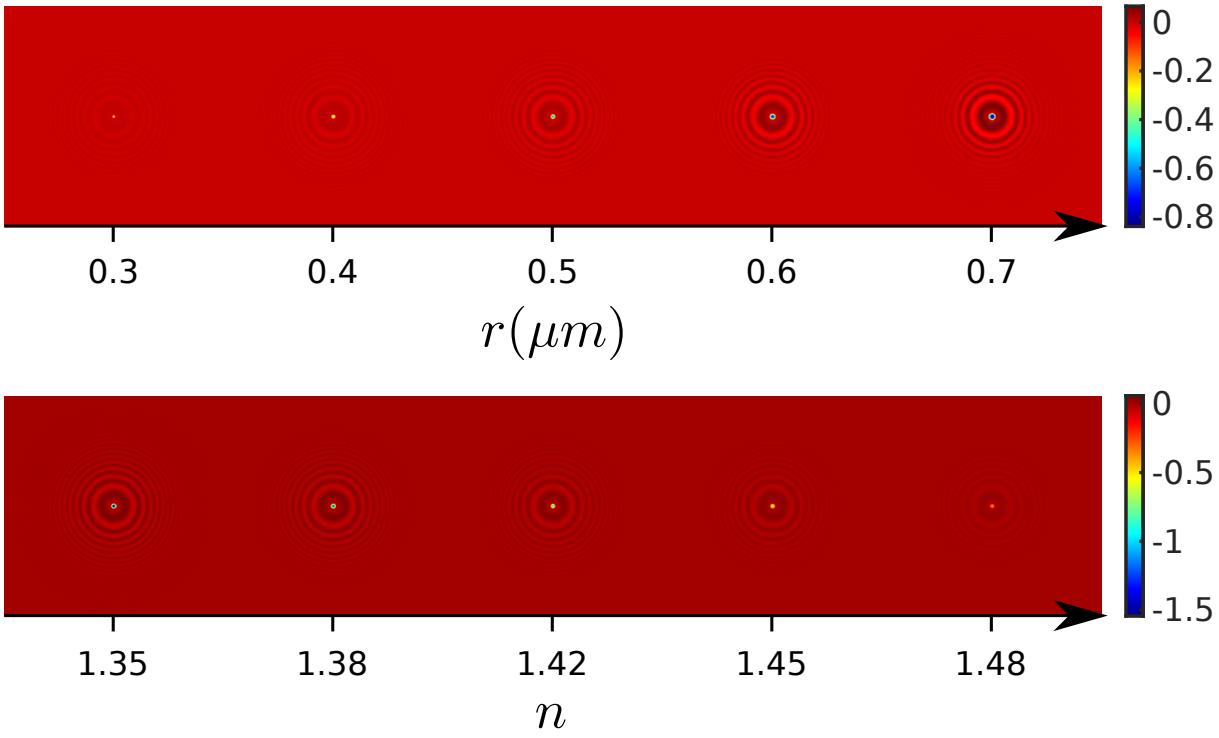

Figure 6.1: Evolution of the twin-image artifacts on calibration beads as a function of the radius r ($n = 1.45$) and the refractive index n ($r = 0.5\mu m$)

In the context of biological observations, samples generally can present a high diversity of objects, and only few of them are of interest, the others being considered as outliers. Hence, "whole-image-based" tuning of hyperparameters do not guarantee a correct reconstruction of the objects of interest. For example, with blood smear samples, most of the energy of the signal corresponds to red blood cells diffraction patterns while the objects of interest, the bacteria, represent only a small part of the signal energy. Thus, the common unsupervised tuning of the hyperparameters may result in the quantitative reconstruction of the red blood cells in spite of the bacteria. To perform quantitative reconstructions of bacteria, the tuning of the regularization should be less "image-driven" and more "object-driven".

To tune automatically the regularization hyperparameter for quantitative reconstructions we propose to use calibration beads added in the sample. In this work, a quality criterion based on the quantitative reconstruction of the beads is described and minimized to improve the quantitativity of the reconstructed bacteria that have similar size

and refractive index difference as beads. This work represent a pre-feasibility study of this automatic hyperparameters tuning method.

In the following section, we detail this methodology starting with the formalization of a bi-level approach. Then this bi-level approach is applied on simulated and experimental data of samples containing a mixture of calibration beads and biological objects.

A Bi-level approach to tune the regularization hyperparameter on calibration object

A.1 Optimization criterion to tune the regularization hyperparameters

One of the main issue with automatic tuning of regularization hyperparameters for quantitative reconstructions is the lack of a ground truth criterion in the reconstruction space, *i.e.* in the transmittance plane domain. Moreover the dependence between the regularization hyperparameters and the size and contrast of the objects induces a quantitative issue in in-line holography. We propose to use calibration beads of size and absolute refractive index difference similar to bacteria to build a reconstruction quality criterion directly in the transmittance plane domain. Using the framework presented in Part II, calibration beads allow to increase the quantitativity of the reconstruction by refining the image formation model. One of the main advantage of using calibration beads is that their image formation model is accurately known such that their reconstructions do not need any prior assumptions and thus are not biased. It is then possible to reconstruct an unbiased transmittance plane equivalent to the beads out of their estimated parameters. This transmittance is computed by back-propagating the complex amplitude of the Mie model of the beads.

The back-propagation of this complex amplitude is an accurate and unbiased estimation of the transmittance plane on the support of the beads $\mathbf{Mask}_{\text{Beads}}$. It can then locally be considered as a ground truth of the reconstructions. It is noted $\underline{\boldsymbol{t}}^{\text{GT}}$. Let us note that if the calibration beads are isolated, as in most of our cases, $\mathbf{Mask}_{\text{Beads}}$ can be extended to bigger areas. In this chapter $\mathbf{Mask}_{\text{Beads}}$ correspond to a 2.5 μm radius disk around each bead. Thus the reconstructions should fit the modulus and the phase of the calibration objects in focus.

We propose this methodology on a regularized reconstruction using a complex edge preserving smoothing prior. To tune the regularization hyperparameters $\boldsymbol{\mu} = \{\mu_{\text{EP}}, \epsilon_{\text{EP}}\}$, it is possible to construct a quality criterion based on the minimization of the discrepancy between the regularized reconstruction $\underline{\boldsymbol{t}}(\boldsymbol{\mu})$ of the calibration beads and $\underline{\boldsymbol{t}}^{\text{GT}}$ on the

reduced field $\mathbf{Mask}_{\text{Beads}}$. This problem can be posed as bi-level problem :

$$
\begin{aligned}
&\boldsymbol{\mu}^{\dagger} = \underset{\boldsymbol{\mu}\in M}{\operatorname{argmin}}\, \mathscr{Q}(\underline{\boldsymbol{t}}^{\dagger}(\boldsymbol{\mu})) \text{ (Upper-level)} \\
&\text{subject to} \\
&\underline{\boldsymbol{t}}^{\dagger}(\boldsymbol{\mu}) = \underset{\underline{\boldsymbol{t}}\in\mathcal{T}}{\operatorname{argmin}}\, \mathscr{L}_{\boldsymbol{\mu}}(\underline{\boldsymbol{t}}) \text{ (Lower-level)} \\
&\text{where} \\
&\mathscr{Q}(\underline{\boldsymbol{t}}(\boldsymbol{\mu})) = \|\underline{\boldsymbol{t}}^{\text{GT}} - \underline{\boldsymbol{t}}^{\dagger}(\boldsymbol{\mu})\|^2_{\boldsymbol{W}_{\text{Beads}}} \\
&\text{where } \boldsymbol{W}_{\text{Beads}} = \text{diag}(\boldsymbol{w}) \text{ where } w_k = \begin{cases} 1 \text{ if pixel } k \in \mathbf{Mask}_{\text{Beads}}, \\ 0 \text{ otherwise} \end{cases}, \\
&\text{and } \mathscr{L}_{\boldsymbol{\mu}}(\underline{\boldsymbol{t}}) = \|\boldsymbol{d} - \boldsymbol{m}(\underline{\boldsymbol{t}})\|^2_{\boldsymbol{W}} + \mu_{\text{EP}}\mathscr{R}^{\text{EP}}_{\epsilon_{\text{EP}}}(\underline{\boldsymbol{t}}) \\
&\text{where } \boldsymbol{W} \text{ is the inverse of the covariance matrix of the noise} \\
&\text{and } \mathscr{R}^{\text{EP}} \text{ the complex total variation regularization term.}
\end{aligned}
\tag{6.1}
$$

As in Chapter 5, the upper-level $\mathscr{Q}$ corresponds to a measurement of the quality of the reconstruction based on the quantitativity of the reconstructed transmittance plane for the calibration beads. The lower-level $\mathscr{L}$ corresponds to a regularized inversion task. The reconstruction depends on the regularization hyperparameter, and the quality criteria to tune the hyperparameter depends on the reconstruction. To tune automatically the regularization hyperparameters it is then required to solve the upper-level equation.

The upper-level is a parametric inverse problem, and can be solved using a Powell method that does not need the knowledge of the cost function gradient [Powell, 2015]. Solving the bi-level problem exposed in this section is time consuming since one computation of the quality criteria $\mathscr{Q}$ needs to compute one reconstruction. However compared to the minimization of the SURE criterion as presented in Chapter 5 the computational time is divided by 2.

The reconstruction algorithm corresponding to the lower-level is solved as presented in Chapter 2.

The method we propose in this Chapter can be performed with the aberration correction presented in Chapter 4.

A.2 Application of the proposed hyperparameters tuning

A.2.1 Tuning the hyperparameter on simulated data

To evaluate the performances of the proposed method 4 silica calibration beads of differents radii varying from $r = 0.25\mu m$ to $r = 3\mu m$ have been simulated. These calibrations beads have a refractive index of $n = 1.45$ and are observed in an immersion oil of refractive index $n_0 = 1.519$ under a coherent illumination at wavelength $\lambda = 622nm$. The objects are simulated at 12 μm from the sensor plane.

Figure 6.2 illustrates the problem of automatic tuning of the hyperparameter with 4 object sizes. These objects have been reconstructed using two unsupervised tuning methods of the regularization hyperparameters: the technique proposed in Section A.1, is compared to the SURE minimization. Both of these criteria are represented to compare the position of their minimum depending on the objects' size. As previously mentioned,

the twin image energy is "object-dependent". Thus the level of regularization must be adapted depending on the objects. As seen on Figure 6.2 the optimum of the SURE criterion is evolving with the size of the bead to reconstruct while the hyperparameters that minimize our criterion stay in a close neighborhood. Thus "image-based" criterion are biased depending on the population of objects in the image.

Our method based on the quantitativity of the reconstructions of the beads ensure that the objects that are similar to the beads, *i.e.* similar radius and similar refractive index difference with the medium, are reconstructed with the correct regularization hyperparameter, whatever the surrounding environment and whatever the noise in the image. This is the main advantage to use this regularization method. Indeed, to provide reproducible reconstructions, the regularization hyperparameter must be tuned independently of the sample and of the imaging system. Based on the reconstruction of the calibration beads, the minimization of our criterion tends to an improved reproducibility of the reconstructions.

Another interesting advantage of the proposed method is that the quality criterion is computed directly in the transmittance plane domain. Thus, biases due to the fact that minimizing the pMSE/SURE criterion is not equivalent to minimizing the MSE are lowered. Indeed, even though the estimated hyperparameter for reconstructing a 1 μm diameter beads (in green) is not corresponding to the hyperparameter that should be used for other size objects, it is closer to the optimal minimum that the one estimated with the pMSE criterion. In conclusion the proposed quality criterion minimization not only provides quantitative reconstruction of objects similar to the "reference" calibration bead but may also help to reconstruct quantitatively the other ones.

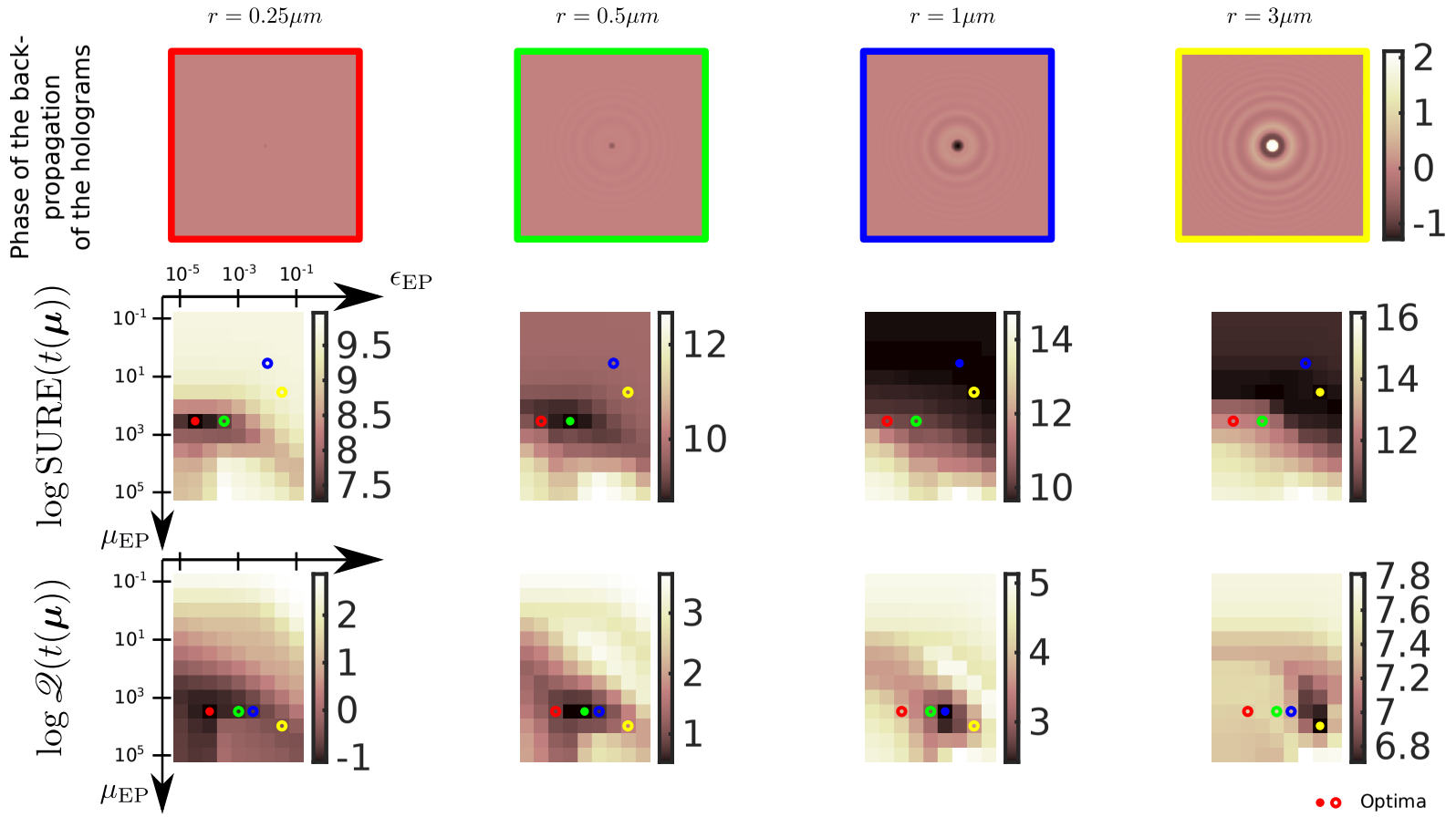

Figure 6.2: Quality criteria based on SURE minimization and minimization of the descrepancy beetwen back-propagation of beads diffraction patterns and regularized inversion. Each color corresponds to a size of object.

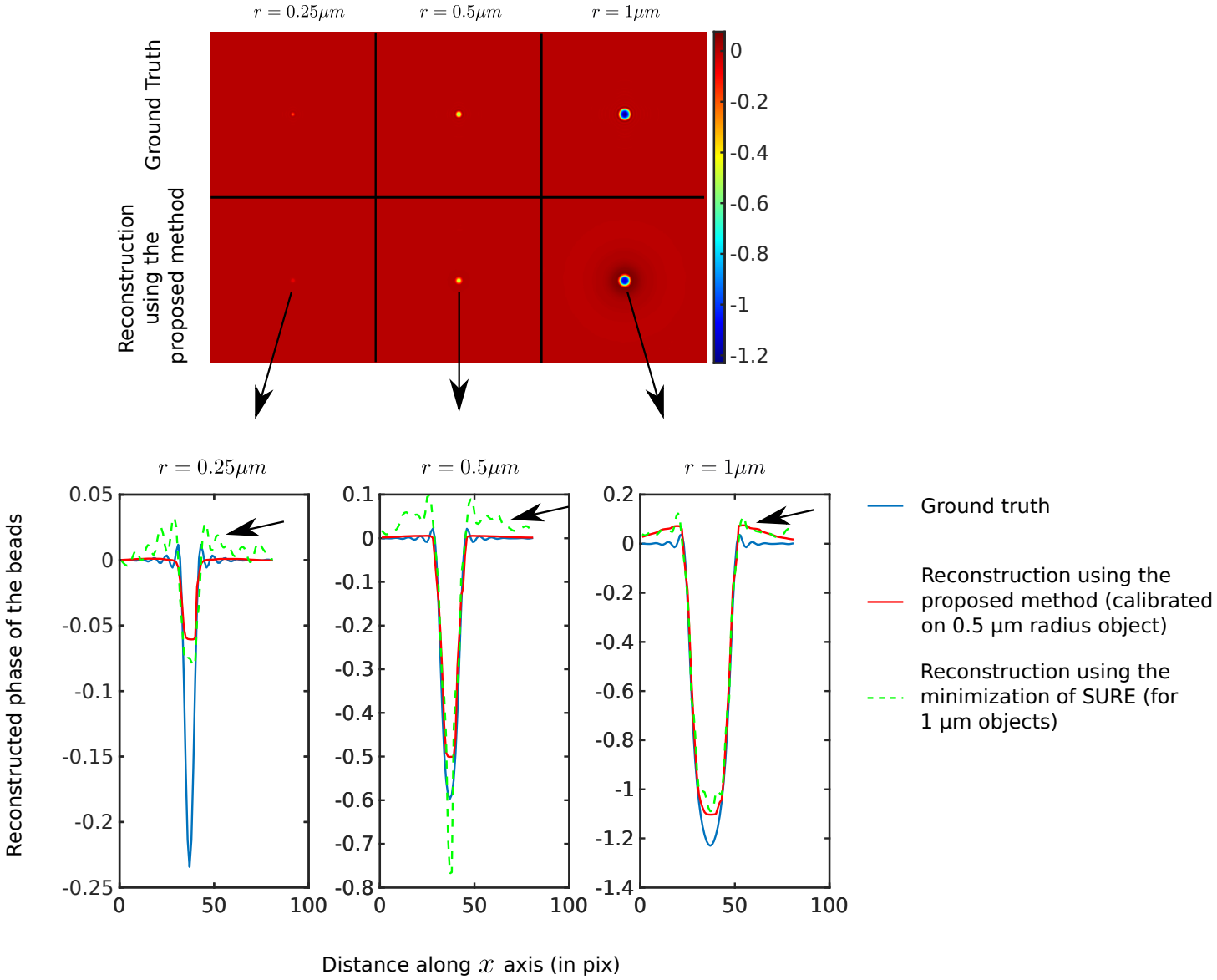

Figure 6.3: Phase reconstruction of objects of various sizes using the proposed method calibrated on 0.5 μm radius beads and SURE minimization for 1 μm radius objects, *i.e.* bigger objects than our objects of interest.

Figure 6.3 presents phase reconstructions of several size of beads using our criterion on calibrated objects (0.5 μm radius beads) and SURE criterion estimated on bigger objects that would be in higher number in the sample like red blood cells. Here the radius of these bigger objects is 1 μm. The reconstruction of the 0.5 μm radius bead is almost quantitative with our method. It can be seen that smaller objects are over-regularized and thus almost disappear in the reconstructions (red curve do not match). On the contrary, bigger object are under-regularized and twin image artifacts are visible at the edges on the support of the bead. On the SURE based reconstructions, as expected, it can be seen that the best quantitativity is obtained for the 1 μm radius. However smaller object, like our objects of interest, are badly reconstructed with quantitativity errors and high twin image artifacts.

A.2.2 Tuning the hyperparameter on experimental data

The regularization hyperparameters have been tuned on experimental data. These data have been acquired using the setup presented in Chapter 2 and corresponds to diffraction patterns of a mixture of red blood cells, bacteria and calibration beads. The sample is stained and the data are acquired at a distance $z \approx 10\mu m$ between the sample and the sensor.

As seen on Figure 6.4, the reconstructions of most of the objects that have the same size and contrast as the beads, like the bacteria, are cleaned of the the twin image artifacts and logically quantitatively reconstructed. However bigger objects, like the red blood cells, still present twin image artifacts on the edges of their support. This can be explained by two main reasons: since the red blood cells are thicker, the defocus distance is badly estimated, and, to reconstruct red blood cells another regularization hyperparameter should have to be chosen. As expected the sample is mostly transparent at this wavelength ($\lambda = 622nm$).

To assess experimentally the reproducibility of the method, more samples would have to be studied.

B Conclusion

In conclusion, we propose in this chapter a reconstruction method based on the minimization of a reconstruction quality criterion directly in the object plane that exploit calibrations beads as ground truth objects. This method is based on the fact that the beads share morphological properties with the objects of interest such that the choice of a regularization hyperparameter value adapted to the beads will also provide quantitative reconstruction of the objects of interest. This method is thus not dependent neither on the bigger or most numerous objects in the sample (in our application, red blood cells) nor on the imaging system noise. It improves then the reproducibility of the reconstructions. Since it is based on the minimization of the MSE on calibration objects, biases due to the minimization of a criterion in the model domain are avoided. The reconstruction of the bacteria are then theoretically more quantitative with this hyperparameter tuning. However the methodology has to be validated on a more complete experimental study. As seen in the two last chapters, the regularization hyperparameters tuning is still a crucial step in the search of quantitativity in in-line holography. To prevent biases inherent to the regularizations, the confidence in the data must be improved.

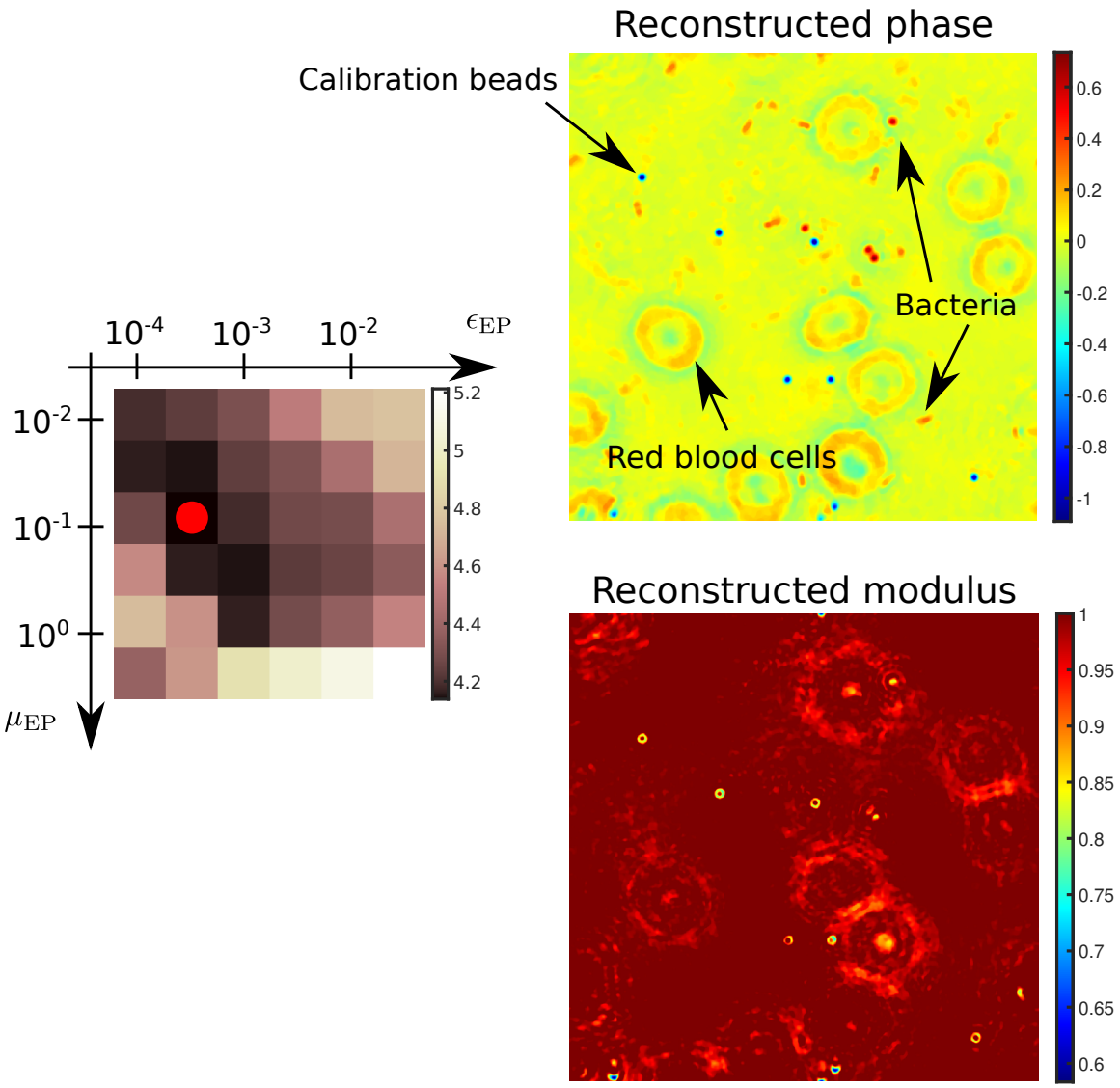

Figure 6.4: Reconstruction of a biological sample using the minimization of the proposed criterion

Part IV

Multispectral reconstruction

CHAPTER 7

Multiwavelength reconstructions in holography using a colocalization prior

Abstract

Multispectral imaging technologies offers the capability to extract spectral information for every pixel of the reconstructed image. This spectral information increases the informative content of the sample. It can also improve the reconstruction quantitativity. Since only the wavelength changes between each acquisition (objects are not moving), multi-spectral acquisition give a redundant information on the morphological properties of the object that can be used to reconstruct the phase by reducing the twin image artifacts. Moreover, the increased number of data allows to reduce the weights of the prior by reconstructing jointly the transmittance plane for each wavelength. We focus in this chapter on the use of objects co-localization prior in regularized inverse problem approach to improve the reconstruction of multi-spectral holograms. In this chapter, after a preliminary section, we present a co-localization prior for multispectral reconstruction. Then we propose reconstructions of experimental multispectral data using this prior. This chapter ends with a discussion on the need of registration between multispectral acquisitions that introduce Chapter 8.

Introduction

Digital in-line holography reconstructions are limited by the twin-image problem caused by the loss of the phase information in the hologram. To overcome this problem, priors can be considered in the reconstruction algorithm as mentioned in Chapter 2. These priors are based on objects a priori statistics and can be added in the reconstruction by using optimization constraints or regularization terms as mentioned in Part III. However, to re-

duce the weights of priors in the reconstructions, phase-diversity can be exploited. Phase diversity consists in recording multiple acquisition of the same objects with additional known phase variation like changing the defocus distance [Allen and Oxley, 2001, Greenbaum and Ozcan, 2012], the wavelength or the illumination angle. Using more views, the reconstructions can afford more confidence in the data and require thus less prior assumptions.

Multispectral in-line holography is a phase imaging technique based on phase diversity. It consists in recording the diffraction patterns of the same sample under several wavelengths illuminations. Thus, the obtained reconstruction are more robust to biases introduced by the prior. Indeed the cleaning of the twin-image is only held by priors based on objects statistics in mono-wavelength reconstruction. [Denis et al., 2009, Song et al., 2016, Jolivet et al., 2018, Momey et al., 2019]. With multispectral acquisitions the twin image problem varies with the wavelength and thus can be treated by using prior exploiting the redundant information in the data [Luo et al., 2015, Isikman et al., 2010].[Herve et al., 2018]. Indeed, if the twin-image varies with the wavelength, the morphological properties of the objects do not.

More than just improving the reconstructions, multispectral acquisitions can be used to extract spectral information from the biological samples [Mo et al., 2009, Allier et al., 2017, Mariën et al., 2020]. Indeed, some biological materials, like Gram stained bacteria, the discrimination is based on their color which can be sometimes elusive. Thus multispectral, quantitative and repeatable information is required.

Thus, by exploiting the redundancy between the acquisitions, multispectral reconstructions provides less "prior-driven" and more "data-driven" reconstructions while reconstructing spectral information of the samples that may help the diagnosis.

In this chapter, we discuss the problem of using co-localization prior in digital in-line and multispectral holographic reconstructions to exploit the redundant information of the data. Using IPA, we reconstruct jointly the 2D transmittance planes equivalent to the objects at several wavelengths.

In the Preliminaries section, we describe the regularization term prior to consider co-localization of the objects in the multi-spectral data. In the second section, we discuss the efficiency of using this prior in our context and the robustness of these method to badly registered data.

A Preliminaries: Regularization colocalization term in multi spectral imaging

Let us consider a sample modeled by a 2D complex transmittance plane $\underline{\boldsymbol{t}}_\lambda$ for all wavelength λ of $\boldsymbol{\Lambda}$. For an infinite aperture and aberration free imaging system, this model is the squared modulus of the convolution between the Rayleigh-Sommerfeld propagation kernel $\underline{\boldsymbol{h}}^{\mathrm{RS}}_{z,\lambda}$ and the transmittance plane $\underline{\boldsymbol{t}}_\lambda$ [Goodman, 2004]:

$$\boldsymbol{m}^{\mathrm{NP}}_\lambda(\underline{\boldsymbol{t}}_\lambda) = \left|\underline{\boldsymbol{h}}^{\mathrm{RS}}_{z,\lambda} * \underline{\boldsymbol{t}}_\lambda\right|^2 \tag{7.1}$$

Note that the Rayleigh-Sommerfeld depends on λ as does the Mie model. Figure 7.1 shows the diffraction pattern of a bead depending on the wavelength. The accurate knowledge of λ is then crucial to model the image formation. In this manuscript, we will

suppose this parameter is accurately known, though it could also be calibrated [Flasseur et al., 2017b].

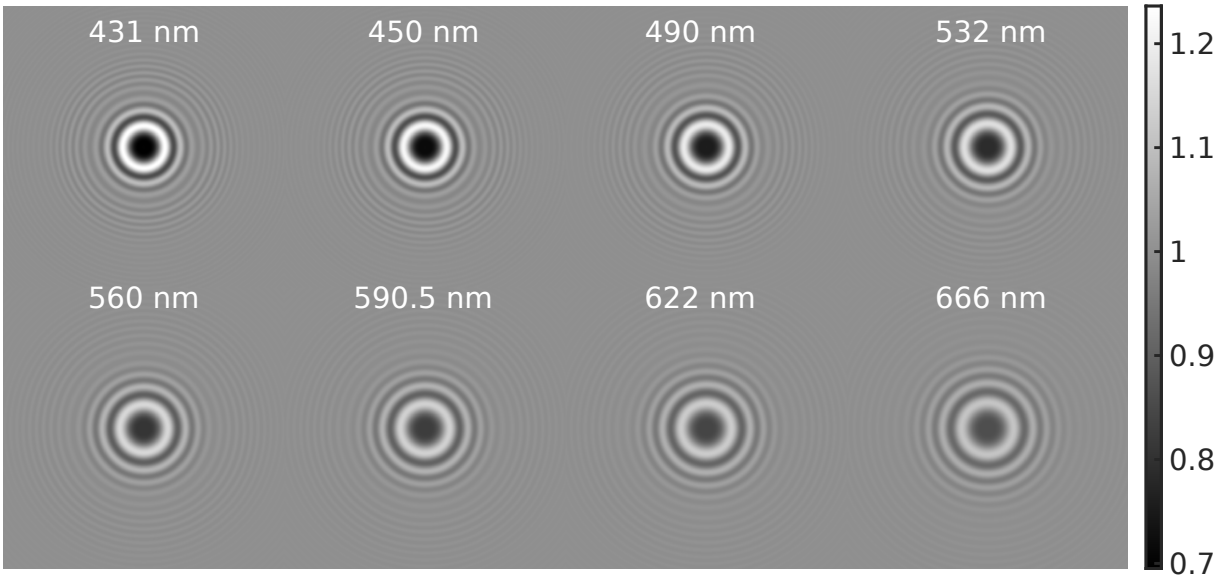

Figure 7.1: Diffraction patterns of a 1µm diameter silica beads ($n = 1.45$) diffraction pattern at distance $z = 10\mu m$ in an oil immersion medium ($n_0 = 1.519$)

Since multispectral acquisitions consist in recording the diffraction patterns of the same objects with multiple illumination wavelengths, the expected reconstructed objects should have the same position independently of the wavelength. This prior can thus be added in the reconstruction algorithm to exploit full multispectral information in order to remove the twin-image. However depending on the object to reconstruct this prior can be considered using several methods:

- If the objects are gray, which means their absorption is not varying with λ, then it is possible to reconstruct only one modulus map $\boldsymbol{A}$ instead of N_Λ modulus maps $\{A_\lambda\}_{\lambda\in\Lambda}$ where N_Λ is the number of wavelengths used for the acquisitions. In this case:
$$\forall\lambda \in \Lambda,\ \underline{\boldsymbol{t}}_\lambda(x,y) = A(x,y)e^{i\Phi_\lambda(x,y)} \tag{7.2}$$
where $\boldsymbol{\Phi_\lambda}$ is the phase to reconstruct for each λ. The prior is in this case directly added in the image formation model.

- If the objects have a refractive index without any dispersion over λ, then it is possible to reconstruct only the optical path difference induced by the objects which corresponds to one map for all λ. In this case:
$$\forall\lambda \in \Lambda,\ \underline{\boldsymbol{t}}_\lambda(x,y) = A_\lambda(x,y)e^{i\frac{2\pi}{\lambda}\mathrm{OPD}(x,y)} \tag{7.3}$$
where OPD is the optical path difference for each λ. The prior is in this case added in the image formation model.

- When none of these assumptions can be done on the objects, then the reconstruction of the absorption and of the phase of the sample must be performed for each wavelength. Thus,
$$\forall\lambda \in \Lambda,\ \underline{\boldsymbol{t}}_\lambda(x,y) = A_\lambda(x,y)e^{i\Phi_\lambda(x,y)} \tag{7.4}$$

Even if the refractive index varies with the wavelength, the phase-shifts introduced by the objects are located at the same position. Thus co-localization of the edges of the phase maps and absorption maps along all wavelengths is added as a regularization term.

The biological samples we are studying are neither gray nor dispersive, thus, the co-localization of the reconstructed objects a prior is added as a regularization term.

Based on a structured norm [Fornasier and Rauhut, 2008], the multi-wavelength total variation regularization term $\mathscr{R}_{\mathbf{\Lambda}}$ promotes the colocalization the edges of the multi-wavelength transmittance planes and has been successfully used in lens-less multispectral holography [Herve et al., 2018].

Mean square error definition

The multi-wavelength total variation regularization term can be expressed as the relaxed L1-norm of the sum between the gradients of the real and imaginary part of the reconstructed transmittance planes $\underline{\boldsymbol{t}}_{\mathbf{\Lambda}}$ over $\lambda \in \mathbf{\Lambda}$:

$$\mathscr{R}_{\mathbf{\Lambda}}(\underline{\boldsymbol{t}}_{\mathbf{\Lambda}}) = \sum_{i,j} \sqrt{\sum_{\lambda \in \mathbf{\Lambda}} \nabla_{i,j} \Re(\underline{\boldsymbol{t}}_{\mathbf{\Lambda}})^2 + \nabla_{i,j} \Im(\underline{\boldsymbol{t}}_{\mathbf{\Lambda}})^2 + \epsilon^2} \tag{7.5}$$

where ϵ is a small valued and positive coefficient used to make Equation 7.5 differentiable and prevent division by 0 in the gradient derivation.

Figure 7.2 illustrates the principle of the multi-spectral total variation regularization term by presenting the regularization value for co-localized and non co-localized examples. Indeed on the left part of the graphs the objects are localized at the same position in terms of real and imaginary part but also along the wavelength stack. Thus, the x and y edges of these objects are also co-localized. The inner sum between the real and imaginary parts promote co-localization of the edges for one wavelength and then the sum over all the wavelength ensure that for all wavelengths the real and imaginary parts are co-localized. As illustrated with this figure when the reconstructed planes are not co-localized the regularization term gets bigger, which will penalize non-colocalized solutions.

B Multiwavelength reconstructions in holography

B.1 Including colocalization a priori in the reconstructions

To improve the reconstructions, multispectral holography takes advantage of spatial redundancy in multiple acquisitions $\boldsymbol{d}_{\mathbf{\Lambda}} = \{\boldsymbol{d}_\lambda\}_{\lambda \in \mathbf{\Lambda}}$.

As presented in Chapter 2, the multispectral reconstructions are performed using a "calibration/reconstruction" scheme based on a parametric IPA for the calibration and a regularized IPA for the reconstruction of the sample. To simplify the reconstructions in this chapter, the calibration step will be performed by considering an aberration-free system.

During the calibration step, it is supposed that the position and the radius of the objects should not change with λ. Thus, the parameters of the beads $\{x, y, z, r\}$ are

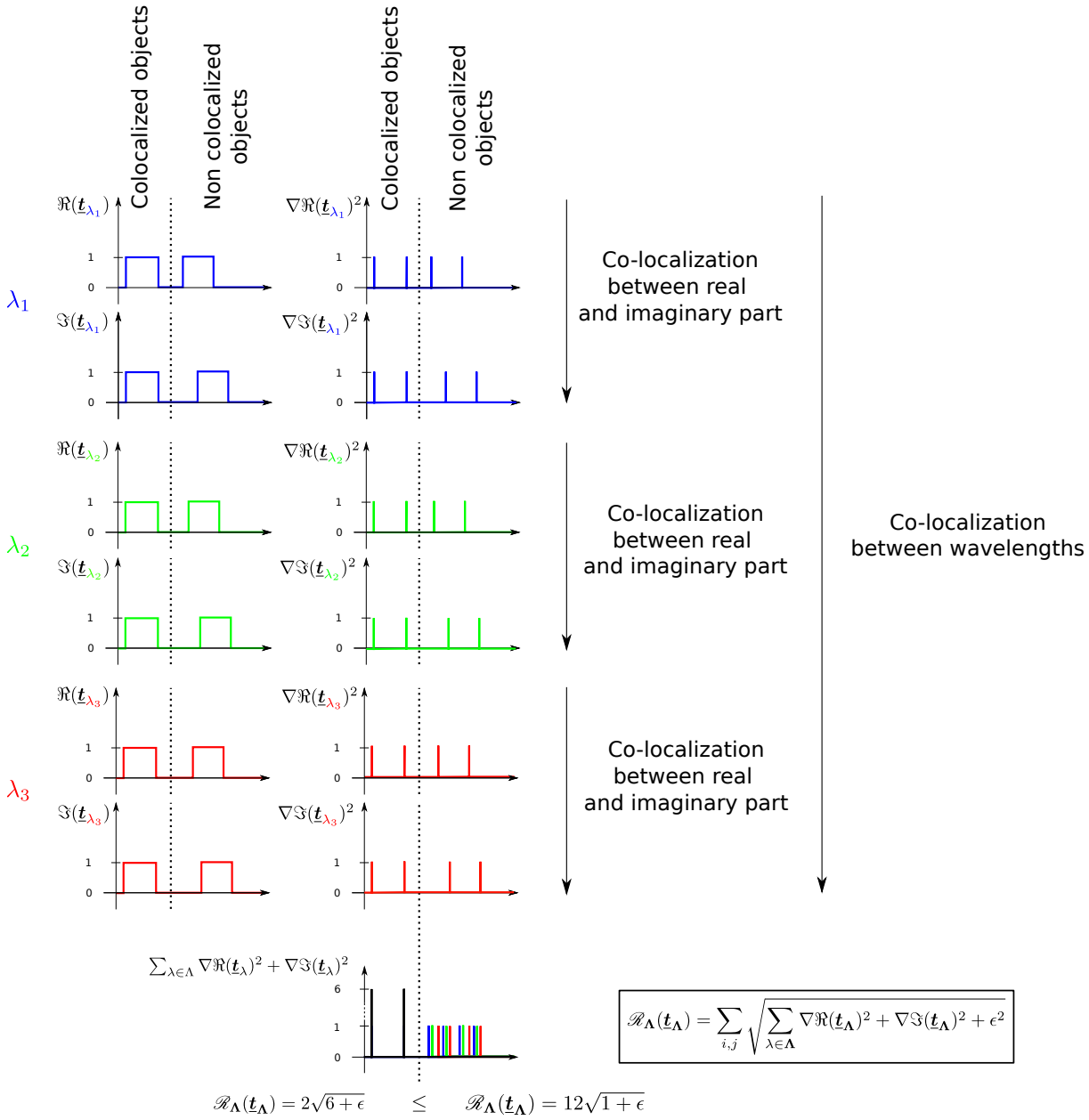

Figure 7.2: Principle of the multiwavelength total variation term. ϵ is a small valued and positive hyperparameter.

estimated using only one wavelength λ_{ref} as in Chapter 2.

In multispectral reconstructions, the regularization term introduced in Section A can be used to promote co-localization of the objects along all wavelengths. The inverse problem to solve for the reconstruction of the multispectral data is then expressed as:

$$\underline{\boldsymbol{t}}_{\boldsymbol{\Lambda}}^{\dagger} = \underset{\underline{\boldsymbol{t}}_{\Lambda} \in \mathbb{T}}{\operatorname{argmin}} \ \mathscr{L}_{\mu}(\underline{\boldsymbol{t}}_{\boldsymbol{\Lambda}}) \tag{7.6}$$

$$\text{with } \mathscr{L}_{\mu}(\underline{\boldsymbol{t}}_{\boldsymbol{\Lambda}}) = \sum_{\lambda \in \Lambda} \|\boldsymbol{d}_{\lambda} - \boldsymbol{m}^{\text{NP}}(\underline{\boldsymbol{t}}_{\boldsymbol{\Lambda}})\|^2_{\boldsymbol{W}_{\lambda}} + \mu \mathscr{R}_{\boldsymbol{\Lambda}}(\underline{\boldsymbol{t}}_{\boldsymbol{\Lambda}}) \tag{7.7}$$

where μ is a regularization hyperparameter and where $\mathbb{T}$ represents reconstructions constraints. In our experiment, we chose $\mathbb{T}$ so that the reconstructed objects are not emmissive *i.e.* $\forall \lambda \in \boldsymbol{\Lambda}, |\underline{\boldsymbol{t}}_{\lambda}| \leq 1$. Note that $\boldsymbol{W}_{\lambda}$, the inverse of the covariance matrix of the noise is varying with λ. Since the power of the light is different for each wavelength, the SNR may be different. It is then necessary to take this into account in the data fidelity term of the cost function by using a different covariance matrix for each wavelength. To perform this minimization a FISTA algorithm is used [Beck and Teboulle, 2009].

To increase the quantitativity of these reconstructions, the dispersion of the refractive index over λ must be taken into account. The dispersion law of the immersion oil and silica are presented on Figure 7.3.

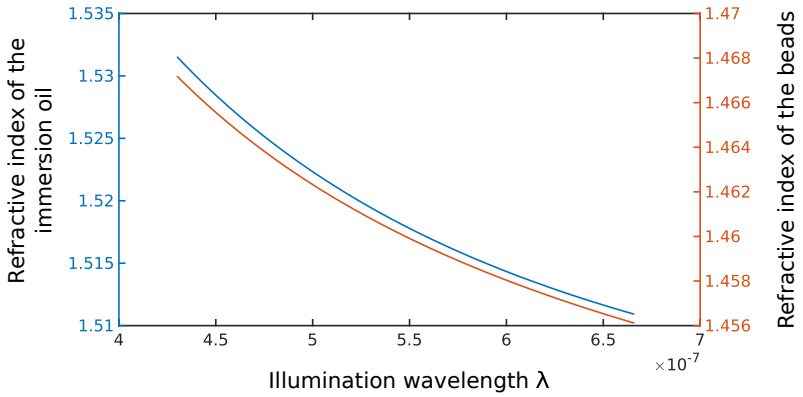

Figure 7.3: Refractive index of the immersion oil and of silica as functions of the wavelength [1]

B.2 Tuning of the regularization hyperparameter

To tune the regularization hyperparameter μ, the method proposed in Chapter 6 is adapted for multi-wavelength reconstructions. In this context, the quality criteria $\mathscr{Q}$ used to tune the hyperparameter is based on a cost function that minimizes the discrepancy between the reconstructed transmittance planes $\underline{\boldsymbol{t}}_{\boldsymbol{\Lambda}}^{\dagger}(\mu)$ and the ground truth $\underline{\boldsymbol{t}}_{\boldsymbol{\Lambda}}^{\text{GT}}$ back-propagation of the Mie model (which parameters are estimated by parametric IPA)

[1] `https://refractiveindex.info/?shelf=glass&book=fused_silica&page=Malitson,https://www.cargille.com/available-refractive-indices-sds-datasheets/`

for all wavelengths. The bi-level inverse problem to solve is written as follows :

$$\begin{aligned}
&\mu^\dagger = \underset{\mu\in\mathbb{M}}{\operatorname{argmin}}\, \mathscr{Q}(\underline{\boldsymbol{t}}^\dagger_{\boldsymbol{\Lambda}}(\mu)) \text{ (Upper-level)} \\
&\text{subject to} \\
&\underline{\boldsymbol{t}}^\dagger_{\boldsymbol{\Lambda}}(\mu) = \underset{\underline{\boldsymbol{t}}_{\boldsymbol{\Lambda}}\in\mathbb{T}}{\operatorname{argmin}}\, \mathscr{L}_\mu(\underline{\boldsymbol{t}}_{\boldsymbol{\Lambda}}) \text{ (Lower-level)} \\
&\text{where}
\end{aligned} \tag{7.8}$$

$$\mathscr{Q}(\underline{\boldsymbol{t}}^\dagger_{\boldsymbol{\Lambda}}(\mu)) = \sum_{\lambda\in\Lambda} \|\underline{\boldsymbol{t}}^{\mathrm{GT}}_{\boldsymbol{\Lambda}} - \underline{\boldsymbol{t}}^\dagger_{\boldsymbol{\Lambda}}(\mu)\|^2_{\mathbf{Mask}_{\mathrm{Beads}}}, \tag{7.9}$$

$$\text{and } \mathscr{L}_\mu(\underline{\boldsymbol{t}}_{\boldsymbol{\Lambda}}) = \sum_{\lambda\in\Lambda} \|\boldsymbol{d}_\lambda - \boldsymbol{m}(\underline{\boldsymbol{t}}_{\boldsymbol{\Lambda}})\|^2_{\boldsymbol{W}_\lambda} + \mu\mathscr{R}_{\boldsymbol{\Lambda}}(\underline{\boldsymbol{t}}_{\boldsymbol{\Lambda}}), \tag{7.10}$$

where $\mathbb{M}$ represent optimization constraints on the regularization hyperparameter and $\mathbf{Mask}_{\mathrm{Beads}}$ is a segmentation of the region of the beads. The minimization of this bi-level problem is performed using a Powell method [Powell, 2015].

Figure 7.4 represents the evolution of the quality criterion $\mathscr{Q}$ as a function of μ and three reconstructions on biological samples that contains calibration beads represented as false color (see Appendix B). When the regularization hyperparameter is under-estimated, the reconstructions are under-regularized, *i.e.* the models fits the noise. Reconstructions artifacts can be observed in the reconstructed modulus and phase images. These reconstructions artifact are characterized by a green halo in the phase reconstruction and a noisy modulus image. In the contrary when the regularization hyperparameter is over-estimated, the reconstructions are over-regularized, *i.e.* the model fits the data less but promote the prior. Almost all the objects disappear and the reconstruction image are blurry in that case. However using the optimum of the quality criterion as suggested in Chapter 6, the reconstructions are sharper and objects are closer to their expected shape. Hopefully the quantitativity of the reconstruction are also enhanced due to the quantitative quality criterion $\mathscr{Q}$ we used.

B.3 Results

In this section, we first apply the proposed reconstruction method on experimental holograms of a biological sample in which calibration beads are inserted. We compare our results with a regularized inversion for each wavelength in the experimental experimental case. Finally we discuss the effects of the co-localization a priori in multispectral reconstructions by testing the limits of the approach on simulations.

B.3.1 Reconstructions on experimental data

The experimental parameters are provided in Appendix A Section C. In this section $\boldsymbol{\Lambda} = \{431 \text{ nm}, 450 \text{ nm}, 490.5 \text{ nm}, 532 \text{ nm}, 560 \text{ nm}, \ 590\text{nm}, \ 622\text{nm}, \ 666\text{nm}\}$, thus $N_\lambda = 8$. The holograms to be reconstructed were defocused of approximately 12μm from the focus position.

They were reconstructed using parametric IPA on beads to find the correct propagation distance z to be used in the regularized reconstructions. As mentioned in Section B.1, we suppose in this chapter that the parameters $\{x, y, z, r\}$ do not vary with λ. Thus,

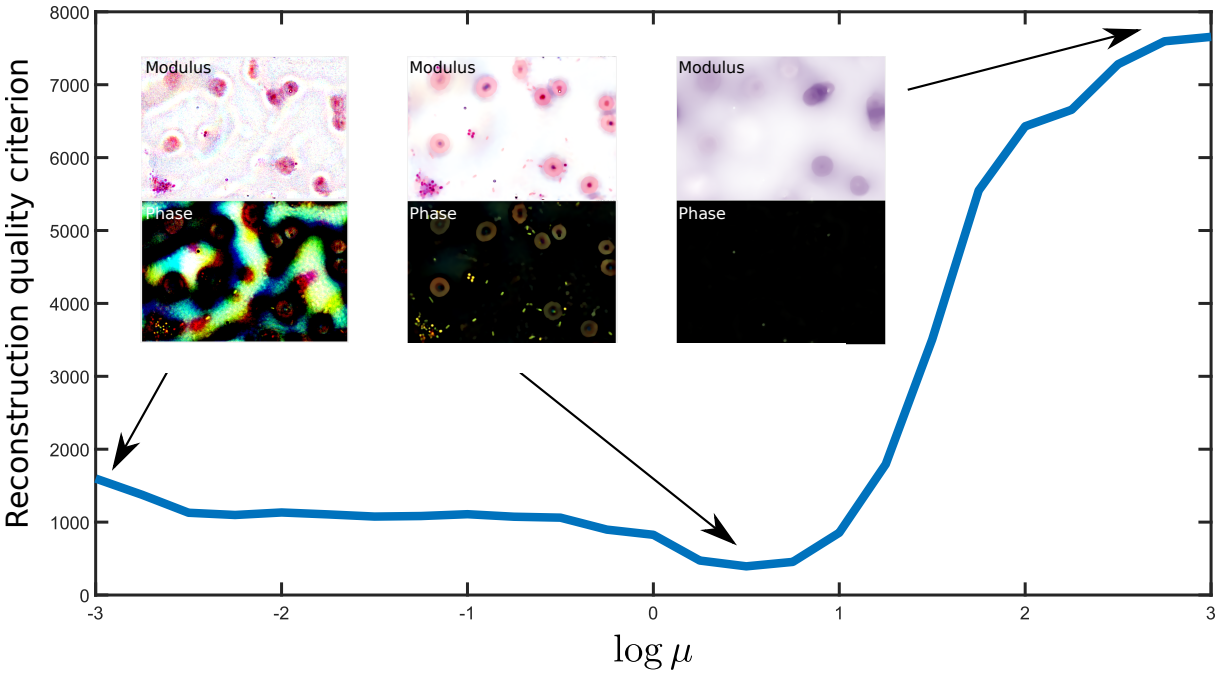

Figure 7.4: Evolution of the reconstruction quality criterion $\mathscr{Q}$ as a function of $\log \mu$ ($\epsilon = 10^{-3}$).

estimation of the propagation distance can be performed using only one acquisition at wavelength $\lambda_{\text{ref}} = 431\text{nm}$. The reconstruction workflow of these approaches is detailed in Chapter 2.

For each hologram, the reconstructions were performed using either the co-localization prior proposed in A or by reconstructing each wavelength independently using a complex hyperbolic total variation regularization prior. The abbreviations Multi-λ-Col (standing for co-localized), and Multi-λ-NotCol(standing for not co-localized) will be used in the following. In this section both performances of algorithm Multi-λ-NotCol and Multi-λ-Col are studied on experimental data.

Figure 7.5 presents the reconstruction results using both methods. The reconstructed absorption color map can be compared with the RGB white light acquisition. The reconstructed objects have a similar shape to the one acquired with white light when the co-localization of the objects on the reconstructed plane is used. When this prior is not considered (Multi-λ-Col reconstructions), the reconstructed objects do not have the same shapes and more critically some of the objects almost disappear in the absorption maps. Moreover the Multi-λ-Col absorption color map provides a better reproducibility on the color of the bacteria since same bacteria types share the same colors (round-shaped bacteria should be purple in this sample, while rod-shaped bacteria should be pink).

Based on the absorption reconstructions, the twin image is reduced with the Multi-λ-NotCol algorithm while twin-image artefacts are still visible on the Multi-λ-NotCol reconstructions. These artefacts can even make some bacteria difficult to detect.

Based on the phase reconstructions, both methods provide a completely different result. Since no ground truth has been measured for the phase, it is difficult to know which one is the most quantitative. However Multi-λ-Col reconstructions are more reproducible in the field of view. The green halo that can be observed with Multi-λ-NotCol algorithm

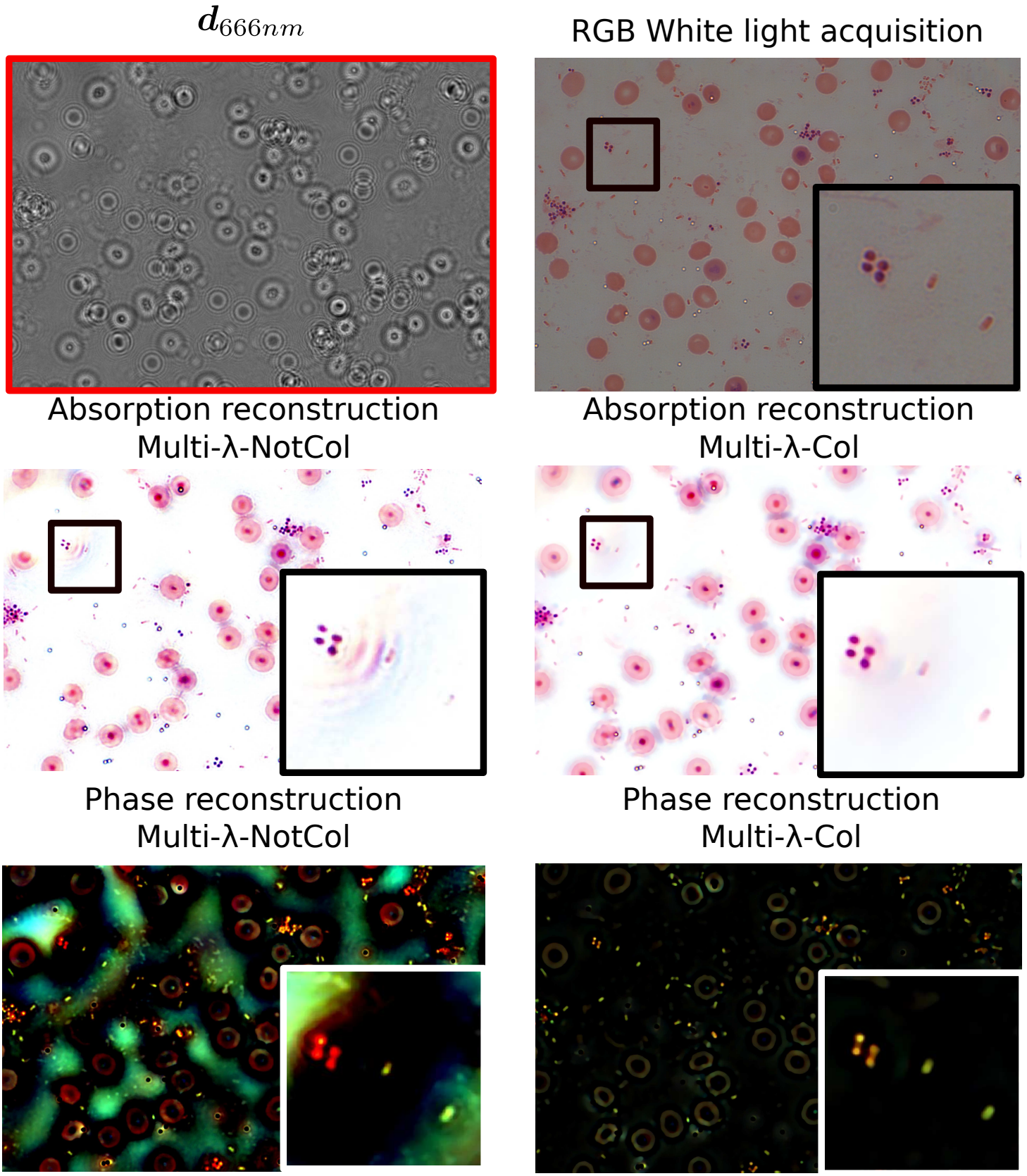

Figure 7.5: Phase and absorption multispectral reconstructions compared to RGB white light acquisition. $\boldsymbol{d}_{666nm}$ is one hologram (*i.e.* data) at 666nm.

is completely cleaned when the co-localization algorithm is taken into account. This halo was a critical issue due to its color, similar to the bacteria, that could thus causes segmentation errors. Using the co-localization prior in the reconstruction algorithm provides thus better reproducibility and more realistic reconstruction both in modulus and phase as well as better elimination of the twin-image.

To highlight the quantitative properties of the reconstructions, Figure 7.6 shows the profile of the reconstructions using both methods for four wavelengths. The modulus and phase profiles along each wavelength are badly colocalized with the Multi-λ-NotCol algorithm. Indeed, some phase shifts and absorption are visble at certain wavelength while being null for others. Even though, the refractive indexes of the biological objects may vary with the wavelength, this result is less physically probable. The Multi-λ-Col reconstructions provides reconstructions that are more colocalized along the wavelengths and thus more physically probable. Moreover the reconstructed objects are smoother and it becomes easy to segment the objects from the background. However it should be noted that even if the co-localization of the objects along the wavelength is better with Multi-λ-Col reconstructions, the sample seems a bit shifted from one wavelength to the other. The shifts in the reconstructions are due to bad registrations of the data. The effect of bad registrations on the quantitativity of the reconstruction with a co-localization prior will be explored in Section B.3.2 on calibration beads simulations.

B.3.2 Robustness of the method to badly registered data

For a better understanding of the colocalization errors in the data, we chose to perform simulations. A bead of $1\mu m$ diameter is simulated at the center of the field with a defocus distance of 12 μm with the Lorenz-Mie model (see Chapter 2). The refractive index of the bead and the medium has been chosen to correspond to the dispersion law of the refractive index of silica and of the immersion oil as represented on Figure 7.3. In this simulation experiment, only 3 wavelengths are considered: $\mathbf{\Lambda} = \{430\ nm, 532\ nm, 666\ nm\}$. The other experimental parameters are the same as the one used for the Section B.3.1. For more realistic simulations, a white Gaussian noise η was added to the simulated holograms, which led to a Signal-to-Noise Ratio (SNR) of 4(SNR $= \frac{\Delta \boldsymbol{m}}{2\sigma_\eta}$, where $\Delta \boldsymbol{m}$ is the peak-to-peak amplitude of the model).

A mosaic of 5×5 in-line beads 512×512 pixels holograms is simulated with registration error as presented in Figure 7.7. The indicated shifts correspond to the shift between the 430 nm and the 532 nm holograms which also corresponds to the shifts between the 532 nm and the 622 nm holograms. To highlight the effect of the errors on the registration of the data, the diffraction pattern obtained for each wavelength was normalized so that they correspond to one of the channel of the RGB image. This normalization is not applied in the reconstructions but only for display.

In this experiment the propagation distance z is considered to be known. To perform the Multi-λ-Col and the Multi-λ-NotCol reconstructions, a FISTA algorithm is used. As silica beads are mostly transparent objects, the quantitativity of the reconstructions is assessed on the phase. Figure 7.8 shows the profile of the phase of the regularized reconstructions with the Multi-λ-Col and the the Multi-λ-NotCol methods.

As seen on Figure 7.8 the Multi-λ-Col algorithm provides smoother and better quantitativity results on the phase of the beads due to the more physical nature of the regularization term. However when reconstructing badly registered data, the prior of co-localization

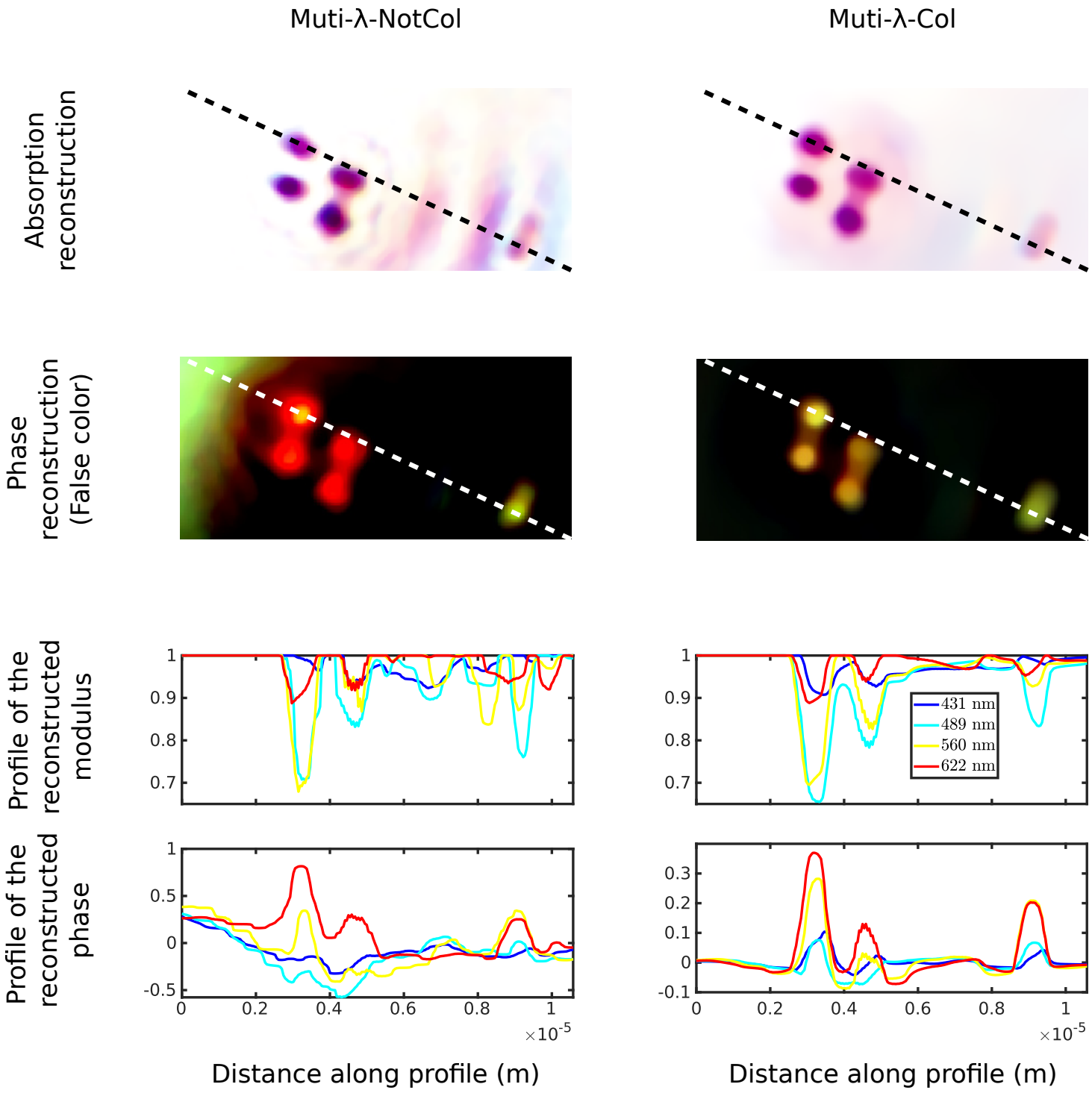

Figure 7.6: Profiles of the reconstructions using Multi-λ-NotCol and Multi-λ-Col on experimental data

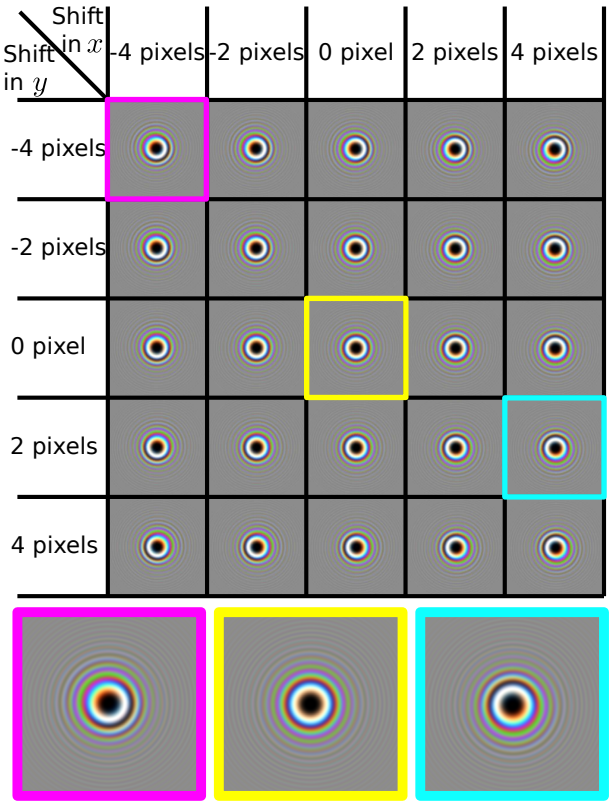

Figure 7.7: RGB simulation of holograms with various wavelength-dependent shifts

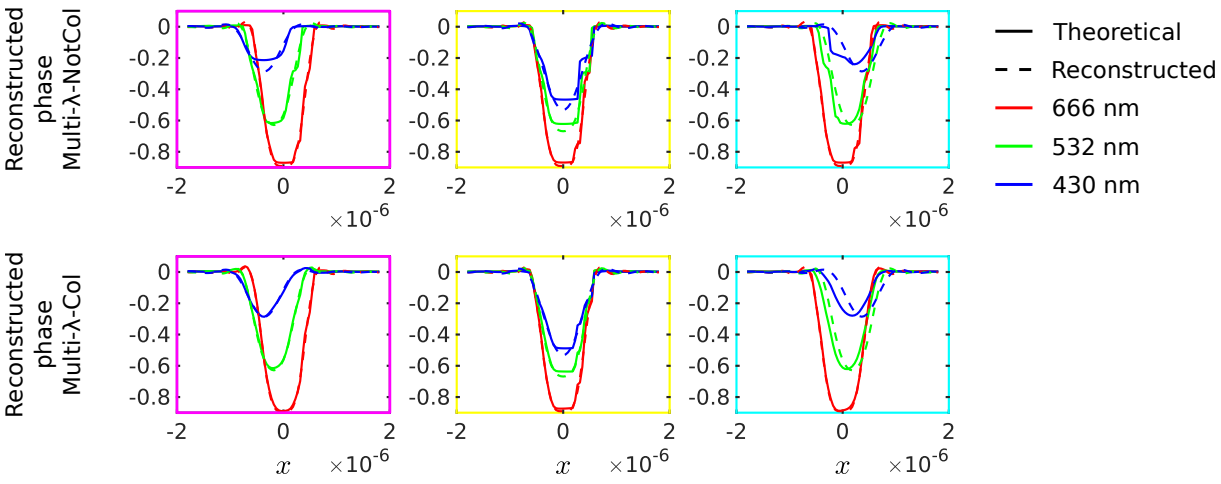

Figure 7.8: Profiles of the phase reconstructions for 3 wavelengths and 3 different shifts. Comparison between the Multi-λ-NotCol and Multi-λ-Col reconstructions

of the objects is not valid anymore, thus reconstructions are biased as seen on the cyan profile. The object is shifted to promote the regularization term in the cost function, *i.e.* the objects are shifted so that their co-localization is improved. Note that when the registration is even worse (magenta case) the reconstruction algorithm performs quantitative results that are not biased due the prior but that are shifted depending on the wavelength. Indeed, the regularization term gets bigger but promoting it would reduce the data fidelity too much. Thus the regularization hyperparameter can be seen as a balance between having co-localized reconstructions or fitting the data.

The Multi-λ-Col algorithm is then sensible to badly registered data depending on the chosen reconstruction hyperparameter. It is thus important to ensure that the multispectral data are correctly registered together. However the registration of the experimental data is not a rigid transformation. Indeed the registration errors are mostly due to chromatic aberrations that varies in the field of view. To perform quantitative and co-localized reconstructions one must take these chromatic aberrations into account.

C Conclusion

In conclusion, the colocalization of the objects for all wavelength is a physical prior that can be added to the regularized inversion of multispectral holograms to provide more physical and quantitative reconstructions of biological samples. We demonstrated that the reconstructions are quantitatively improved in phase and modulus. Due to the spectral colocalization, the biological samples like bacteria can then be spectrally characterized. This spectral information can then help to discriminate biological objects. With this a priori the twin-image is better suppressed. The regularization is applied on the whole multispectral transmittance stack and thus does not require regularization hyperparameters for each wavelength. The tuning of the regularization hyperparameter can be done automatically in multispectral context using an adapted version of the method proposed in Chapter 6.

However, the quality of the reconstructions depends on the registration of the data. Geometric and chromatic aberrations change the propagation model and may introduce distortions of the holograms from one wavelength to another. Therefore, geometric and chromatic aberrations must be taken into account to increase both the quantitativity and colocalization, in order to have a better multiwavelength reconstruction. It is the subject of next chapter.

CHAPTER 8

Improving multispectral reconstructions by taking into account chromatic aberrations

Abstract

Multispectral acquisitions provide quantitative reconstructions of the transmittance plane of the sample by using colocalization priors. However, these priors require a good registration between the data. As mentioned in Chapter 4 misalignments in the optical system or chromatic aberrations can have a significant impact on the image formation model. We focus in this chapter on the use of calibration objects for the estimation of chromatic aberrations. These estimations are then used to reconstruct multispectral holograms. In this chapter, we present a chromatic aberrations model estimation. Then we propose to reconstruct experimental multispectral data. At last a discussion on the reconstructed spectral information is provided.

Introduction

Multispectral reconstructions aim at increasing the quantitativity of the spectral reconstructions by considering a more physical prior based on the co-localization of the objects in a multispectral data stack. As mentioned in Chapter 7, this prior is highly sensitive to bad registrations between the data. Thus, a preliminary study, that should be performed before the reconstruction of multispectral images, consists in checking that the objects are colocalized with the wavelength.

The estimation, for each wavelength, of the position of calibration beads is a simple and accurate way to measure accurately the registrations errors. Figure 8.1 illustrates several calibration beads in a whole field of view that have been reconstructed using parametric inverse problems approach (as described in Chapter 3). Their 3D positions have been represented depending on the wavelength of the acquisition.

First, it should be noticed that the estimated propagation distance z highly depends

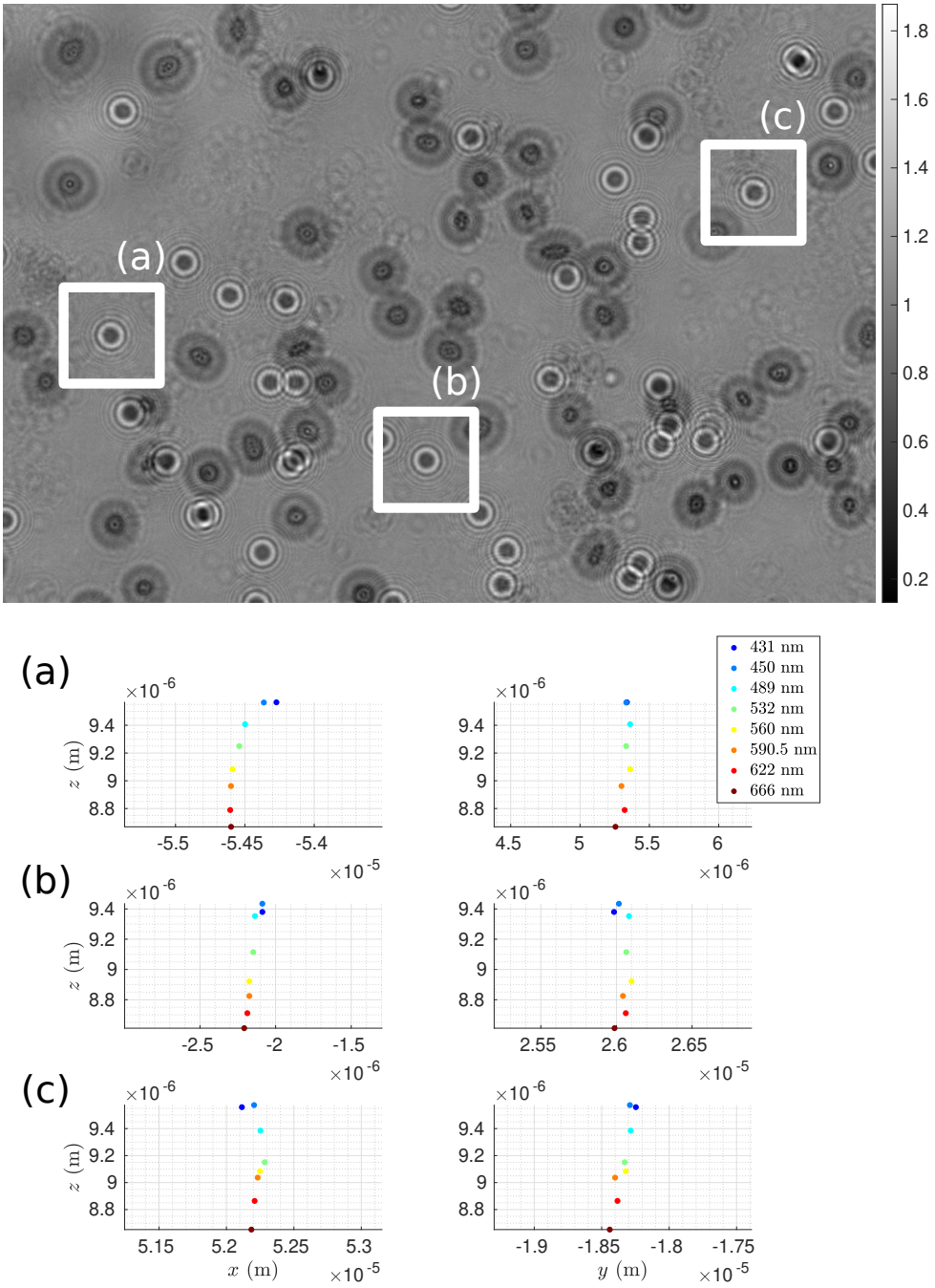

Figure 8.1: Estimated 3D positions of the calibration objects as a function of the wavelength

on the wavelength. Indeed, since the refractive index of the optics is evolving with the wavelength, a longitudinal aberration can be observed. This longitudinal aberration may introduce error in the reconstructions. However it can be accounted for by using a different propagation distance z_λ for each wavelength λ.

Lateral chromatic aberrations can also be observed, these aberrations are critical since they introduce lateral shifts of the objects that depend on the wavelength. Here, the origins of the aberrations are mainly due to the dispersion of the refractive index of the optics and to alignment errors in the digital holographic microscopy setup. Due to the

shifts introduced by these aberrations, the prior consisting in supposing the objects to be colocalized is compromised.

The lateral shifts of the beads from one wavelength to another are not uniform in the field of view. This problem is the same as presented in Chapter 4. The PSF is varying in the field of view and with the wavelength. Thus, rigid registration of the data is not possible.

We propose in this chapter a similar method to the one applied in Chapter 4 to take into account chromatic aberrations in multispectral reconstructions. This method is based on the estimation of Zernike coefficients on calibration beads for each wavelength. The reconstruction of the sample is then performed by using image formation models that take into account these chromatic aberrations.

In the following section, we detail this method. Then, we present the results on multispectral experimental data reconstructions of samples containing a mixture of calibration beads and biological objects.

A Chromatic aberrations model

As presented in Chapter 2 ,the diffraction pattern of a spherical bead is modeled by the Lorenz-Mie model which depends on the set of bead parameters $\boldsymbol{\vartheta}_\lambda = \{x, y, z_\lambda, r, n_\lambda\}$, where x, y, z_λ corresponds to the 3D position, r is the radius and n_λ is the refractive index. Note that the propagation distance z_λ and the refractive index n_λ depend on the wavelength. $\boldsymbol{\alpha}_\lambda = \{\alpha_n^m(\lambda)\}$ is a vector of aberration parameters that varies with the wavelength. In this context, the model can be expressed as a Mie model that has been convoluted by a PSF correction that depends on α_λ. Thus, in the multispectral case Equation 4.3 can be written:

$$\boldsymbol{m}_\lambda^{\mathrm{P}}(\boldsymbol{\vartheta}_\lambda, \boldsymbol{\alpha}_\lambda) = \left| \mathscr{F}^{-1}\left[\underline{\widetilde{p}}(\boldsymbol{\alpha_\lambda}) \odot \underline{\widetilde{\boldsymbol{a}}}_\lambda^{\mathrm{Mie}}(\boldsymbol{\vartheta}_\lambda) \right] \right|^2 \tag{8.1}$$

with

$$\underline{\widetilde{p}}(\kappa_x, \kappa_y, \boldsymbol{\alpha}_\lambda) = e^{i\left[\sum\limits_{n,m} \alpha_n^m(\lambda) \boldsymbol{Z}_n^m(\kappa_x, \kappa_y)\right]} \tag{8.2}$$

Accurate estimates of the aberrations and beads parameters can be obtained by maximizing a least squares cost function as proposed in Chapter 4. In the context of multispectral reconstructions, this parameters estimation must be performed for each wavelength:

$$\left\{ \boldsymbol{\vartheta}_\lambda^\dagger, \boldsymbol{\alpha_\lambda}^\dagger \right\} = \underset{\boldsymbol{\vartheta}_\lambda \in \mathbb{C}, \boldsymbol{\alpha} \in \mathbb{D}}{\operatorname{argmin}} \| \boldsymbol{d}_\lambda - \boldsymbol{m}_\lambda^{\mathrm{P}}(\boldsymbol{\vartheta}_\lambda, \boldsymbol{\alpha}_\lambda) \|_{\boldsymbol{W}}^2 \tag{8.3}$$

where $\mathbb{C}$ and $\mathbb{D}$ are optimization constraints. Since the (x, y) position and the radius r of the beads are the same for each wavelength, they are only estimated for one wavelength $\lambda_{\mathrm{Ref}} = 431\mathrm{nm}$. Aberrations parameters corresponding to lateral shifts $\{\alpha_1^1(\lambda_{\mathrm{Ref}}), \alpha_1^{-1}(\lambda_{\mathrm{Ref}})\}$ are set to 0 for the calibration of $\boldsymbol{\alpha}_{\lambda_{\mathrm{Ref}}}$. However, for all the other wavelengths, the aberrations may introduce shifts of the acquisition, thus $\{\alpha_1^1(\lambda), \alpha_1^{-1}(\lambda)\}$ are estimated. As previously done in Chapter 4 Section B.1.1, the piston coefficient α_0^0 is set to 0.

Once the aberrations are modeled, they are taken into account to better reconstruct the modulus and the phase of the objects of interest. In order to account for aberrations

in the image formation model, an aberrated PSF model is considered:

$$\widetilde{\underline{\boldsymbol{h}}_z}(\boldsymbol{\alpha}_\lambda, \lambda) = \widetilde{\underline{p}}(\boldsymbol{\alpha}_\lambda) \odot \widetilde{\underline{\boldsymbol{h}}_z}^{\mathrm{RS}}(\lambda) \tag{8.4}$$

Thus, the aberration corrected non-parametric models $\boldsymbol{m}_\lambda^{\mathrm{NP}}$ are expressed as:

$$\boldsymbol{m}_\lambda^{\mathrm{NP}}(\underline{\boldsymbol{t}}_\lambda, \boldsymbol{\alpha}_\lambda) = \left| \underline{\boldsymbol{h}}_z(\boldsymbol{\alpha}_\lambda, \lambda) * \underline{\boldsymbol{t}}_\lambda \right|^2 \tag{8.5}$$

To reconstruct the multispectral transmittance planes using this model, the following cost function must be minimized:

$$\mathscr{L}_{\boldsymbol{\mu}}(\underline{\boldsymbol{t}}_{\boldsymbol{\Lambda}}) = \sum_{\lambda \in \Lambda} \| \boldsymbol{d}_\lambda - \boldsymbol{m}_\lambda^{\mathrm{NP}}(\underline{\boldsymbol{t}}_\lambda, \boldsymbol{\alpha}_\lambda) \|^2_{\boldsymbol{W}_\lambda} + \mu \mathscr{R}_{\boldsymbol{\Lambda}}(\underline{\boldsymbol{t}}_{\boldsymbol{\Lambda}}) \tag{8.6}$$

where $\boldsymbol{\Lambda}$ is the set of the wavelengths and $\mathscr{R}_{\boldsymbol{\Lambda}}$ is the colocalization term defined in Chapter 7. The optimization domain is restricted to the unitary disk corresponding to a non-emissive object hypothesis. A FISTA algorithm is used to perform this minimization [Beck and Teboulle, 2009].

Since the PSF is varying in the field of view, the hologram has been divided into 512x512 pixels patches. These patches overlap with an overlap ratio of 0.5. Each of these patches have been reconstructed independently using its own PSF. After reconstruction, only the 256x256 pixels central part of the patches is kept to avoid border effects. Then, all of the patches are mosaiced to produce a reconstruction of the whole field of view. Note that PSF interpolation is a well-studied subject and that further improvements of this method could be performed to reduce border effects in the reconstructions [Denis et al., 2011, Denis et al., 2015]

As mentioned, each patch is reconstructed using its own PSF. This PSF is computed using a locally weighted polynomial regression (LOWESS) of z_λ and $\boldsymbol{\alpha}_\lambda$. Thus, the uniformity of the distribution of the beads in the field of view may change the quality of the interpolation. This subject will not be covered in this Chapter.

B Reconstruction of experimental data by accounting for aberrations

In this section, we apply the proposed method on the same experimental data as the one used in Chapter 7. Figures 8.2 and 8.3 illustrate the reconstruction of the phase and the absorption of the sample and compare them with the Multi-λ-Col method proposed in Chapter 7. Figure 8.4 provides a zoom on these reconstructions. These figures show that the main improvement is in the phase reconstructions. With our method, the bacteria are more contrasted on a more uniform background. On these figures, it can be seen that similar bacteria types have similar reconstructed phase, *i.e.* the reconstruction are more uniform for one type of bacteria, thus, the repeatability of the method is increased. Moreover the shape of the absorption reconstruction is more similar to the phase reconstruction (cyan and magenta arrows). This can be explained by the use of the colocalization prior. Indeed, aberrations compromised this prior. For the same reason, objects that were reconstructed with the aberration correction are bigger than the ones reconstructed with Multi-λ-Col algorithm.

On bacteria clusters (green zone), the phase reconstructions are also improved. Bacteria that had almost disappeared in the phase with Multi-λ-Col reconstructions are now reconstructed with almost the same phase value as the isolated ones (orange arrows). On the absorption maps of bacteria clusters, it can also be seen that the twin-image artifacts have been reduced (green arrows).

At last this aberration correction provides better resolved reconstruction as seen in the blue zone. Two bacteria (yellow arrow) appeared as only one with the Multi-λ-Col phase reconstructions instead of two as observed with the proposed method.

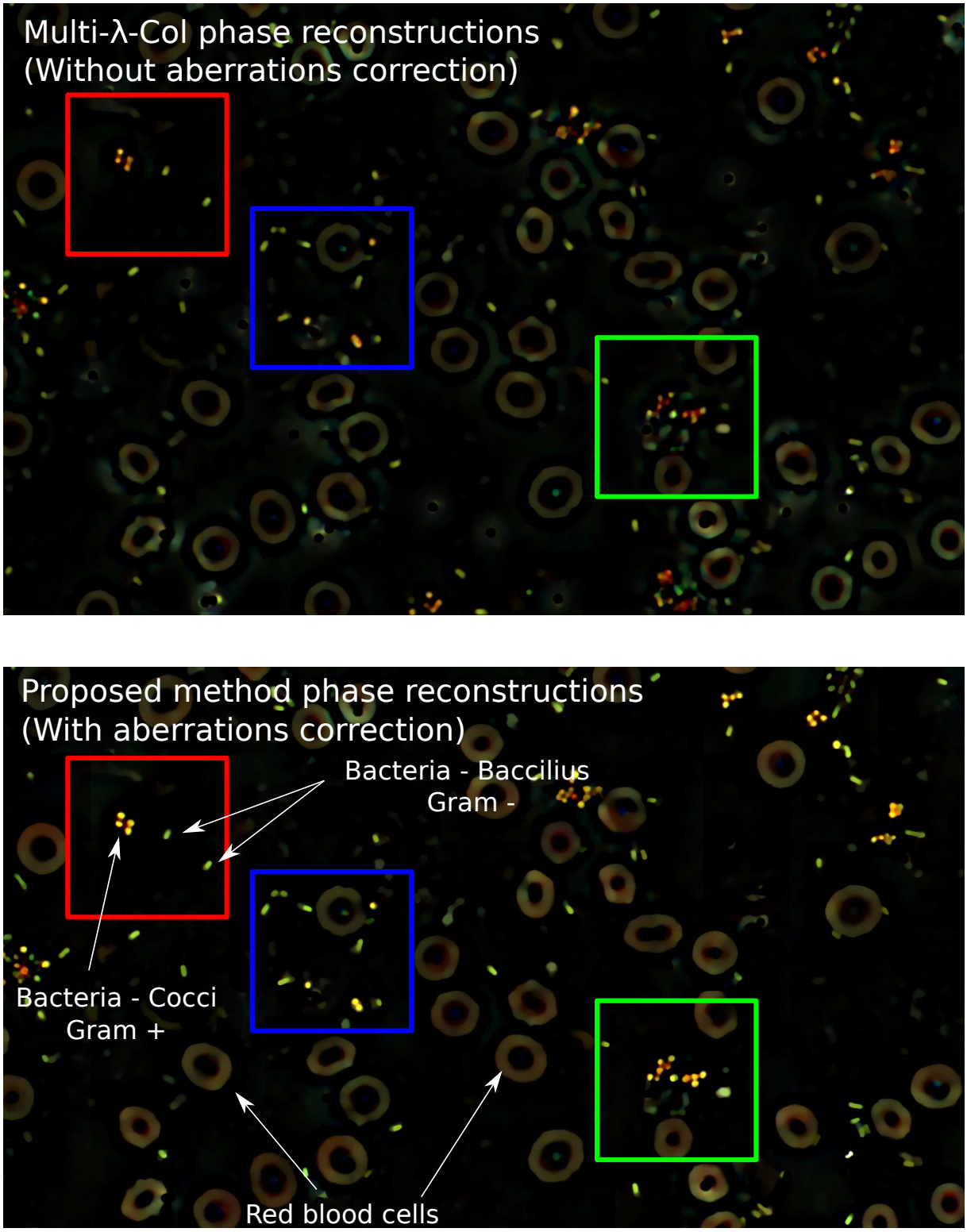

Figure 8.2: Phase reconstructions of multispectral acquisition using the Multiλ-Col and proposed aberrations-corrected method.

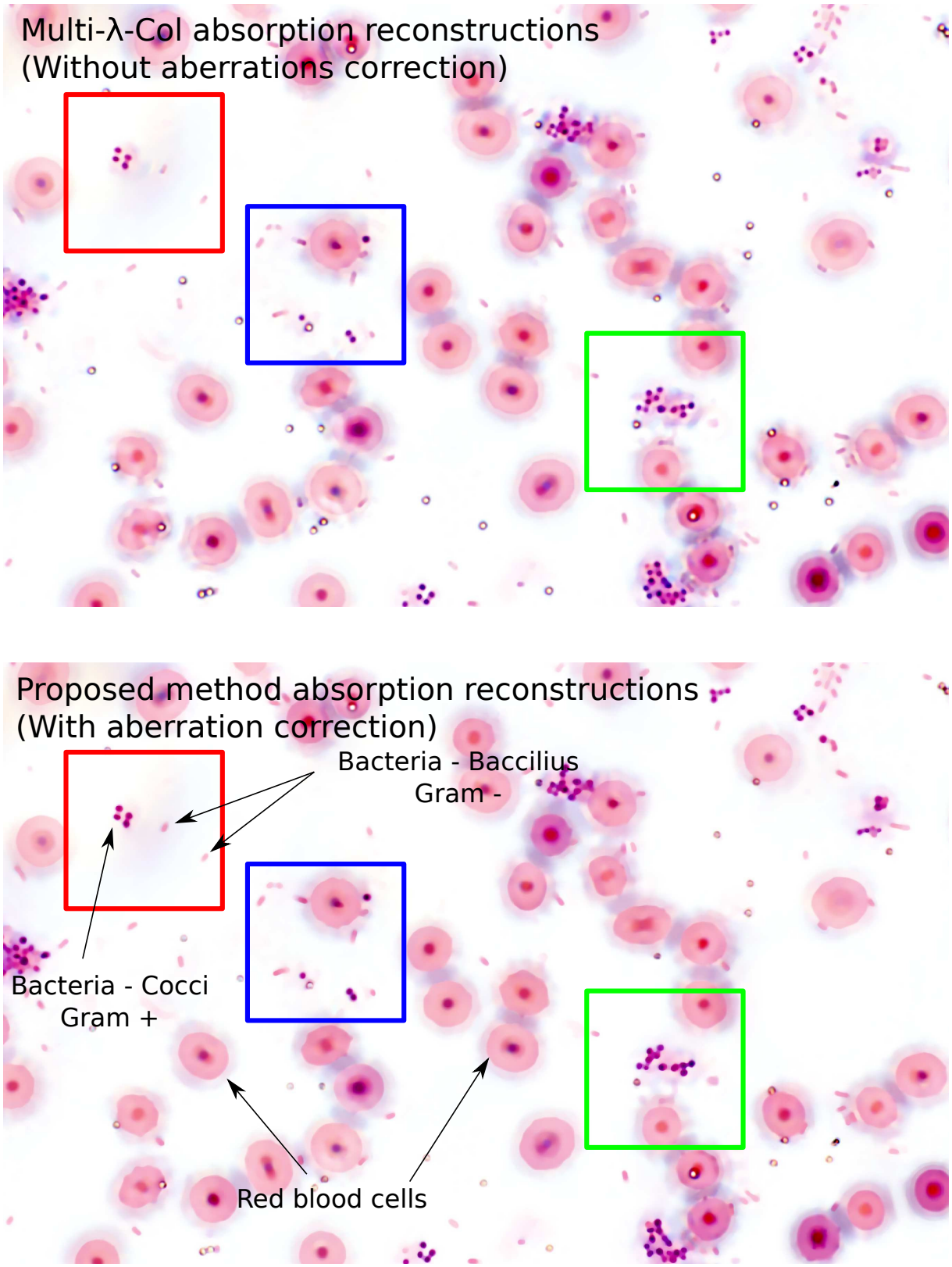

Figure 8.3: Absorption reconstructions of multispectral acquisition using the Multiλ-Col and proposed aberrations-corrected method

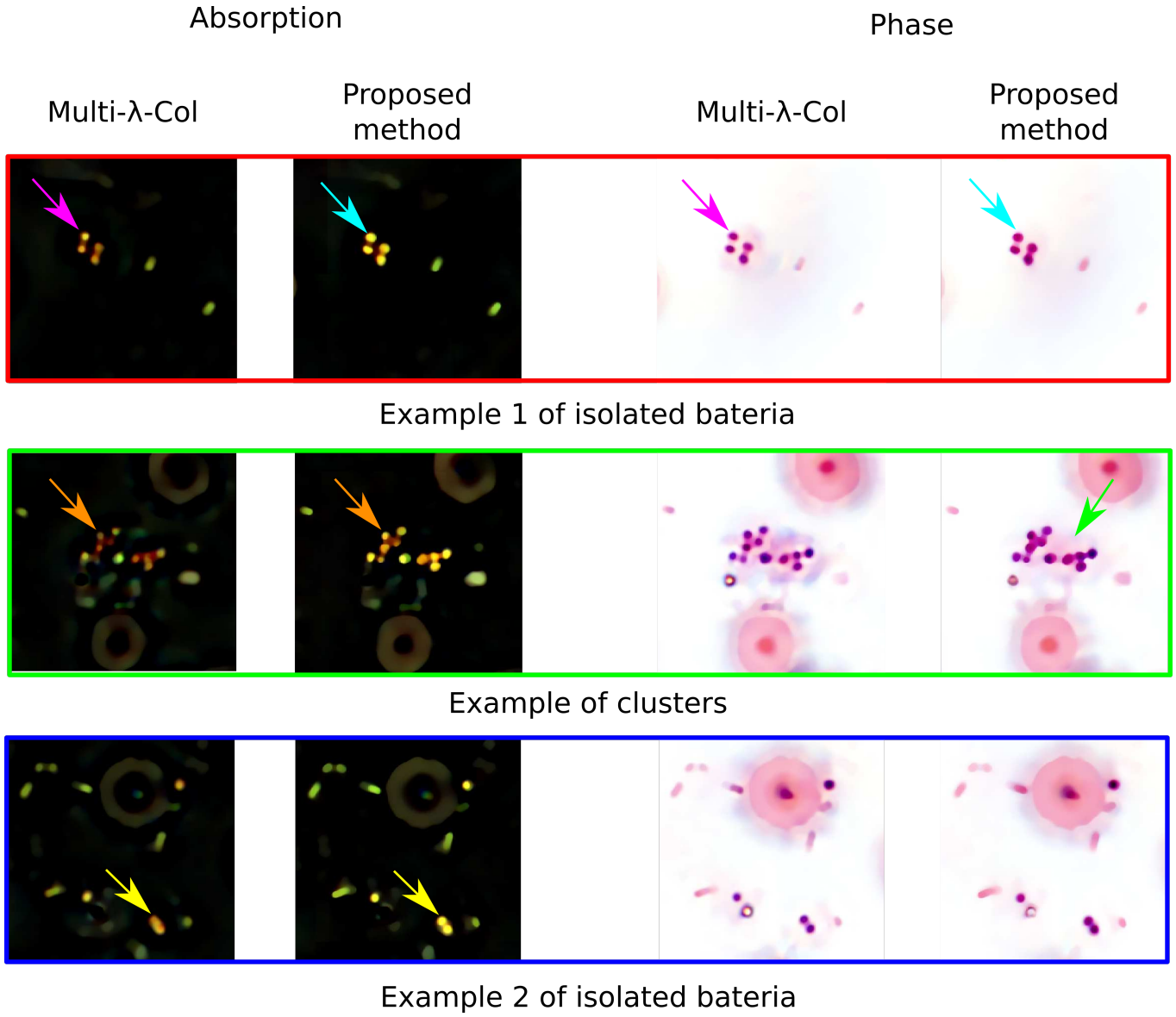

Figure 8.4: Zoom on the phase and absorption reconstructions of multispectral acquisition using the Multiλ-Col and proposed aberrations-corrected method

Using the aberration corrections, the discrimination between bacteria becomes easier as their spectral response is different. As illustrated with Figure 8.5, the twin-image artefacts have been correctly cleaned for all wavelength. As expected, using Kramer-Krönigs laws [Lucarini et al., 2005], the phase-shift introduced by the bacteria is increasing after the absorption peak (reached at $\lambda \approx 532nm$). The phase reconstruction is also discriminant for the bacteria at this wavelength.

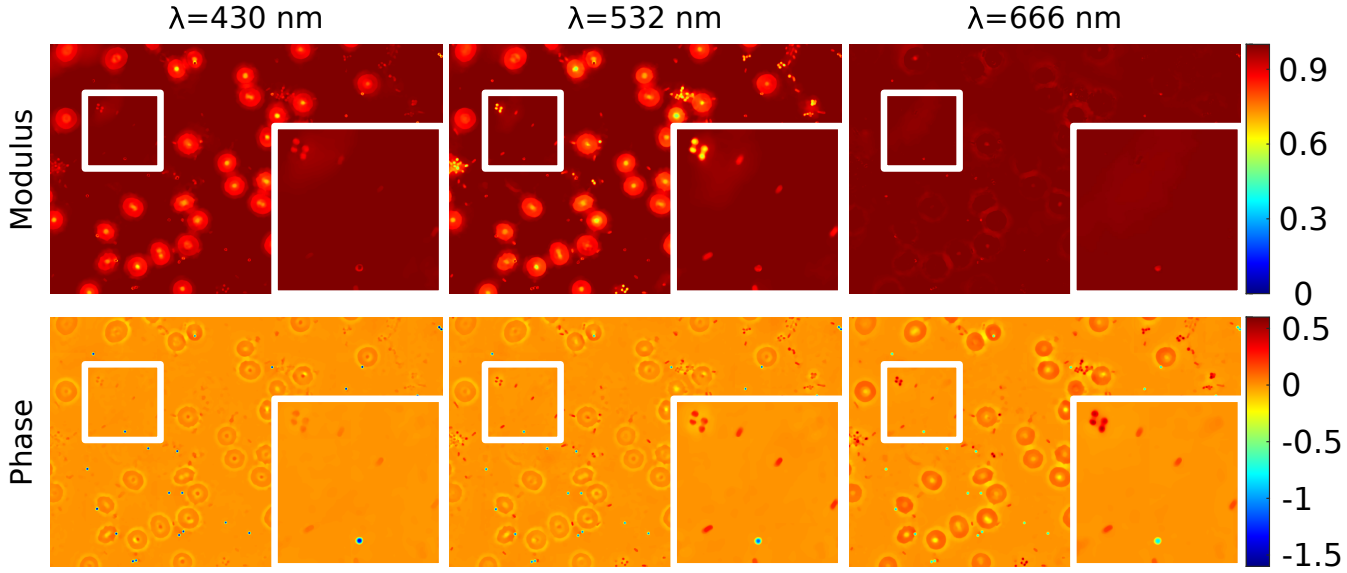

Figure 8.5: Modulus and phase reconstruction for several wavelength using the proposed aberrations-corrected method

A basic segmentation task is then performed on the field of view presented in Figure 8.2 to study the transmission and the refractive properties of both bacteria types (Gram+, Gram-). Figure 8.6 illustrates the evolution of the transmission and optical path with the wavelength for both bacteria types using the Multi-λ-Col algorithm and the proposed method. The values have been obtained by averaging the modulus and the phase maps on the pixels area that correspond to each type of bacteria (approximately 20 bacteria). As shown in Figure 8.6, the absorption spectrum is quite similar using both algorithms. However, the Optical Path Difference (OPD) reconstructions are really different. Indeed, using the Multi-λ-col reconstructions, discriminating the bacteria using the reconstructed OPD information was a difficult task due to the small difference and the dispersion of the reconstructed values. With our method, the standard deviation of the reconstructed OPD is almost unchanged, however the bacteria have a higher average OPD. Thus, these reconstructions indicates a possibility of discriminating them only with the OPD for the higher wavelengths.

These last results only highlight the significance of accounting for aberrations in the reconstructions. Indeed, a ground truth would be needed to ensure that the proposed method is quantitative in terms of absolute values. However the reconstructions are performed more rigorously using a more accurate model and provide more physical results (for example, the object have similar shapes in phase and absorption).

It should be noticed that these samples were stained, thus it is difficult to know if the measured phase comes from the staining of the bacteria, or from the bacteria itself. Further investigations on label-free samples should be done.

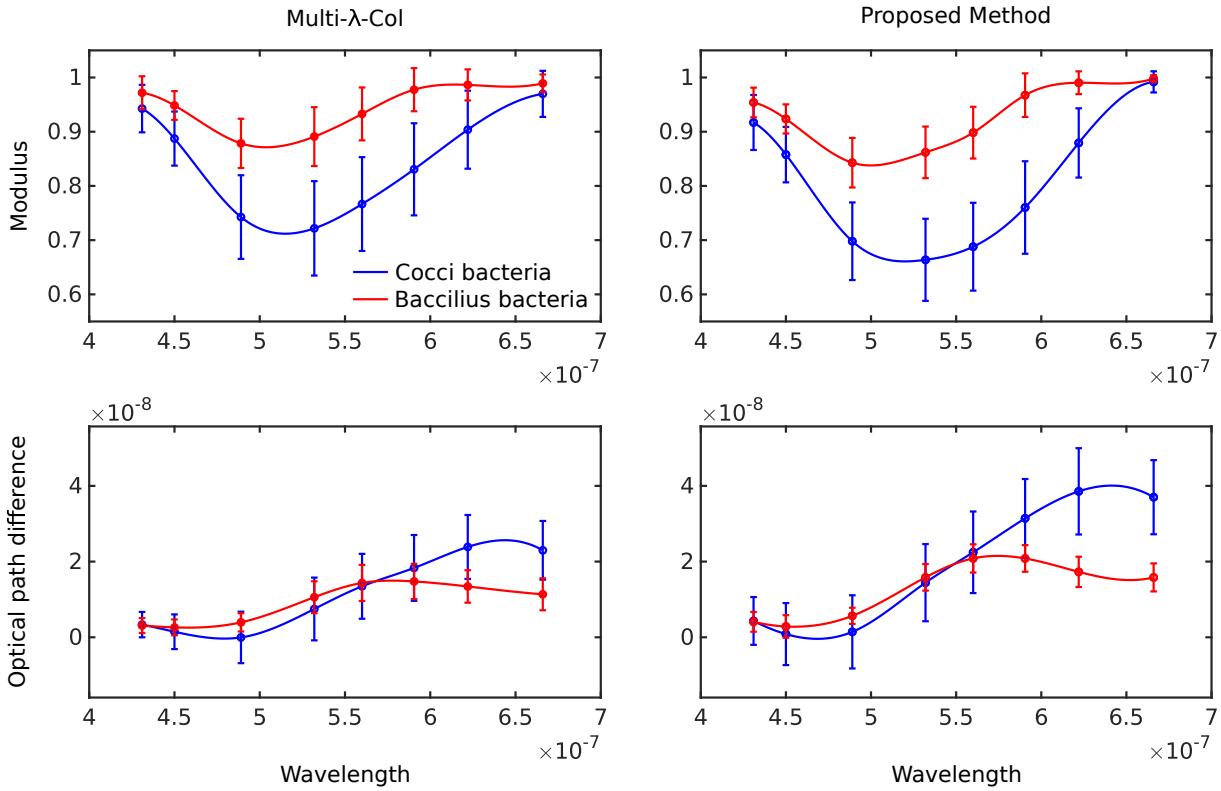

Figure 8.6: Average and standard deviation of the reconstructed modulus and OPD introduced by baccilus (Gram-) and cocci bacteria (Gram+)

C Conclusion

In this chapter, we underlined the significance of chromatic aberrations in multispectral reconstructions. The quantitativity and the repeatability of the reconstructed phase is strongly affected by these aberrations even though they are quite low in the presented example. Indeed, because of aberrations, the image formation model is changed leading to two main consequences: the minimization of the data fidelity is biased and the prior based on the colocalization of the object for all transmittance planes is not valid. We proposed a method based on calibration beads to estimate accurately the parameters of chromatic aberrations and then compensate them in the regularized reconstruction. The obtained results are more physical and show an increase of the contrast between the objects of interest. Further studies on label-free samples will have to be done to determine if the difference between the two types of bacteria without staining is enough to be discriminant. However, with stained samples, it seems that multispectral phase reconstruction give interesting discrimination information as pointed out by Figure 8.6. Indeed, the OPD is almost identical at 560 nm while it is really different at 622 nm or 666 nm. These results results must however be taken with great care since only two types of Gram+/Gram- bacteria have been reconstructed.

Conclusion, ongoing and future works

A Summary of the main contributions

In this thesis, we have proposed several methods dedicated to the reconstructions of in-line holograms. In particular, these methods have been applied to increase the repeatability, the reproducibility and the quantitativity of biological sample holograms reconstructions. These methods follows three methodological solutions:

First methodological solution - Self-calibration of the image formation model

In in-line holography, the autofocusing step is performed numerically making this technique low cost (precise z stage is no longer obligatory) and ideal for automatization. However, this autofocusing step requires an accurate image formation model. Calibration beads, on which most of the contributions of this thesis are based, are accurately described by the Lorenz-Mie model. Thus, we suggest to use these beads to calibrate the image formation model:

- In Chapter 2, we proposed a method consisting in inserting calibration beads into the sample to retrieve the slide plane. The slide plane is fitted thanks to the estimation of the beads parameters by a parametric inverse problems approach. This method improves the repeatability of the reconstruction since the estimation of the propagation distance z is performed using an objective criterion, *i.e.* that does not depend on the sample.
- In Chapter 3, we tackle the robustness issue of bead detection in the sample. We extended the robust detection proposed by Fitch so that the detection of calibration objects, as needed for the image formation model calibration, becomes more efficient. The presented algorithm exploits a low rank approximation of robust cost functions to compute efficiently robust detection maps using Fast Fourier Transforms.
- In Chapter 4, we proposed a method to take into account aberrations in inverse problem approaches in holography. This methodology is based on the estimation of Zernike coefficients on calibration beads at several position in the field-of-view. Then a correction of the PSF can be computed in order to be used in regularized reconstruction. This improvement of the image formation model improves morphologically and quantitatively the reconstructions. The whole imaging setup, from the illumination to the objective, is thus characterized leading to better reproducibility of the imaging device.

Second methodological solution - Unsupervised tuning of the regularization hyperparameters

To reconstruct an in-line hologram using inverse problem approaches, the balance between full confidence in the data and physical priors on the reconstruction must be tuned. The tuning of regularization hyperparameters is a critical step in the search of reproducible and quantitative reconstructions:

- In Chapter 5, we assessed the performances of an unsupervized method, based on the minimization of SURE, to tune the regularization hyperparameters. This method provides qualitative reconstructions but is, as all "image-based" criteria, dependent on the sample to reconstruct.

- In Chapter 6, we proposed an objective criteria to perform the reconstructions based on the quantitativity of the reconstruction of calibration objects. This method is more reproducible as long as the calibration objects are mono-disperse. Moreover if the calibration objects have similar morphological and refractive index difference than the objects of interest, bacteria in our case, the reconstruction will specifically be more quantitative for these objects.

Third methodological solution - Exploiting phase diversity in multispectral reconstructions
To improve the reconstructions and to discriminate stained bacteria, multispectral data have been reconstructed:

- In Chapter 7, we reconstructed a multispectral data stack using a multispectral colocalization prior in a regularized inverse problems approach. Even though using a multispectral prior improves the quantitativity of the reconstruction, these prior are sensitive to the registration of the data.

- In Chapter 8, we show that the registration between the multispectral acquisitions should vary in the field of view and thus, cannot be considered to be rigid. Indeed, the registration error mainly comes from aberrations of the optical setup. Using a methodology similar to the one proposed in Chapter 4, these chromatic aberrations can be corrected such that the quantitativity and reproducibility of the reconstructions is improved. The reconstruction results are repeatable and show a relevant spectral information in the phase of the studied sample.

All the algorithms presented in this manuscript have been developed using the framework GlobalBioIm [Soubies et al., 2019]. A toolbox dedicated to in-line inverse problems approach reconstructions, that includes all the codes for the contribution of this thesis, is to be released.

B Ongoing and future works

In this section we discuss some ongoing and possible future works related to each methodological solution studied in this thesis.

First methodological solution - Self-calibration of the image formation model
In this manuscript we improved the image formation model by estimating the parameters of calibration beads inserted in the sample. Some of the perspective provided by this methodology have been summarized in the following:

- **Partial coherence models:**
  If in-line holography requires coherence of the light source, this condition is not very restrictive. Thus, partially coherent light sources (that are cheaper than lasers) can be used to decrease the speckle noise of the in-line holograms. However to perform more quantitative reconstructions, the partial coherence of the light source has to be taken into account in the direct model. This subject has been studied during this thesis and first results have been described in [Olivier et al., 2022]. They show that taking into account the partial coherence of the illumination reduces biases in the estimation of calibration beads parameters. However, in these experiments, the experimental parameters that describes the partial coherence were supposed to be known. During Thomas Brard's internship (Master 1), we studied the estimation of these parameters on calibration beads using parametric inverse problems approach. First results on simulations have achieved great performances. These results should be validated on experimental data and used in regularized reconstructions. Let us notice that a preliminary study of the correlation between the estimated parameters should be performed.

- **Choice of the calibration beads:**
  To improve the quantitativity of the reconstructions, the calibration beads choice could be optimized in a co-design approach. The parameters of the calibration beads could be optimized, using statistical tools as the Cramér-Rao lower bounds, in order to improve the estimation accuracy of z and of the Zernike coefficients.
  Moreover several populations of mono-dispersed beads could be inserted in the sample. The exploitation of the diversity of their parameters to improve the accuracy of the estimations could be studied.

- **More complex or low quality setups:**
  In this manuscript we aim at reconstructing quantitatively in-line holograms by modeling the optical setup. However, the methodology is much more wide ranging. It could be used to account for aberrations in more complex optical setups or with low cost optics and should improve also the quantitativity of the reconstructions. This study would be interesting to assess the limits of our method and to extend it to other configurations.

Second methodological solution - Unsupervised tuning of the regularization hyperparameters
To increase the quantitativity of the regularized reconstruction of specific objects, in our case bacteria, we proposed to use an objective quality criterion based on the reconstruction of calibration beads. Perspectives of this work are summarized in the following:

- **Computational time reduction:**
  In the proposed method the whole hologram should be reconstructed to compute the quality criterion. However, when this criterion is based on the reconstruction of

calibration beads, only these regions need to be reconstructed. Thus, the computational time could be highly reduced.

- **Assessing the quantitativity of the reconstructions of the bacteria:**
  In this manuscript, we assumed that the optimal regularization hyperparameters for the beads are the optimal regularization hyperparameters for the bacteria. The validity of this assumption can be studied using a quantitative measurement of the phase, for example by comparing our reconstruction with off-axis holograms reconstruction of the same sample.

Third methodological solution - Exploiting phase diversity in multispectral reconstructions
In this manuscript, we proposed an unsupervised method to reconstruct multispectral holograms using a colocalization prior. Some of the perspectives provided by this method have been summarized in the following:

- **Spectral regularization**
  To increase the quantitativity of the reconstructions, spectral priors could be added in the reconstruction algorithm. These priors could for example be based on the Kramers-Kronig laws that describe the link between the real part of the refractive index and its imaginary part (*i.e.* for semi-transparent objects, the modulus and the phase) [Sai et al., 2020].

- **PSF design for multispectral reconstruction**
  With the methodological tools developed during this thesis, co-design approaches based on the estimation of an optimal PSF for multispectral reconstruction could be performed. These approaches would consists in finding the multispectral PSF that provides discriminative information to reconstruct the bacteria.

- **Classification**
  For biomedical purpose, further study on the ability of a classification tool to discriminate bacteria should be done. During Thomas Bultingaire's internship (Master 1), deep learning solutions have been tested on few holograms leading to promising results that must be confirmed with a bigger database.

- **Label-free samples reconstructions**
  In this manuscript, holograms reconstructions were performed on stained sample. However, phase imaging is interesting to reconstruct non stained samples. Thus, further study on label-free samples should be performed [Kim et al., 2022]. These studies could exploit dynamic phenomena (cells mobility, reactions to changes in its environment, etc) [Wang et al., 2016].

In addition of these perspectives, more general perspectives can be added:

- **Reproducibility**
  The reproducibility of the method should be furthermore studied with other in-line holographic setups. Indeed in this thesis the reproducibility of the method has only be studied on the two setups presented in Appendix A.

- **Computational time of the reconstruction reduction**
  Inverse problem approaches reconstruction may be time consuming. Thus, computational improvements are necessary to make these techniques applicable in practical conditions. Deep-learning solutions have been studied during this thesis with Carlos Valdares' internship (Master 1) for reducing the computational time of the parametric approaches, and with Dorian Pillard internship (Master 1) on the learning of inverse problem approach reconstruction of experimental data to reconstruct in-line holograms.

- **Applications to other coherent imaging techniques**
  At last, most of the methods presented in this manuscript can be applied to other coherent imaging techniques [Denneulin et al., 2022].

Annexes

APPENDIX A

Experimental protocol

In this Appendix, we present the two in-line holographic setups used in this work. Section A provides a description of the setup used at LaHC and is referred as Setup-LaHC in the manuscript. This setup is used for beads monochromatic hologram acquisition in Chapter 4. Section B describes the setup used at BIOASTER for acquisition of multispectral blood smear holograms that are processed in the other chapters. It is referred as Setup-BIOASTER. At last, a discussion on the choice of the calibration objects and other experimental parameters is provided in Section C.

A Description of Setup-LaHC

This section has been adapted from [Olivier et al., 2022].

The LaHC home-made experimental setup is presented in Fig. A.1. The setting of a spatially coherent illumination may be difficult in a microscopy setup as it is very sensitive to any stray reflections or dust particles and leads to complex, sometime unstable speckle patterns. In this setup, the coherent illumination is set by illuminating a $200\mu m$-pinhole (P) and a lens (L) set in a $2f$ configuration. Thus, an airy pattern illuminates the sample, with a large enough central peak to illuminate the whole field of view, but without inserting too much stray light in the imaging system. This leads to moderate vignetting which is corrected by dividing the holograms by a background intensity image.

A coherent illumination with a laser at 637.6nm was used. The illumination power was sufficient to keep exposure times as short as 5ms with our Thorlabs-S805MU1 camera. The sensor pixel size was $5.5\mu m$. With 22.6mm diagonal, the sensor covers an important part of the field of view of the microscope (the objective field number is 26.5mm, which represents the maximum possible field of view of the objective). The microscope objective was a water immersion microscope objective (Olympus PlanSApo, 60×, 1.2NA) with a coverslip correction collar. The tube lens was a 200mm-focal length apochromatic TTL200MP lens from Thorlabs that was used in a telecentric configuration. The measured magnification was 66.5, and not 60, as the tube lens has a greater focal length than the Olympus standard (180mm).

Experimental parameters related to this microscope are summarized in Table A.1.

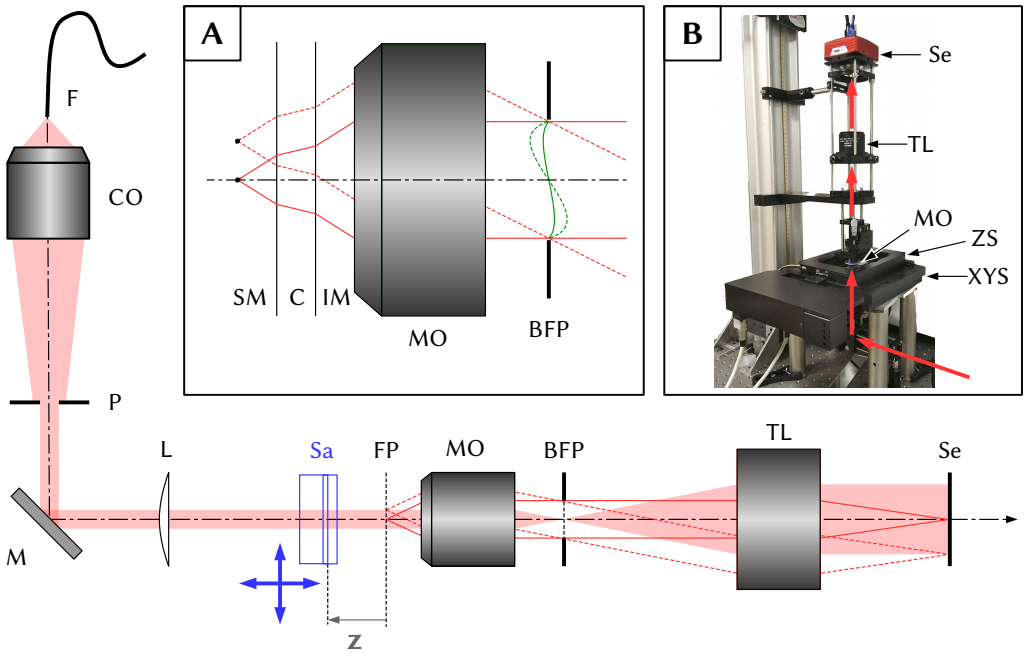

Figure A.1: Experimental setup. F: monomode fiber coupled laser source, P: 200μm-pinhole, M: mirror, L: lens, Sa: sample that can be precisely moved in XYZ-directions, z: defocus distance of the sample from the focus plane, FP: objective focal plane, MO: microscope objective, BFP: objective back focal plane, TL: tube lens, Se: sensor. **Inset A:** zoom on the sample and the objective showing the refraction of the rays occurring through the coverslip. SM: sample medium, C: coverslip, IM: immersion medium. **Inset B:** Picture of the setup showing the imaging system and the precision piezo-stage (ZS) and the XY-translation stage (XYS).

Wavelength	637.6nm
Magnification	66.5
Pixel pitch	83nm
Total field of view	273×204μm
Beads diameter*	(1.0±0.06)μm
Beads refractive index*	1.587 (polystyrene)
Refractive index of immersion medium	1.47 (glycerol)
Coverslip thickness	(0.170±0.001)mm
Typical defocus	12μm

Table A.1: Experimental parameters of Setup-LaHC (*from manufacturer, ThermoFisher Scientific, Inc.)

B Description of Setup-BIOASTER

This section has been adapted from [Brault et al., 2022b]. The BIOASTER setup is also a home-made microscopy setup.

In this setup a partially coherent illumination based on LED is used. Even though the coherence of the illumination beam is needed in holography, this condition is not very restrictive because the patterns that constitutes the hologram comes from the interference between the wave diffracted by a micrometer thick object and the illumination beam (background), which corresponds to a short optical path difference. Thus, for in-line holographic microscopy, the minimum requirements for temporal and spatial coherence may be quite low.

In this setup, LED sources at $\mathbf{\Lambda} = \{431$ nm , 450 nm , 490.5 nm , 532 nm , 560 nm , 590 nm , 622 nm , 666 nm $\}$ are used.

In order to accurately control the illumination aperture and field, an adapted Köhler illumination has been set up (see Fig.A.2). The output of the fiber has been magnified with a microscope objective and imaged on the aperture diaphragm. This diaphragm has been set in the focal plane of a 150 mm focal length condenser lens. In these conditions, the illuminated field can be controlled by a field diaphragm to eliminate stray light in the microscope. The aperture can also be controlled in order to set up precisely the spatial coherence, which is important to test various partially coherent illuminations. To address the problem of spectral coherence, bandpass filters were used with a spectral half width at half maximum of 10 nm. For all holograms processed in this manuscript, the divergence of the spatially incoherent illumination was 10 mrad with an aperture diameter of 3 mm.

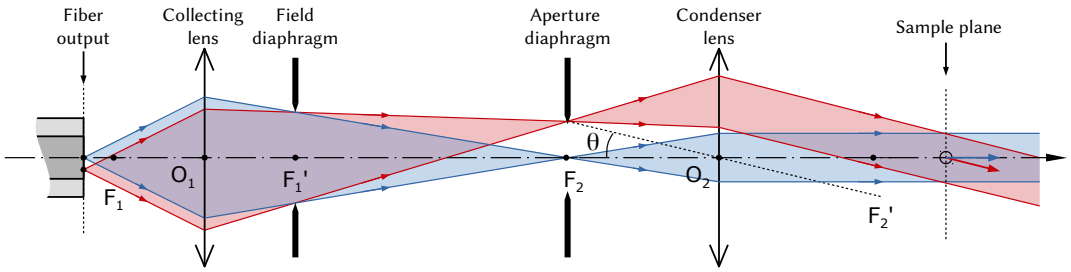

Figure A.2: Illustration of the Köhler partially coherent illumination with an extended source (fiber output), a collecting lens, a condenser lens, a field diaphragm and an aperture diaphragm. In these conditions, the sample is illuminated by a partially coherent beam composed of multiple incoherent plane waves with various incident angles with a maximum angle θ given by the focal length of the condenser and the diameter of the aperture.

Experimental parameters related to this microscope are summarized in Table A.2.

Note that this microscopy setup has two different ports. One port is designed for brightfield, in-focus microscopy, with a color sensor located in the image focal plane of a first tube lens. The other port is designed for in-line holography, with a monochrome sensor located few millimeters away from the image focal plane of a second tube lens. In these conditions, when the system is in-focus on the brightfield port, the holography port is out-of-focus with an equivalent axial shift (defocus) of $9.9\mu m$.

Wavelength	431nm, 450nm, 490.5nm, 532nm, 560nm, 590nm, 622nm, 666nm
Magnification	100
Numerical Aperture	1.4
Pixel pitch	45nm
Typical defocus	10μm

Table A.2: Experimental parameters of Setup-BIOASTER

C Choice of the calibration objects

The choice of the calibrated object is important as it depends on the type of sample and its preparation. In this section we provide details on the choice of the calibration objects to add in blood smear samples in order improve the reconstructions. Spherical geometry increases the accuracy of estimated parameters, as Lorenz-Mie based models are well known and thus provide highly constrained parametric inverse problems reconstructions.

The choice of the calibration objects was made in the context of blood smear sample observations with high magnification objectives. For our application, this choice has several advantages:

- The **size** (1μm) is similar to the biological objects in the sample (blood cells, platelets, bacteria, etc.) and is small enough to allow an accurate axial positioning.
- The **transparency** of the silica beads is an advantage as, whatever the wavelength used, they can be considered as purely phase objects. Moreover, it is best to use transparent calibration objects to observe stained samples, as they can be more easily differentiated from the stained biological structures.
- The **refractive index** is not so different from the surrounding immersion medium , which provides moderately contrasted holograms to prevent too much disturbance caused by the calibrated objects. The refractive index is also lower than the immersion medium refractive index, contrary to the case of fixed biological objects, which is particularly discriminating.

With blood smear holograms acquisition, the sample has been stained. In this case, the choice of silica beads is appropriate. Indeed silicon dioxyde is dense, which allows sedimentation on the slide, non-porous (which prevents the beads from being stained), solvent and heat resistant (which prevents the beads from being damaged by the fixation process). Preparation of the blood smear begins with the mixing of a small volume of blood with an appropriate dilution of silica beads in aqueous suspension. The dilutions are calibrated beforehand to obtain a representative number of beads in each field of view. A drop of this mix is then spread on a glass slide using the traditional "wedge or push" technique. The sample is then fixed with ethanol and Gram stained. In this case, the parameters of the beads are summarized in Table A.3.

Note that in Chapter 4, no blood smears were analyzed, but only beads to study the aberration correction approach. For that, a water immersion objective was used with a coverslip correction collar. However, beads are moving in water because of the Brownian motion. For practical reasons, these studies were then performed with latex beads ($n = 1.59$) in glycerol ($n = 1.47$) to reduce the Brownian motion with the high viscosity of glycerol.

Beads diameter	(1.0±0.06)μm
Beads refractive index	1.445 (silica)

Table A.3: Experimental parameters of the silica beads(from manufacturer, ThermoFisher Scientific, Inc.)

APPENDIX B

Vizualisation of multispectral reconstructionions

To represent the multispectral information in this manuscript, it has been chosen to use a RGB image. Since multispectral reconstructions aim at retrieving the modulus and the phase of the 2D transmittanc, it is possible to extract from this information a absorption color map corresponding to an image similar to the one that would be obtained using bright-field imaging. To compute this image we used this approach illustrated by Figure B.1.

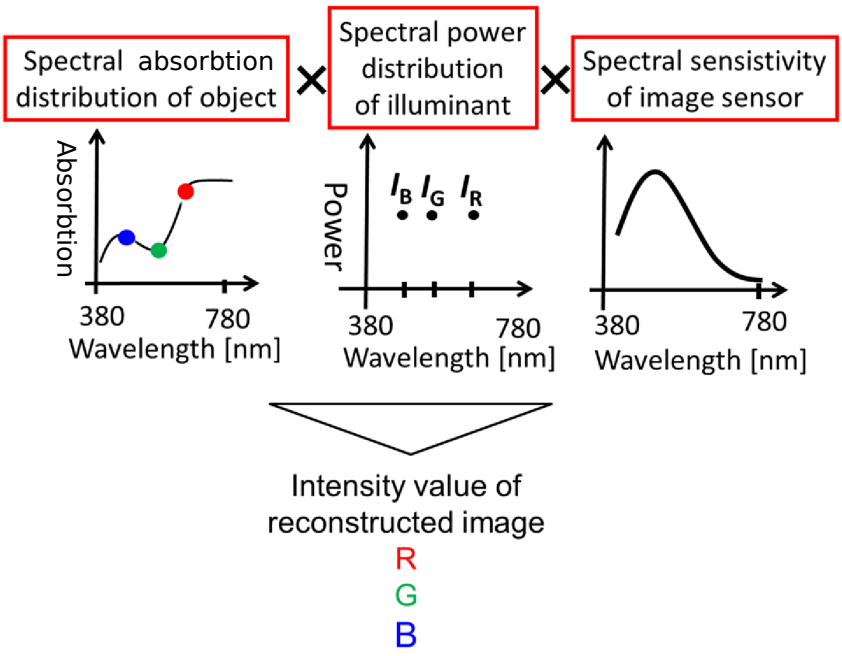

Figure B.1: Flow of color reproduction of color digital holography. Figure adapted from [Xia et al., 2011].

In this approach, the absorption color map is computed from multispectral reconstruction and multiplied with the spectral power of the illumination and with the spectral sensitivity of the camera. The absorption maps presented in Chapter 7 and Chapter 8, uses the same principle, however the spectral power of the illumination is supposed to be

constant with the wavelength.

For phase color representation, we use the same algorithm. Since most of the objects observed in this manuscript introduce a small positive phase shift, it has been chosen to represent the multispectral phase as a linear combination of the phase reconstruction for which the coefficient correspond to the spectral sensitivity of the sensor. Thus in these false color images, the beads can not be seen since their phase is negative. All biological objects can however be seen since the phase shift they introduce is positive.

Bibliography

[Alexander et al., 2020] Alexander, R., Leahy, B., and Manoharan, V. N. (2020). Precise measurements in digital holographic microscopy by modeling the optical train. *Journal of Applied Physics*, 128(6):060902.

[Allen and Oxley, 2001] Allen, L. and Oxley, M. (2001). Phase retrieval from series of images obtained by defocus variation. *Optics communications*, 199(1-4):65–75.

[Allier et al., 2017] Allier, C., Morel, S., Vincent, R., Ghenim, L., Navarro, F., Menneteau, M., Bordy, T., Hervé, L., Cioni, O., Gidrol, X., et al. (2017). Imaging of dense cell cultures by multiwavelength lens-free video microscopy. *Cytometry Part A*, 91(5):433–442.

[Altman and Grier, 2020] Altman, L. E. and Grier, D. G. (2020). Catch: Characterizing and tracking colloids holographically using deep neural networks. *The Journal of Physical Chemistry B*, 124(9):1602–1610.

[Aristov et al., 2018] Aristov, A., Lelandais, B., Rensen, E., and Zimmer, C. (2018). ZOLA-3D allows flexible 3D localization microscopy over an adjustable axial range. *Nature Communications*, 9(1):2409.

[Barenfanger et al., 2008] Barenfanger, J., Graham, D. R., Kolluri, L., Sangwan, G., Lawhorn, J., Drake, C. A., Verhulst, S. J., Peterson, R., Moja, L. B., Ertmoed, M. M., et al. (2008). Decreased mortality associated with prompt gram staining of blood cultures. *American journal of clinical pathology*, 130(6):870–876.

[Beck and Teboulle, 2009] Beck, A. and Teboulle, M. (2009). Fast gradient-based algorithms for constrained total variation image denoising and deblurring problems. *IEEE transactions on image processing*, 18(11):2419–2434.

[Bian et al., 2020] Bian, Z., Guo, C., Jiang, S., Zhu, J., Wang, R., Song, P., Zhang, Z., Hoshino, K., and Zheng, G. (2020). Autofocusing technologies for whole slide imaging and automated microscopy. *Journal of Biophotonics*, 13(12):e202000227.

[Bon et al., 2015] Bon, P., Bourg, N., Lécart, S., Monneret, S., Fort, E., Wenger, J., and Lévêque-Fort, S. (2015). Three-dimensional nanometre localization of nanoparticles to enhance super-resolution microscopy. *Nature Communications*, 6(1):7764–.

[Brault et al., 2022a] Brault, D., Denis, L., Dixneuf, S., Olivier, T., Faure, N., and Fournier, C. (2022a). Fast and robust pattern detection: Application to spherical bead localization in holographic microscopy. accepted in IEEE European Signal Processing Conference (EUSIPCO), 09/2022.

[Brault et al., 2022b] Brault, D., Fournier, C., Olivier, T., Faure, N., Dixneuf, S., Thibon, L., Mees, L., and Denis, L. (2022b). Automatic numerical focus plane estimation in digital holographic microscopy using calibration beads. *Applied Optics*, 61(5):B345–B355.

[Brault et al., 2022c] Brault, D., Olivier, T., Soulez, F., Joshi, S., Faure, N., and Fournier, C. (2022c). Accurate unsupervised estimation of aberrations in digital holographic microscopy for improved quantitative reconstruction. *Optics Express*, 30(21):38383–38404.

[Cai et al., 2016] Cai, T. T., Li, X., and Ma, Z. (2016). Optimal rates of convergence for noisy sparse phase retrieval via thresholded wirtinger flow. *The Annals of Statistics*, 44(5):2221–2251.

[Candes et al., 2013] Candes, E. J., Strohmer, T., and Voroninski, V. (2013). Phaselift: Exact and stable signal recovery from magnitude measurements via convex programming. *Communications on Pure and Applied Mathematics*, 66(8):1241–1274.

[Chang et al., 2016] Chang, H., Lou, Y., Ng, M. K., and Zeng, T. (2016). Phase retrieval from incomplete magnitude information via total variation regularization. *SIAM Journal on Scientific Computing*, 38(6):A3672–A3695.

[Chang et al., 2021] Chang, X., Bian, L., and Zhang, J. (2021). Large-scale phase retrieval. elight 1, 4.

[Charbonnier et al., 1997] Charbonnier, P., Blanc-Féraud, L., Aubert, G., and Barlaud, M. (1997). Deterministic edge-preserving regularization in computed imaging. *IEEE Transactions on image processing*, 6(2):298–311.

[Chen et al., 2003] Chen, J.-H., Chen, C.-S., and Chen, Y.-S. (2003). Fast algorithm for robust template matching with m-estimators. *IEEE Transactions on signal processing*, 51(1):230–243.

[Cheong et al., 2010] Cheong, F. C., Krishnatreya, B. J., and Grier, D. G. (2010). Strategies for three-dimensional particle tracking with holographic video microscopy. *Optics express*, 18(13):13563–13573.

[Colomb et al., 2006] Colomb, T., Cuche, E., Charrière, F., Kühn, J., Aspert, N., Montfort, F., Marquet, P., and Depeursinge, C. (2006). Automatic procedure for aberration compensation in digital holographic microscopy and applications to specimen shape compensation. *Applied optics*, 45(5):851–863.

[Colson et al., 2007] Colson, B., Marcotte, P., and Savard, G. (2007). An overview of bilevel optimization. *Annals of operations research*, 153(1):235–256.

[Deledalle et al., 2014] Deledalle, C.-A., Vaiter, S., Fadili, J., and Peyré, G. (2014). Stein unbiased gradient estimator of the risk (sugar) for multiple parameter selection. *SIAM Journal on Imaging Sciences*, 7(4):2448–2487.

[Denis et al., 2016] Denis, L., Ferrari, A., Mary, D., Mugnier, L., and Thiébaut, E. (2016). Fast and robust detection of a known pattern in an image. In *2016 24th European Signal Processing Conference (EUSIPCO)*, pages 2206–2210. IEEE.

[Denis et al., 2009] Denis, L., Lorenz, D., Thiébaut, E., Fournier, C., and Trede, D. (2009). Inline hologram reconstruction with sparsity constraints. *Optics letters*, 34(22):3475–3477.

[Denis et al., 2011] Denis, L., Thiébaut, E., and Soulez, F. (2011). Fast model of space-variant blurring and its application to deconvolution in astronomy. In *2011 18th IEEE International Conference on Image Processing*, pages 2817–2820. IEEE.

[Denis et al., 2015] Denis, L., Thiébaut, E., Soulez, F., Becker, J.-M., and Mourya, R. (2015). Fast approximations of shift-variant blur. *International Journal of Computer Vision*, 115(3):253–278.

[Denneulin, 2020] Denneulin, L. (2020). *Approche inverse pour la reconstruction des environnements circumstellaires en polarimétrie avec l'instrument d'imagerie directe ESO / VLT SPHERE IRDIS*. PhD thesis. Thèse de doctorat dirigée par Langlois, Maud-Pustelnik, Nelly et Thiébaut, Éric Astrophysique Lyon 2020.

[Denneulin et al., 2022] Denneulin, L., Momey, F., Brault, D., Debailleul, M., Taddese, A. M., Verrier, N., and Haeberlé, O. (2022). Gsure criterion for unsupervised regularized reconstruction in tomographic diffractive microscopy. *J. Opt. Soc. Am. A*, 39(2):A52–A61.

[Dey et al., 2015] Dey, N., Ashour, A., and Singh, A. (2015). Digital analysis of microscopic images in medicine. *Journal of Advanced Microscopy Research*, 10:1–13.

[Dubois et al., 2006] Dubois, F., Schockaert, C., Callens, N., and Yourassowsky, C. (2006). Focus plane detection criteria in digital holography microscopy by amplitude analysis. *Opt. Express*, 14(13):5895–5908.

[Eldar, 2008] Eldar, Y. C. (2008). Generalized sure for exponential families: Applications to regularization. *IEEE Transactions on Signal Processing*, 57(2):471–481.

[Ferraro et al., 2003] Ferraro, P., Nicola, S. D., Finizio, A., Coppola, G., Grilli, S., Magro, C., and Pierattini, G. (2003). Compensation of the inherent wave front curvature in digital holographic coherent microscopy for quantitative phase-contrast imaging. *Applied Optics*, 42(11):1938–1946. Publisher: Optica Publishing Group.

[Ferréol Soulez, TBP] Ferréol Soulez, E. T. (TBP). Les problèmes inverses pour la reconstruction d'image en holographie. In Fournier, C. and Haéberlé, O., editors, *Systèmes d'imageries optiques non conventionnelles pour la biologie*, chapter 3. ISTE.

[Fienup, 1980] Fienup, J. (1980). Iterative method applied to image reconstruction and to computer-generated holograms. *Optical Engineering*, 19(3):297–305.

[Fienup, 1982] Fienup, J. R. (1982). Phase retrieval algorithms: a comparison. *Applied optics*, 21(15):2758–2769.

[Fitch et al., 2005] Fitch, A. J., Kadyrov, A., Christmas, W. J., and Kittler, J. (2005). Fast robust correlation. *IEEE Transactions on Image Processing*, 14(8):1063–1073.

[Flasseur et al., 2017a] Flasseur, O., Denis, L., Fournier, C., and Thiébaut, E. (2017a). Robust object characterization from lensless microscopy videos. In *2017 25th European Signal Processing Conference (EUSIPCO)*, pages 1445–1449. IEEE.

[Flasseur et al., 2019] Flasseur, O., Denis, L., Thiébaut, É., Olivier, T., and Fournier, C. (2019). Expaco: detection of an extended pattern under nonstationary correlated noise by patch covariance modeling. In *2019 27th European Signal Processing Conference (EUSIPCO)*, pages 1–5. IEEE.

[Flasseur et al., 2017b] Flasseur, O., Fournier, C., Verrier, N., Denis, L., Jolivet, F., Cazier, A., and Lépine, T. (2017b). Self-calibration for lensless color microscopy. *Applied optics*, 56(13):F189–F199.

[Fogel et al., 2016] Fogel, F., Waldspurger, I., and d'Aspremont, A. (2016). Phase retrieval for imaging problems. *Mathematical programming computation*, 8(3):311–335.

[Forbes et al., 2007] Forbes, B. A., Sahm, D. F., Weissfeld, A. S., et al. (2007). *Diagnostic microbiology*. Mosby St Louis.

[Fornasier and Rauhut, 2008] Fornasier, M. and Rauhut, H. (2008). Recovery algorithms for vector-valued data with joint sparsity constraints. *SIAM Journal on Numerical Analysis*, 46(2):577–613.

[Fournier et al., 2010] Fournier, C., Denis, L., and Fournel, T. (2010). On the single point resolution of on-axis digital holography. *JOSA A*, 27(8):1856–1862.

[Fournier et al., 2017] Fournier, C., Jolivet, F., Denis, L., Verrier, N., Thiebaut, E., Allier, C., and Fournel, T. (2017). Pixel super-resolution in digital holography by regularized reconstruction. *Applied optics*, 56(1):69–77.

[Gabor, 1948] Gabor, D. (1948). A New Microscopic Principle. *Nature*, 161:777–778.

[Gabor, 1948] Gabor, D. (1948). A new microscope principle. *Nature*, (1161):777.

[Garcia-Sucerquia et al., 2006] Garcia-Sucerquia, J., Xu, W., Jericho, S. K., Klages, P., Jericho, M. H., and Kreuzer, H. J. (2006). Digital in-line holographic microscopy. *Applied optics*, 45(5):836–850.

[Gerchberg, 1972] Gerchberg, R. W. (1972). A practical algorithm for the determination of plane from image and diffraction pictures. *Optik*, 35(2):237–246.

[Gibson and Lanni, 1991] Gibson, S. F. and Lanni, F. (1991). Experimental test of an analytical model of aberration in an oil-immersion objective lens used in three-dimensional light microscopy. *JOSA A*, 8(10):1601–1613.

[Gillespie and King, 1989] Gillespie, J. and King, R. A. (1989). The use of self-entropy as a focus measure in digital holography. *Pattern recognition letters*, 9(1):19–25.

[Golub et al., 1979] Golub, G. H., Heath, M., and Wahba, G. (1979). Generalized cross-validation as a method for choosing a good ridge parameter. *Technometrics*, 21(2):215–223.

[Goodman, 2004] Goodman, J. W. (2004). *Introduction to Fourier optics, 3rd ed.* Roberts & Co. Publishers, Englewood, Colorado.

[Goodman, 2005] Goodman, J. W. (2005). Introduction to fourier optics, roberts & co. *Publishers, Englewood, Colorado*.

[Goodwin and Wyant, 2006] Goodwin, E. P. and Wyant, J. C. (2006). Field guide to interferometric optical testing. SPIE Bellingham, WA.

[Greenbaum and Ozcan, 2012] Greenbaum, A. and Ozcan, A. (2012). Maskless imaging of dense samples using pixel super-resolution based multi-height lensfree on-chip microscopy. *Optics express*, 20(3):3129–3143.

[Hadamard, 1902] Hadamard, J. (1902). Sur les problèmes aux dérivées partielles et leur signification physique. *Princeton university bulletin*, pages 49–52.

[Haeberlé, 2004] Haeberlé, O. (2004). Focusing of light through a stratified medium: a practical approach for computing fluorescence microscope point spread functions. Part II: confocal and multiphoton microscopy. *Optics Communications*, 235:1–10.

[Hansen, 1992] Hansen, P. C. (1992). Analysis of discrete ill-posed problems by means of the l-curve. *SIAM review*, 34(4):561–580.

[Hansen and O'Leary, 1993] Hansen, P. C. and O'Leary, D. P. (1993). The use of the l-curve in the regularization of discrete ill-posed problems. *SIAM journal on scientific computing*, 14(6):1487–1503.

[Herve et al., 2018] Herve, L., Cioni, O., Blandin, P., Navarro, F., Menneteau, M., Bordy, T., Morales, S., and Allier, C. (2018). Multispectral total-variation reconstruction applied to lens-free microscopy. *Biomedical Optics Express*, 9(11):5828.

[Holland and Welsch, 1977] Holland, P. W. and Welsch, R. E. (1977). Robust regression using iteratively reweighted least-squares. *Communications in Statistics-theory and Methods*, 6(9):813–827.

[Hsieh et al., 2020] Hsieh, Y., Yu, Y., Lai, Y., Hsieh, M., and Chen, Y.-F. (2020). Integral-based parallel algorithm for the fast generation of the zernike polynomials. *Optics Express*, 28(2):936–947.

[Huber, 2011] Huber, P. J. (2011). *Robust statistics*. Springer.

[Isikman et al., 2010] Isikman, S. O., Sencan, I., Mudanyali, O., Bishara, W., Oztoprak, C., and Ozcan, A. (2010). Color and monochrome lensless on-chip imaging of Caenorhabditis elegans over a wide field-of-view. *Lab on a Chip*, 10(9):1109–1112. Publisher: The Royal Society of Chemistry.

[Jolivet, 2018] Jolivet, F. (2018). *Approches "problèmes inverses régularisées pour l'imagerie sans lentille et la microscopie holographique en ligne*. PhD thesis. Thèse de doctorat dirigée par Fournel, Thierry et Fournier, Corinne.

[Jolivet et al., 2018] Jolivet, F., Momey, F., Denis, L., Méès, L., Faure, N., Grosjean, N., Pinston, F., Marié, J.-L., and Fournier, C. (2018). Regularized reconstruction of absorbing and phase objects from a single in-line hologram, application to fluid mechanics and micro-biology. *Optics express*, 26(7):8923–8940.

[Karl, 2005] Karl, W. C. (2005). Regularization in image restoration and reconstruction. In *Handbook of Image and Video Processing*, pages 183–V. Elsevier.

[Kay, 1993] Kay, S. M. (1993). *Fundamentals of statistical signal processing*. Prentice Hall PTR.

[Keller, 1976] Keller, J. B. (1976). The american mathematical monthly. *Inverse Problems*, 83:107–118.

[Kim et al., 2022] Kim, G., Ahn, D., Kang, M., Park, J., Ryu, D., Jo, Y., Song, J., Ryu, J. S., Choi, G., Chung, H. J., Kim, K., Chung, D. R., Yoo, I. Y., Huh, H. J., Min, H.-s., Lee, N. Y., and Park, Y. (2022). Rapid species identification of pathogenic bacteria from a minute quantity exploiting three-dimensional quantitative phase imaging and artificial neural network. *Light, Science & Applications*, 11:190.

[Kreis, 2006] Kreis, T. (2006). *Handbook of holographic interferometry: optical and digital methods*. John Wiley & Sons.

[Lakshminarayanan and Fleck, 2011] Lakshminarayanan, V. and Fleck, A. (2011). Zernike polynomials: a guide. *Journal of Modern Optics*, 58(7):545–561.

[Lamadie et al., 2012] Lamadie, F., Bruel, L., and Himbert, M. (2012). Digital holographic measurement of liquid–liquid two-phase flows. *Optics and Lasers in Engineering*, 50(12):1716–1725.

[Langehanenberg et al., 2011] Langehanenberg, P., von Bally, G., and Kemper, B. (2011). Autofocusing in digital holographic microscopy. *3D Research*, 2(1):1–11.

[Latychevskaia and Fink, 2007] Latychevskaia, T. and Fink, H.-W. (2007). Solution to the twin image problem in holography. *Physical review letters*, 98(23):233901.

[Latychevskaia and Fink, 2015] Latychevskaia, T. and Fink, H.-W. (2015). Reconstruction of purely absorbing, absorbing and phase-shifting, and strong phase-shifting objects from their single-shot in-line holograms. *Appl. Opt.*, 54(13):3925–3932.

[Lawson and Hanson, 1995] Lawson, C. L. and Hanson, R. J. (1995). *Solving least squares problems*. SIAM.

[Lee et al., 2007] Lee, S.-H., Roichman, Y., Yi, G.-R., Kim, S.-H., Yang, S.-M., Van Blaaderen, A., Van Oostrum, P., and Grier, D. G. (2007). Characterizing and tracking single colloidal particles with video holographic microscopy. *Optics express*, 15(26):18275–18282.

[Leith and Upatnieks, 1962] Leith, E. N. and Upatnieks, J. (1962). Reconstructed wavefronts and communication theory. *JOSA*, 52(10):1123–1130.

[Li et al., 2017] Li, J., Xue, F., and Blu, T. (2017). Fast and accurate three-dimensional point spread function computation for fluorescence microscopy. *JOSA A*, 34(6):1029–1034. Publisher: Optica Publishing Group.

[Li et al., 2018] Li, J., Xue, F., Qu, F., Ho, Y.-P., and Blu, T. (2018). On-the-fly estimation of a microscopy point spread function. *Optics Express*, 26(20):26120–26133. Publisher: Optica Publishing Group.

[Lucarini et al., 2005] Lucarini, V., Saarinen, J. J., Peiponen, K.-E., and Vartiainen, E. M. (2005). *Kramers-Kronig relations in optical materials research*, volume 110. Springer Science & Business Media.

[Luo et al., 2015] Luo, W., Greenbaum, A., Zhang, Y., and Ozcan, A. (2015). Synthetic aperture-based on-chip microscopy. *Light: Science & Applications*, 4(3):e261–e261. Number: 3 Publisher: Nature Publishing Group.

[Malik et al., 2020] Malik, R., Sharma, P., Poulose, S., Ahlawat, S., and Khare, K. (2020). A practical criterion for focusing of unstained cell samples using a digital holographic microscope. *Journal of Microscopy*, 279(2):114–122.

[Mallat and Zhang, 1993] Mallat, S. G. and Zhang, Z. (1993). Matching pursuits with time-frequency dictionaries. *IEEE Transactions on signal processing*, 41(12):3397–3415.

[Mariën et al., 2020] Mariën, J., Stahl, R., Lambrechts, A., van Hoof, C., and Yurt, A. (2020). Color lens-free imaging using multi-wavelength illumination based phase retrieval. *Optics Express*, 28(22):33002–33018.

[Marquet et al., 2005] Marquet, P., Rappaz, B., Magistretti, P. J., Cuche, E., Emery, Y., Colomb, T., and Depeursinge, C. (2005). Digital holographic microscopy: a noninvasive contrast imaging technique allowing quantitative visualization of living cells with subwavelength axial accuracy. *Optics letters*, 30(5):468–470.

[Martin et al., 2021] Martin, C., Leahy, B., and Manoharan, V. N. (2021). Improving holographic particle characterization by modeling spherical aberration. *Optics Express*, 29(12):18212.

[McNally et al., 1999] McNally, J. G., Karpova, T., Cooper, J., and Conchello, J. A. (1999). Three-Dimensional Imaging by Deconvolution Microscopy. *Methods*, 19(3):373–385.

[Méès et al., 2013] Méès, L., Grosjean, N., Chareyron, D., Marié, J.-L., Seifi, M., and Fournier, C. (2013). Evaporating droplet hologram simulation for digital in-line holography setup with divergent beam. *JOSA A*, 30(10):2021–2028.

[Memmolo et al., 2014] Memmolo, P., Paturzo, M., Javidi, B., Netti, P. A., and Ferraro, P. (2014). Refocusing criterion via sparsity measurements in digital holography. *Optics letters*, 39(16):4719–4722.

[Min et al., 2017] Min, J., Yao, B., Ketelhut, S., Engwer, C., Greve, B., and Kemper, B. (2017). Simple and fast spectral domain algorithm for quantitative phase imaging of living cells with digital holographic microscopy. *Optics Letters*, 42(2):227–230.

[Mo et al., 2009] Mo, X., Kemper, B., Langehanenberg, P., Vollmer, A., Xie, J., and von Bally, G. (2009). Application of color digital holographic microscopy for analysis of stained tissue sections. In *European Conference on Biomedical Optics*, page 7367_18. Optica Publishing Group.

[Momey et al., 2019] Momey, F., Denis, L., Olivier, T., and Fournier, C. (2019). From fienup's phase retrieval techniques to regularized inversion for in-line holography: tutorial. *JOSA A*, 36(12):D62–D80.

[Nocedal and Wright, 2006] Nocedal, J. and Wright, S. (2006). *Numerical optimization*. Springer Science & Business Media.

[Noll, 1976] Noll, R. J. (1976). Zernike polynomials and atmospheric turbulence. *JOSA*, 66(3):207–211.

[Olivier et al., 2022] Olivier, T., Brault, D., Joshi, S., Brard, T., Brodoline, A., Méès, L., and Fournier, C. (2022). Effects of some model approximations in the reconstructions of digital in-line holograms: simulations, experiments on calibrated objects and model refinement assessment. In Georges, M. P., Popescu, G., and Verrier, N., editors, *Unconventional Optical Imaging III*, volume 12136, pages 7 – 17. International Society for Optics and Photonics, SPIE.

[Oraintara et al., 2000] Oraintara, S., Karl, W. C., Castanon, D. A., and Nguyen, T. Q. (2000). A method for choosing the regularization parameter in generalized tikhonov regularized linear inverse problems. In *Proceedings 2000 International Conference on Image Processing (Cat. No. 00CH37101)*, volume 1, pages 93–96. IEEE.

[Popescu, 2011] Popescu, G. (2011). *Quantitative phase imaging of cells and tissues*. McGraw-Hill Education.

[Powell, 2015] Powell, M. J. (2015). On fast trust region methods for quadratic models with linear constraints. *Mathematical Programming Computation*, 7(3):237–267.

[Prescott et al., 2002] Prescott, L. M. et al. (2002). *Microbiology*.

[Ramani et al., 2008] Ramani, S., Blu, T., and Unser, M. (2008). Monte-carlo sure: A black-box optimization of regularization parameters for general denoising algorithms. *IEEE Transactions on image processing*, 17(9):1540–1554.

[Rivenson et al., 2016] Rivenson, Y., Wu, Y., Wang, H., Zhang, Y., Feizi, A., and Ozcan, A. (2016). Sparsity-based multi-height phase recovery in holographic microscopy. *Scientific reports*, 6(1):1–9.

[Rodriguez et al., 2013] Rodriguez, J. A., Xu, R., Chen, C.-C., Zou, Y., and Miao, J. (2013). Oversampling smoothness: an effective algorithm for phase retrieval of noisy diffraction intensities. *Journal of applied crystallography*, 46(2):312–318.

[Rousseeuw and Hubert, 2011] Rousseeuw, P. J. and Hubert, M. (2011). Robust statistics for outlier detection. *Wiley interdisciplinary reviews: Data mining and knowledge discovery*, 1(1):73–79.

[Rudin et al., 1992] Rudin, L. I., Osher, S., and Fatemi, E. (1992). Nonlinear total variation based noise removal algorithms. *Physica D: nonlinear phenomena*, 60(1-4):259–268.

[Sai et al., 2020] Sai, T., Saba, M., Dufresne, E. R., Steiner, U., and Wilts, B. D. (2020). Designing refractive index fluids using the Kramers–Kronig relations. *Faraday Discuss.*, 223(0):136–144. Publisher: The Royal Society of Chemistry.

[Sarder and Nehorai, 2006] Sarder, P. and Nehorai, A. (2006). Deconvolution methods for 3-D fluorescence microscopy images. *IEEE Signal Processing Magazine*, 23(3):32–45.

[Shechtman et al., 2014] Shechtman, Y., Beck, A., and Eldar, Y. C. (2014). Gespar: Efficient phase retrieval of sparse signals. *IEEE transactions on signal processing*, 62(4):928–938.

[Sibiryakov, 2011] Sibiryakov, A. (2011). Fast and high-performance template matching method. In *CVPR 2011*, pages 1417–1424. IEEE.

[Singh et al., 2012] Singh, A. S., Anand, A., Leitgeb, R. A., and Javidi, B. (2012). Lateral shearing digital holographic imaging of small biological specimens. *Opt. Express*, 20(21):23617–23622.

[Sinha et al., 2017] Sinha, A., Malo, P., and Deb, K. (2017). A review on bilevel optimization: from classical to evolutionary approaches and applications. *IEEE Transactions on Evolutionary Computation*, 22(2):276–295.

[Slimani et al., 1984] Slimani, F., Gréhan, G., Gouesbet, G., and Allano, D. (1984). Near-field lorenz-mie theory and its application to microholography. *Applied optics*, 23(22):4140–4148.

[Smith et al., 2018] Smith, K. P., Kang, A. D., and Kirby, J. E. (2018). Automated interpretation of blood culture gram stains by use of a deep convolutional neural network. *Journal of Clinical Microbiology*, 56(3):e01521–17.

[Song et al., 2016] Song, J., Leon Swisher, C., Im, H., Jeong, S., Pathania, D., Iwamoto, Y., Pivovarov, M., Weissleder, R., and Lee, H. (2016). Sparsity-based pixel super resolution for lens-free digital in-line holography. *Scientific reports*, 6(1):1–9.

[Sotthivirat and Fessler, 2004] Sotthivirat, S. and Fessler, J. A. (2004). Penalized-likelihood image reconstruction for digital holography. *JOSA A*, 21(5):737–750.

[Soubies et al., 2019] Soubies, E., Soulez, F., McCann, M. T., Pham, T.-a., Donati, L., Debarre, T., Sage, D., and Unser, M. (2019). Pocket guide to solve inverse problems with globalbioim. *Inverse Problems*, 35(10):104006.

[Soulez et al., 2007a] Soulez, F., Denis, L., Fournier, C., Thiébaut, É., and Goepfert, C. (2007a). Inverse-problem approach for particle digital holography: accurate location based on local optimization. *JOSA A*, 24(4):1164–1171.

[Soulez et al., 2007b] Soulez, F., Denis, L., Thiébaut, É., Fournier, C., and Goepfert, C. (2007b). Inverse problem approach in particle digital holography: out-of-field particle detection made possible. *JOSA A*, 24(12):3708–3716.

[Soulez et al., 2012] Soulez, F., Denis, L., Tourneur, Y., and Thiebaut, E. (2012). Blind deconvolution of 3D data in wide field fluorescence microscopy. In *2012 9th IEEE International Symposium on Biomedical Imaging (ISBI)*, pages 1735–1738, Barcelona, Spain. IEEE.

[Soulez et al., 2022] Soulez, F., Rostykus, M., Moser, C., and Unser, M. (2022). A COnstrained Method for lensless Coherent Imaging of thin samples. *Applied optics*, 61(9):F34–F46.

[Stein, 1981] Stein, C. M. (1981). Estimation of the mean of a multivariate normal distribution. *The annals of Statistics*, pages 1135–1151.

[Tarantola, 2005] Tarantola, A. (2005). *Inverse problem theory and methods for model parameter estimation*. SIAM.

[Tikhonov, 1963] Tikhonov, A. N. (1963). On the solution of ill-posed problems and the method of regularization. In *Doklady Akademii Nauk*, volume 151, pages 501–504. Russian Academy of Sciences.

[Tillmann et al., 2016] Tillmann, A. M., Eldar, Y. C., and Mairal, J. (2016). Dolphin—dictionary learning for phase retrieval. *IEEE Transactions on Signal Processing*, 64(24):6485–6500.

[Turchin et al., 1971] Turchin, V. F., Kozlov, V. P., and Malkevich, M. S. (1971). The use of mathematical-statistics methods in the solution of incorrectly posed problems. *Soviet Physics Uspekhi*, 13(6):681.

[Verrier et al., 2014] Verrier, N., Fournier, C., Méès, L., and Fournel, T. (2014). In-line particle holography with an astigmatic beam: setup self-calibration using an "inverse problems" approach. *Applied optics*, 53(27):G147–G156.

[Wahba, 1990] Wahba, G. (1990). *Spline models for observational data*. SIAM.

[Wang et al., 2016] Wang, A., Garmann, R. F., and Manoharan, V. N. (2016). Tracking E. coli runs and tumbles with scattering solutions and digital holographic microscopy. *Opt. Express*, 24(21):23719–23725. Publisher: Optica Publishing Group.

[Wolf, 1969] Wolf, E. (1969). Three-dimensional structure determination of semi-transparent objects from holographic data. *Optics Communications*, 1(4):153–156.

[Xia et al., 2011] Xia, P., Shimozato, Y., Ito, Y., Tahara, T., Kakue, T., Awatsuji, Y., Nishio, K., Ura, S., Kubota, T., and Matoba, O. (2011). Improvement of color reproduction in color digital holography by using spectral estimation technique. *Appl. Opt.*, 50(34):H177–H182.

[Xu et al., 2001] Xu, L., Peng, X., Miao, J., and Asundi, A. K. (2001). Studies of digital microscopic holography with applications to microstructure testing. *Applied Optics*, 40(28):5046–5051. Publisher: Optica Publishing Group.

[Zernike, 1942] Zernike, F. (1942). Phase contrast, a new method for the microscopic observation of transparent objects. *Physica*, 9(7):686–698.

[Zhang et al., 2017] Zhang, Y., Wang, H., Wu, Y., Tamamitsu, M., and Ozcan, A. (2017). Edge sparsity criterion for robust holographic autofocusing. *Optics letters*, 42(19):3824–3827.

[Zheng et al., 2013] Zheng, G., Ou, X., Horstmeyer, R., and Yang, C. (2013). Characterization of spatially varying aberrations for wide field-of-view microscopy. *Optics Express*, 21(13):15131–15143. Publisher: Optical Society of America.

List of publications

Journal

[1] Laurence Denneulin, Fabien Momey, **Dylan Brault**, Matthieu Debailleul, Asemare Mengistie Taddese, Nicolas Verrier, and Olivier Haeberlé. Gsure criterion for unsupervised regularized reconstruction in tomographic diffractive microscopy. *J. Opt. Soc. Am. A*, 39(2):A52–A61, Feb 2022.

[2] **Dylan Brault**, Corinne Fournier, Thomas Olivier, Nicolas Faure, Sophie Dixneuf, Louis Thibon, Loïc Mees, and Loïc Denis. Automatic numerical focus plane estimation in digital holographic microscopy using calibration beads. *Applied Optics*, 61(5):B345–B355, 2022.

[3] **Dylan Brault**, Thomas Olivier, Ferréol Soulez, Sachin Joshi, Nicolas Faure, and Corinne Fournier. Accurate unsupervised estimation of aberrations in digital holographic microscopy for improved quantitative reconstruction. *Optics Express*, 30(21):38383–38404, 2022.

IEEE International Conferences

[4] **Dylan Brault**, Loïc Denis, Sophie Dixneuf, Thomas Olivier, Nicolas Faure, and Corinne Fournier. Fast and robust pattern detection: Application to spherical bead localization in holographic microscopy. accepted in IEEE European Signal Processing Conference (EUSIPCO), 09/2022.

Other International Conferences

[5] Laurence Denneulin, Fabien Momey, and **D. Brault**. Gsure criterion for unspervised regularized reconstruction in tomographic diffractive microscopy. In *OSA Imaging and Applied Optics Congress 2021 (3D, COSI, DH, ISA, pcAOP)*, page DM5E.5. Optica Publishing Group, 2021.

[6] Corinne Fournier, **Dylan Brault**, Thomas Olivier, Nicolas Faure, Sophie Dixneuf, Louis Thibon, Loïc Méès, and Loïc Denis. Robust autofocus for digital-holographic

microscopy. In *Digital Holography and Three-Dimensional Imaging*, pages DM5E–4. Optica Publishing Group, 2021.

[7] Corinne Fournier, **Dylan Brault**, Thomas Olivier, Nicolas Faure, Sophie Dixneuf, Louis Thibon, Loic Mees, and Loïc Denis. Focus plane estimation in digital holographic microscopy. In Marc P. Georges, Gabriel Popescu, and Nicolas Verrier, editors, *Unconventional Optical Imaging III*, volume PC12136, page PC1213615. International Society for Optics and Photonics, SPIE, 2022.

[8] Thomas Olivier, **Dylan Brault**, Sachin Joshi, Thomas Brard, Alexey Brodoline, Loïc Méès, and Corinne Fournier. Effects of some model approximations in the reconstructions of digital in-line holograms: simulations, experiments on calibrated objects and model refinement assessment. In Marc P. Georges, Gabriel Popescu, and Nicolas Verrier, editors, *Unconventional Optical Imaging III*, volume 12136, pages 7 – 17. International Society for Optics and Photonics, SPIE, 2022.

[9] **Dylan Brault**, Anthony Berdeu, Ferréol Soulez, Fabien Momey, Thomas Olivier, Loïc Denis, and Corinne Fournier. Reconstruct-to-refocus: joint reconstruction of a biological sample and of calibration objects for accurate auto-focusing in digital holography. In *Digital Holography and Three-Dimensional Imaging*, pages DW4C–8. Optica Publishing Group, 2021.

[10] **Dylan Brault**, Thomas Olivier, Corinne Fournier, and Arun Anand. Inverse problem approach for the reconstruction of lateral shearing digital holograms. In Corinne Fournier, Marc P. Georges, and Gabriel Popescu, editors, *Unconventional Optical Imaging II*, volume 11351, page 1135111. International Society for Optics and Photonics, SPIE, 2020.

[11] Carlos Valadares, **Dylan Brault**, Loïc Denis, and Corinne Fournier. Spherical object segmentation in digital holographic microscopy by deep-learning. In *Unconventional Optical Imaging II*, volume 11351, pages 207–216. SPIE, 2020.

GdR Workshops

[12] Laurence Denneulin, Fabien Momey, and **Dylan Brault**. Approche inverse non-supervisée pour la microscopie tomographique diffractive (poster). Journées de l'Imagerie Optique Non Conventionnelle (JIONC) -GdR ISIS, 2021.

[13] Laurence Denneulin, Fabien Momey, **Dylan Brault**, Matthieu Debailleul, Asemare Mengistie Taddese, Nicolas Verrier, and Olivier Haeberlé. Approche inverse régularisée non supervisée pour la reconstruction 3d en microscopie tomographique diffractive. Journées de l'Imagerie Optique Non Conventionnelle (JIONC) -GdR ISIS, 2022.

[14] Corinne Fournier, **Dylan Brault**, Thomas Olivier, Nicolas Faure, Sophie Dixneuf, Louis Thibon, and Loïc Denis. Autofocus numérique en microscopie holographique. Journées de l'Imagerie Optique Non Conventionnelle (JIONC) -GdR ISIS, 2022 (POSTER).

[15] **Dylan Brault**, Anthony Berdeu, Ferréol Soulez, Fabien Momey, Thomas Olivier, Loïc Denis, and Corinne Fournier. Reconstruction conjointe d'échantillons biologiques and d'objands d'étalonnage pour la mise au point automatique en microscopie holographique. Journées de l'Imagerie Optique Non Conventionnelle (JIONC) -GdR ISIS, 2021.

[16] **Dylan Brault**, Thomas Olivier, Corinne Fournier, and Arun Anand. Approche problème inverse pour la reconstruction d'hologrammes obtenus par interféromètrie à décalage latéral. Journées de l'Imagerie Optique Non Conventionnelle (JIONC) -GdR ISIS, 2020.

[17] **Dylan Brault**, Thomas Olivier, Ferréol Soulez, Sophie Dixneuf, Nicolas Faure, and Corinne Fournier. Reconstructions multisprectrales d'échantillons biologiques avec autocalibration des aberrations chromatiques. Journées de l'Imagerie Optique Non Conventionnelle (JIONC) -GdR ISIS, 2022.

Informal Communications

[18] **Dylan Brault**, Anthony Berdeu, Ferréol Soulez, Fabien Momey, Thomas Olivier, Loïc Denis, and Corinne Fournier. Mise au point automatique and reconstruction d'échantillons biologiques par insertion d'objands d'étalonnage en microscopie holographique. In GRETSI Summer School, 2021.

[19] **Dylan Brault**, Loïc Denis, Sophie Dixneuf, Thomas Olivier, Nicolas Faure, and Corinne Fournier. Fast and robust dandection of calibration objects for in-line holography (poster). In Mifobio - GDR Imabio, 2021.

[20] **Dylan Brault**, Thomas Momey, Fabien Olivier, Ferréol Soulez, Sachin Joshi, and Corinne Fournier. Problèmes inverses pour la reconstruction quantitative de phase en microscopie holographique : une méthodologie pour l'auto-étalonnage des reconstructions. This presentation was realized during a seminar for the Image Science and Computer Vision team at laboratoire Hubert Curien, 2022.

[21] **Dylan Brault**, Thomas Olivier, Fabien Momey, Ferréol Soulez, Loïc Denis, and Corinne Fournier. Holographic microscopy for biological samples analysis. This poster was realized for the HCERES evalutation of the laboratory, 2020.

[22] **Dylan Brault**, Ferréol Soulez, Thomas Olivier, Fabien Momey, and Corinne Fournier. Problèmes inverses pour la reconstruction quantitative de phase appliqués à la microscopie holographique. Journée de la recherche de l'Université Jean Monnet 2022.

Résumé :
L'holographie en ligne est une méthode de choix pour s'affranchir de la problématique de la mise au point indispensable à l'analyse d'échantillons en microscopie en la remplaçant par une mise au point numérique, rendant cette dernière totalement automatisable. L'absorption des objets et le déphasage introduit par ces derniers peuvent être reconstruits et une information spectrale peut être exploitée pour classifier les objets. Dans ce contexte, les approches problèmes inverses offrent un cadre rigoureux. Cependant, la qualité des reconstructions peut être limitée par différents aspects tels qu'un manque de précision sur le modèle de formation d'image ou encore un mauvais réglage des hyperparamètres nécessaires à la reconstruction. Pour lever ces différents verrous, nous proposons une méthodologie basée sur l'insertion de billes d'étalonnage dans l'échantillon. Ainsi la mise au point et l'étalonnage des aberrations du modèle de formation d'image sont traités au moyen d'approches inverses paramétriques robustes. Le réglage d'hyperparamètres de régularisation est optimisé pour reconstruire quantitativement les objets d'intérêt. Enfin, la reconstruction d'informations multispectrales est améliorée par la prise en compte des aberrations chromatiques. Ceci permet une reconstruction plus reproductible dans le champ et d'un instrument à un autre, facilitant ensuite l'utilisation d'algorithmes de machine learning. Toute la méthodologie de reconstruction développée dans le cadre de cette thèse, illustrée dans le cas de l'analyse de Gram, est très générale et peut être appliquée dans d'autres contextes de microscopie ou à d'autres modalité d'imagerie non conventionnelle.

Abstract:
Holography is a method of choice to avoid the experimental focusing problem in sample analysis by replacing it by a numerical refocus. Thus, sample analysis can be completely automatized. The absorption of the objects and the phase shift they introduce can be reconstructed and a spectral information can be exploited to classify the objects. In this context, inverse problems approaches are a rigorous framework to perform the reconstructions. However, their quality can be limited by several aspects such as a lack of accuracy on the image formation model or a bad tuning of the hyperparameters needed for the reconstruction. To tackle these different issues we propose a method based on the insertion of calibration beads directly into the sample. Thus, the autofocusing problem or the accurate model calibration considering aberrations of the optical system are addressed using robust parametric inverse problems approaches. The tuning of the regularization hyperparameters is automated such that the objects of interest are quantitatively reconstructed. At last, the reconstructed spectral information is improved by accounting for chromatic aberrations of the optical system. The reconstructions are thus more reproducible in the field of view and from one setup to another. Machine learning algorithm can thus be used regardless of the setup. The method developed in this thesis, illustrated by Gram stained samples, is general and can be applied in other microscopy context and other non-conventional imaging modalities.